FAULT DIAGNOSIS OF GEARBOX AND ELECTROMECHANICAL SYSTEM USING HYBRID DEEP LEARNING ARCHITECTURES

Ph.D. Thesis

By YOGESH SAHEBRAO ANDHALE



DEPARTMENT OF MECHANICAL ENGINEERING INDIAN INSTITUTE OF TECHNOLOGY INDORE

FEBRUARY 2025

FAULT DIAGNOSIS OF GEARBOX AND ELECTROMECHANICAL SYSTEM USING HYBRID DEEP LEARNING ARCHITECTURES

A THESIS

Submitted in partial fulfillment of the requirements for the award of the degree

of

DOCTOR OF PHILOSOPHY

by

YOGESH SAHEBRAO ANDHALE



DEPARTMENT OF MECHANICAL ENGINEERING INDIAN INSTITUTE OF TECHNOLOGY INDORE

FEBRUARY 2025



INDIAN INSTITUTE OF TECHNOLOGY INDORE

I hereby certify that the work which is being presented in the thesis entitled FAULT DIAGNOSIS OF GEARBOX AND ELECTROMECHANICAL SYSTEM USING HYBRID DEEP LEARNING ARCHITECTURES in the partial fulfillment of the requirements for the award of the degree of DOCTOR OF PHILOSOPHY and submitted in the DEPARTMENT OF MECHANICAL ENGINEERING, INDIAN INSTITUTE OF TECHNOLOGY INDORE is an authentic record of my own work carried out during the time period from August 2020 to February 2025 under the supervision of Prof. ANAND PAREY, Professor, Department of Mechanical Engineering, IIT Indore.

The matter presented in this thesis has not been submitted by me for the award of any other degree of this or any other institute.

TO GESHANDHALLE
YOGESH SAHEBRAO ANDHALE
This is to certify that the above statement made by the candidate is correct to the best of
my/our knowledge.
and
PROF. ANAND PAREY
YOGESH SAHEBRAO ANDHALE has successfully given his Ph.D. Oral Examination
held on Date of PhD Oral Examination .

(01/08/2025) PROF. ANAND PAREY

iii

Dedicated to

My parents (late) Smt. Sindhu and

Shr. Sahebrao who shaped me as the person

I am today

and

My wife Dr. Kavita and my daughter Yashika and son
Ishan have been a tremendous source of support for me
in achieving my goals

ACKNOWLEDGEMENT

I would like to express my deepest gratitude to my enthusiastic supervisor, **Prof. Anand Parey**, for his unwavering support throughout my research journey. My Ph.D. experience has been truly enriching, and I sincerely thank Prof. Parey not only for his invaluable academic guidance but also for believing in me and providing countless opportunities that contributed to my overall development.

I extend my heartfelt thanks to my Ph.D. progress committee members, **Dr. Saptarshi Ghosh** and **Dr. Girish Chandra Verma**, for their insightful suggestions and guidance from the very beginning of my research work. I am also immensely grateful to **Prof. Shanmugam Dhinakaran**, Head of the Department of Mechanical Engineering, for facilitating my research by providing essential infrastructure and opportunities.

A special note of appreciation goes to **Mr. Sandeep Patil**, Deputy Manager of the Vibration and Noise Control Lab, for his unwavering assistance and support throughout my experimental work.

I am profoundly thankful to my past and present laboratory colleagues, **Dr. Dada**Saheb Ramteke, **Dr. Palash Dewangan**, **Dr. Pavan Gupta**, **Dr. Anupam Kumar**, **Mr.**Santosh Yadav, **Mrs. Pallavi Gautam**, **Dr. Vikas Sharma**, **Dr. Naresh Kumar**Raghuwanshi, **Dr. Ankur Saxena**, **Dr. Yogesh Pandya**, and all the members of the Vibration and Noise Control Lab and System Dynamics Lab. Their constant encouragement and camaraderie made my Ph.D. journey both productive and memorable.

I would also like to extend my sincere thanks to my research colleagues and friends, especially **Dr. Anuj Kumar**, **Dr. Rajnish Modanwal**, **Dr. Devashish Chorey**, **Dr. Vivek Rana**, **Dr. Pankaj Gupta**, **Dr. Vishal Jagdale**, and **Dr. Bhavesh Chaudhary**, for their endless support and motivation throughout the course of my research.

My deepest gratitude goes to my parents, my late mother, Mrs. Sindhu Andhale, and my father, Mr. Sahebrao Andhale, for their sacrifices, unwavering support, and wise guidance. Their belief in me has been a pillar of strength throughout my life. I am also grateful to my brother, Mr. Nilesh Andhale, and sister-in-law, Sheetal Andhale, for their encouragement and love.

A special and heartfelt thanks to my beloved wife, **Dr. Kavita Andhale**, for her unconditional love, care, and support. Her patience and understanding have been my

greatest source of strength. I also express my love and gratitude to my wonderful children, Yashika Andhale and Ishan Andhale, for being my constant source of joy and stress relief.

Lastly, I extend my gratitude to all those who supported and helped me, directly or indirectly, throughout this journey. Above all, I thank the **Almighty** for His countless blessings and guidance.

Yogesh Sahebrao Andhale

ABSTRACT

Gearboxes, being essential elements in sectors such as manufacturing, transportation, and power generation, are highly susceptible to failures, including gear cracks, misalignment, and wear. Such faults can cause catastrophic system breakdowns, prolonged production downtimes, and costly repairs. Early detection of these faults is crucial for preventing system failures and ensuring smooth operation. Similarly, electromechanical (EM) systems are widely used in industries for various applications. EM systems mostly have an electric motor as a prime mover and a mechanical load, such as a rotor, gearbox, pumps, etc., coupled. EM systems may have combined faults, i.e., faults in motors and faults in loads. Diagnosing combined faults is challenging due to overlapping symptoms and their compounded effects. Hence, advanced fault detection and classification methods are necessary to improve the reliability of gearboxes and EM systems, optimize maintenance scheduling, reduce downtime, and enhance productivity while cutting costs.

This thesis contributes to the field with three significant research developments. The first work introduces an entropy-based feature extraction method for gearbox fault detection. This approach leverages statistical characteristics, higher-order statistical features, and modified entropy measures, including Renyi entropy, modified log-energy entropy, and Shannon entropy, to detect gearbox faults. A hybrid classifier (HC) model combining bidirectional long short-term memory (Bi-LSTM) and recurrent neural network (RNN), optimized using the Opposition-based Artificial Hummingbird Crow Search Algorithm (OAHCSA), is pro- posed. The outputs of the two classifiers are averaged to improve accuracy, allowing effective fault detection at various frequency levels. The results demonstrate exceptional performance and computational efficiency of the proposed OAHCSA-HC model for gearbox fault diagnosis. This model significantly reduced computational time, processing data at 3.30 seconds at 15 Hz, which is approximately 56% faster than the previous CSA-HC model. It also displayed outstanding classification accuracy, with an overall accuracy rate of 99.61% at 15 Hz, which was improved to 99.62% when statistical features were incorporated. The model also showed a high specificity of 99.88%, precision of 99.79%, and sensitivity of 99.54% at 15 Hz, indicating its ability to minimize false positives while accurately detecting faults. These findings state the OAHCSA-HC model is an efficient, precise, and computationally advantageous solution for gearbox fault diagnosis.

The second contribution focuses on an enhanced entropy-based feature extraction method, combining time-frequency domain, frequency-domain, and time-domain characteristics with altered entropy measurements. A pre-processing approach called enhanced complete ensemble empirical mode decomposition with adaptive noise (CEEMDAN) is used to minimize the noise in the obtained raw vibration signal. Data augmentation is used to improve the feature set. Additionally, the combined classification model is applied to the enhanced feature set in order to categorize the various gear crack levels. This hybrid model combines enhanced deep belief network (IDBN) classifiers with Bi-LSTM. The findings demonstrate that integrating Bi-LSTM with IDBN achieved an impressive 99.82% accuracy while maintaining a low computational time of 0.74 seconds. These results demonstrate how well the proposed approach performs as a highly accurate and efficient way to detect gear faults.

The third contribution presents the design of a modified LinkNet and DenseNet-based fault classification model, MLiDNet, to diagnose combined faults in EM systems. The signal preprocessing employs improved synchro-squeezing wavelet transform (ISSWT) and entropy-based feature extraction, including norm, spectral, threshold, and wavelet energy entropy. The extracted features are fed into the MLiDNet hybrid deep learning classifier for accurate and early fault detection. The findings demonstrated that, when trained on 90% of the data at a frequency of 30 Hz, MLiDNet produced exceptional results. The results showed an accuracy of 99.79%, a precision of 99.68%, and an F-measure of 99.37%. MLiDNet maintains efficiency at 2.57 seconds with 90% data and achieves a low computational time of 1.54 seconds with 60% training data, in contrast to other models with more pronounced increases in computational time as the training data increases. In this way, the thesis offers data-driven and experimental methods for classifying bevel gear and electromechanical system faults.

Keywords: Gearbox fault diagnosis, Combined Fault, combined classification model, recur- rent neural network (RNN), deep belief network (DBN), bidirectional long short-term memory (Bi-LSTM), data augmentation, deep learning.

TABLE OF CONTENTS

ACKNOWLEDGEMENT	6
ABSTRACT	8
LIST OF FIGURES	12
LIST OF TABLES	16
Chapter 1	24
1.1 Introduction	24
1.2 Gear and Its Modes of Failure	24
1.3 Machine Condition Monitoring.	26
1.4 Vibration Analysis for Gearbox Fault Diagnosis	27
1.5 Signal Processing Techniques for Gear Fault Detection: An Overview	28
1.6 Electromechanical Systems and Their Common Failures	30
1.7.1 Overview of Machine Learning and Deep Learning Techniques for Gearbox and	EM
system Fault Analysis	36
1.8 Conclusions	39
1.9 Outcomes of the Literature Review	40
1.10 Objectives	42
1.11 Organization of the thesis	42
Chapter 2	44
2.1 Introduction	44
2.2 Proposed Methodology	46
2.3 Extraction of Features	54
2.4 Hybrid Classifiers with Opposition-based Artificial Hummingbird Crow Search	
Algorithm-Based Tuning	58
2.5 Experimental Setup and Data Acquisition	66

	2.6 Res	sults and Discussion	70
	2.7 Co	nclusion	82
C	hapter 3	S	83
	3.1 Inti	roduction	83
	3.2 Pro	pposed Methodology	85
	3.3 Fea	ature Extraction: Overview of Time and Frequency Domain Features and Entrop	ру-
	Bas	sed Features	91
	3.4 BI-	LSTM	97
	3.5 Imp	proved DBN	98
	3.6 Da	ta Acquisition and Experimental Analysis	101
	3.7 Res	sults and Discussion	104
	3.8 Co	nclusion	113
C	hapter 4		115
	4.1 Inti	roduction	115
	4.3 Fea	ature Selection using Chi-Square Test	128
	4.4 Fau	alt Detection via Modified LinkNet and DenseNet Network Model	129
	4.10	Evaluation of Computation Time for Dataset 1	151
	4.11	Evaluation of Computation Time for Dataset 2	154
	4.12	Ablation Evaluation for Dataset 1	158
	4.13	Ablation Study of Proposed Fault Diagnosis for Dataset 2	162
	4.15	Receiver Operating Characteristic Curve Analysis for Dataset 2	171
	4.16	Conclusion	175
C	hapter 5	5	177
	5.1 Co	nclusion	177
	5.2 Fut	ture Scope	179
	REFEE	RENCES	180

LIST OF FIGURES

Figure 1. 1: Various types of gear faults [2]
Figure 1. 2: Schematic representation of Electromechanical system31
Figure 2. 1: Architectural diagram of proposed fault detection model
Figure 2. 2: Time, frequency, and time-frequency domain representations of the healthy
signal
Figure 2. 3: Time, frequency, and time–frequency domain representations of the faulty
signal
Figure 2. 4: Pre-processing analysis of median filtering over conventional methods for
healthy signals (a) Gaussian filtering (b) Low-pass Butterworth filtering (c) Wiener
filtering (d) Median filtering
Figure 2. 5: Pre-processing analysis of median filtering over conventional methods for
faulty signals (a) Gaussian filtering (b) Low-pass Butterworth filtering (c) Wiener
filtering (d) Median filtering53
Figure 2. 6: Experimental test setup
Figure 2. 7: Magnetic break and tri-axial accelerometer
Figure 2. 8: The severity of abrasive wear fault for (a) incipient, (b) slight, (c)
moderate, (d) severe
Figure 2. 9: Comparison of classifiers for (a) Precision, (b) Accuracy, (c) Specificity,
and (d) Sensitivity at 15 Hz
Figure 2. 10: Comparison of classifiers for (a) FDR, (b) FNR, and (c) FPR at 15 Hz 73
Figure 2. 11: Comparison of classifiers for (a) MCC, (b) NPV, and (c) F1-score at 15
Hz
Figure 2. 12: Convergence Study of OAHCSA-HC over existing models
Figure 3. 1: Structure of the proposed methodology85
Figure 3. 2: Various degrees of Raw bevel-gear vibration signals for crack gear faults.8
Figure 3. 3: Signals Preprocessed for Conventional CEEMDAN decomposition a) 15
Hz, b) 20 Hz, c) 25 Hz, and d) 30 Hz
Figure 3. 4: Preprocessed signals for improved CEEMDAN decomposition a) 15 Hz, b)
20 Hz, c) 25 Hz, and d) 30 Hz
Figure 3. 5: An illustration of the crack-level categorization model
Figure 3. 6: The flow of the proposed model98

Figure 3. 7: Swi-Mish activation function with IDBN100
Figure 3. 8: Experimental Setup
Figure 3. 9: Electromechanical elements analytical test rig
Figure 3. 10: Gear health:(a) Healthy (b) A 0.25 mm crack-length gear; (c) a 0.50 mm
crack-length gear; (d) a 0.75 mm crack-length gear; and (e) a 1.00 mm crack-length
gear103
Figure 3. 11: Evaluation of Learning Rate Vs. Computational Time
Figure 3. 12: Confusion matrix for proposed approach a) 15 Hz, b) 20 Hz, c) 25 Hz, and
d) 30 Hz
Figure 3. 13(a): Evaluation of proposed methods in comparison to traditional
techniques for 15 Hz, a) Accuracy, b) F-measure, and c) Precision
Figure 3. 13(b): Evaluation of proposed method in comparison to traditional techniques
for 20 Hz: a) Accuracy, b) F-measure, and c) Precision
Figure 3. 13(c): Evaluation of proposed method in comparison to traditional techniques
for 25 Hz: a) Accuracy, b) F-measure, and c) Precision
Figure 3. 13(d): Evaluation of proposed method in comparison to traditional techniques
for 30 Hz: a) Accuracy, b) F-measure, and c) Precision
Figure 3. 14: Computational time comparison between traditional and proposed
approaches for (a) 15 Hz, (b) 20 Hz, (c) 25 Hz, and (d) 30 Hz110
Figure 4. 1: The suggested MLiDNet model for fault detection
Figure 4. 2: Signal analysis of the following: (a) healthy vibration signal, (b) SSWT
output, and (c) recommended ISSWT output for dataset 1
Figure 4. 3: Analysis of the following signals: (a) faulty vibrational signal, (b) SSWT
output, and (c) suggested output for dataset 112
Figure 4. 4: Analysis of (a) the healthy vibrating signal, (b) the output of the SSWT, and
(c) the output of the proposed technique for dataset 2122
Figure 4. 5: Analysis of the following signals: (a) faulty vibrating signal, (b) SSWT
result, and (c) output from the proposed technique for dataset 2123
Figure 4. 6: Model fusion between ML-Net and D-Net
Figure 4. 7: A structural perspective of the ML-Net model
Figure 4. 8: D-Net method structure
Figure 4. 9: Experimental test rig setup used for rotating machinery fault diagnosis. 130
Figure 4. 10: Magnetic Brake with a gearbox and magnetic

Figure 4. 11: Installed tri-axial accelerometer on IM.	137
Figure 4. 12: Healthy Rotor.	137
Figure 4. 13: Unbalanced Rotor.	137
Figure 4. 14: Unbalanced rotor fault in the motor	138
Figure 4. 15: Bearing fault in the motor	138
Figure 4. 16: Matrix of Confusion proposed model a) 10, b) 20, and c) 30 I	Hz for
dataset 1	141
Figure 4. 17: Matrix of Confusion proposed model (a) 30 Hz, (b) 35 Hz, (c)) 40 Hz, (d)
45 Hz, and (e) 50 Hz for dataset 2	142
Figure 4. 18: Evaluation of suggested and traditional methods in comparis	on at 10 Hz
for dataset 1	144
Figure 4. 19Evaluation of suggested and traditional methods in compariso	n at 20 Hz
for dataset 1	145
Figure 4. 20: Evaluation of proposed and traditional methods in comparison	on at 30 Hz
for dataset 1	146
Figure 4. 21: Evaluation of proposed and traditional methods in comparison	on at 30 Hz
for dataset 2	147
Figure 4. 22: Evaluation of proposed and traditional methods in comparison	on at 35 Hz
for dataset 2	148
Figure 4. 23: Evaluation of proposed and traditional methods in comparison	on at 40 Hz
for dataset 2	149
Figure 4. 24: Evaluation of proposed and traditional methods in comparison	on at 45 Hz
for dataset 2	150
Figure 4. 25: Evaluation of proposed and traditional methods in comparison	on at 50 Hz
for dataset 2	151
Figure 4. 26: ROC Curve analysis using 60% for dataset 1 at a) 10 Hz, b)	20 Hz, and c)
30 Hz comparing suggested and conventional models.	168
Figure 4. 27: ROC Curve analysis using 70% for dataset 1 at a) 10 Hz, b)	20 Hz, and c)
30 Hz comparing suggested and conventional models.	169
Figure 4. 28: ROC Curve analysis using 80% for dataset 1 at a) 10 Hz, b)	20 Hz, and c)
30 Hz comparing suggested and conventional models.	170
Figure 4. 29: Comparison of the suggested and existing models' ROC curv	es at a) 10
Hz, b) 20 Hz, and c) 30 Hz using 90% for dataset 1	171
Figure 4. 30: Comparison of the proposed and existing models' ROC curve	es at a) 30

Hz, b) 35 Hz, c) 40 Hz, d) 45 Hz, and e) 50 Hz using 60% for dataset 2
Figure 4. 31: Comparison of the suggested and existing models' ROC curves at a) 30
Hz, b) 35 Hz, c) 40 Hz, d) 45Hzand e) 50 Hz using 70% for dataset 2
Figure 4. 32: With 80% for dataset 2, the ROC Curve performance compares the
suggested and conventional models at a) 30 Hz, b) 35 Hz, c) 40 Hz, d) 45 Hz, and e) 50
Hz
Figure 4. 33: With 90% for dataset 2, ROC curve performance comparing suggested
and existing models at a) 30 Hz, b) 35 Hz, c) 40 Hz, d) 45 Hz, and e) 50 Hz

LIST OF TABLES

Table 2. 1: Quantitative analysis for healthy signal
Table 2. 2: Quantitative analysis for faulty signal
Table 2. 3: Parameters of the classifiers
Table 2. 4: Describes how the optimization algorithm's parameter settings are set 65
Table 2. 5: Parameters of the optimization algorithms
Table 2. 6: Technical specifications of the gearbox
Table 2. 7: Different types of abrasive wear faults have different severity levels 69
Table 2. 8: Operating parameters of the laser machine
Table 2. 9: Training and testing data70
Table 2. 10: Comparison of different classifiers at 20 Hz
Table 2. 11: Comparison of different classifiers at 25 Hz
Table 2. 12: Comparison of different classifiers at 30 Hz
Table 2. 13: Ablation study of OAHCSA-HC approach at 15 Hz
Table 2. 14: Ablation study of OAHCSA-HC approach at 20 Hz
Table 2. 15: Ablation study of OAHCSA-HC approach at 25 Hz
Table 2. 16: Ablation study of OAHCSA-HC approach at 30 Hz78
Table 2. 17: Computational time analysis
Table 2. 18: Analysis of K-fold validation for suggested OAHCSA-HC model over
conventional methods at various frequencies81
Table 3. 1: Features of the time domain
Table 3. 2: Frequency domain features
Table 3. 3: Gearbox Description
Table 3. 4: Learning Rate vs. Accuracy Analysis
Table 3. 5: Evaluation of ablation at 15 Hz, 20 Hz, 25 Hz, and 30 Hz using the
proposed method with existing techniques111
Table 4. 1 (a): Quantitative Analysis of signals for dataset 1
Table 4. 1 (b): Quantitative Analysis of signals for dataset 2
Table 4. 2: Specifics of training and testing are essential for 10 Hz, 20 Hz, and 30 Hz
for dataset 1
Table 4. 3: Specifics of training and testing are essential for 30 Hz, 35 Hz, 40 Hz, 45
Hz, and 50 Hz for dataset 2

Table 4. 4: Analysis of MLiDNet's computational time in comparison to traditional
models at 10 Hz
Table 4. 5: Analysis of MLiDNet's computational time in comparison to traditional
models at 20 Hz
Table 4. 6: Analysis of MLiDNet's computational time in comparison to traditional
models at 30 Hz154
Table 4. 7: Analysis of MLiDNet's computational time in comparison to traditional
models at 30 Hz
Table 4. 8: Analysis of MLiDNet's computational time in comparison to traditional
models at 35 Hz
Table 4. 9: Analysis of MLiDNet's computational time in comparison to traditional
models at 40 Hz
Table 4. 10: Analysis of MLiDNet's computational time in comparison to traditional
models at 45 Hz
Table 4. 11: Analysis of MLiDNet's computational time in comparison to traditional
models at 45 Hz
Table 4. 12: Ablation analysis of proposed method compared to existing models at 10
Hz for dataset 1
Table 4. 13: Ablation evaluation of dataset 1 using the suggested approach in
comparison to current models at 20 Hz
Table 4. 14: Ablation analysis of dataset 1 using the suggested approach in comparison
to conventional techniques at 30 Hz
Table 4. 15: Cross-speed generalization performance trained on 10 Hz and 20 Hz,
tested on 30 Hz for Dataset 1
Table 4. 16: Ablation evaluation of proposed method compared to existing models at 30
Hz for dataset 2
Table 4. 17: Ablation examination of dataset 2 using the suggested approach in
comparison to current approaches at 35 Hz
Table 4. 18: Ablation evaluation of the proposed method compared to existing
approaches at 40 Hz
Table 4. 19: Ablation analysis of the suggested approach compared to existing models
at 45 Hz
Table 4. 20: Comparison of proposed ablation analysis at 50 Hz with traditional SSWT,
SE. and L-Net models

Table 4. 21: Cross-speed generalization performance trained on 10 Hz and 20 Hz,	
tested on 30 Hz for Dataset 2	. 167

NOMENCLATURE

N Sample number

 y_i ith vibration signal

Ci ith intrinsic mode functions

 r_n nth residual component

ω_k Center frequencies

λ Lagrangian multipliers

τ Noise tolerance

f_{gm} Gear mesh frequency

2f_{gm} Harmonic of gear mesh frequency

 $u_e(t)$ Upper envelope

 $l_e(t)$ Lower envelope

 $r_1(t)$ Residue function

 $\varphi_n(\omega)$ Scaling function

 $\psi_n(\omega)$ Wavelet function

φ₀ Standard deviation of white noise

 μ_{th} Threshold

 E_{Le} Log energy entropy

E_{th} Threshold entropy

E_{sure} Sure entropy

E_{sha} Shannon entropy

E_{ne} Norm entropy

ACRONYMS

EM Electromechanical

ML Machine Learning

DL Deep Learning

IM

NN Neural Network

CBM Condition-Based Maintenance

CM Condition Monitoring

MCSA Machine Current Signature Analysis

Induction Motors

FFT Fast Fourier Transform

CWT Continuous Wavelet Transform

DWT Discrete Wavelet Transform

HHT Hilbert Huang Transform

WPT Wavelet Packet Transform

SSWT Synchro squeezing Wavelet Transform

AI Artificial Intelligence

DNNs Deep Neural Networks

SVM Support Vector Machines

STFT Short Time Fourier Transform

CNNs Convolutional Neural Networks

KNN K Nearest Neighbors

PNN Probabilistic Neural Network

WT Wavelet Transform

MSFFCNN Multi-Scale Feature Fusion Convolutional Neural Network

ML KNN KNN Multi-Label Learning

RF Random Forest

ML RFKNN Random Forest Multi-Label Learning

ML SResNet Simple Residual Network Multi-Label Learning

AE Acoustic Emission

TSA Time Synchronous Averaging

SNR Signal-to-Noise Ratio

EMD Empirical Mode Decomposition

EEMD Ensemble Empirical Mode Decomposition

CEEMDAN Complete Ensemble Empirical Mode Decomposition with

Adaptive Noise

DT Decision Tree

DBNs Deep Belief Networks

SAEs Stack Auto Encoders

RNNs Recurrent Neural Networks

GANs Generative Adversarial Networks
VMD Variational Mode Decomposition

Bi LSTM Bidirectional Long Short-Term Memory

OAHCSA Opposition-based Artificial Hummingbird Crow Search

Algorithm

SSAE Stacking Sparse Autoencoder
ANN Artificial Neural Networks

SL Supervised Learning

LSTM Long Short-Term Memory

ELM Extreme Learning Machines

GA Genetic Algorithms

PSO Particle Swarm Optimization

HOS Higher Order Statistical Features

MF Median Filter

DAP Dynamic Awareness Probability

OBL Opposition-Based Learning

MFS Machine Fault Simulator
VFD Variable Frequency Drive

DAQ Data Acquisition System

FNR False Negative Rate

FDR False Discovery Rate

FPR False Positive Rate

NPV Negative Predictive Value

MCC Matthews Correlation Coefficient

TP True Positive
TN True Negative
FP False Positive
FN False Negative

IDBN Improved Deep Belief Network

SPCC Statistical Process Control Charts

RMS Root Mean Square

HL Hidden Layer

RBM Restricted Boltzmann Machine
S MAF Swi-Mish Activation Function

SLC Small Crack
IC Incipient Crack
MC Moderate Crack

SRC Severe Crack

OWPD Optimal Wavelet Packet Decomposition

FFNN Feed Forward Neural Networks

DCNN Deep Convolutional Neural Networks
Bi GRU Bi-directional Gated Recurrent Units
MLiDNet Modified LinkNet and DenseNet

D Net DenseNet

C TR2FFT Cooley Tukey Radix 2 FFT Method

CS Chi-Square

ML Net Modified LinkNet

BN Batch Normalization

ReLU Rectified Linear Unit

ROC Receiver Operating Characteristic Curve

AUC Area Under Curve

SE Spectral Entropy

MLiDNet Modified LinkNet and DenseNet

HC Hybrid Classifier

AHA Artificial Hummingbird Algorithm

Chapter 1

Introduction and literature review

1.1 Introduction

Gears and electric motors are essential components in various industrial and automotive systems, playing critical roles in transmitting power and motion. The seamless interaction between these elements is crucial for the efficient operation of machinery, where any faults can significantly impact performance and reliability. Gearboxes are key elements in torque transmission and are susceptible to faults such as wear, pitting, and cracking, which often manifest through changes in vibration and noise signals. Similarly, an electromechanical (EM) system comprises mechanical and electrical parts, including belt pulley drives, gearboxes, couplings, rotor-bearing systems, electric motors, and generators. Electric motors are prone to electrical and mechanical faults such as bearing wear, rotor imbalances, and winding failures, disrupting the system's operation.

Accurate fault detection and classification in these systems are vital to minimizing downtime and maintenance costs while ensuring operational safety. This research focuses on leveraging advanced signal processing techniques and deep learning (DL) machine learning (ML) algorithms to diagnose gear faults and combined faults in EM systems, offering a robust framework for improving the dependability of vital mechanical systems and performing predictive maintenance [138][181].

1.2 Gear and Its Modes of Failure

A gear is a critical part of rotating machinery, and it has teeth that connect with other toothed parts and transfer the torque. When two or more gears work together, they form a gearbox. There are various types of gears used in mechanical systems, including spur gears, helical gears, bevel gears, worm gears, rack and pinion gears, planetary gears, and hypoid gears, each with unique characteristics and strengths suited for specific applications. This research focuses on bevel gears, which are widely used in mechanical systems such as differential drives, helicopter and aircraft power transmissions, floodgate lift mechanisms, industrial plants, and marine propulsion systems. However, gears are prone to wear, damage, and failure over time due to factors like high stress concentration, material fatigue, misalignment, lubrication deficiencies, and overload

conditions. These issues can lead to costly downtime, equipment malfunctions, and potential safety hazards. The gear's operation produces the phenomena of modulation of amplitude, frequency, or mixed modulation because the meshing frequency and its double frequency signal of the vibration signal are modulated by the shaft frequency. Vibrations are a type of dynamic non-stationary signal. The dynamic signal analysis method must be applied in order to address the gear vibration signal. Nevertheless, precise matching with sophisticated pattern recognition techniques is still required to be effective because of the intricacy of the extracted signal's frequency and amplitude [1].

Despite their widespread use, gears are susceptible to wear, damage, and eventual failure due to factors such as high-stress concentration, material fatigue, misalignment, lubrication issues, and overload conditions. Such issues can lead to expensive downtime, machinery malfunctions, and safety risks. As illustrated in Figure 1.2, gear faults can manifest in various forms, including wear and cracks. Wear is a persistent issue observed across numerous engineering fields and can result in significant financial and operational losses. Studies suggest that the cost of abrasive wear alone can account for up to 1-4% of a nation's gross national product. Additionally, wear is responsible for 55% of the loss of material utility in industrial applications. Emphasizing the need for thorough wear fault analysis in gear systems.

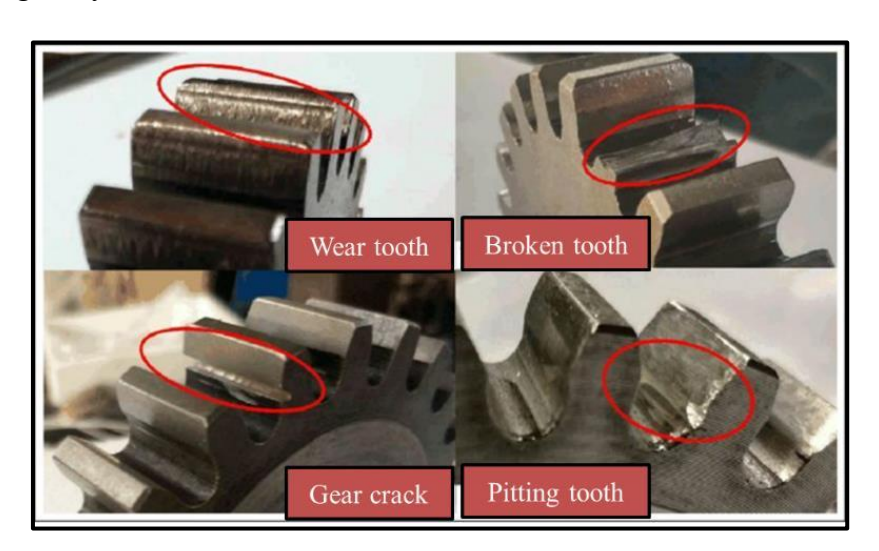


Figure 1. 1: Various types of gear faults [2]

Figure 1.1 shows the various types of gear faults. Previous research has focused on diagnosing common gear faults such as missing teeth, chipped teeth, cracks at the root, and face wear, particularly in spur gears [1-4]. However, limited research has focused on

micron-level wear and the varying severity of crack faults in bevel gear fault analysis, leaving this area largely unexplored. This research aims to address that gap by diagnosing micron level wear and varying crack faults in bevel gears, offering insights into the early detection and management of these issues to improve gear reliability and performance.

1.3 Machine Condition Monitoring

Machine CM is essential for maintaining industrial facilities' reliable and cost-effective operation. It involves continuously tracking the performance of machines to detect faults in their early stages, enabling corrective actions to be taken before any breakdowns or catastrophic failures occur. Implementing continuous CM allows facilities to schedule planned maintenance and repairs, improving operational efficiency and reducing environmental impact. Various technologies have been integrated into these monitoring processes to enhance CM systems' effectiveness, accuracy, and dependability [5]. Real-time data acquisition and processing have become widely accepted in CM for their ability to detect issues promptly. Choosing the right CM system is crucial for boosting machine availability, optimizing performance, extending equipment lifespan, minimizing spare parts inventory, and avoiding costly breakdown repairs.

In industrial settings, maintenance typically represents 15-40% of manufacturing costs [6]. As a result, adopting an effective maintenance strategy is essential to reduce these expenses. One practical approach is CBM, which is based on structural health monitoring. CBM has become increasingly popular because it can prevent unnecessary breakdowns by recommending maintenance actions only when required. By implementing CBM, companies can significantly save time and cost, leading to more efficient operations and reduced downtime.

Industrial machine monitoring uses a variety of methods to evaluate the state of the machinery. These methods include visual and aural inspections, temperature monitoring, wear debris analysis, vibration analysis, acoustic emission (AE) analysis, and noise monitoring. Visual and aural inspections rely on skilled personnel who use their senses to assess a machine's condition. However, these methods have limitations in detecting faults at early stages, making them less effective for proactive monitoring [7].

Temperature monitoring, which uses sensors including thermometers, thermocouples, and thermal cameras, is essential for detecting excessive heat generation, which is a major sign of possible problems [8]. This method is critical for detecting

abnormal temperature fluctuations that may signal challenges within the machine. Wear debris analysis is another traditional method used in CM. It focuses on examining the size and level of contamination of wear particles in the lubricant, providing insight into the condition of machine components and helping identify potential issues [9][10].

AE [11][12] monitoring detects stress waves generated by material deformation, such as crack initiation or movement of dislocation. These stress waves typically fall within the ultrasonic frequency range of 20 kHz to 1 MHz and can provide early indications of structural issues within the machine.

Vibration monitoring is among the most popular methods for CM across various industrial machines. It effectively detects faults such as gear and bearing faults, misalignment, eccentric shafts, and improper clearances. Vibration analysis is utilized in approximately 82% of fault diagnosis methods, making it a key approach for identifying mechanical issues and ensuring operational reliability [13,14].

1.4 Vibration Analysis for Gearbox Fault Diagnosis

Gearbox failures can occur in various ways during operation, often marked by increased noise and vibration as early warning signs before complete failure occurs. A gearbox's complex and non-stationary vibration signal is made up of harmonics, fault transients, noise, teeth meshing frequency, shaft frequency, and other elements under real-time operating conditions [15,16]. The behavior of the gearbox vibration signal is influenced by factors such as operating speed, load, gear tooth meshing, tooth surface condition, and friction [17-20]. Furthermore, other components within the gearbox, such as bearings, also impact the vibration signal. As a result, acquiring vibration signals and applying appropriate signal processing techniques are critical for detecting gear faults.

Shipley [21] highlighted that one of the primary causes of gearbox failures is localized or widespread faults in the gear teeth. Vibration analysis and signal processing methods have proven effective in identifying gearbox faults under constant speed conditions [22-26]. Vibration signals are typically captured using accelerometers mounted on the gearbox bearing casing. Operating variables, such as speed fluctuations and gear tooth meshing, contribute to modulations in the gearbox vibration signals, which may mask

fault-related modulations [27-29]. Therefore, signal processing techniques are essential for analyzing gearbox vibration signals and detecting faults.

1.5 Signal Processing Techniques for Gear Fault Detection: An Overview

Techniques for signal processing are crucial for identifying gear faults by analyzing vibration signals generated during gearbox operation. Gearboxes produce non-stationary vibration signals due to various dynamic factors in real-life conditions [30]. The three main reasons why gears fail are (i) design errors, (ii) application errors, and (iii) manufacturing errors. Improper gear geometry, incorrect material selection, poor quality, lubrication, and other criteria can all lead to design problems. Problems with vibration, mounting and installation, cooling, and maintenance are examples of application faults, whereas manufacturing errors can be caused by mishandled machinery or issues with heat treatment. Vibration measurement is highly effective, non-intrusive, and cost-efficient for monitoring machine health during startups, shutdowns, and normal operations. These signals typically contain a mixture of deterministic and random elements, with random signals being either stationary or non-stationary and deterministic signals classified as periodic or non-periodic. Using various signal processing techniques, such as wavelet trans- form and frequency and time domain analysis, important information is extracted from vibration signals to enable early fault diagnosis. While these methods are valuable for identifying gear faults, each has its limitations, and selecting the appropriate technique depends on the specific fault characteristics and operational conditions.

Local faults are the most harmful because, once initiated, they tend to evolve quickly and generally have essential impacts on energy transmission. If not identified soon, the most significant local faults can have drastic implications with teeth breakage, pitting, and scoring. Vibration signals and acoustic emissions are status surveillance's most prevalent waveform information. The waveform also includes information on engine presence, partial release, and ultrasonic sounds. In literature, time and frequency domain evaluation are the two main approaches used to evaluate stationary waveform information.

1.5.1 Time Domain Analysis

In order to extract statistical features that offer important insights into the gear system's state, time-domain analysis entails tracking the vibration signal throughout time. The

metrics mean, standard deviation, skewness, kurtosis, energy ratio, and time synchronous averaging (TSA) are examples of these statistical characteristics, which are referred to as time-domain indicators. These indicators can provide details on the vibration signal's amplitude and distribution, which may point to gear faults such as tooth wear or cracks. However, this method's inability to record frequency-related data is a drawback. By utilizing statistical features to detect gear cracks under various speed conditions, the improved TSA approach enhances the signal-to-noise ratio (SNR) [31]. Furthermore, wind turbine gearbox CM has employed RMS and peak vibration signal values, showing that these indicators may accurately evaluate a gearbox's condition when applied appropriately [32]. The impulsive nature of gear tooth spall faults has also been successfully detected using a fault detection technique based on maximal kurtosis [33].

1.5.2 Frequency Domain Analysis

Frequency domain analysis is another key signal processing technique for detecting gear faults, focusing on examining the frequency content of vibration signals to identify fault-specific frequencies and their characteristics [34]. One of the most commonly used methods in frequency domain analysis is the FFT, which converts a time-domain vibration signal into the frequency domain. In a frequency domain plot, the y-axis represents dis- placement, velocity, or acceleration amplitude, while the x-axis represents the frequency. This graphic illustrates how the signal's amplitude varies with frequency.

In gear fault identification, the FFT is particularly useful for identifying frequencies associated with gear faults, such as the gear meshing frequency and its harmonics. The sidebands around the gear meshing frequency can also be analyzed using it, as these could reveal the existence of wear, pitting, or cracks in the gear teeth [35].

1.5.3 Time-Frequency Domain Analysis

A method for analyzing signals with time-varying frequency content is time-frequency domain analysis. It offers insights into how a signal's frequency content changes over time by combining the best features of frequency domain and time domain studies. A time-frequency plot provides a detailed representation of the signal, showcasing its components within a specific frequency range and their sequences, causality, and frequency variations over time in a single plot. This method is useful for examining non-stationary signals, including those produced by gear failures. However, extracting meaningful information from these complex signals using traditional methods can be challenging.

Advanced signal processing methods have been developed to address these challenges and improve the accuracy of gear fault detection [35].

The wavelet transform is a common method for analyzing non-stationary data in terms of time and frequency. It divides the signal into different frequency bands and provides information on the phase and amplitude of each component. Wavelet-based techniques have been successfully applied to detect gear faults [36]. Advanced signal processing methods, such as empirical mode decomposition (EMD), ensemble empirical mode decomposition (EEMD), HHT, complete ensemble empirical mode decomposition with adaptive noise (CEEMDAN), and adaptive filtering algorithms, are designed to enhance signal quality, reduce noise, and improve the detection of fault-related features in the time-frequency domain. However, these methods often rely on expert judgment to assess gearbox health. Modern industrial applications increasingly adopt automated fault detection methods to address this limitation. Integrating advanced signal processing techniques with ML algorithms and DL models has significantly improved gear fault diagnosis in vibration signals. These approaches enable automatic analysis and classification of gear faults, yielding promising results.

1.6 Electromechanical Systems and Their Common Failures

Induction motors (IM) play a vital role in electromechanical (EM) systems, serving as key components in industrial applications for converting electrical energy into mechanical power. The electrical and mechanical components of an EM system are depicted in Figure 1.2 [37,38]. A catastrophic breakdown of the entire system results from the failure of any one of these parts, which shuts down manufacturing or industrial operations [39-41]. In EM systems, early fault identification and monitoring are therefore essential. Preventive and condition-based maintenance (CBM) can be scheduled during planned outages thanks to this proactive approach, which reduces the possibility of prolonged outages brought on by broad system failures [42-45]. Consequently, this approach reduces maintenance expenses while increasing overall performance and availability [46-48]. The two main types of faults in EM systems are mechanical and electrical. Electrical faults in IM include insulation failures, rotor bar breakage, and stator winding issues [49–51]. Conversely, mechanical faults include misalignments, rotor imbalances, bearing failures, and faults with the gearboxes or belt and pulley systems. This research focuses on the mechanical faults in IMs and coupled loads, where the IM serves as the prime mover and connects to other mechanical components such as shafts,

bearing rotor systems, belt and pulley drives, and gearboxes. This section investigates faults such as unbalanced loads in motors, bearing faults in motors, and unbalanced rotors in mechanical loads. These specific faults are critical because they can significantly impact on the longevity and functionality of the EM system.

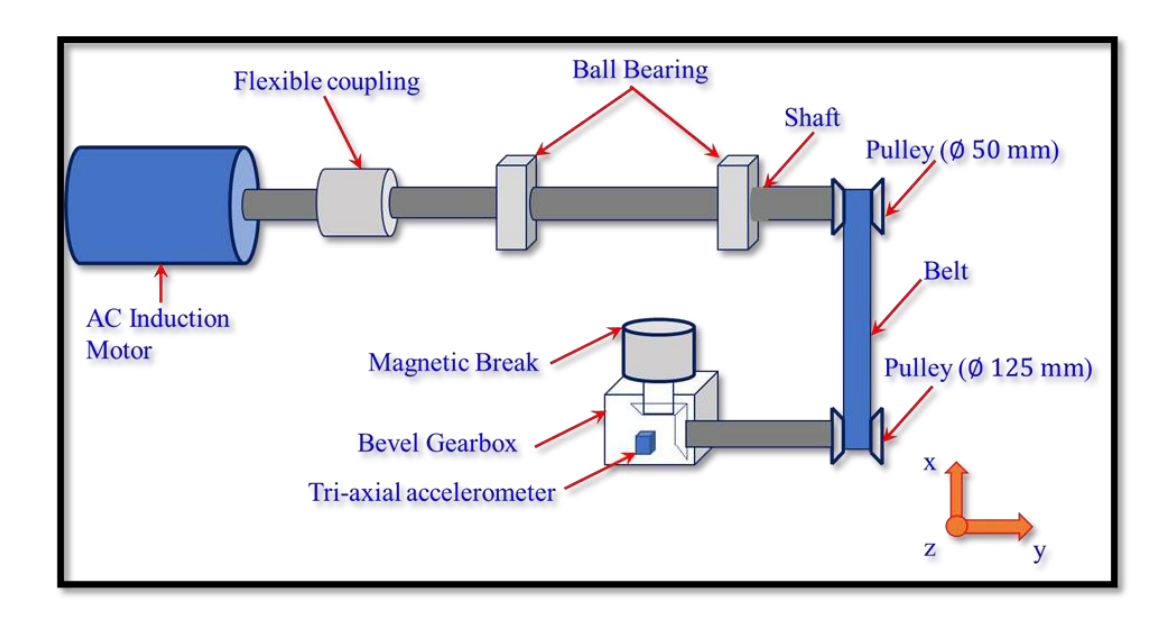


Figure 1. 2: Schematic representation of Electromechanical system

1.6.1 Condition Monitoring of Combined Fault in EM System

This section provides a literature survey highlighting various techniques and advancements in EM systems' condition monitoring (CM) and fault diagnosis. Catastrophic failures in EMs can result from the malfunction of components such as the stator, rotor, gearbox, or bearings. CM techniques have been developed to detect these faults, including vibration signal monitoring, current signal monitoring, and noise signal monitoring.

Mechanical faults such as misalignment, bowing, imbalanced rotors, and bearing faults can be efficiently identified by vibration monitoring [52]. It can also be used to detect electrically related issues, such as broken rotor bars, phase imbalances, and stator winding faults [53][54]. Tri-axial accelerometers can be placed on machines in specific locations to capture vibration signals for monitoring purposes. The fundamental principle of vibration-based monitoring relies on mechanical components generating vibrations during operation [55]. When faults occur, they alter system dynamics, leading to noticeable deviations in vibration patterns. By applying suitable data analysis algorithms, these variations can be detected, enabling an accurate assessment of the condition of EMs. Machine current signature analysis (MCSA), another name for current monitoring, is

frequently used to find electrically combined faults, including broken rotor bars and faults with the stator windings [56]. MCSA can detect mechanically related faults in addition to electrical ones [57][58]. Sensors such as current probes attached to the motor's supply connections are used in MCSA to record current signals. The substantial changes in current signals brought on by malfunctioning EM components provide the basis of the current-based monitoring concept. As with vibration monitoring, these current variations can be analyzed using appropriate data analysis methods to diagnose faults effectively. The process of measuring and evaluating the noise spectrum is known as acoustic noise monitoring [59]. The machine's iron surfaces are subject to Maxwell's stresses, which is what makes the noise. Microphones and specialized devices like sound level meters are often used as sensors for noise measurement. This method works especially well for identifying faults in the stator structure and air-gap eccentricity.

EM faults have been found using a variety of CM approaches. Nevertheless, a lot of these techniques are intrusive, intricate, expensive, and have a limited capacity to offer thorough details regarding the working circumstances of EMs. Additionally, most techniques are designed to detect specific faults, making them unsuitable for identifying multiple types of faults using the same approach. Vibration and current signal-based CM are the most widely used methods in the industry [60]. Kral et al. (2003) [61] highlighted that vibration-based CBM is reliable for detecting bearing and other mechanical faults. Hu et al. (2016) [62] studied the use of vibration signatures to detect multiple types of faults, including misalignment and rotor eccentricities, in industrial-grade motors. Their findings demonstrated the ability of vibration analysis to identify both mechanical and electrical faults effectively, making it suitable for complex systems. Sharma et al. (2024) [63] analyzed combined mechanical and electrical faults in EMs using vibration signatures. The study validated that vibration analysis could capture fault interactions and provide a comprehensive overview of system health, which traditional techniques often miss. Allmark (2016) [64] investigated fault combinations in EMs, including rotor imbalances and stator faults. Their research confirmed that vibration monitoring could effectively isolate and identify simultaneous fault conditions, reducing downtime and maintenance costs.

Based on these studies, vibration-based CM emerges as the most reliable and versatile method for identifying combined faults in EM systems. It provides insights into mechanical and electrical fault interactions and supports proactive maintenance strategies, making it the best choice for CM in industrial applications.

Vibration-based monitoring is preferred for EM fault diagnosis because it is non-intrusive, reliable, and cost-effective. It offers high accuracy in signal analysis, effectively represents machine conditions, excels at detecting and distinguishing mechanical faults, and supports online monitoring for real-time fault detection.

1.6.2 Vibration Analysis for EM System Fault Diagnosis

Vibration is one of the most often observed characteristics in the CM of rotating machinery. It is extensively used in industrial applications due to its sensitivity to machine faults and ease of measurement. Vibration analysis plays a vital role in industries such as material handling, aerospace, and power generation [65]. Faulty machine components, such as damaged bearings or gears, generate specific vibration signals that can be analyzed to identify the nature and severity of the fault. These signals vary depending on the size, location, and type of damage present [66][67].

Vibration-based diagnostic methods are advantageous due to their cost-effectiveness, straightforward implementation, and ability to provide detailed insights into damage location and severity. For instance, rolling element bearings generate characteristic vibration patterns when faults such as inner or outer race faults, ball faults, or cage issues are present. These patterns can be effectively captured using accelerometers and processed using advanced signal-processing techniques [68][69].

Even in the absence of significant faults, vibration is an inherent characteristic of machine operation. Manufacturing imperfections, material properties, and operational conditions contribute to baseline vibration levels. Some common sources of vibration include localized faults such as indentations, pits, or scratches, as well as larger-scale issues like raceway damage [70]. Advanced techniques in signal processing, such as denoising and spectral analysis, can now identify important fault signatures even when there is background noise, enabling more accurate and reliable fault detection [71][72].

1.6.3 Signal Processing Methods for EM System Combined Fault

Advanced signal processing methods are essential for detecting faults in EM systems early, enabling effective monitoring and diagnosis before significant failures occur [73]. These techniques, classified into invasive and non-invasive approaches, are critical for accurately identifying faults in complex systems. Commonly used tools such as discrete wavelet transform (DWT), Fast Fourier transform (FFT), Hilbert-Huang transform (HHT), continuous wavelet transform (CWT), and wavelet packet transform (WPT) pro- vide valuable insights by analyzing signals in time and frequency domains [74].

Although these techniques are crucial for fault detection, they have drawbacks, such as high computing requirements and vulnerability to non-stationary signals. These challenges are addressed by the Synchro-squeezing wavelet transform (SSWT) signal processing technique, which emphasizes instantaneous frequencies and improves time-frequency representation. However, SSWT still encounters limitations in noisy environments and computational complexity [62]. Despite these challenges, advanced signal processing remains crucial in enhancing the precision and dependability of fault detection in a variety of applications by deriving valuable information from intricate vibration signals [75].

1.7. Artificial Intelligence in Combined Fault of Electromechanical system

In recent years, sophisticated artificial intelligence (AI)-based methods have replaced conventional methods for the CM and fault detection of rotating machinery. With the progressive enhancement in automation, the expanding scale, and the growing complexity of EM systems, these advancements bring significant operational benefits and introduce numerous safety and reliability challenges. Addressing the complexity of modern EM systems requires robust safety assurance, reliability assessment, and diagnostic strategies.

DL-based fault diagnosis algorithms have emerged as effective solutions by leveraging advanced mathematical frameworks to process complex, high-dimensional datasets. These algorithms enable hierarchical feature extraction, uncover latent patterns, and enhance fault diagnosis performance, showcasing unique advantages in feature engineering and pattern recognition. The development of deep neural networks (DNNs) [76] facilitates the extraction of hidden data features and the mining of abstract information. However, the "black box" nature of DNNs makes it challenging to interpret

the extracted features, requiring domain expertise to map these features to specific fault patterns. In the domain of data-driven fault diagnosis, Wan [77] proposed a diagnostic model integrating nonlinear fluid learning and support vector machines (SVM), utilizing time and frequency domain parameters using EM systems to build a feature space with great dimensions. This model demonstrated fault diagnosis accuracy exceeding 95%. Similarly, Li [78] introduced a combined approach combining short-time Fourier transforms (STFT) and convolutional neural networks (CNNs) for fault pattern recognition, enabling end-to-end intelligent diagnostics with improved performance as fault types and datasets expand. Zhang et al. [79] developed a probabilistic generative model, which utilized a deep confidence net- work constructed from stacked restricted Boltzmann machines and achieved enhanced diagnostic accuracy.

CNNs are particularly prevalent among DL architectures due to their local connectivity, weight-sharing mechanisms, and pooling operations, which collectively reduce network complexity while improving robustness and generalization. The integration of DL techniques has driven significant advancements in data-driven fault diagnosis, offering innovative frameworks for diagnosing faults in complex EM systems and enabling new paradigms in intelligent maintenance and predictive analytics. An ML model is used by Han et al. [80] to offer a unique method for recognizing and categorizing instant messaging errors. Additionally, the technique involves intentionally creating three different kinds of problems and detecting them using an auto-tunable SVM technique dependent on the rotation speed and motor stator current spectrum properties. The method showed excellent sensitivity, resilience, and diagnostic accuracy, which qualified it for use in industrial settings. Manarikkal et al. [81] use CWT and AI to identify and diagnose stator winding faults in permanent magnet synchronous motors. They analyze CWTs using a generalized Morse wavelet, focusing on inter-turn short circuit symptoms. They also test automated classification using ML techniques, including multilayer perceptron, SVM, and K-nearest neighbors (KNN). A probabilistic neural network (PNN), wavelet trans- form (WT), and finite element analysis are used in a method by Liu et al. [82] to detect broken rotor bar faults in IMs. To determine the rotor state, they look at the amplitudes of the stator current signals. Numerical simulations are used to demonstrate the effectiveness of this strategy.

Additionally, Shao et al. [83] suggested a CNN-based DL-based multi-fault diagnostic method for sensor data analysis. The results demonstrate that the recommended strategy outperforms the traditional method by a significant margin.

Choudhary et al. [84] developed a vibroacoustic fusion technique for fault diagnosis in rotating machine com- ponents by combining vibration and metric inputs with a multiinput CNN. Additionally, the results demonstrate that it can accurately diagnose issues with instant messaging systems and other rotating machinery. To diagnose IM faults, Sun et al. [85] suggest a back-propagation neural network and a convolutional discriminative feature learning technique. Their strategy, which uses an SVM classifier and a feedforward convolutional pooling architecture, significantly outperforms current techniques in terms of performance. Using stator phase current data, El-Dalahmeh et al. [86] created a method for continuous fault identification in permanent magnet synchronous motors. Their method effectively detects faults in a variety of operating conditions by combining CNN for fault classification, HHT for feature extraction, and variational mode decomposition (VMD) for signal decomposition. The diagnostic method developed by Song et al. [87] used a multi-scale feature fusion convolutional neural network (MSFFCNN) to account for the multi-scale character of fault signals and the dependability of fault detection for EMAs in complex operating environments. It is possible to efficiently gather and learn fault-related information by using attention mechanism-based feature fusion and the learning structure of multiple scales. This enhances the network's diagnostic performance and identification capabilities. He et al. [88] have suggested that PV systems with multi-fault coupling use a composite fault diagnosis schema based on multi-label categorization. Additional useful features to properly distinguish between faults are extracted from the pre-processed Current-Voltage (I-V) curves. Then, two different diagnostic models are developed to diagnose compound faults: a basic residual network multi-label learning (ML-SResNet) and K-NN multi-label learning (ML-KNN) combined with random forest multi-label learning (ML-RFKNN).

1.7.1 Overview of Machine Learning and Deep Learning Techniques for Gearbox and EM system Fault Analysis

The health status of spinning machinery has been diagnosed using machine learning techniques. As a mechanical extension of pattern recognition theory, fault diagnosis technologies aim to solve the problem of state classification in engineering systems and operational equipment. Fault diagnosis systems need to be able to do three things: fault identification, fault detection, and fault isolation (Xu et al., 2020a) [89]. Unlike traditional diagnostic methods that heavily rely on human expertise for feature engineering, ML techniques leverage algorithms to learn and generalize patterns from the data,

significantly reducing dependency on manual intervention. However, ML models often require well-structured and domain-specific features as inputs, which can limit their performance in cases of noisy or complex datasets.

ML approaches have demonstrated remarkable potential in the area of diagnosing and identifying faults, offering improved accuracy and efficiency over traditional techniques. The most widely used algorithms include SVMs, decision tree (DT), RF, and K-NN. These models are adept at identifying fault patterns by analyzing extracted features from various signal domains, such as time, frequency, and time-frequency. Researchers have successfully applied ML models to diagnose specific and combined faults in gearbox fault detection. For example, Yang et al. [90] utilized an SVM-based approach to detect gear tooth wear and misalignment, showcasing the algorithm's effectiveness in classifying subtle fault signatures. Similarly, Wan et al. [91] employed RF classifiers to diagnose gear and bearing faults, achieving high classification accuracy with minimal preprocessing of vibration signals.

Despite their advantages, traditional ML models often struggle with high-dimensional data and non-stationary signals, which are common in real-world fault detection scenarios. Consequently, combined models have been suggested to combine advanced signal processing techniques or domain expertise with machine learning techniques. For example, Li et al. [92] showed how signal processing and machine learning techniques can work together by combining wavelet transform with SVMs to enhance the identification of transient gear faults.

Furthermore, three steps are involved in the intelligent fault detection approach based on traditional machine learning: pattern recognition, artificial feature extraction, and data collecting. Nevertheless, the upper limit of algorithm performance is low because traditional ML techniques typically lack a deep architecture and are somewhat close. In contrast to conventional machine learning techniques, the DL-based fault detection model is a common end-to-end model capable of extracting data features during optimization and has enhanced nonlinear mapping fitting capabilities. In traditional machine learning methods, it makes up for the shortcomings of the extraction of features manually and reduces the need for mechanism research and subjective assessment.

Combined models are required in fault detection because they combine the strengths of different methodologies to address the limitations of standalone approaches. Traditional signal processing techniques are effective for feature extraction but struggle with complex, non-linear relationships in fault data. ML methods can classify faults based on extracted features but rely heavily on the quality and relevance of these features. DL models, while powerful in automatic feature extraction and handling large datasets, can be computationally intensive and may be overfitted with limited labeled data. Combined models integrate these approaches, such as combining DL for feature extraction with ML for classification, to leverage their complementary strengths. This integration improves fault detection accuracy, especially in noisy environments or when handling combined faults, overlapping signal characteristics, and imbalanced datasets. By uniting diverse techniques, combined models provide a more robust, flexible, and scalable solution for diagnosing faults in complex systems like gearboxes and EM systems.

It enhances the diagnosis's precision and intelligence to a certain degree. The automatic and large-scale diagnosis of mechanical equipment faults is increasingly feasible with its help. These days, the most often utilized deep learning techniques in trouble-shooting include CNN, generative adversarial networks (GANs), recurrent neural networks (RNNs), stack auto-encoders (SAEs), and deep belief networks (DBNs). In the area of fault diagnostics, DL models are also being used. In order to detect rolling bearing faults, Gao et al. [93] used DBNs to extract the bearings' signal. According to experiments, the rolling bearing faults detection model, which Niu et al. [94] presented and was based on DBNs, had good fault detection capabilities and could correctly identify all types of faults.

Zhao et al. [95] have suggested SAEs are an efficient DL technique. This technique solved the gearbox fault detection fault by removing the need for human characteristics by extracting essential features from the frequency domain data. Chen et al. [96] interacts with a sparse auto-encoder and a denoising auto-encoder, proposed the stacked sparse denoising auto-encoder diagnosis model, and applied the model to rolling bearing fault detection. Liu et al. [97] combined RNN and autoencoders to realize the intelligent fault detection of rolling bearings. Jiang al. [98] used RNN to realize the intelligent fault detection of bearings under time-varying working conditions [99] [35].

Lin and Shih-Lin [100] investigated DenseNet and VMD for bearing fault diagnosis. A motor fault diagnosis model is constructed using DenseNet; it has a

straightforward structure and quick computation times. With a 92% VMD-DenseNet prediction accuracy rate, the experimental findings demonstrate that the approach can correctly identify four frequent motor faults. An enhanced NL-LinkNet network, called NL-LinkNet-SSR, was presented by Jing Wang et al. [101] and specifically created for fault detection activities. To increase the accuracy of the model and resilience in fault identification, the suggested NL-LinkNet-SSR combines a SimAM attention module with a Sobel edge detection module.

Overall, ML and DL have become a cornerstone of modern fault diagnosis, offering scalable and intelligent solutions for gearboxes. With continued advancements in algorithm design, data pre-processing, and feature engineering, ML and DL models are poised to deliver even greater accuracy and robustness in diagnosing both gearbox faults and combined faults in mechanical systems [4].

1.8 Conclusions

The reviewed literature shows that fault detection in gearboxes and EM systems has gained significant importance due to their critical roles in power transmission and industrial applications. Gearboxes and EM systems are subjected to various operational stresses, making them prone to faults such as gear tooth wear, cracks, misalignment, pitting, motor winding faults, rotor imbalances, and insulation degradation. Combined faults, where multiple faults occur simultaneously, pose additional challenges due to the complex interaction between fault mechanisms and overlapping signal characteristics across interconnected components.

Vibration signal analysis has emerged as a reliable technique for early detection and diagnosis of gearbox and EM system faults. The three main techniques for fault detection are DL, ML, and signal processing based. Time-domain, frequency-domain, and time-frequency-domain studies are employed in signal processing methods to detect essential signals that point to gearbox and electromechanical system faults. These methods are particularly effective in fault detection and classification, including those caused by motor imbalances or gearbox wear.

ML techniques have shown significant potential in diagnosing gearbox and combined faults in EM systems with minimal human intervention. These techniques use algorithms such as SVMs, DT, and NN to enable precise fault classification based on extracted features. It is crucial to customize solutions to particular fault scenarios and

adjust them to the interconnected nature of gearboxes and EM systems because the effectiveness of machine learning approaches depends on elements like feature relevance, algorithm selection, and training data quality.

The DL technique facilitates automatic feature extraction and classification, which advances fault detection. These models, such as RNN, LSTM, DBN, and CNN, can handle complex datasets and identify patterns associated with combined faults in gearboxes and EM systems. For instance, DL models can effectively detect overlapping characteristics in vibration signals, enabling comprehensive fault diagnosis across EM systems. This capability is particularly advantageous in scenarios where faults coexist in multiple components, such as motors, gearboxes, and bearings.

In conclusion, integrating advanced signal processing techniques with ML and DL approaches has paved the way for more accurate and robust fault detection systems, particularly in gearboxes and EM systems. These advancements address challenges such as combined faults, noisy environments, and data imbalance. Future developments in sensor technology, data fusion, and combined diagnostic frameworks are expected to further enhance the reliability and efficiency of fault detection across entire EM systems, ensuring improved performance and reduced downtime in industrial applications.

1.9 Outcomes of the Literature Review

The literature on gearbox faults and combined fault detection in EM systems, including their applications and failure modes, has been thoroughly examined. A comprehensive review of various CM methods, explicitly focusing on AI techniques, has also been conducted. The significance of such techniques in detecting various faults in gears is presented in detail. Here are the key findings derived from the literature review. These findings underscore the promising future of AI models in achieving more accurate, efficient, and reliable detection of gearbox faults and combined faults in EM systems for industrial applications.

- Despite the numerous techniques employed in fault detection for gearboxes, challenges such as noise interference, data imbalance, and the complexity of handling multiple fault types persist.
- EM systems often experience combined faults, where faults in both electric (motor, power supply) and mechanical (bearings, gears) components occur simultaneously. These combined faults pose significant challenges in

- detection due to overlapping symptoms and interdependent fault behaviors, making it difficult to pinpoint the exact fault source.
- Traditional signal processing techniques such as FFT and wavelet transforms are widely used. However, they struggle with noisy environments and non-stationary signals. These methods can be ineffective when faulty signatures are weak or buried in noise.
- Signal processing methods include wavelet transform, Fourier transform, and spectral analysis. At the same time, widely used, they often struggle with accurately extracting features in highly noisy environments or when the data exhibits non-stationary behavior.
- For optimal performance, ML classifiers such as SVM, DT, and RF depend heavily on accurately labeled and structured data. Their efficiency significantly declines in noisy signals, data imbalance, or incomplete datasets.
- Although more adept at feature extraction and handling noise, DL techniques, such as RNNs, LSTMs, DBN, and CNNs, require substantial computational resources and extensive labeled datasets for training, which can limit their practicality in real-time applications with constrained environments.
- Combined models that combine DL architecture offer a more robust approach to detecting combined faults in EM systems. However, they face challenges related to model complexity, increased risk of overfitting, and the need for longer training times, especially when dealing with high-dimensional data.
- A combined architecture that combines the LinkNet and DenseNet models offers a more robust approach to fault detection by leveraging the strengths of both networks. However, integrating these two architectures may introduce challenges such as increased computational complexity, longer training times, and the need for careful balancing to prevent overfitting, especially when working with large, high-dimensional datasets.

Based on the outcomes of the literature, the aims and objectives of the thesis work can be derived and presented in the subsequent section.

1.10 Objectives

This part presents the objectives and scope of the present work, with the objectives of developing an advanced fault detection methodology for gearboxes and combined faults using signal processing and ML techniques. The scope of the study may include the identification and classification of different faults occurring in various types of gearboxes under different operational conditions toward enhanced reliability and reduced downtimes.

Objectives of the works are as follows.

- To create a reliable wear fault detection technique for bevel gearboxes by utilizing an optimized combined classifier and updated entropy-based feature extraction.
- ii. To create a deep learning combined model for automatic gear crack identification based on an improved CEEMDAN model.
- iii. To design a modified combined architecture of LinkNet and DenseNet for detecting combined faults in electromechanical systems.

1.11 Organization of the thesis

The thesis is organized into the following chapters:

Chapter 1: Introduces the research background and reviews existing literature on fault detection using signal processing, ML, and combined DL methods. It identifies gaps in cur- rent approaches and defines the objectives and scope of the thesis. The chapter concludes with the organization of the thesis.

Chapter 2: Proposes a novel entropy-based feature extraction technique combined with a hybrid classifier for detecting gearbox faults. Experimental validation and results demonstrate the model's efficacy and robustness. Key findings are discussed to establish their contribution to fault detection research.

Chapter 3: Focuses on CEEMDAN-based combined DL model for automated detection of gear cracks. The methodology, experimental setup, and performance analysis are detailed. The chapter highlights the model's superiority in handling complex fault detection scenarios.

Chapter 4: Focuses on developing a combined architecture that integrates LinkNet and DenseNet to address combined faults in EM systems. Experimental results illustrate the model's capability in multi-fault detection scenarios. The comparative analysis emphasizes its performance improvements.

Chapter 5: Conclusions are made by summarizing the research contributions and significant findings in fault detection. Limitations of the current work are acknowledged, and future research directions are proposed to advance the field. Potential applications of the proposed techniques are also discussed.

Chapter 2

Gearbox Fault Detection Using Entropy-Based Feature Extraction and Hybrid Classifier

This chapter suggests a novel combined DL-based method for classifying and detecting gearbox faults, leveraging the strengths of advanced statistical and ML techniques. The technique combines Shannon features, modified log-energy entropy, modified Renyi entropy, statistical characteristics, and higher-order statistical features to extract diverse and significant information from gearbox data. A strong DL architecture that combines RNN and Bi-LSTM networks is used to detect and classify faults. This makes it possible for the system to learn forward and backward temporal connections. An optimization mechanism is introduced to improve the performance of the model further, where the opposition- based artificial Hummingbird crow search algorithm (OAHCSA) is employed to optimize the RNN weights. This combined approach ensures efficient parameter tuning and improves the learning capability of the model, leading to more precise fault diagnosis. By incorporating these advancements, the proposed methodology aims to provide a comprehensive solution to gearbox fault diagnosis, addressing challenges associated with feature extraction, classification accuracy, and computational efficiency.

2.1 Introduction

Gearbox fault diagnosis is a crucial process, as the gearbox plays a vital role in ensuring vehicle performance, efficiency, and safety. It is responsible for transmitting power from the engine to the wheels and controlling the vehicle's speed [102-103]. However, due to the mechanical complexity and harsh operational conditions, gearboxes are prone to faults such as gear wear, misalignment, bearing damage, and lubrication issues. Early and accurate fault detection is essential to prevent severe damage, reduce downtime, and minimize maintenance costs [104-108]. Traditional gearbox fault diagnosis methods often involve time and frequency-domain signal analysis and vibration-based techniques. Time- domain methods analyze raw data collected from sensors, whereas frequency-domain methods use signal processing techniques like FFT to identify fault characteristics based on spectral information [109]. While these methods can be effective for more straight forward fault scenarios, they struggle to capture the intricate and non-linear relationships in

more complex fault patterns, particularly in modern gearboxes with advanced designs and a wider range of potential failures. As such, there is a growing demand for more sophisticated, intelligent systems capable of providing a higher level of fault diagnosis, accuracy, and efficiency.

Significant progress has been made in the use of ML and DL approaches for gearbox fault diagnostics in recent years. Existing approaches have included models such as SVM, DT, random forest (RF), and CNN, which rely on data-driven learning from large datasets of operational and fault-related signals [110-113]. In fault classification, these techniques have demonstrated encouraging outcomes and tackle the issue of nonlinearity in fault patterns [114]. Because they can successfully address the drawbacks of conventional techniques, like difficulty in handling non-linear patterns, reliance on manual feature engineering, limited scalability, and sensitivity to noise, SAE has drawn more interest since the emergence of unsupervised DL techniques [107]. In fault detection, DL approaches such as CNN, stacking sparse autoencoder (SSAE), artificial neural networks (ANN), and DBN outperform supervised learning (SL) [115]. However, a large dataset is required for these strategies to be successful. Furthermore, the natural evolution theory (the genetic algorithm) and the bionics theory (the ant colony algorithm) are employed for fault identification in rotating machines. Kumar et al. (2019) [116] investigated the effectiveness of wavelet-based parameters for fault identification using PSVM and SVM. According to this study, PSVM is superior to SVM.

Recent studies have proposed combined techniques to address these challenges more effectively. For instance, by capturing spatial and temporal connections, ML models combined with DL architecture such as CNN and LSTM networks have demonstrated considerable potential in increasing fault detection accuracy. Additionally, methods such as extreme learning machines (ELM) and deep autoencoders have been used for fault detection, where the autoencoders learn to reconstruct sensor data, and any deviation from the expected reconstruction is interpreted as a fault. In order to improve model performance and convergence, optimization methods like particle swarm optimization (PSO) and genetic algorithms (GA) have occasionally been used to fine-tune model parameters. These solutions, while effective, still face challenges in achieving optimal performance under real-time conditions. Incorporating more advanced optimization techniques, such as the OAHCSA, has been proposed to further enhance model performance by efficiently optimizing the weight parameters of DL models, thereby

addressing accuracy and computational efficiency concerns.

2.2 Proposed Methodology

This study provides a novel approach for classifying and detecting gearbox faults utilizing a combined DL technique specifically designed to have minimal computational time. The process involves several steps, such as pre-processing, feature extraction, and classification with optimized training. First, the pre-processing is done by median filtering (MF), in which the input is a signal. Subsequently, key features are extracted from the processed data, including statistical measures, higher-order statistical (HOS) features, modified Renyi entropy, and adjusted log-energy entropy [116]. These extracted features are then fed into a hybrid classifier (HC) model, which combines the strengths of two classifiers: the RNN and the Bi-LSTM. Optimizing the RNN's weight using the OAHCSA algorithm enhances the hybrid model's performance. The final step involves utilizing the model's predictions for effective fault detection. Figure 2.1 illustrates the architectural flow of this proposed detection framework.

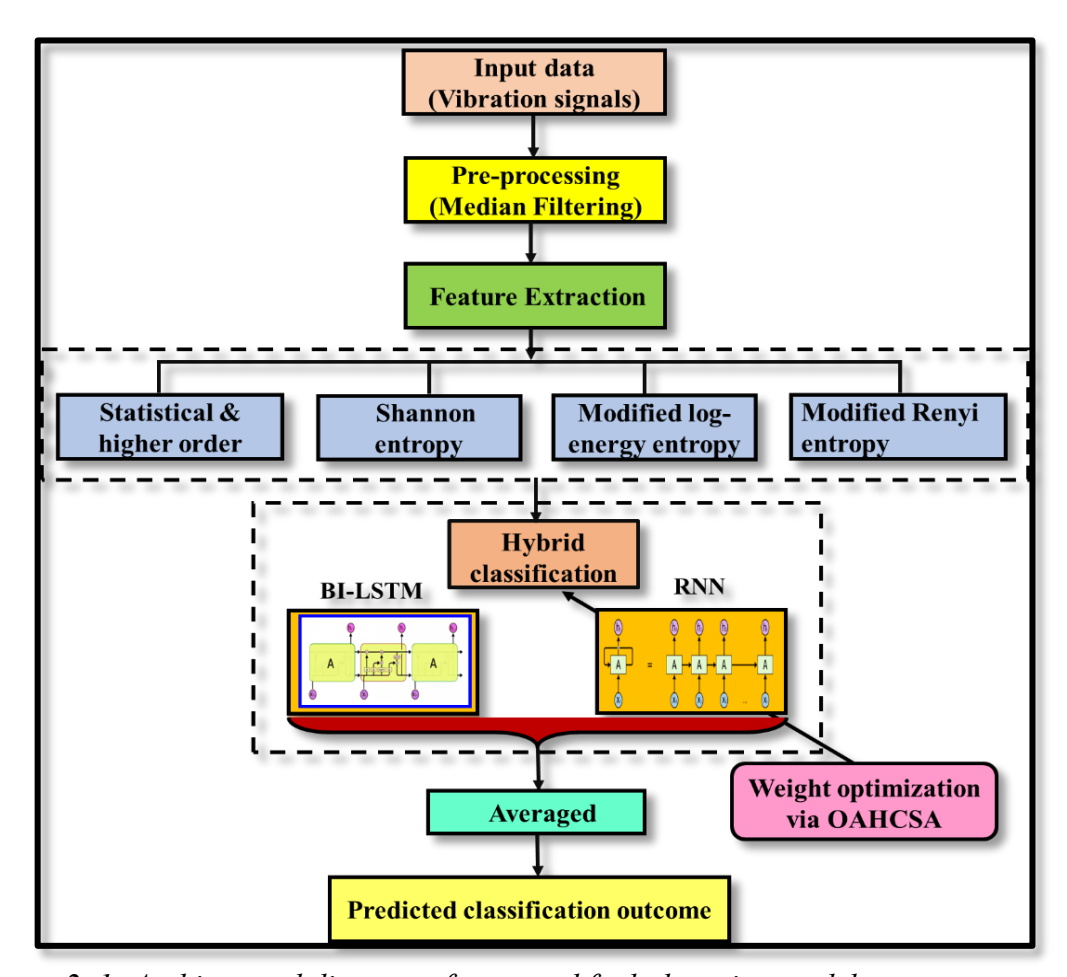


Figure 2. 1: Architectural diagram of proposed fault detection model.

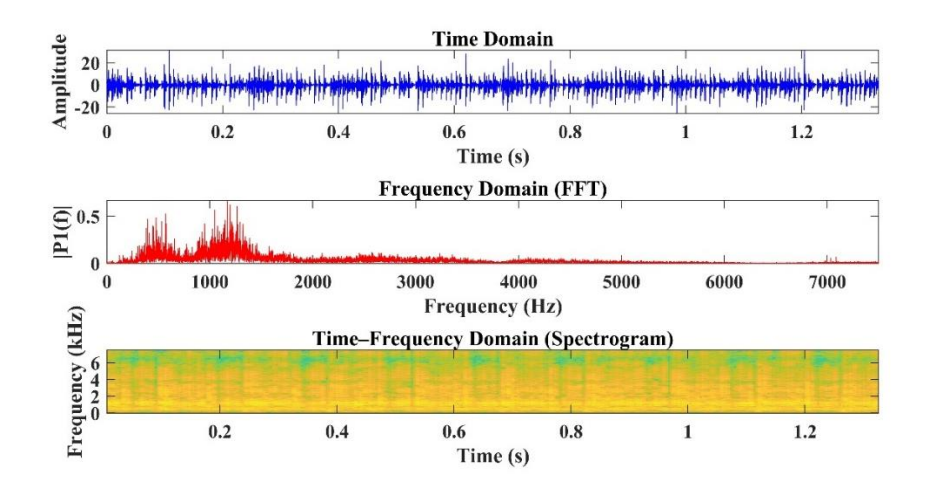
2.2.1 Pre-processing by Median Filtering

Data pre-processing is an essential initial step in data analysis that involves transforming raw data into usable format for further exploration, modeling, and interpretation. Its purpose is to prepare data for analysis by cleaning, transforming, and organizing it. The proposed method makes use of MF as the technique for pre-processing. This approach preserves the signal's most essential characteristics and remains noise-robust, which is vital for classification tasks. In fault detection, keeping the edges of data and removing impulsive noise is crucial; MF filtering is excellent [117-118]. Unlike Gaussian or mean filtering, MF does not distort the signal as much, making it more appropriate for preserving the integrity of features indicative of faults. By using the MF technique, the input signal's quality has improved. This non-linear signal or image processing technique is where every data point gets replaced by the median value of its neighbors. So, the noise is diminished, and fine details and edges are retained. MF is very effective in reducing noise without blurring the edges. Hence, MF is less sensitive to outliers. Application of this technique ensures that input data accurately depicts fault conditions and consequently makes the classifications more reliable. This filter reduces noise while keeping important features, enhancing the accuracy of the fault detection model in capturing temporal patterns and anomalies characterizing faults. This work denoises the input signal, smoothed, and processed using the MF, as demonstrated in Equation (2.1). Using a 3×3 pixel mask, the method achieves a balance between noise reduction and detail preservation by assigning each pixel the median value of its 3×3 neighboring grids. The usage of this filter size accomplishes effective noise suppression with the maintenance of critical details. Equation (2.1) shows how effective this filtering process is,

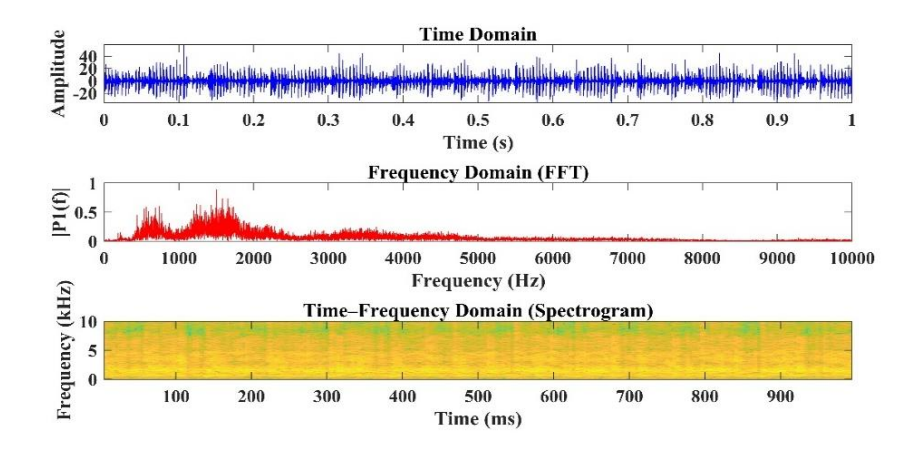
$$\sigma_{med}^2 = \frac{1}{4hF^2(h)} \approx \frac{\sigma_c^2}{h + \frac{\pi}{2} - 1} \cdot \frac{\pi}{2}$$
 (2.1)

In Equation (2.1), σ_c denotes the variance of the input noise power, h represents the size of the MF mask, and F(h) is the noise density function. To ensure that the MF is applied uniformly to the entire dataset, including edges, edge handling techniques such as edge padding are used during the filtering process. These parameters guarantee efficient noise reduction while maintaining the signal's essential characteristics. The filter's mask size and noise density function enable it to vary according to changing noise density without losing necessary signal features. Edge handling ensures smooth processing of areas close to the boundary as artifacts frequently occur there, leading to a uniform reduction of noise from the signal. Thus, raw vibration signals can be analyzed using the MF approach.

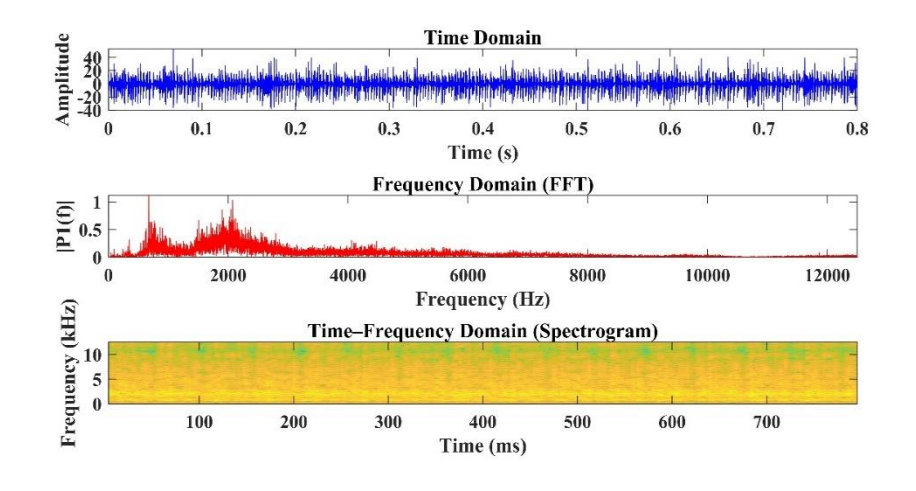
The representation of healthy and faulty signals in the time domain, frequency domain (FFT), and time-frequency (TF) domain are represented in Figure 2.2 and Figure 2.3. These representations provide a baseline understanding of the signal characteristics before applying the suggested feature extraction and classification techniques.



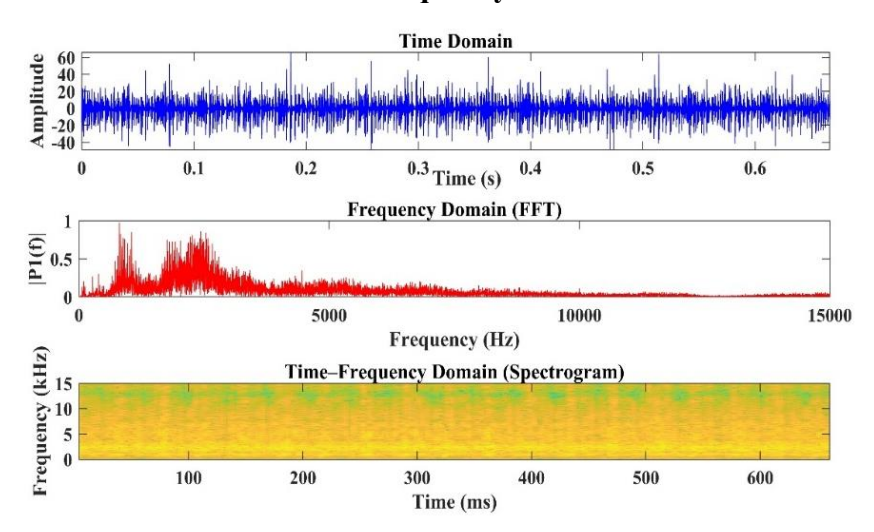
Frequency = 15 Hz



Frequency = 20 Hz

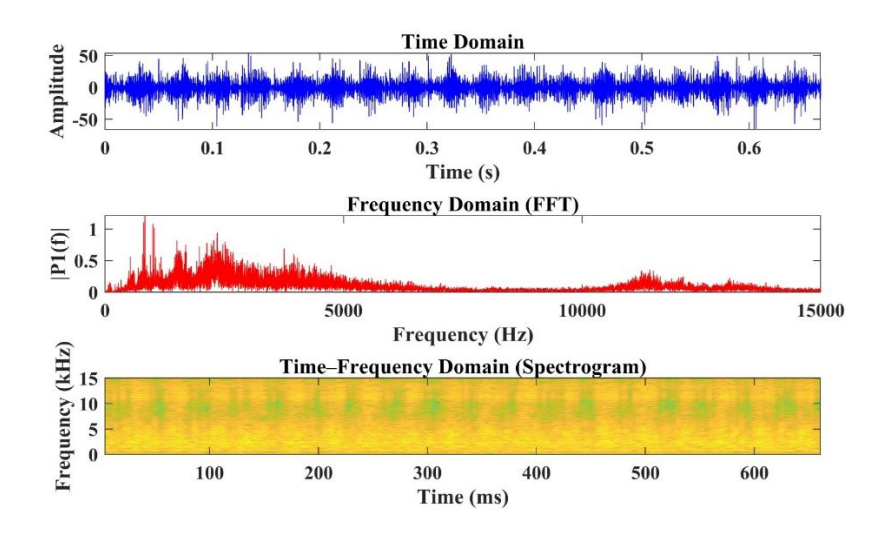


Frequency = 25 Hz

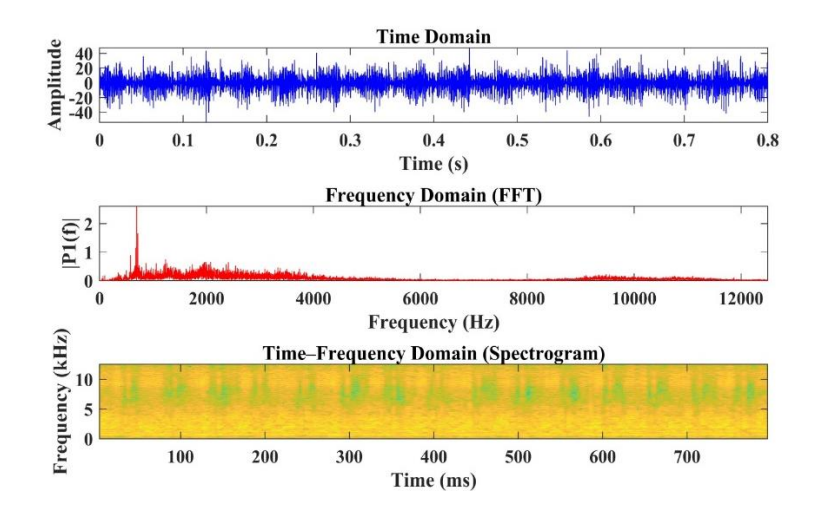


Frequency = 30 Hz

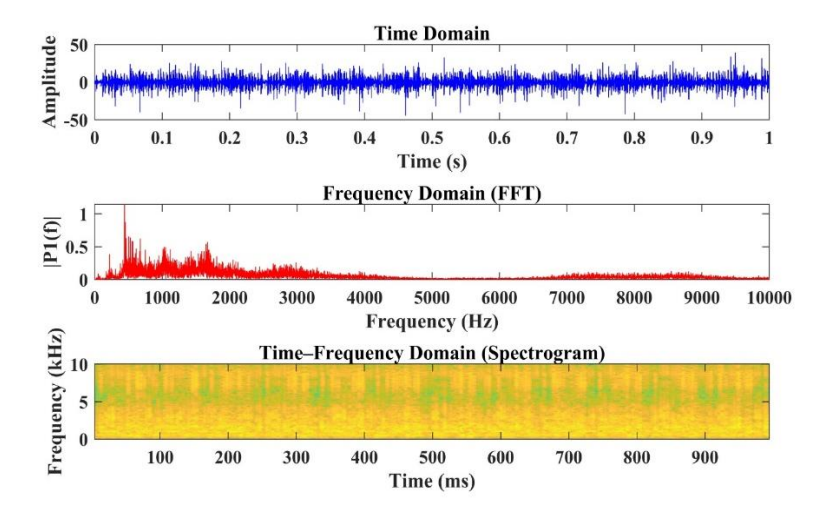
Figure 2. 2: Time, frequency, and time—frequency domain representations of the healthy signal



Frequency = 15 Hz



Frequency = 20 Hz



Frequency = 25 Hz

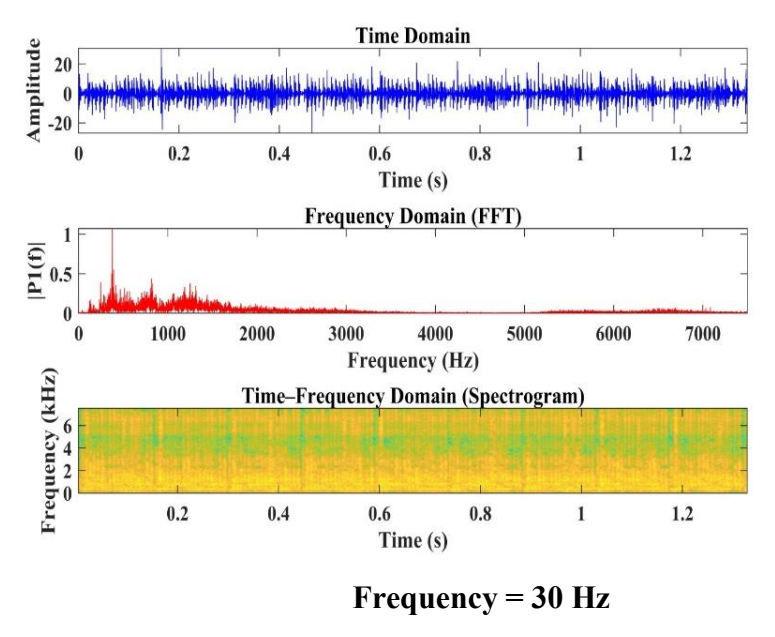


Figure 2. 3: Time, frequency, and time–frequency domain representations of the faulty signal

Figure 2.4 depicts the performance of median filtering in preprocessing against the traditional approach for healthy signals. Figure 2.5 shows the same analysis for faulty signals. The result depicts that median filtering works more effectively than the conventional approach, which is done in the form of Gaussian filtering, low-pass Butterworth filtering, and Wiener filtering for gearbox fault detection. A non-linear filtering approach, median filtering is specifically better suited to eliminating impulse noise without making severe compromises in the signal features [94-95]. Traditional methods typically lack robust signal integrity: low-pass Butterworth filtering can eliminate high-frequency details critical to fault information; Gaussian filtering tends to blur significant high-frequency information; and even with its adaptability to noise characteristics, Wiener filtering brings potential phase shift-induced damage to the signal structure.

MF clearly shows superiority in terms of giving cleaner signal representations for healthy and faulty conditions at all the frequencies considered for evaluation, namely 15 Hz, 20 Hz, 25 Hz, and 30 Hz [98]. This robustness improves the reliability of feature extraction as important information is preserved for further analysis. Ultimately, median filtering ends up being the best of all the pre-processing techniques incorporated, which significantly improves the accuracy of combined DL models in fault classification. This approach provides a sturdier basis for detecting gearbox failure, thus further enhancing the overall dependability of the system.

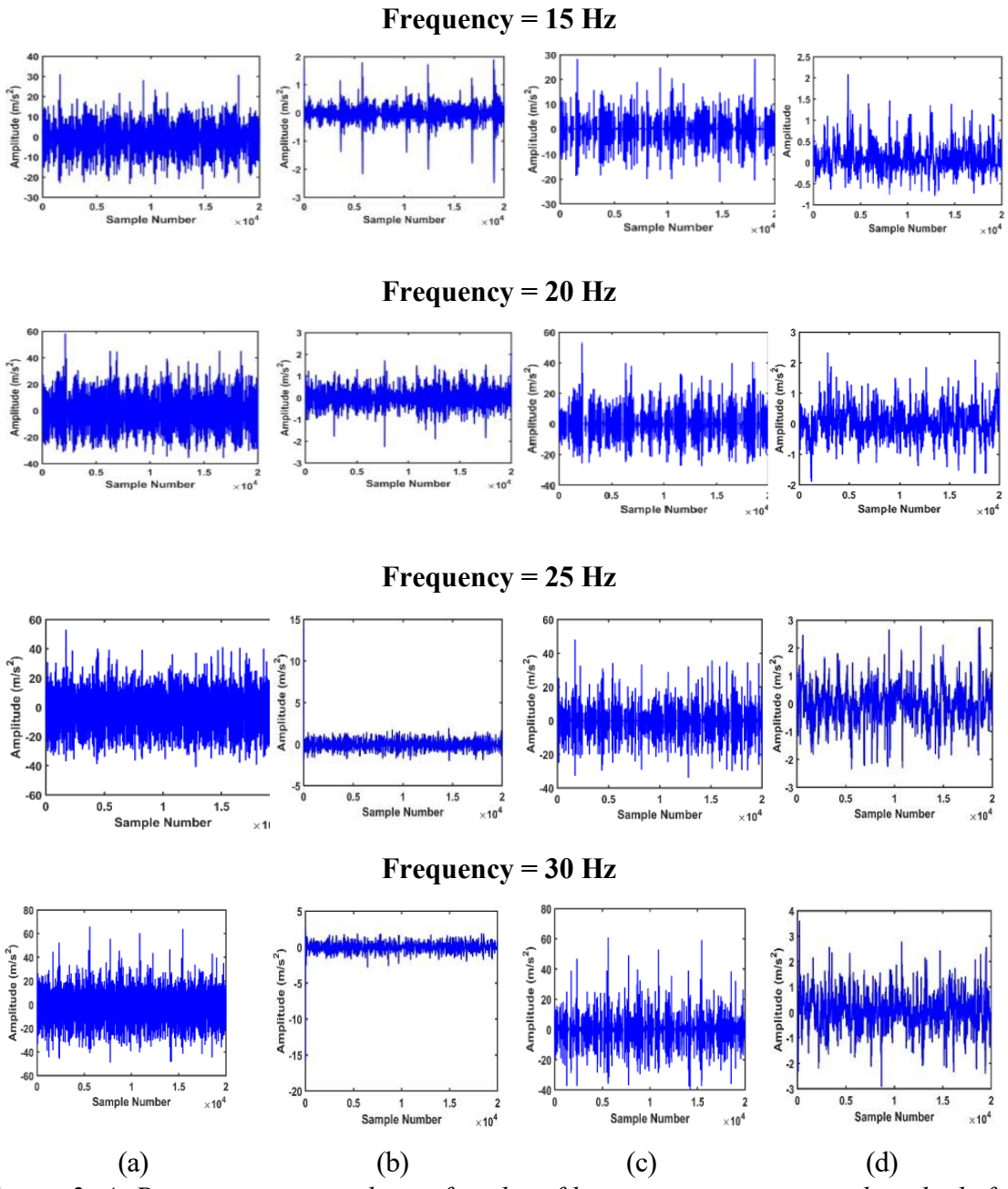


Figure 2. 4: Pre-processing analysis of median filtering over conventional methods for healthy signals (a) Gaussian filtering (b) Low-pass Butterworth filtering (c) Wiener filtering (d) Median filtering.

Table 2. 1: Quantitative analysis for healthy signal

Filter	SNR (dB)	MSE
Gaussian	15.2	0.025
Butterworth	18.5	0.018
Wiener	20.1	0.014
Median	23.4	0.010

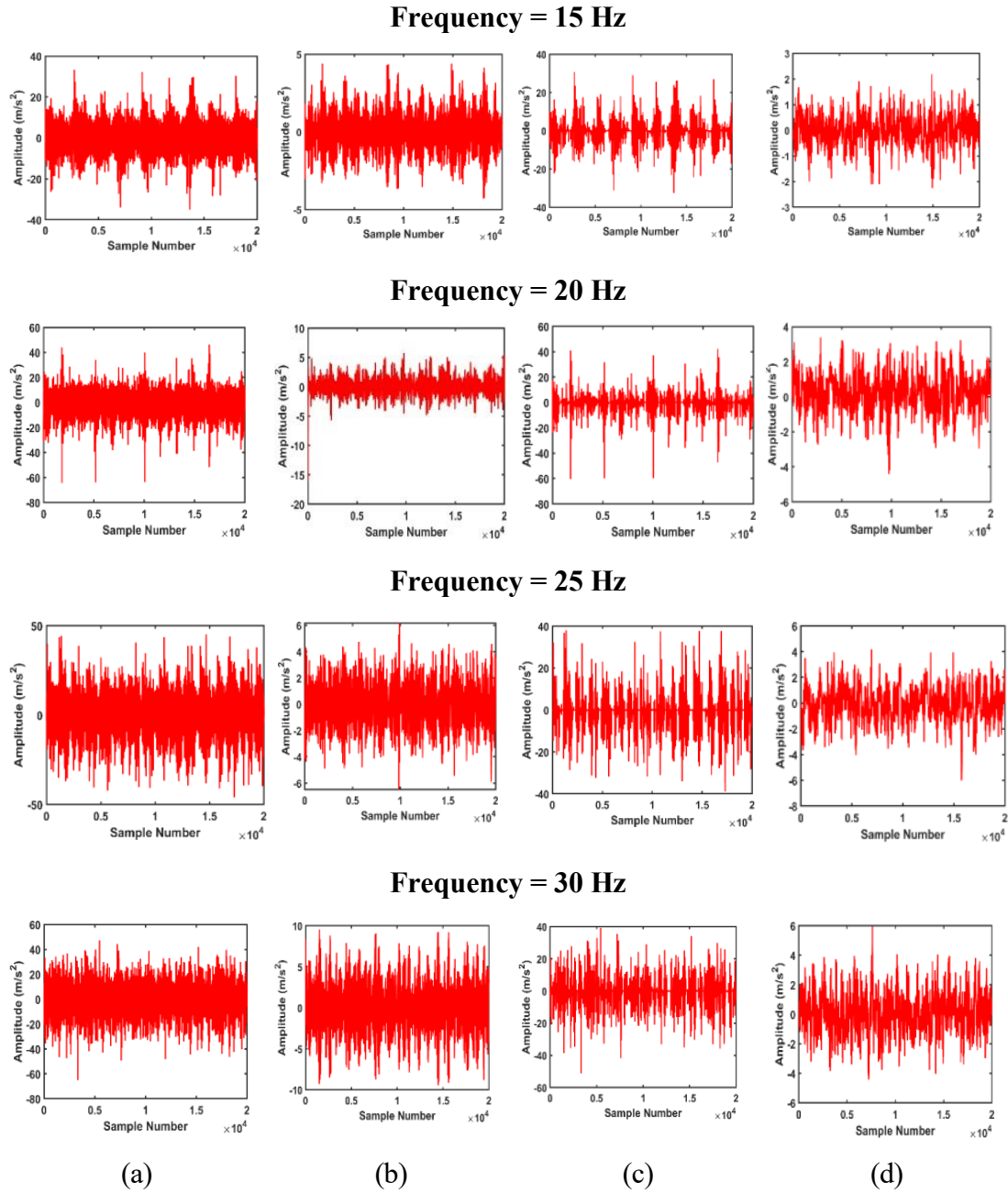


Figure 2. 5: Pre-processing analysis of median filtering over conventional methods for faulty signals (a) Gaussian filtering (b) Low-pass Butterworth filtering (c) Wiener filtering (d) Median filtering.

Table 2. 2: Quantitative analysis for faulty signal

Filter	SNR (dB)	MSE
Gaussian	16.7	0.021
Butterworth	19.4	0.016
Wiener	21.2	0.012
Median	24.8	0.008

The evaluation metrics, such as Signal-to-Noise Ratio (SNR) and Mean Squared Error

(MSE) for the healthy and faulty signals are tabulated in Tables 2.1 and 2.2, respectively. From the tables, the median filtering demonstrated the highest SNR of 23.4 dB for healthy and 24.8 dB for faulty signals, and the lowest MSE of 0.010 for healthy and 0.008 for faulty signals among all filters. These values quantitatively confirm the enhanced noise suppression and better preservation of signal features of the proposed approach, which are crucial for accurate fault detection.

2.3 Extraction of Features

Feature extraction is one of the essential processes, as it identifies features that are most representative of the data while disregarding insignificant ones; therefore, it ensures appropriate identification of the characteristic aspects of the data, which helps in analyzing and classifying more effectively. Added to all this is the benefit of providing entropy-based features that take cognizance of the measurement of complexity and the dynamics of change within a nonlinear time series. Entropy is one of the most powerful tools to understand non-linear behaviors. It has been extensively studied in the field of mechanical fault diagnosis, especially for gearbox fault monitoring applications. A variety of entropy-based methods, including sample entropy and permutation entropy, can be applied to non-linear vibration signals to extract valuable information. However, conventional entropy approaches suffer from instability and loss of critical feature information. Thus, to counter such limitations, this work incorporates advanced feature extraction techniques such as a combination of:

Shannon entropy: determines how much uncertainty and information are in a signal.

Improved log energy entropy: Provides higher signal sensitivity, promoting higher fault-related features.

Improved Renyi entropy: It provides a more generalized framework to capture the complexity of nonlinear signals.

Statistical features include mean, variance, skewness, and kurtosis measures, these describe signal properties.

HOS Features: This leads to more profound insight into nonlinear and non-Gaussian properties of signals.

The proposed method effectively eliminates the shortcomings of traditional entropybased approaches through advanced feature extraction techniques. Thus, the developing features could increase the robustness and precision of fault detection for the effective mechanical fault diagnosis platform.

2.3.1 Shannon Entropy Features

A statistical indicator of information's unpredictability or uncertainty is Shannon's entropy. It has its roots in information theory and is useful when addressing the complexity and variability of a system or signal since it can be applied to the distribution of data among input, output, and intermediate variables. Strategies such as edge padding in signal processing allow for the application of a filter, say, an MF, homogeneously to the entire dataset and the boundary regions. Such strategies are helpful in retaining the integrity of the signal by keeping the desired features with efficient noise suppression. Shannon's entropy plays a key role in data analysis regarding randomness and distribution characteristics [119][120]. It is mathematically given as in Equation (2.2), where $P(y_i)$ refers to the probability of a single event.

G(y) symbolizes the relationship or transformation applied to the probabilities to calculate entropy, n represents the total number of distinct events, log_b denotes logarithm to the base, which can be 2 (for bits).

$$fe^{SE} = G(y) = \sum_{i=1}^{n} [P(y_i) * log_b(1/P(y_i))]$$
(2.2)

The extracted Shannon's entropy features are specified as fe^{SE} .

2.3.2 Improved Log Energy Entropy

Entropy quantifies a system's degree of randomness or information content, while log energy entropy explicitly measures signal complexity, focusing on energy distribution [121]. The traditional formula for calculating log energy entropy fe^{SE} is shown in Equation (2.3). This metric evaluates the logarithmic distribution of signal energy and is often applied to analyze signals with complex patterns. The log energy entropy calculation in the proposed method is refined by incorporating a weighting mechanism. Attributes with lower entropy values are assigned to higher weights, emphasizing their significance and reducing the risk of losing critical information during aggregation. These weighting factors are empirically derived from the data using the SoftMax function, ensuring adaptability and relevance to the dataset. The enhanced log energy entropy is represented in Equation (2.5).

$$fe^{le}(y) = -\sum_{i=0}^{n-1} (log_2(P_i(y)))^2$$
(2.3)

$$fe^{ile}(y) = -\sum_{i=0}^{n-1} (log_2(P_i(y)))^2 * we$$
 (2.4)

$$we = \frac{e^{-E(y_i)}}{\sum_{i=1}^{n} e^{-E(y_i)}}$$
 (2.5)

The extracted log energy entropy features are revealed by fe^{ile} .

2.3.3 Improved Renyi Entropy

The Renyi entropy is used to measure diversity in ecology and statistics and plays an essential role in quantum information, specifically in quantifying entanglement. It can be explicitly calculated in the Heisenberg XY spinning chain model due to its relationship with a subset of the modular group. In theoretical computer science, randomness extractors are studied using min-entropy [121–132]. In mathematics, the Renyi entropy for rank α is commonly represented by equations (2.6). However, due to its non-linear dependence on the density matrix, a new augmented Renyi entropy model based on weight is built, as shown in equation (2.7). Here, α represents the rank parameter of the Renyi entropy $G_{\alpha}(y)$ represents the mathematical formulation of Renyi entropy, P_i indicates the probability of the i^{th} event, $||P||_B$ represents the B norm of the probability vector P. This sensitivity is increased in the enhanced version, allowing for the detection of minute changes in the signal that other entropy measures could overlook. It is helpful in locating early faults that show slight entropy variances in the signal.

$$fe^{Re} = G_{\alpha}(y) = \frac{1}{1-\alpha} \log \sum_{i=1}^{n} P_i^{\alpha}$$
(2.6)

$$fe^{IRe} = G_{\alpha}(y) = \frac{\alpha}{1-\alpha} log(\parallel P \parallel_B) * wei$$
 (2.7)

$$||P||_B = \left(\sum_{i=1}^n P_i^B\right)^{\frac{1}{B}} \tag{2.8}$$

The extracted improved Renyi entropy features are indicated by fe^{IRe} .

2.3.4 Higher-Order Statistics and Statistical Features

Statistical features and other higher-order attributes, such as kurtosis and moment, were computed to analyze the data for gearbox fault detection. Such features are used to detect the signal characteristics that may signify faults [122].

Kurtosis measures the "tailedness" of a probability distribution and measures the amount of departure of the dataset from the normal distribution. High kurtosis values usually indicate that the data contains extreme values or outliers and are generally associated with sudden changes or impulsive events in the signal [123-125]. This property is specifically helpful for detecting gearbox faults, as high kurtosis values in vibration signals might indicate crack, wear, or misalignment faults. Lower kurtosis values indicate lighter-tailed distributions with fewer outliers, often representing smoother or less erratic signals. This metric is beneficial for fault detection since sudden energy spikes or anomalies in the vibration data are strong indicators of irregularities in the gearbox system [35]. Importance in gearbox diagnostics: Kurtosis [124] is helpful in identifying nonnormal distributions in vibration signals, thus aiding in identifying healthy and faulty operation conditions. This feature makes the analysis sensitive to irregularities associated with mechanical faults.

$$Kur = \frac{\sum_{i=1}^{M} (Z_i - \bar{Z})^4 / M}{K^4}$$
 (2.9)

According to Esmael et al. (2013) [125], in probability and statistics, this is the point at which the random variable experiences probability dispersion. The mean value of the specified integer power separates the mean from the random variable. Moments are numerical measurements associated with the graph form of a function. Higher-order moments can provide details about the variability and distribution shape, but the first moment, the mean, represents the central tendency. Moments can be used to discover deviations from normal operation in the behavior of the signal, which is helpful in fault identification. Very often, such deviations represent anomalies caused by faults such as misalignment, imbalance, or wear in the gear. Moments enable the system to detect signal pattern changes that are not performing as they should, thereby allowing the early classification of faults. Thus, variation in vibration signal works is a crucial characteristic explaining moments in mechanical fault diagnosis.

The extracted higher and statistical-order features are denoted by fe^{ht} and fe^{st} , in that order. The extracted features fe are indicated by Equation (2.10).

$$fe^{SE} + fe^{ile} + fe^{IRe} + fe^{st} + fe^{ht} = fe$$
 (2.10)

The model can use the extracted features to distinguish fault conditions from normal operating states. A combined classifier uses a combination of several algorithms using the retrieved characteristics as an input to increase accuracy and robustness in detecting faults. The integration further improves the system's capability to identify and classify gearbox faults, hence ensuring the reliable maintenance and operation of the machinery. Combining the signal's informational content with variabilities through Shannon entropy, enhanced logarithmic energy entropy, better Renyi entropy, as well as statistical measurements yields a comprehensive analysis that surpasses others with even stronger and more trustworthy fault detection, hence assuring no easy swaying by such mechanical mistakes or any kinds of deviation for the said system.

2.4 Hybrid Classifiers with Opposition-based Artificial Hummingbird Crow Search Algorithm-Based Tuning

The RNN DL model is designed to retain sequential data and be used for prolonged periods in a prediction, making it very useful and appropriate for time series predictiveness in many applications. The size does not change with the magnification of the input signal. However, Bi-LSTM networks capture more content by processing the data back and forth, thus increasing the richness of information available for the algorithm. The method combines an RNN with a Bi-LSTM to identify fault conditions in a gearbox. However, even though prolonged training durations tend to work, overfitting circumstances often exist where, eventually, the model commences understanding noise and spurious conditions within the train data, over-generalizing worthwhile trends [74]. Eventually, the model may degrade as far as performance is concerned with datasets not yet seen and miss faults outside its training sets. It deals with all these by improving the RNN's training process, which the researcher conducts using this novel OAHCSA algorithm. Such an improvement shall help decrease overfitting by not letting the model focus solely on recognizing redundant patterns that do not lead to actual data relationships; this can enhance its capabilities in better fault detection and classification.

2.4.1 Hybrid Classifiers

The RNN and Bi-LSTM are used to detect faults, and outcomes are achieved by averaging the RNN and Bi-LSTM outputs. Bi-LSTM and RNN are combined to create the combined classifier because of their complementing abilities to handle sequential input and capture intricate temporal relationships. RNNs are suited for time-series analysis because they are skilled at processing sequences and keeping hidden states that reflect information from

previous time steps. However, due to shrinking gradients, RNNs might have trouble handling long-term dependencies by themselves. In order to overcome this, Bi-LSTM networks are constructed. These networks use bidirectional processing and gating methods to efficiently manage long-term relationships and collect background information from previous and upcoming time steps. The combined technique enhances fault detection accuracy by leveraging the combined strengths of the RNN's ability to handle sequential data and the Bi-LSTM's superior understanding of temporal connections, resulting in a more comprehensive data analysis.

RNN: Neural network (NN) components make up an RNN [124] designed to analyze a series of data D^{sim} , with a time step index of t. The three steps of the RNN are input, hidden state, and output. Here, $D_{1,2,\dots,M}^{sim}(t)$ refers to the input sequence, whereas M refers to the input vector's count at the time t, and the previous values of U(t) are represented by the output vector, $D_{1,2,\dots,M}^{sim}(t)$. The concealed state U(t) is modeled in equation (2.11); The ReLU and tanh get symbolized by fun, while the weight matrices are implied by H, W, V.

$$U(t) = fun.(H.D^{sim}(t) + W.U(t-1))$$
(2.11)

The steps in RNN include:

Step 1:H, W, V, and bias functionsb, care initialized with 0's.

Step 2: The SoftMax function is used to get the output's normalized probability \hat{Y} .

Step 3: Equations (2.12) to (2.15) are used to compute the forward pass. Here, a(t) is an intermediate activation calculation at time, b represents a bias term added to the activation, Q(t) denotes the raw output at time, c represents another bias term used in the output calculation, $\hat{Y}(t)$ signifies the predicted output at the time.

$$a(t) = b + H.I(t) + WU(t-1)$$
 (2.12)

$$U(t) = tanh.(a(t))$$
(2.13)

$$Q(t) = c + U(t).V \tag{2.14}$$

$$\hat{Y}(t) = soft \max(Q(t)) \tag{2.15}$$

Step 4: Equation (2.16) estimates the loss function. Here, $y_{o,r}$ represents the actual label (class label) for the output corresponding to the r^{th} class, $g_{o,r}$ represents the predicted probability of the output belonging to the r^{th} class.

$$Loss = -\sum_{c=1}^{J} y_{o,r} \cdot log(g_{o,r})$$
 (2.16)

Bi-LSTM: A number of recurrent LSTM cells [126] are covered by the Bi-LSTM [126] classifier. Each Bi-LSTM cell has input, output, and forget gates. Assuming that variables Z and D are concealed, the cell state, (X_t, D_{t-1}, Z_{t-1}) and (Z_t, D_t) , designates refer to the output/input layer. At the timet, forget output and input gates are signified as F_t , O_t , I_t . Bi-LSTM initially utilizes F_t to arrange data that is modeled as in equation (2.17). Here, X_t represents the input data at a time, D_{t-1} denotes the previous output or hidden state from the previous time step, Z_{t-1} symbolizes the previous cell state and F_t signifies the forget gate activation at a time.

$$F_t = \sigma(J_{IF}X_t + L_{IF} + J_{ZF}Z_{t-1} + L_{ZF}) \tag{2.17}$$

In equation (2.17), (J_{ZF}, L_{ZF}) and (J_{IF}, L_{IF}) refer to weight along with bias limitation for hidden state mapping as well as input to forget gate and refer to activation function σ .

Bi-LSTM used the input gate by equations (2.18) to (2.20), where (J_{ZG}, L_{ZG}) and (J_{IG}, L_{IG}) Correspondingly, it refers to weight along with bias limitation for hidden state mapping and input to the cell gate. (J_{ZI}, L_{ZI}) and (J_{II}, L_{II}) entail weight along with bias for hidden state mapping and input layers toward I_t . I_t indicates the input gate activation at the time, σ denotes the sigmoid activation function used for the gates, G_t represents the candidate cell state generated at time, J, L are weight matrices and bias terms, respectively, associated with the various gates.

$$G_t = tanh(J_{IG}X_t + L_{IG} + J_{ZG}Z_{t-1} + L_{ZG})$$
(2.18)

$$I_t = \sigma(J_{II}X_t + L_{II} + J_{ZI}Z_{t-1} + L_{ZI})$$
(2.19)

$$D_t = F_t D_{t-1} + I_t G_t (2.20)$$

$$O_t = \sigma(J_{IO}X_t + L_{IO} + J_{ZO}Z_{t-1} + L_{ZO})$$
(2.21)

$$Z_t = O_t \tanh(D_t) \tag{2.22}$$

Equation (2.21) indicates that the output gate provides the Bi-LSTM cell with a concealed state, which is shown in equation (2.22), in which (J_{ZO}, L_{ZO}) and (J_{IO}, L_{IO}) refer to weight as well as a bias for hidden state mapping and input layer to O_t , respectively. O_t represents the output gate activation at the time; the results of the RNN and Bi-LSTM are averaged to get the final output. The classifiers' parameter settings are detailed in Table 2.3.

Table 2. 3: Parameters of the classifiers

Models	Parameter values		
Bi-LSTM	No of hidden units = 100		
	Learning rate $= 0.01$		
	Sequence Input Layer - 1		
	Bi-LSTM Layer - 1		
	Fully Connected Layer - 1		
	Softmax Layer - 1		
	Classification Layer - 1		
	Activation function = SoftMax		
	Optimizer = 'sgdm'-Stochastic gradient descent with		
	momentum.		
S-Net	Learning rate = 0.01		
	Convolution - 1		
	Fire module - 8		
	Activation - Relu		
	Max Pooling - 2		
	Global Average Pooling - 1		
	within Fire module:		
	Convolution - 2		
	Activation layer (Relu) – 2		
R-Net	Learning rate $= 0.01$		
	Convolution - 1		
	Max Pooling - 1		
	Activation – Relu		
RNN	Learning rate $= 0.01$		
	Input Layer		
	LSTM Layer (100); 100 refers to the number of hidden		
	units		
	Fully Connected Layer (384); 384 refers to the number		
	of neurons in the next FC hidden layer		
	Softmax Layer		
	Classification Layer		

2.4.2 Opposition- Based Artificial Hummingbird Crow Search Algorithm for Tuning Optimal Weights

Optimal fine-tuning of hyperparameters, including weights, batch size, and learning rate in deep learning, is not definitively achievable. In practice, these parameters play a crucial role in model performance, and improper tuning can lead to suboptimal results. A primary focus of this combined classification model, RNN-Bi-LSTM, is the optimization of its weights, using the algorithm known as OAHCSA to minimize those errors. The OAHCSA algorithm dynamically adjusts its internal parameters during training to yield fewer prediction errors and better detection performance. For gearbox fault detection, very finetuning of complex parameters of DL models such as RNNs and Bi- LSTMs is required. The proposed OAHCSA algorithm combines several optimization strategies to enhance the combined model's functionality. OAHCSA combines various optimization methodologies in order to improve the quality of the solutions and the effectiveness of the search process. Integration of Opposition Learning and AHCSA pro- vides robust optimization capabilities. Opposition Learning expands the searching space and avoids getting trapped in the local minima by simultaneously searching for both existing and opposite solutions. In this case, the crow search algorithm (CSA) [127] is modeled after the social behavior of foraging by crows together with memory to find the best solutions through cooperation. In contrast, the artificial Hummingbird algorithm (AHA)

[110] balances exploration with exploitation while replicating the adaptive foraging patterns of hummingbirds. An efficient and comprehensive search process improves accuracy and speed during model training for fault detection. It will ensure the creation of a robust and accurate system that can provide reliable diagnostics and ensure good operation of the system under consideration.

Objective function: The objective Obj, of the research is to minimize the error er, as given in equation (2.23). The weight W of RNN is selected using the OAHCSA approach.

$$Obj = min(er) (2.23)$$

The CSA is known for providing optimal solutions in various applications with limited control parameters. While offering fast convergence, the algorithm can become trapped in a local optimum. Although the algorithm efficiently finds a good solution, its greedy nature may prevent it from reaching the best solution. The OAHCSA approach combines the AHA concept proposed by Zhao et al. (2022) with CSA to address the limitations of conventional CSA. Meanwhile, the developed OAHCSA model attains

numerous advantages, such as faster convergence and intense global search with minimum time (i.e., the solution obtained is trustworthy). Specific search space issues are believed to be amenable to hybridized optimization strategies [132-136].

The original CSA is improved by the OAHCSA, which incorporates sophisticated ways to get over its drawbacks, like becoming caught in local optima. After initializing crow placements at random, OAHCSA uses opposition learning to investigate complementary solutions, expanding the search space. Then, it employs dynamic awareness probability (DAP) to balance exploration and exploitation. A high DAP value results in AHA-based updates that refine positions using dynamic parameters. In contrast, a low DAP value initiates exploration utilizing a formula that modifies crow positions based on the locations of other crows. Crows adjust their memory in accordance with fitness evaluations, which decide whether new postures are better than prior ones. This combined approach reduces the likelihood of local minima and improves global search and solution quality. It creates faster convergence and more reliable optimization by fusing the benefits of CSA with the adaptive techniques of AHA and opposition learning.

The mathematical modeling of the OAHCSA model is described in a detailed way as given below:

The CSA mimics the intelligent characteristics of a crow. The flock size is referred to as M, and the i^{th} crow location iteration, it, inside the search, region-depicted as $Z^{i,it}i = (1,2...M;it = 1,2...it_{max})$, in which $Z^{i,it} = \begin{bmatrix} Z^{it}_1, Z^{it}_2, ... Z^{it}_d \end{bmatrix}$ as well as it_{max} refers to the maximal iteration count. At it, the crow i's position and hidden crow location are depicted by $v^{i,it}$. The finest position that crow i has so far managed to secure is thought to be this one. Furthermore, opposition-based learning (OBL) is used to generate opposite solutions in crow search. Considering that it; crows j require arranging their hidden area, $v^{j,it}$; at it, crow i finds the crow j to shift to crow j hidden location. Here, there are two steps.

Step 1: The Crow j is unaware of the crow i follows it. Here, the crow i tries to find the crow j hidden place, and equation (2.25) describes how the crow usually reaches its fresh position. According to OAHCSA, DAP is calculated using equation (2.24), where NP_i states the current size of the population. If DAP <random count r_i . Then, the update of CSA is performed based on AHA, as shown in equation (2.26); otherwise, a local search will be performed as shown in equation (2.25).

$$DAP = AP_{min} + (AP_{max} - AP_{min})\frac{NP_i}{NP}$$
(2.24)

$$Z^{it+1} = Z^{it} + r_i \times fl^{it} \times (\nu^{j,it} - Z^{i,it})$$
(2.25)

$$Z^{it+1} = Z_{i,tar}(it) + a.D. \left(Z_i(it) - Z_{i,tar}(it) \right)$$
 (2.26)

Conversely, whenever memory fitness (v) is less than the current fitness (Z), then a random update will be done.

Step 2: Crow j finds that crow i is finding it. Crow j thus deceives crow i by moving to several locations to get their meal. As in equation (2.27), states 1 and 2 are mentioned jointly.

$$Z^{i,it+1} = \begin{cases} Z^{it} + r_i \times fl^{it} \times \left(v^{j,it} - Z^{i,it}\right) & v \ge Z^{it} \\ a \ random \ position & Otherwise \end{cases} \tag{2.27}$$

Phase 1: Provide the constraint modifications and the problem.

Phase 2: The memories of crow and places should be assigned based on Eqns. (2.28) and (2.29), in which drefers to the decision constraints count.

$$Crows = \begin{bmatrix} Z_1^1 & Z_2^1 & \dots & Z_d^1 \\ Z_1^2 & Z_2^2 & \dots & Z_d^2 \\ \vdots & \vdots & \dots & \vdots \\ Z_1^M & Z_2^M & \dots & Z_d^M \end{bmatrix}$$
(2.28)

$$Memory = \begin{bmatrix} v_1^1 & v_2^1 & \dots & v_d^1 \\ v_1^2 & v_2^2 & \dots & v_d^2 \\ \vdots & \vdots & \dots & \vdots \\ v_1^M & v_2^M & \dots & v_d^M \end{bmatrix}$$
(2.29)

Phase 3: Evaluate fitness function.

Phase 4: Construct a unique location. When a crow i wants to find a new location, it will pick a single flock at random and follow it to find the food source that the crow v^j has hidden. The unique position that crow i has attained and maintained is shown by equation (2.29).

Phase 5: Verify whether additional positions are possible. The crow will update its position if a new one can be found; otherwise, it will stay in the currently displayed zone. Phase 6: Every time there is a new update of crow's, evaluate the fitness function.

Phase 7: Modify memory. In equation (2.30), the crow's memory update is depicted, where $f(v^{i,it})$ denotes the objective.

$$v^{i,it+1} = \begin{cases} Z^{i,it+1} & f(Z^{i,it+1}) is better than f(v^{i,it}) \\ v^{i,it} & Otherwise \end{cases}$$
(2.30)

Phase 8: Check the termination requirements. The optimal location is seen to be the solution to the optimization issues, even though termination is gained.

Table 2. 4: Describes how the optimization algorithm's parameter settings are set

```
Algorithm: Proposed OAHCSA model
Decide on M crows' location at random.
Generate OBL
Computing crow position
Assign every crow's memory.
while it < it_{max}
  for i = 1: M
     Choose row arbitrarily
     Define DAP
         if DAP < r_i,
              Update formula as per AHA in equation (2.26)
         Else
              Update formula
              as per CSA in equation (2.25)
         End if
  end for
Calculate potential outcomes for current positions.
Get the crows' current location.
Modifying crow memory
end while
```

Table 2. 5: Parameters of the optimization algorithms

Algorithms	Parameter values	
CSA	AP = 0.1; % Awareness probability	
CSA	fl = 2; % Flight length (fl)	
	Mature age = 3	
LA	Max strength = 3	
	$\max = 10$	

 $mutation \ rate = 0.15$ $Max \ age = 3$ $AP = 0.1; \% \ Awareness \ probability$ $fl = 2; \% \ Flight \ length$

2.5 Experimental Setup and Data Acquisition

The experiment is conducted to capture vibration signals of a bevel gearbox using the machine fault simulator (MFS) from Spectra Quest, as shown in Figure. 2.6. The dataset used for experimentation is considered from the previous study [132]. The main parts of the experiment test rig are a single-stage bevel gearbox, a magnetic brake, a belt and pulley arrangement, a variable frequency drive (VFD), an AC motor, and a bearing housing plate. A three-phase AC motor is connected to a shaft in the experimental test rig that has a belt and pulley arrangement to a single-stage bevel gearbox through a flexible coupling. A magnetic brake applies the load to the gearbox to generate the required test torque, and the tri-axial accelerometer (PCB-Piezotronics 356A26 SN 225948, Sensitivity: 5.13 $mV/m/s^2$, y-axis 4.85 $mV/m/s^2$, z-axis 4.87 $mV/m/s^2$) is installed to record the vibration signals on the single-stage bevel gearbox, as seen in Figure 2.7. The accelerometer is connected to an OROS-OR34 data acquisition system (DAQ) to collect vibration readings from the gearbox. A laptop running NV Gate software is linked to the DAQ in order to evaluate the signals that have been recorded. This study selects four motor speeds: 15 Hz, 20 Hz, 25 Hz, and 30 Hz. These speeds are chosen to cover a range of operating conditions, with the maximum speed (30 Hz) based on the motor's maximum rotational capacity. The speeds are regulated using a VFD. A mechanically controllable magnetic brake is utilized to impart different loads on the gearbox's output shaft. The brake has a load range of 0 to 5 Nm, and for this study, loads between 0 and 4 Nm are applied to capture signals under different speed and load conditions. In addition, different faults exhibit distinct characteristics at various speeds and load conditions. Therefore, a sufficient range of speeds that MFS can readily accomplish is considered to provide exhaustive data sets. The model can recognize faults based on their distinct fingerprints under various operating conditions because it was trained on a dataset with a range of variables. Under operating conditions, the gearbox's 10-second vibration signature is recorded with a sample frequency of 12.8 kHz, resolution of 1.5625 Hz, and overlap of 20%.

fault severity levels in gears Abrasive wear are simulated using a laser cutting machine. A fiber laser system doped with rare earth elements like erbium, ytterbium, and neodymium that was purchased from Scantech Laser Pvt. makes up the experimental setup. Its 50 W rated power output and Galvo scanner, which has a 0.2 mm spot diameter and a 287 mm focal length, allow for two-way beam manipulation. Table 2.7 depicts the process conditions and time duration to impose laser machine abrasive wear faults on the bevel gear. The cutting depth was measured using the DEW507 Optical Microscope from Dewinter Optical Inc., and the obtained values were used in the calculation of abrasive wear severity. Figure illustration of the bevel gear fault of the Abrasive wear is presented as follows in Figure 2.8.

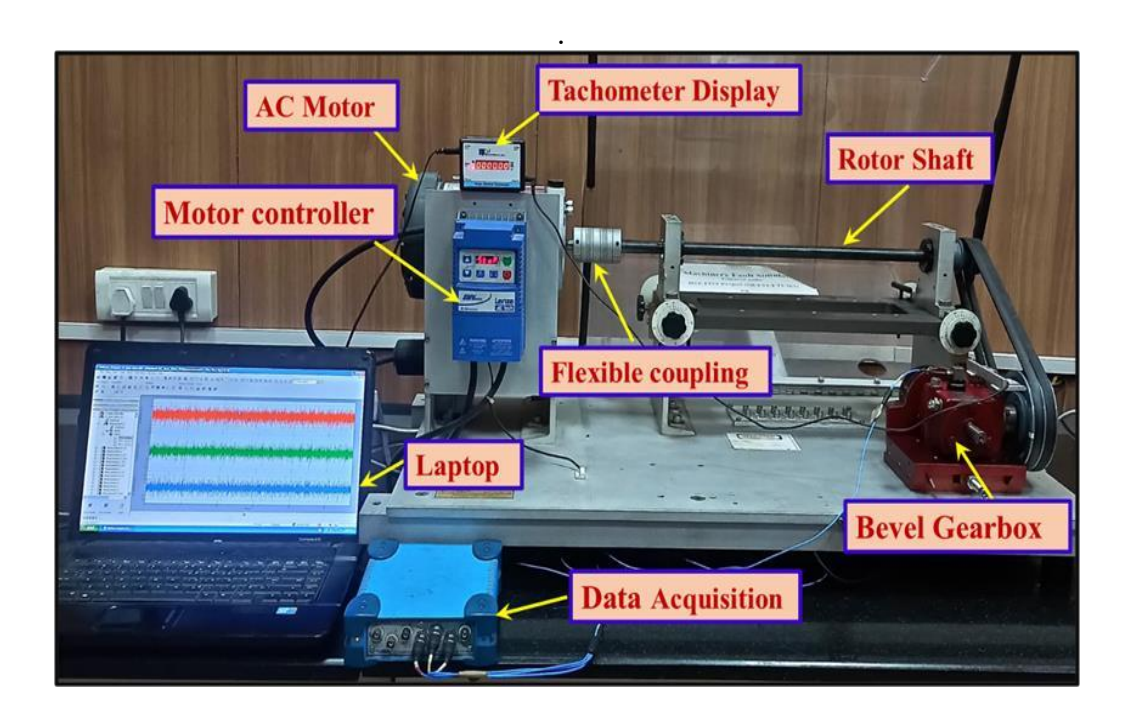


Figure 2. 6: Experimental test setup.

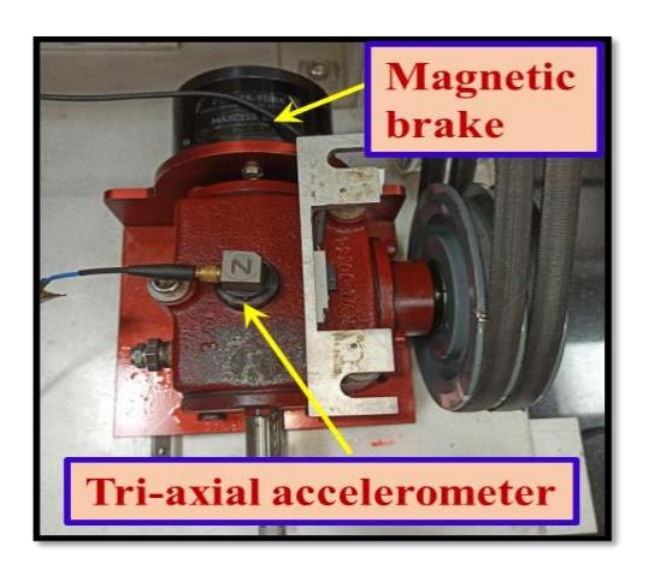


Figure 2. 7: Magnetic break and tri-axial accelerometer.

Table 2. 6: Technical specifications of the gearbox

Backlash tolerance (gear and pinion)	0.0254-0.127 mm
Pitch angle (pinion)	33°41'
Pitch diameter (gear)	42.8625 mm
Pressure angle (pinion and gear)	20°
Module (pinion and gear)	2 mm
Number of teeth (pinion)	18
Pitch diameter (pinion)	28.575 mm
Number of teeth (gear)	27
Material (pinion and gear)	Forged steel
Pitch angle (gear)	56°19'
Gear ratio	1.5:1

Table 2. 7: Different types of abrasive wear faults have different severity levels

Gears (Bevel)	Fault description	Fault Dimension	Image of fault
0	Healthy	Nil	
1	Incipient	20 Micron	THE REAL PROPERTY.
2	Slight	30 Micron	
3	Moderate	40 Micron	
4	Severe	50 Micron	MA
	(a)	20 micron	30 micron
	(c)	40 micron	50 micron

Figure 2. 8: The severity of abrasive wear fault for (a) incipient, (b) slight, (c) moderate, (d) severe.

Table 2. 8: Operating parameters of the laser machine

S. No	Level of abrasive wear fault	Number of passes	Operating power (w)	Cutting depth (micron)
(A)	Incipient	10	30	20
(B)	Slight	15	40	30
(C)	Moderate	15	50	40
(D)	Severe	70	50	50

2.6 Results and Discussion

2.6.1 Simulation Procedure

All experiments and model implementations are conducted using MATLAB R2020b. DL models and the OAHCSA are developed from scratch within this environment. This strategy requires a processor with an 11th Gen Intel® Core™ i5-1135G7 @ 2.40 GHz and 16.0 GB of RAM (15.7 GB useable), among other computational resources. The x64-based processor and 64-bit operating system power the system, which is utilized for all model training and evaluation tasks in this study. The same setup is employed for all training and evaluation processes in the study. The dataset contains 25 samples of the healthy class, while each fault class, namely incipient, slight, moderate, and severe, includes 10 samples. These five fault classes, each with unique identification, will allow us to categorize and recognize gearbox fault conditions. Table 2.8 displays training and testing data distribution. which contains percentages for training and testing. The split for 60% of data to be used for training leaves 40% for testing. That 70% were assigned to 30% tests, while for the 80% training scheme, only 20% was allocated for testing. This variation will produce an exhaustive assessment of the models under different fault detection conditions and make it more robust in terms of performance.

Table 2. 9: Training and testing data

Training percentage	Training data	Testing data
60	780×9	520×9
70	910×9	390×9
80	1040×9	260×9

2.6.2 Performance Analysis

The effectiveness of the proposed model is evaluated using positive, negative, and neutral criteria in relation to the prior model. False positive rates (FPR), false negative rates (FNR), and false discovery rates (FDR) are compared against positive measures like sensitivity, specificity, accuracy, and precision. Neutral metrics are also used, including the F1 score, Matthew's correlation coefficient (MCC), and negative predictive value (NPV). The values for false positive (FP), false negative (FN), true positive (TP), and true negative (TN) are evaluated for each method. The performance of the OAHCSA-HC method is compared with other approaches such as AHA-HC, CSA-HC, LA-HC, PRO-

HC, deep LSTM, CNN-FFT, R-Net, and S-Net. Neural networks such as CNN-FFT [134] learn patterns without storing input data, whereas LSTMs address the vanishing gradient problem, and S-Net optimizes computing resources, as shown in Figures 2.10, 2.11, and 2.12. The high accuracy achieved at 15 Hz is 99.62%, with a precision of 99.79%, a specificity of 99.87%, and a sensitivity of 99.54%. It has also got very low values for FNR (0.45%), FDR (0.20%), and FPR (0.12%), indicating low misclassifications. Neutral measures such as NPV of 99.87%, MCC of 99.56%, and F1-score of 99.66% further confirm its superiority in performance. Figure 2.10 b depicts that OAHCSA-HC has made significant headway with entropy-based feature extraction, which captures the feature information, rather than a combined classifier combining multiple algorithms to improve prediction accuracy. Convergence is improved, and local minimum is avoided with OAHCSA optimization. Performance metrics, such as the all-in-one set, ensure reliability in classification results while simultaneously reducing false positives and negatives. Overall, architecture proves effective in modeling complex patterns, and it gets better results than other algorithms for fault detection with respect to accuracy and reliability.

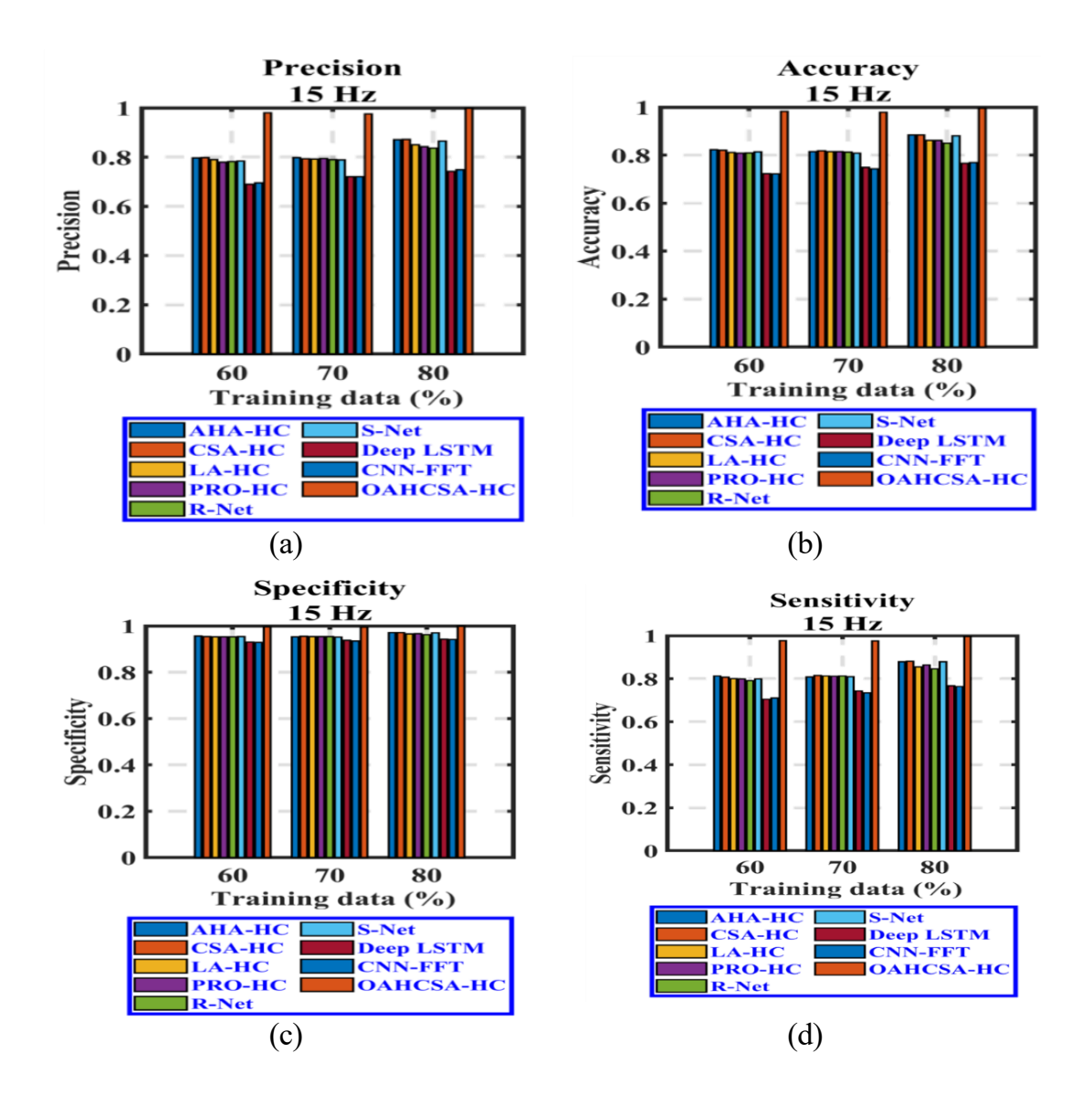


Figure 2. 9: Comparison of classifiers for (a) Precision, (b) Accuracy, (c) Specificity, and (d) Sensitivity at 15 Hz.

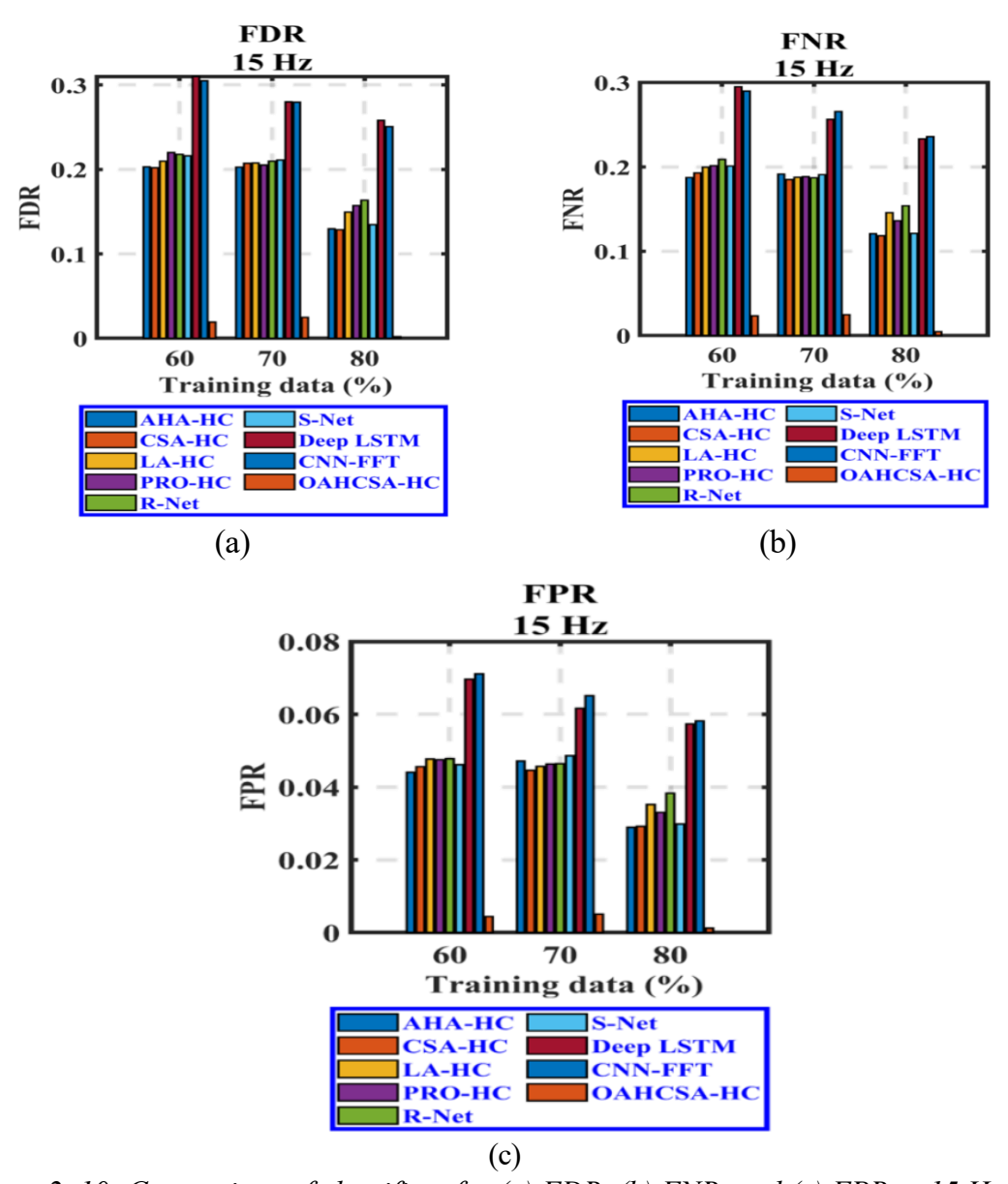


Figure 2. 10: Comparison of classifiers for (a) FDR, (b) FNR, and (c) FPR at 15 Hz.

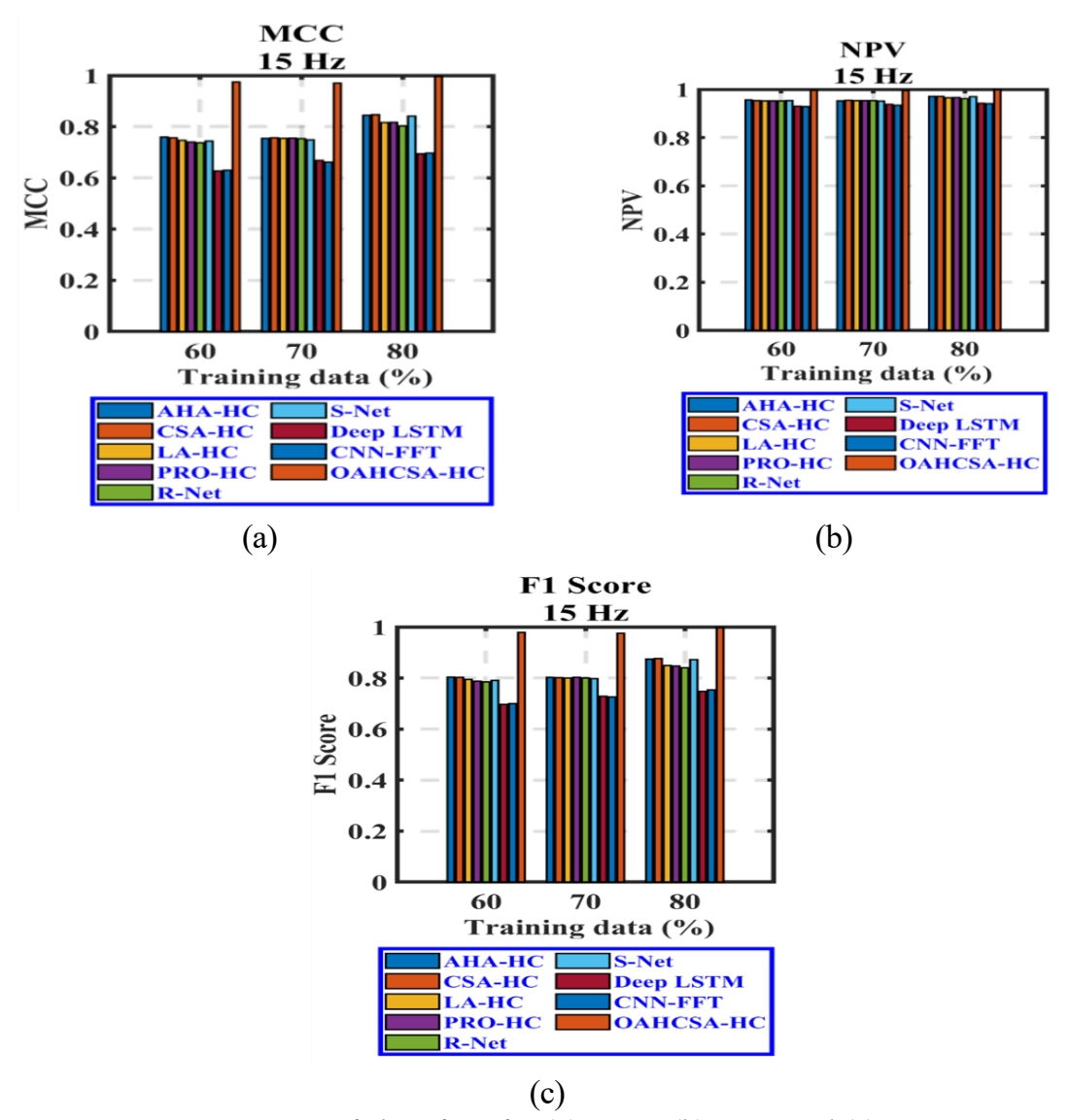


Figure 2. 11: Comparison of classifiers for (a) MCC, (b) NPV, and (c) F1-score at 15 Hz.

Three types of measurements, positive, negative, and neutral, were presented in Tables 2.7-2.9 for operating frequencies of 20, 25, and 30 Hz, respectively. The OAHCSA-HC method always produced better results than those from other methods, yielding an accuracy level of 99.62% at 15 Hz with 80% training data. It showed a lower FNR and FPR than R-Net, AHA-HC, CSA-HC, LA-HC, PRO-HC, deep LSTM, CNN-FFT, and S-Net across the 80% training data. Besides, the method comes with high specificity at 99.88% throughout the 20 Hz, 25 Hz, and 30 Hz frequencies. The improved performance is attributed to enhancements in the modified log-energy entropy and Renyi entropy features, which contribute to the superior effectiveness of the proposed OAHCSA-based HC method over other compared techniques.

Table 2. 10: Comparison of different classifiers at 20 Hz

Metrics	AHA-	CSA-	LA-	PRO-	Deep	CNN-	R-Net	S-Net	OAHCSA-
Metrics	HC	HC	HC	HC	LSTM	FFT	N-Met	5-1161	HC
NPV	0.971	0.965	0.967	0.967	0.942	0.929	0.738	0.850	0.997
Sensitivity	0.880	0.856	0.862	0.856	0.785	0.723	0.736	0.846	0.986
MCC	0.840	0.808	0.822	0.813	0.703	0.630	0.936	0.962	0.984
Precision	0.863	0.816	0.851	0.840	0.743	0.686	0.713	0.836	0.989
F1-Score	0.867	0.843	0.855	0.844	0.758	0.698	0.064	0.038	0.987
FPR	0.029	0.035	0.033	0.033	0.058	0.071	0.720	0.840	0.003
FNR	0.120	0.144	0.138	0.144	0.215	0.277	0.657	0.802	0.014
Specificity	0.971	0.965	0.967	0.967	0.942	0.929	0.264	0.154	0.997
FDR	0.137	0.166	0.149	0.160	0.257	0.314	0.936	0.962	0.011
Accuracy	0.885	0.858	0.869	0.865	0.769	0.715	0.287	0.164	0.988

Table 2. 11: Comparison of different classifiers at 25 Hz

					Deep	CNN			OAHC
	AHA	CSA-	LA-	PRO	LST	-FFT	R-		SA-
Metrics	-HC	HC	HC	-НС	M		Net	S-Net	HC
NPV	0.961	0.968	0.965	0.962	0.935	0.931	0.762	0.873	0.998
Sensitivity	0.827	0.859	0.846	0.835	0.741	0.716	0.753	0.857	0.990
FPR	0.039	0.032	0.035	0.038	0.065	0.069	0.942	0.967	0.002
Precision	0.823	0.860	0.831	0.832	0.714	0.689	0.736	0.868	0.990
MCC	0.786	0.828	0.802	0.795	0.661	0.632	0.058	0.033	0.988
F1-Score	0.824	0.859	0.838	0.832	0.724	0.699	0.739	0.861	0.990
FNR	0.173	0.141	0.154	0.165	0.259	0.284	0.683	0.829	0.010
Specificity	0.961	0.968	0.965	0.962	0.935	0.931	0.247	0.143	0.998
FDR	0.177	0.140	0.169	0.168	0.286	0.311	0.942	0.967	0.010
Accuracy	0.846	0.877	0.858	0.855	0.742	0.723	0.264	0.132	0.992

Table 2. 12: Comparison of different classifiers at 30 Hz

Matrias	AHA-	CSA-	LA-	PRO-	Deep	CNN-			OAHCSA-
Metrics	HC	HC	HC	HC	LSTM	FFT	R-Net	S-Net	HC
NPV	0.962	0.965	0.969	0.968	0.941	0.935	0.762	0.885	0.998
Sensitivity	0.853	0.863	0.870	0.870	0.750	0.739	0.761	0.888	0.990
MCC	0.802	0.808	0.826	0.824	0.679	0.657	0.942	0.971	0.988
Precision	0.829	0.830	0.848	0.845	0.731	0.712	0.731	0.872	0.990
FPR	0.038	0.035	0.031	0.032	0.059	0.065	0.058	0.029	0.002
F1-Score	0.840	0.842	0.857	0.855	0.736	0.718	0.741	0.879	0.990
FNR	0.147	0.137	0.130	0.130	0.250	0.261	0.685	0.849	0.010
Specificity	0.962	0.965	0.969	0.968	0.941	0.935	0.239	0.112	0.998
FDR	0.171	0.170	0.152	0.155	0.269	0.288	0.942	0.971	0.010
Accuracy	0.850	0.854	0.873	0.869	0.762	0.735	0.269	0.128	0.992

2.6.3 Ablation Study

Ablation research is done to evaluate the efficacy of the suggested approach, comparing it with different features for various motor speeds. The results in Tables 2.10–2.13 show that the OAHCSA-HC method outperformed other components, including traditional log entropy, Renyi entropy, and the combined model without features. It also performed better than the proposed model without statistical features and HC without optimization. At a motor speed of 15 Hz, the OAHCSA-HC method achieved a high specificity rate of 99.88%. Similarly, it achieved a remarkable NPV of 99.87% and an increased sensitivity of 99.54%, indicating its proficiency in accurately predicting negatives and capturing true positives. The model also showed a high positive value for all motor operating frequencies.

Additionally, the modified Renyi entropy and modified log-energy entropy approaches produced helpful results for this investigation. The proposed method achieves superior rates when compared with the model without statistical features. The model without statistical features obtained a lower accuracy value of 88.84%, while the proposed OAHCSA-HC-based model acquired the most remarkable accuracy of 99.61% values at 15 Hz. This experimental result demonstrates the efficiency of statistical features in the proposed model.

Table 2. 13: Ablation study of OAHCSA-HC approach at 15 Hz

Metrics	OAHCSA- HC	Without	Using conventional	Using conventional	HC without	Model without statistical
		optimization	log entropy	Renyi	features	
NPV	0.999	0.923	0.915	0.899	0.897	0.971
Sensitivity	0.995	0.670	0.570	0.547	0.450	0.882
MCC	0.996	0.556	0.471	0.620	0.457	0.855
Precision	0.998	0.610	0.552	0.520	0.385	0.887
F1-Score	0.997	0.621	0.551	0.502	0.485	0.883
FPR	0.001	0.077	0.085	0.101	0.103	0.029
FNR	0.005	0.330	0.430	0.453	0.550	0.118
Specificity	0.999	0.923	0.915	0.899	0.897	0.971
FDR	0.002	0.390	0.448	0.321	0.457	0.113
Accuracy	0.996	0.692	0.654	0.615	0.577	0.888

Table 2. 14: Ablation study of OAHCSA-HC approach at 20 Hz

Metrics	OAHCSA- HC	Without optimization		Using conventional Renyi	HC without features	Model without statistical features
NPV	0.997	0.939	0.933	0.922	0.825	0.968
Precision	0.989	0.838	0.551	0.669	0.311	0.864
Sensitivity	0.986	0.743	0.533	0.689	0.440	0.877
MCC	0.984	0.731	0.529	0.598	0.513	0.838
FPR	0.003	0.061	0.067	0.078	0.175	0.032
F1-Score	0.987	0.776	0.667	0.669	0.387	0.869
FNR	0.014	0.257	0.467	0.311	0.560	0.123
Specificity	0.997	0.939	0.933	0.922	0.825	0.968
FDR	0.011	0.162	0.449	0.331	0.696	0.136
Accuracy	0.988	0.788	0.731	0.692	0.308	0.873

Table 2. 15: Ablation study of OAHCSA-HC approach at 25 Hz

Metrics	OAHCSA- HC	Without optimization	Using conventional log entropy	Using conventional Renyi	HC without features	Model without statistical features
NPV	0.998	0.929	0.926	0.953	0.861	0.963
Sensitivity	0.990	0.592	0.614	0.750	0.408	0.855
MCC	0.988	0.523	0.628	0.840	0.491	0.812
Precision	0.990	0.610	0.613	0.707	0.324	0.846
F1-Score	0.990	0.579	0.556	0.687	0.310	0.848
FPR	0.002	0.071	0.074	0.047	0.139	0.037
FNR	0.010	0.408	0.386	0.250	0.592	0.145
Specificity	0.998	0.929	0.926	0.953	0.861	0.963
FDR	0.010	0.390	0.330	0.207	0.629	0.155
Accuracy	0.992	0.692	0.692	0.808	0.385	0.854

Table 2. 16: Ablation study of OAHCSA-HC approach at 30 Hz

Metrics	OAHCSA- HC	Without optimization	Using conventional log entropy	Using conventional Renyi	HC without features	Model without statistical features
MCC	0.988	0.481	0.493	0.539	0.507	0.827
Sensitivity	0.990	0.563	0.510	0.583	0.583	0.866
FPR	0.002	0.080	0.073	0.078	0.064	0.033
Precision	0.990	0.577	0.475	0.667	0.461	0.855
F1-Score	0.990	0.531	0.809	0.600	0.531	0.859
Specificity	0.998	0.920	0.928	0.922	0.936	0.967
FNR	0.010	0.437	0.490	0.417	0.417	0.134
NPV	0.998	0.920	0.928	0.922	0.936	0.967
FDR	0.010	0.423	0.525	0.333	0.570	0.145
Accuracy	0.992	0.654	0.692	0.739	0.731	0.869

2.6.4 Convergence Analysis

Convergence is a static point found in the sequence of solutions via iterations. It also shows how many iterations are required to achieve minimum error (cost), which is close to zero. Figure 2.12 illustrates the convergence of the OAHCSA-HC method over AHA-HC, CSA-HC, LA-HC, and PRO-HC over various iterations. Because we optimized and made advances in modified Renyi entropy and modified log energy entropy, OAHCSA-HC proved less expensive than the other evaluated methods. Furthermore, from the 4th to the 25th, the OAHCSA-HC cost function is significantly lower. In this case, PRO-HC showed the worst results at high costs.

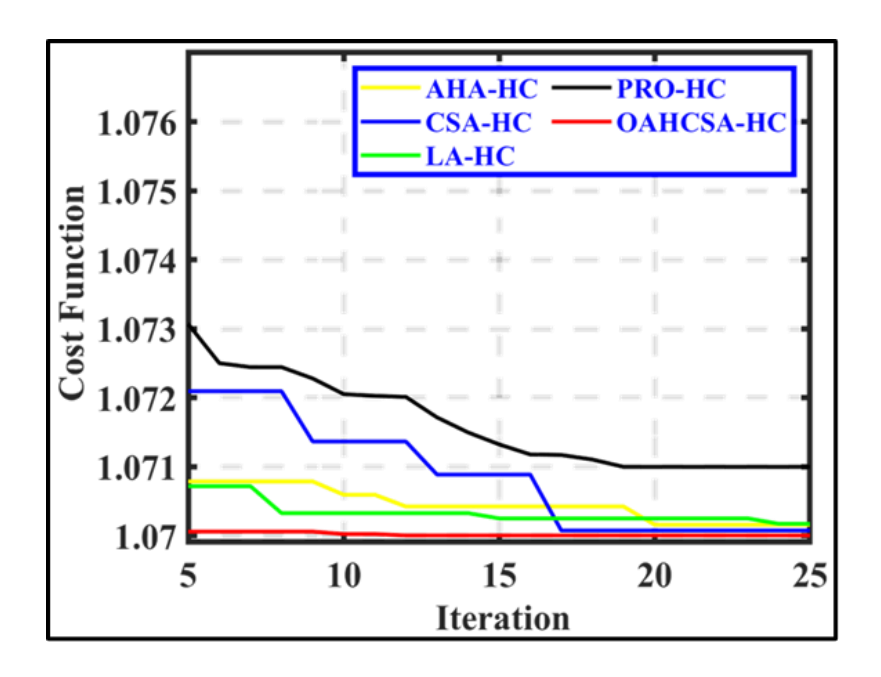


Figure 2. 12: Convergence Study of OAHCSA-HC over existing models.

2.6.5 Analysis of Computational Time

The analysis of computational time for frequencies such as 15 Hz, 20 Hz, 25 Hz, and 30 Hz is presented in Table 2.16. The results demonstrate that HC, in conjunction with the OAHCSA, regularly outperforms other models in terms of computing efficiency. OAHCSA consistently shows the lowest computational time across all tested frequencies, with times of 3.305 seconds at 15 Hz and below 4.15 seconds at higher frequencies. The OAHCSA model achieves a time reduction of approximately 56% compared to the highest time-consuming method, CSA-HC, which takes 10.52 seconds at 25 Hz. The outcomes highlight how well the OAHCSA-HC model balances high fault detection accuracy with minimal computational overhead. Because it strikes a compromise between

high accuracy and quick computation times, the OAHCSA-HC model is a reliable option for gearbox fault detection applications at various frequencies.

Table 2. 17: Computational time analysis

Computation time (seconds)				
Models	Frequency	Frequency	Frequency	Frequency
Models	= 15 Hz	=20 Hz	= 25 Hz	=30 Hz
AHA-HC	3.84	6.27	4.05	7.59
CSA-HC	5.74	4.39	10.52	4.37
LA-HC	6.36	4.98	5.12	4.26
PRO-HC	4.06	3.68	5.54	8.82
R-Net	4.76	4.36	4.39	5.22
S-Net	7.51	5.8	4.01	6.23
Deep LSTM	4.28	8.43	4.97	10.45
CNN-FFT	3.53	4.32	5.9	4.71
OAHCSA-HC	3.3	3.52	3.66	4.15

2.6.5 K-Fold Validation Analysis

One statistical technique for assessing the proficiency of ML models is K-fold validation. It is frequently employed to evaluate how effectively a statistical analysis's findings would transfer to another set of data. As part of the process, the dataset is separated into 'k' folds, or subsets. The goal of getting a more precise measurement of model prediction performance leads to the requirement for k-fold validation. K-fold validation ensures that every measurement from the original dataset has an equal chance of showing up in the training and test sets, hence mitigating overfitting. The k-fold validation analysis of the suggested OAHCSA-HC model over traditional techniques at different frequencies is displayed in Table 2.17. At 15 Hz, OAHCSA-HC attains the highest level of precision of 99.2% with 4-fold validation, significantly surpassing the best conventional model, LA-HC, which has an accuracy of 87.3%. At 20 Hz, OAHCSA-HC maintains its lead with an accuracy of 98.8%, while LA-HC achieves 86.%. This trend continues at 25 Hz, where OAHCSA-HC again outperforms with an accuracy of 98.9%, compared to LA-HC's 85.9%. Lastly, at 30 Hz, OAHCSA-HC scores 98.9%, again surpassing LA-HC, which records 86.8%. Its ability to maintain excellent accuracy at higher frequencies indicates

the model's adaptability and promise for gearbox failure detection. The OAHCSA-HC model performs noticeably better than conventional techniques across all evaluated frequencies. Its strong k-fold validation accuracy scores indicate that it is a stable and dependable option for gearbox fault detection that needs accurate control and stability.

Table 2. 18: Analysis of K-fold validation for suggested OAHCSA-HC model over conventional methods at various frequencies

	Fre	equency = 15 Hz	Z		
Methods	k-fold = 2	k-fold = 3	k-fold = 4	k-fold = 5	
AHA-HC	0.816	0.814	0.861	0.822	
CSA-HC	0.816	0.810	0.868	0.805	
LA-HC	0.818	0.810	0.873	0.815	
PRO-HC	0.809	0.814	0.870	0.826	
S-Net	0.827	0.816	0.868	0.813	
R-Net	0.812	0.814	0.865	0.809	
Deep LSTM	0.732	0.735	0.732	0.725	
CNN-FFT	0.720	0.732	0.724	0.736	
OAHCSA-HC	0.983	0.984	0.992	0.982	
Frequency = 20 Hz					
AHA-HC	0.820	0.818	0.855	0.826	
CSA-HC	0.808	0.815	0.860	0.815	
LA-HC	0.817	0.816	0.860	0.818	
PRO-HC	0.820	0.816	0.859	0.820	
S-Net	0.808	0.813	0.845	0.818	
R-Net	0.813	0.820	0.854	0.818	
Deep LSTM	0.727	0.730	0.729	0.735	
CNN-FFT	0.729	0.739	0.736	0.731	
OAHCSA-HC	0.982	0.983	0.988	0.985	
	Fre	equency = 25 Hz	Z		
АНА-НС	0.825	0.821	0.864	0.808	
CSA-HC	0.816	0.814	0.862	0.818	
LA-HC	0.816	0.821	0.859	0.825	
PRO-HC	0.818	0.821	0.858	0.815	
S-Net	0.820	0.821	0.856	0.804	

R-Net	0.816	0.811	0.853	0.815
Deep LSTM	0.736	0.735	0.728	0.728
CNN-FFT	0.733	0.734	0.732	0.732
OAHCSA-HC	0.984	0.983	0.989	0.984
	Freq	uency = 30 Hz		
AHA-HC	0.812	0.809	0.854	0.818
CSA-HC	0.815	0.817	0.855	0.810
LA-HC	0.824	0.822	0.860	0.815
PRO-HC	0.816	0.813	0.862	0.821
S-Net	0.809	0.809	0.857	0.815
R-Net	0.808	0.812	0.852	0.813
Deep LSTM	0.732	0.738	0.729	0.734
CNN-FFT	0.736	0.730	0.727	0.734
OAHCSA-HC	0.983	0.986	0.989	0.985

2.7 Conclusion

This chapter presents a three-stage technique for gearbox fault identification. First, the raw input signal is processed using median filters, after which pertinent features are extracted. Then, faults are detected through combined classifiers. The proposed OAHCSA algorithm is used to fine-tune the hyperparameters of the RNN to enhance accuracy. An excellent performance metric is achieved by averaging the outputs of the RNN and Bi- LSTM models. The classification accuracy reaches 99.62%, while specificity, sensitivity, and precision are 99.88%, 99.54%, and 99.79%, respectively. Additionally, the model attains an F1-score of 99.66%, demonstrating its robustness. Moreover, compared to existing techniques such as deep LSTM, CNN-FFT, R-Net, S-Net, AHA-HC, CSA-HC, LA-HC, and PRO-HC, the proposed approach gives better false negatives and FPR. Furthermore, the OAHCSA-HC model's higher performance over conventional techniques across a range of frequencies is confirmed by the k-fold validation analysis. At 15 Hz, OAHCSA-HC achieves 99.2% accuracy with 4-fold validation, which is much higher than LA-HC's 87.3%, demonstrating the model's versatility and resilience in detecting gearbox faults.

Chapter 3

Deep Hybrid Model for Automated Gear Crack Detection Using Enhanced CEEMDAN

This chapter aims to develop an automated method for classifying and identifying gear crack faults of varying severity. The proposed approach utilizes a multi-step methodology that begins with pre-processing the acquired signal using an advanced complete ensemble empirical mode decomposition with adaptive noise (CEEMDAN) algorithm. Numerous features, including entropy-based and time and frequency-domain features, are extracted from the previously processed signal. Data augmentation is applied before subjecting the augmented features to a hybrid classifier model to improve the feature set further. This model combines the Bi-LSTM and IDBN classifier, and the results are then processed using a score-level fusion technique to produce a single output. The proposed system has demonstrated high accuracy and efficiency, making it a viable option for accurately detecting gear faults.

3.1 Introduction

Gearboxes are crucial parts of many sectors because they distribute torque and power among shafts in devices like hand drills, printing presses, and automobile machinery [134-135]. Their primary function is to ensure efficient and smooth transmission of rotational energy [136]. However, gear faults, including cracks, misalignment, wear, and tooth damage, can emerge during operation, posing significant risks to the reliability and efficiency of mechanical systems [137-138]. Gear cracks are especially concerning as they tend to propagate, causing failures that lead to increased vibrations, reduced transmission efficiency, and, ultimately, gearbox breakdowns [139-140]. Timely fault detection is crucial for preventing catastrophic failures and minimizing downtime, making detecting and analyzing gear faults an essential aspect of machinery maintenance [141]. Automated systems for fault identification offer significant advantages by quickly analyzing data, thus enhancing the understanding of gearbox performance and enabling timely interventions [142].

Numerous cutting-edge methods for identifying faults in rotating machinery have been investigated in recent studies. With an 80.41% detection rate, Mohammed et al.

[137] suggested an NN-based method for identifying gear-tooth cracks. Brito et al. [143] presented a Depth-based Feature Importance technique using the Isolation Forest algorithm. Because it doesn't require labeled data, it can be used in industrial settings where there aren't many labeled datasets. Although this approach evaluates vibration characteristics in both the frequency and temporal domains, its performance varies based on the types of machinery and fault circumstances. In their study of tooth root crack faults in spiral bevel gear pairs, Han et al. [136] determined the maximum force on the tooth's roots and highlighted the importance of assembly faults. Although they did not address crack localization, Jorani et al. [142] demonstrated exceptional early and accurate crack identification by integrating Statistical Process Control Charts (SPCC) with vibration analysis to identify tooth crack faults. Other techniques, like those introduced by Yu and Liu [144] and Cheng et al. [139], have focused on unsupervised learning and analog tachometer signals for improving fault detection. Still, challenges such as noise and signal complexity persist.

Vibration-based, non-intrusive fault detection has become a key method for monitoring gear systems. Fault detection employs various signal processing techniques, including time-domain averaging, wavelet transform, and cepstrum estimation. However, techniques such as EMD and VMD often struggle with mode mixing [145]. A more advanced technique, CEEMDAN, has been developed to address these limitations, offering enhanced noise reduction and signal decomposition [136]. Additionally, researchers have investigated combining CEEMDAN with other techniques, such as timesynchronous averaging and cross-correntropy-based feature extraction, to enhance fault detection in noisy or non-Gaussian data [146-147]. Despite the success of DL models like DBN in diagnosing faults from compressed signals, current methods still face challenges in detecting subtle changes in vibration levels and accurately pinpointing fault locations. Hybrid classifier techniques, which combine multiple approaches, have been shown to improve prediction accuracy and reduce iteration requirements. However, significant research gaps remain, such as the need for better feature interpretability, the handling of residual noise, and improved classification accuracy for complex faults. The hybrid detection model proposed in this study combines the IDBN and Bi-LSTM architecture, trained using enhanced CEEMDAN signals, to address these challenges and improve gearbox fault detection.

3.2 Proposed Methodology

The following stages comprise the proposed approach for identifying gear cracks: (a) Data acquisition, (b) Preprocessing, (c) Feature extraction and data augmentation, and (d) Classification. As shown in Figure 3.1, the procedure starts with data collection and then moves on to preprocessing, where the input vibration signal is broken down into IMFs using the CEEMDAN algorithm. From the decomposed signal, characteristics such as time-domain and frequency-domain attributes are subsequently retrieved.

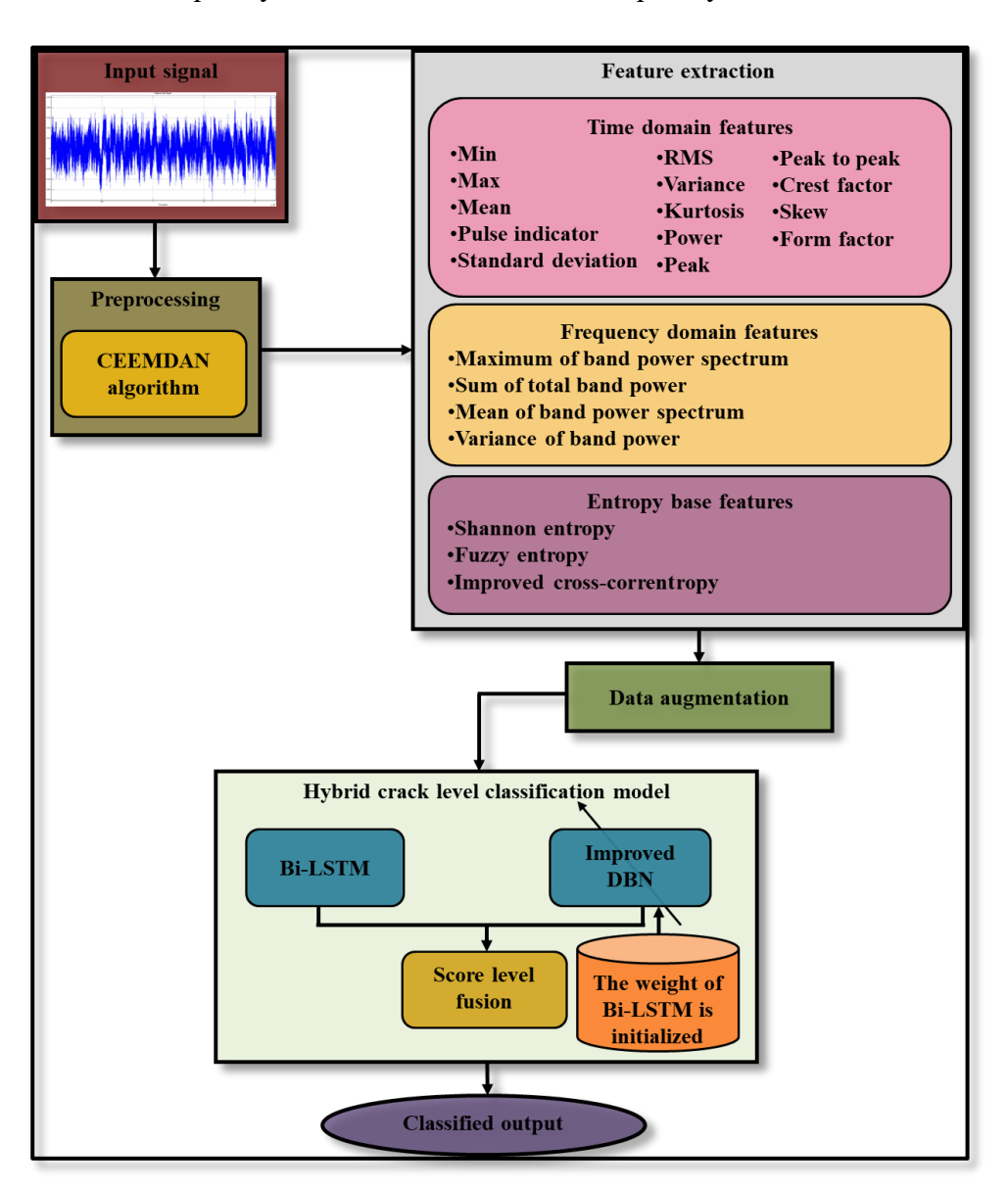


Figure 3. 1: Structure of the proposed methodology.

This research selects the CEEMDAN signal processing technique for signal denoising, as it offers distinct advantages over traditional filtering methods. The primary objective of using CEEMDAN is to preserve the gear mesh frequencies' intrinsic properties, ensuring that these characteristics are maintained for better and more accurate gear

crack fault detection. The method used by CEEMDAN is data-driven and particularly effective for processing non-stationary signals. It effectively separates noise components while extracting important signal components using filter banks, making it well-suited for gear signal analysis. Previous studies have shown that CEEMDAN effectively detects gear fault in real-world applications by evaluating non-stationary gear signals and lowering gearbox noise without conventional processing filters. The role of preprocessing in gear fault detection is crucial, as it significantly improves signal quality, hence improving the efficacy of fault detection techniques. By their very nature, gear signals are non-stationary, and CEEMDAN is particularly adept at handling these complex signals due to its superior decomposition capabilities. In this research, an improved CEEMDAN method is employed to process the input signal (I_s) , reducing its noise level and ensuring that the critical features of the gear frequencies are preserved. EEMD has traditionally been used due to its ability to reconstruct the original signal effectively while performing spectral decomposition with minimal computational cost. However, CEEMDAN offers improvements by decomposing intricate signals into their IMFs, addressing the issue of mode mixing, and providing more stable and reliable results. The residue rate, or the residual fraction of the signal, is computed following the extraction of the IMFs using decomposition. The rate of residue is assessed for the signal, and this process is described mathematically in Equation (3.1), which outlines how the residue rate is quantified in this context.

Through EEMD $\overline{IMK_k}$ is acquired, and decomposition modes are denoted by $\overline{IMK_k}$.

$$r_1 = I_s - \overline{IMF_1} \tag{3.1}$$

The residual value obtained through the EEMD model often includes residual noise, particularly pulse noise, which can manifest across multiple signal modes. Moreover, EEMD filters according to the local extrema of the signal and interpolates between them to accomplish signal decomposition. The harmonic information of the signal is not specifically taken into account by this method, though, which may lead to a less accurate separation of the signal's constituent parts. To address the abovementioned limitations, the CEEMDAN method introduces a more robust solution that explicitly considers the signal's harmonic information, resulting in a more precise separation of signal components. It adds weight based on distance to the harmonic mean evaluation to enhance the denoising capabilities of the decomposition process. This improvement allows for more accurate separation of the signal components. The enhanced CEEMDAN

technique is capable of distinguishing between harmonic and oscillatory components within the signal by utilizing these distance-based weights, which improves the decomposition's precision and ensures that the harmonic information is effectively captured.

The stages for the suggested improved CEEMDAN technique are as follows:

Step 1: The weighted harmonic mean is computed and deducted from the original signal to determine the initial decomposition mode. Using Equation (3.2), the first decomposition mode is obtained.

$$\overline{IMK_1} = I_S - HM^w[I_S] \tag{3.2}$$

Where HM^w represents the weighted harmonic mean, which may be calculated using Equation (3.3). Here, E_s it denotes ensemble size and w_i denotes distance from the mean weight.

$$HM^{w}[I_{s}] = \frac{\sum_{i=1}^{E_{s}} w_{i}}{\sum_{i=1}^{E_{s}} \frac{w_{i}}{I_{s}}}$$
(3.3)

The distance between each element and the signal average is used to calculate the separation from the average weight. This suggests that the element closest to the mean will be given the most weight, whereas the element furthest from the mean will be given the least amount. Additionally, weight is determined by taking the average of the signals, and the absolute difference between each element is assessed. The calculation of distance from mean weight is expressed in equation (3.4). Here, μ denotes the mean of the signal

$$I_s. w_i = \frac{1}{|I_s - \mu|}, w_i > 0, \sum w_i = 1$$
 (3.4)

Step 2: The first residue is assessed using Equation (3.5) at the first level (N = 1). N here stands for modes.

$$r_1 = I_s - \overline{IMF_1} \tag{3.5}$$

Step 3: The second mode can be expressed using Equation (3.7), and the second residue can be calculated as the mean of local means using the decomposition of realizations as in Equation (3.6). Here, M represents the local mean.

$$r_2 = r_1 + \beta_1 E_2(w_i) \tag{3.6}$$

$$\overline{IMF} = r_1 - r_2 = r_1 - [M(r_1 + \beta_1 E_2(w_i))]$$
(3.7)

Step 4: Using Equation (3.8), E_N determine the N^{th} residue for each $N=3,\ldots n$ here

stands for the N^{th} mode that EMD gained.

$$r_N = [M(r_{N-1} + \beta_{N-1}E_N(w_i))]$$
(3.8)

Step 5: Evaluate N^{th} mode as in Equation (3.9).

$$\overline{IMF_k} = r_{N-1} - r_N \tag{3.9}$$

Step 6: Go to step 4 for the further *N*.

Where $\beta_N = \varepsilon_N std(r_N)$ represents the variable needed to obtain a necessary SNR between the additional noise and the residue. The preprocessed signal can, therefore, be shown as I_s^{pre} .

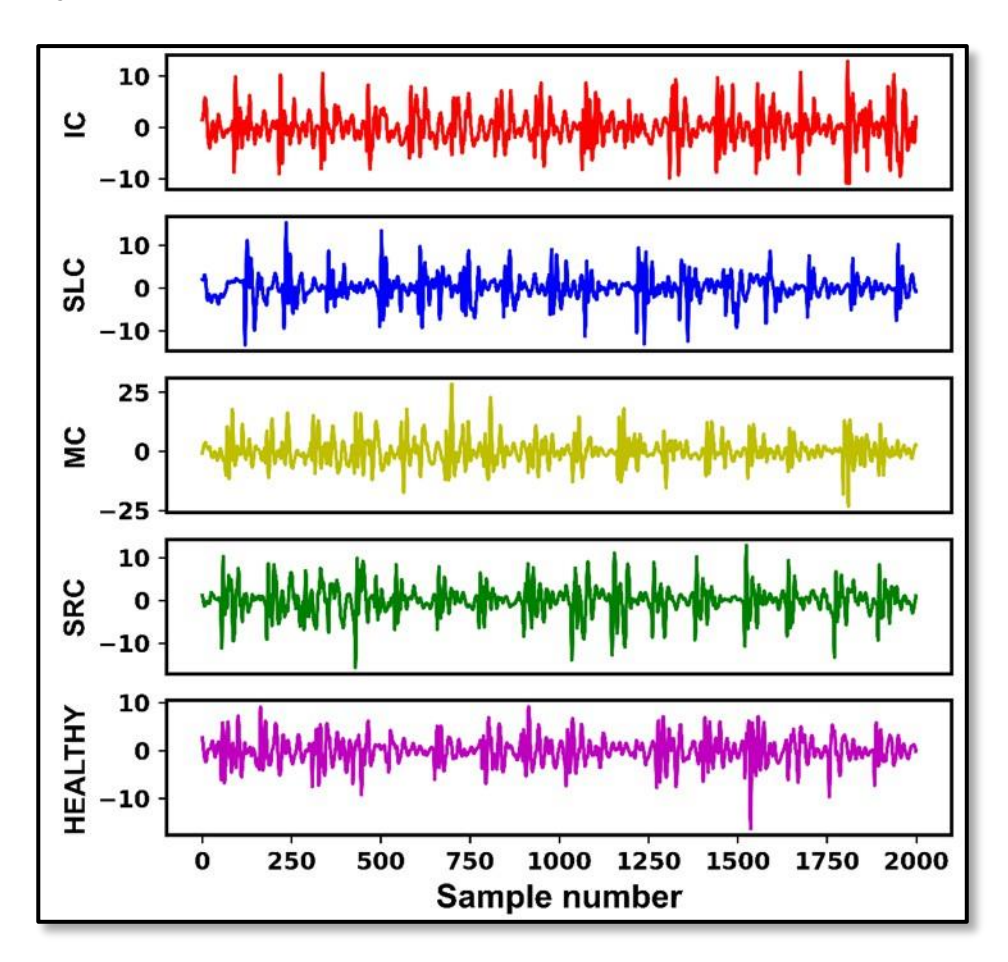


Figure 3. 2: Various degrees of Raw bevel-gear vibration signals for crack gear faults.

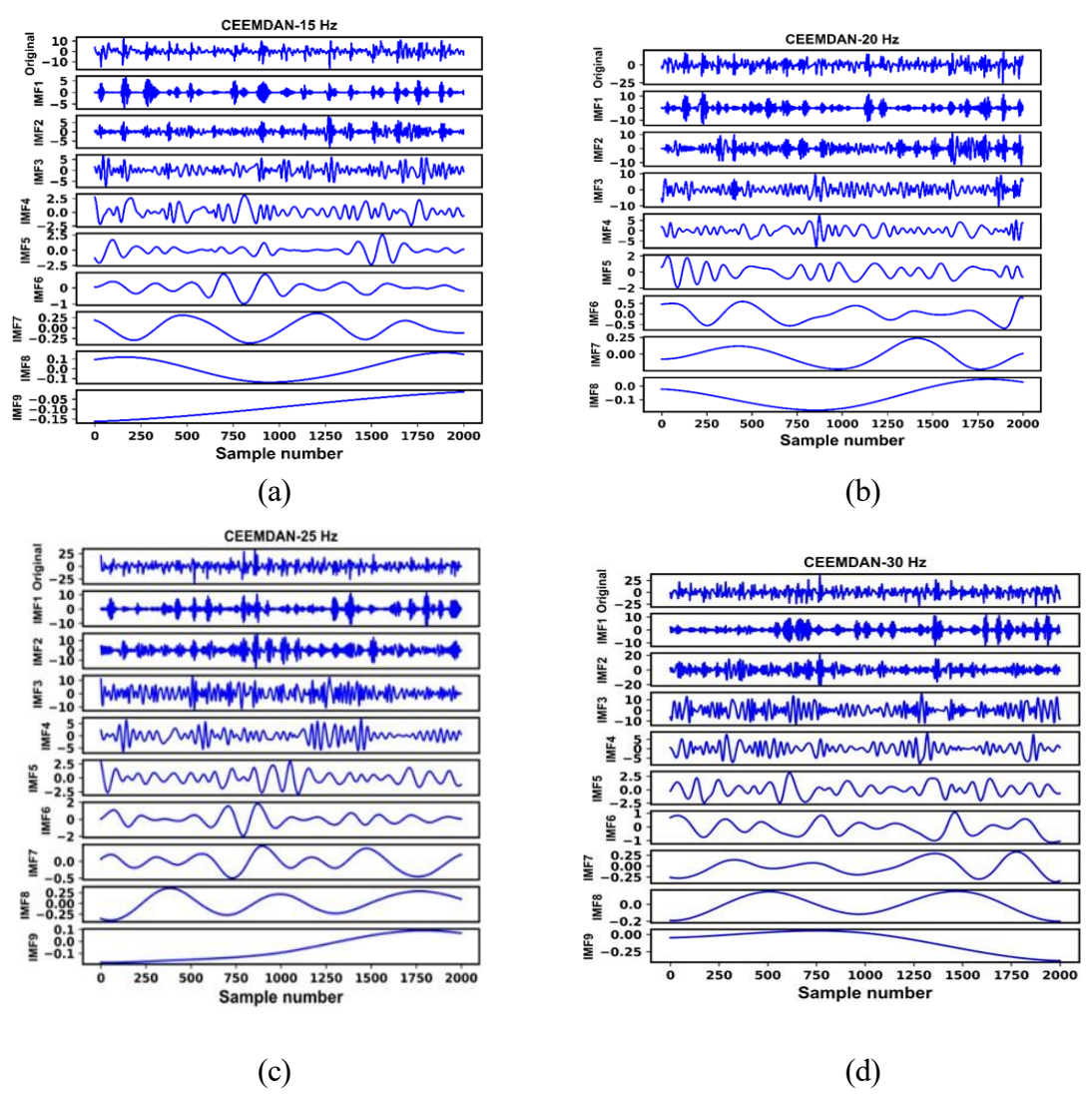


Figure 3. 3: Signals Preprocessed for Conventional CEEMDAN decomposition a) 15 Hz, b) 20 Hz, c) 25 Hz, and d) 30 Hz.

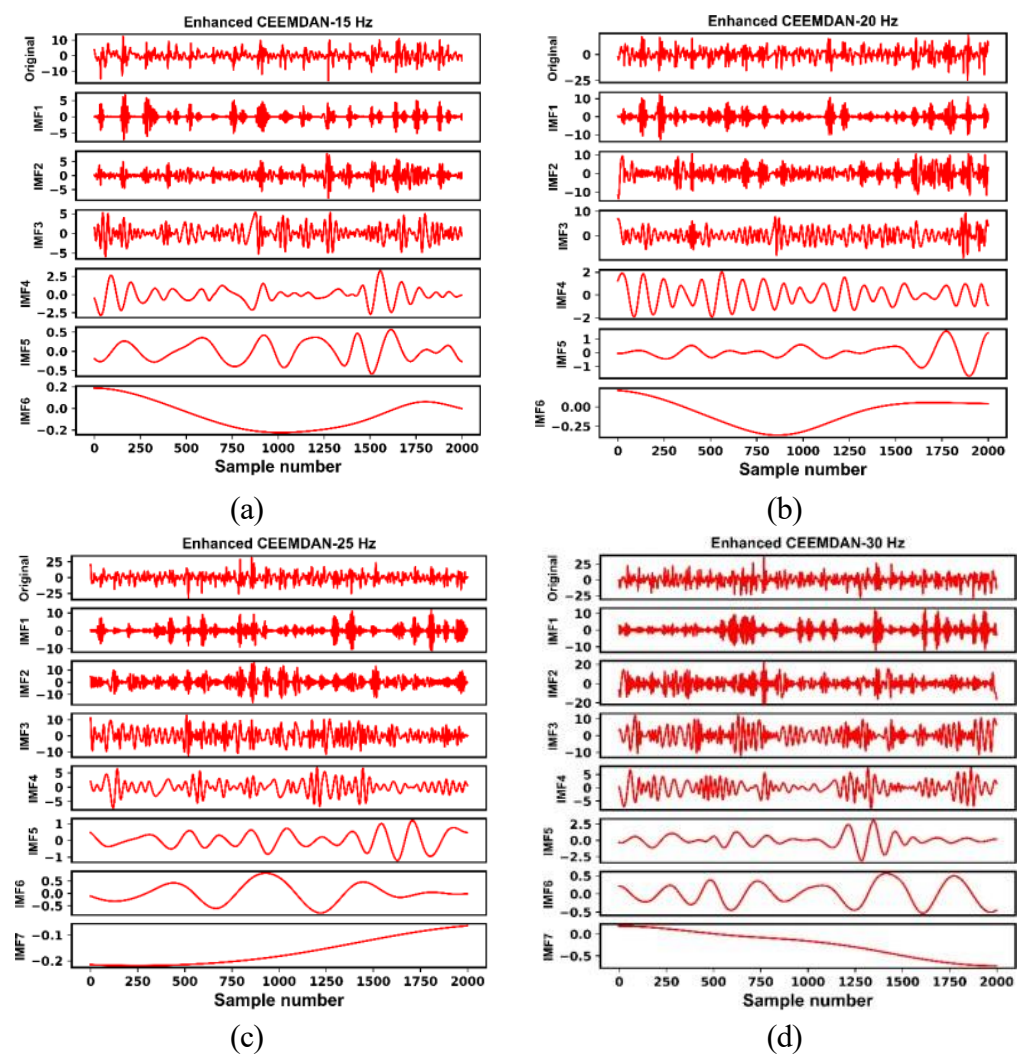


Figure 3. 4: Preprocessed signals for improved CEEMDAN decomposition a) 15 Hz, b) 20 Hz, c) 25 Hz, and d) 30 Hz.

Furthermore, Figure 3.2, 3.3 and 3.4 shows the preprocessed and raw signals from the conventional and enhanced CEEMDAN breakdown. The vibration shape of the signal after it was extracted from the dataset is shown in Figure 3.2. Figure 3.3 shows the signal following preprocessing using the conventional CEEMDAN method. Figure 3.4 displays the preprocessed signal using the updated CEEMDAN technique signal. The original signal is clearly broken down into nine IMFs when looking at Figures 3.3 and 3.4. The signal's high-frequency components are captured by IMFs 1 through 3, with IMF1 having excellent frequency components and amplitude values ranging from -5 to 5. Components of intermediate frequency, represented by IMFs 4 and 5, with amplitudes ranging from -2.5 to 2.5. IMF6's less-frequency ranges from -1.0 to 1.0, whereas IMFs 7 and 9's extremely low-frequency components range. Compared to the existing method, the proposed technique, which includes harmonic mean evaluation, generates comparable IMFs but may offer advantages to reduce noise and feature extraction. A quantitative

comparison between the raw and CEEMDAN-preprocessed signals highlights the effectiveness of the decomposition method. The signal-to-noise ratio (SNR) improved from approximately 9.8 dB in the raw signal to 13.6 dB after CEEMDAN processing, indicating better noise suppression. Additionally, the energy concentration in the first three intrinsic mode functions (IMF1–IMF3) increased from 48% to 72%, suggesting improved capture of fault-relevant features. This enhancement directly contributed to a rise in fault classification accuracy from 86.2% using raw features to 92.8% with CEEMDAN-based features, demonstrating the practical benefit of the preprocessing approach. This leads to a more effective separation of signal components, leading to better signal quality and fault detection capabilities.

3.3 Feature Extraction: Overview of Time and Frequency Domain Features and Entropy-Based Features

The critical and complex feature extraction process transforms the pre-processed signal into relevant characters in gear fault classification. These features capture the essential characteristics of the pre-processed signals, making them suitable for further analysis and fault detection algorithms. The most pertinent qualities, such as spectral properties, are the only ones selected to guarantee the classification process's effectiveness. The extracted features are vital for distinguishing between different gear conditions and detecting faults accurately. The pre-processed signal can yield a large number of features, including both frequency and time-domain traits. These features are fed into machine learning and classification algorithms to ascertain the existence and seriousness of problems. The features taken from the pre-processed signal are described in the next section along with how they influence the gear fault detection procedure.

3.3.1 Time Domain Features

Table 3.1 lists statistical variables associated with signal processing as time domain features. These features give insight into the signal's temporal fluctuations.

Table 3. 1: Features of the time domain

Measures	Description	Formulae
Min	It selects the variable with the minimum value.	$Min(x_i)$
Max	It uses the set of variables' maximum value.	$Max(x_i)$

Mean	The mean of every variable set.	$\overline{x} = \frac{1}{n} \sum_{i=1}^{n} x_i$
RMS	It specifies a signal's power or intensity.	$RMS = \sqrt{\frac{1}{n} \sum_{i=1}^{n} x_i^2}$
Variance	It calculates the variability or scatter of data points with respect to the mean.	$Var = \frac{\sum_{i=1}^{n} (x_i - \overline{x})^2}{n-1}$
Pulse indicator	It shows the actions to detect a signal's pulses or spikes.	$PI = \frac{Peak}{x}$
Standard deviation	It determines the mean deviation of each data point from the mean.	$Sd = \sqrt{\frac{\sum_{i=1}^{n} (x_i - \overline{x})^2}{n-1}}$
Kurtosis	It gauges how often and how severe outliers are in the data.	$Kur = \frac{1}{n} \sum_{i=1}^{n} \left(\frac{x_i - \overline{x}}{sd} \right)^4$
Power	It specifies how much energy is transformed in a certain amount of time.	$Pow = \frac{1}{n} \sum_{i=1}^{n} x_i^2$
Peak	It determines the precise location and magnitudes of the spikes or pulses.	$Peak = Max(x_i)$
Crest factor	By dividing the signal's peak amplitude, it is calculated by its RMS rate.	$CF = \frac{Peak}{RMS}$
Skew	It determines how much and in which direction a distribution deviates from symmetry.	$Sk = \frac{n\sum(x_i - \overline{x})^3}{(n-1)(n-2)\sigma^3}$
Peak to Peak	It describes the precise difference between a waveform's maximum and minimum values.	$ptp = Max(x_i) - Min(x_i)$
factor Form	It provides information that is pertinent to a signal's relative energy distribution.	$FF = \frac{RMS}{x}$

The time domain features that were extracted are shown as Tf.

3.3.2 Frequency Domain Features

The frequency domain describes how a signal's energy is distributed across different frequency bands within a given range. The FFT of the signal is first computed to extract these features, followed by the analysis of the resulting power spectrum. This process allows for identifying the signal's frequency components and their corresponding power

levels. The signal's primary frequency domain characteristics that are retrieved are parameters that quantify the energy present at various frequencies, helping to identify distinct patterns that may indicate faults. These parameters shed light on the frequency characteristics of the signal, which are essential for diagnosing issues in mechanical systems such as gearboxes. Table 3.2 outlines the frequency domain features derived from the FFT and their respective roles in fault detection.

Table 3. 2: Frequency domain features

Measures	Description	Formulae
Maximum band power spectrum	It indicates the maximum amplitude or power level in a given frequency band.	$S^{Max} = Max(S_i)$ Where, S_i represent the spectrum frequency.
Band power spectrum Mean	It provides data pertinent to the main power rate trend within a chosen band.	$\overline{S} = \frac{1}{n} \sum_{i=1}^{n} S_i$
Band power Variation	It establishes how much power rates vary within a specific frequency band.	$S_{Var} = \frac{\sum_{i=1}^{n} (S_i - \overline{S})^2}{n-1}$
The sum of the overall band power	It calculates the total power of every frequency element in a chosen band.	$S_{sum} = \sum_{i=1}^{n} S_i$

The frequency domain features that were extracted are shown as Ff.

3.3.3 Entropy-Based Features

The pre-processed signal's inherent uncertainty and unpredictability were measured by extracting entropy features. Entropy provides a crucial understanding of the complexity of the signal by quantifying the degree of disorder or information content in the data. Among the several types of entropy, enhanced cross-correntropy, fuzzy entropy, and Shannon entropy are frequently employed in gear fault detection. Shannon entropy, in particular, evaluates the signal's average information content and gives a gauge of its level of disorder or uncertainty. It is calculated using the formula provided in Equation (3.10) [148] and helps understand the signal's informational complexity, which is crucial for effective fault detection.

Here, R_k indicates the signal occurring probability.

$$H = -\sum [R_k * log(R_k)] \tag{3.10}$$

Fuzzy entropy is described as taking into account data with uncertainty or fuzzy boundaries [149]. Additionally, it measures the degrees of each member of a fuzzy data collection. Every M sample time sequence is described using Equation (3.11), and for the provided o, the series vector $\{Y_i^o, i = 1..., W - o + 1\}$ is generated. Y_i^o refers to o consecutive v values that start at the ith point and spread out by removing the baseline, as in Equation (3.12).

$$Y_i^o = \{u(i), u(i+1), \dots u(i+o-1)\} - u(i)$$
(3.11)

$$u_o(i) = \frac{1}{o} \sum_{j=0}^{o-1} u(i+j)$$
(3.12)

The distance $dis_{i,j}^o$ between Y_j^o and Y_i^o is then calculated; according to Equation (3.13), this is the most significant difference of the pertinent elements.

$$dis_{i,j}^{o} = dis[Y_i^{o}, Y_j^{o}] = \underset{o \in 0, o-1}{Max} |u(i+k) - u_o(i) - (u(j+k) - u_o(j))|$$
(3.13)

Using a fuzzy function $\lambda(dis_{i,j}^o, w, g)$ for the provided w and g, determine a similar degree distance $Dis_{i,j}^o$ between a given vector Y_j^o and Y_i^o in accordance with Equation (3.14). In this case, the fuzzy or exponential value is represented by $\lambda(dis_{i,j}^o, w, g)$.

$$Dis_{i,j}^{o}(w,g) = \lambda(dis_{i,j}^{o}, w, g)$$
 (3.14)

To evaluate the exponential function, use Equation (3.15).

$$\lambda(dis_{i,j}^q, m, g) = exp\left(-\frac{(dis_{i,j}^q)^m}{g}\right)$$
(3.15)

Moreover, the function ϕ^q is defined according to Equation (3.16). Similarly, generate $\{X_j^{q+1}\}$ and obtain the function ϕ^{q+1} according to Equation (3.17).

$$\phi^{q}(m,g) = \frac{1}{M-q} \sum_{i=1}^{M-q} \left(\frac{1}{M-q-1} \sum_{j=1,j\neq i}^{M-q} Disq_{i,j} \right)$$
(3.16)

$$\phi^{q+1}(m,g) = \frac{1}{M-q} \sum_{i=1}^{M-q} \left(\frac{1}{M-q-1} \sum_{j=1,j\neq i}^{M-q} Dis_{i,j}^{q+1} \right)$$
(3.17)

Eventually, the fuzzy entropy parameter FuzzyEnt(q, m, g) of the series expressed as the deviation of the series' negative natural logarithm ϕ^q from ϕ^{q+1} is defined as in Equation (3.18).

$$FuzzyEnt(q, m, g) = \lim_{M \to \infty} [\ln \phi^{q}(m, g) - \ln \phi^{q+1}(m, g)]$$
(3.18)

Additionally, the statistics can be used to calculate the fuzzy entropy parameter for finite datasets using Equation (3.19).

$$FuzzyEnt(q, m, g, M) = \ln \phi^{q}(m, g) - \ln \phi^{q+1}(m, g)$$
(3.19)

Cross-correntropy is a measure of similarity between two arbitrary variables, which can be used to assess their correlation more broadly. The standard cross-correntropy [150] is computed by evaluating the joint distribution between two signals, capturing both linear

and nonlinear dependencies. Equation (3.15) represents the conventional cross-correntropy in its mathematical form, which quantifies the similarity between the two signals, making it a valuable feature for detecting faults by identifying patterns of interest in the signal. The improved cross-correntropy enhances this method by refining the measure for better accuracy in fault detection. Here, L and D represent variables in arbitrary and nto the collection of samples that were discussed via $(L_i, D_i)_{i=1}^N$.

$$Corr(L,D) = \frac{1}{n} \sum_{i=1}^{n} G_{\sigma} \left(L_i - D_i \right)$$
(3.20)

 $G_{\sigma}(L_i - D_i)$ is a Gaussian kernel and is expressed in Equation (3.21). Here, σ is used to preserve the breadth of the kernel parameters.

$$G_{\sigma}(L_i - D_i) = exp(-\frac{\|L_i - D_i\|^2}{2\sigma^2})$$
(3.21)

The Gaussian kernel in conventional cross-correntropy is typically employed to capture similarities at a global level. However, this approach tends to diminish the significance of local patterns by smoothing out smaller, localized information in the data. Exponential kernels are used in the improved cross-correntropy method to overcome this limitation. Exponential kernels are highly sensitive to local similarities, enabling them to highlight the relationships between samples that are in close proximity, thereby preserving local patterns. Additionally, to improve separability, class-dependent feature weights [151] are included between different classes to improve interpretability and reduce noise. Each feature is given one of these features weights according to how crucial it is to the classification procedure, ensuring that more relevant features receive higher emphasis, ultimately improving the overall accuracy of fault detection. The steps below describe how to extract features from the enhanced cross-correntropy approach.

Step 1: Calculate feature weights that vary by class. The following approach is utilized to calculate the feature weight, which depends on the class.

Algorithm: Class-dependent feature weights approach

Given the decomposed signal $I_s^{pre} \subset \Re^{n \times m}$ and the labels $Z \in \{1, 2, ... L\}$ where L are the classes.

Compute
$$\beta$$
 for all $L: \beta = \frac{Uniqueclass}{\sum Uniqueclass}$

$$For l = 1: Ldo$$

Class samples $Ls \leftarrow \{Y|X=l\}$ // Select samples belonging to the current class c.

Class weight $Lw \leftarrow \frac{1}{n} \sum_{i=1}^{n} Ls_i$ // Compute the weight of each

sample for the current class.

End for

Computing feature weight: $\alpha = \sum_{i=1}^{l} \beta * Lw$

Return α

Step 2: Use the class-dependent feature weight and exponential kernel to estimate cross-correntropy, as shown in equation (3.22). K_{α} represent exponential kernel, L_i represent samples, and D_i represent labels, and nrepresents samples mentioned via $(L_i, D_i)_{i=1}^N$.

$$Corr(L,D) = \frac{1}{n} \sum_{i=1}^{n} K_{\alpha} (L - D_i)$$
(3.22)

Equation (3.23) is used to calculate the exponential kernel. Here, α represent feature weight.

$$K_{\alpha}(L_i - D_i) = exp(-\alpha | L_i - D_i|)$$
(3.23)

Next, the entire entropy-based characteristics can be shown as $E^{Feat} = [H, FuzzyEnt(o, w, g, W), Corr(L, D)]$. Consequently, the features that were taken from the frequency and time domain and enhanced entropy features are shown as $F_{Ext} = [Tf, Ff, E^{Feat}]$.

3.3.4 Hybrid Model for Identifying Gear Crack Faults

The enhanced feature set is then fed into the combined approach to precisely determine the gear crack levels following feature augmentation. As shown in Figure 3.3, the model aims to reduce computational time by combining Bi-LSTM and IDBN. After initializing the weights of the Bi-LSTM, the IDBN model uses the Swish and Mish activation functions for better classification performance. Unlike traditional activation functions such as sigmoid and ReLU, which suffer from vanishing gradients, the Swi-Mish function combines Swish and Mish to help maintain smoother gradient flow and mitigate the vanishing gradient issue. The Swish function ensures smooth curve transitions, while the Mish function is approximately zero-centered, facilitating effective weight updates. These features make Swi-Mish more suitable for backpropagation, improving network efficiency. The predictions produced by combining the scores from the two classifiers using a score-level fusion method increase the accuracy and robustness of categorization. The final output categorizes the gear crack into five levels.

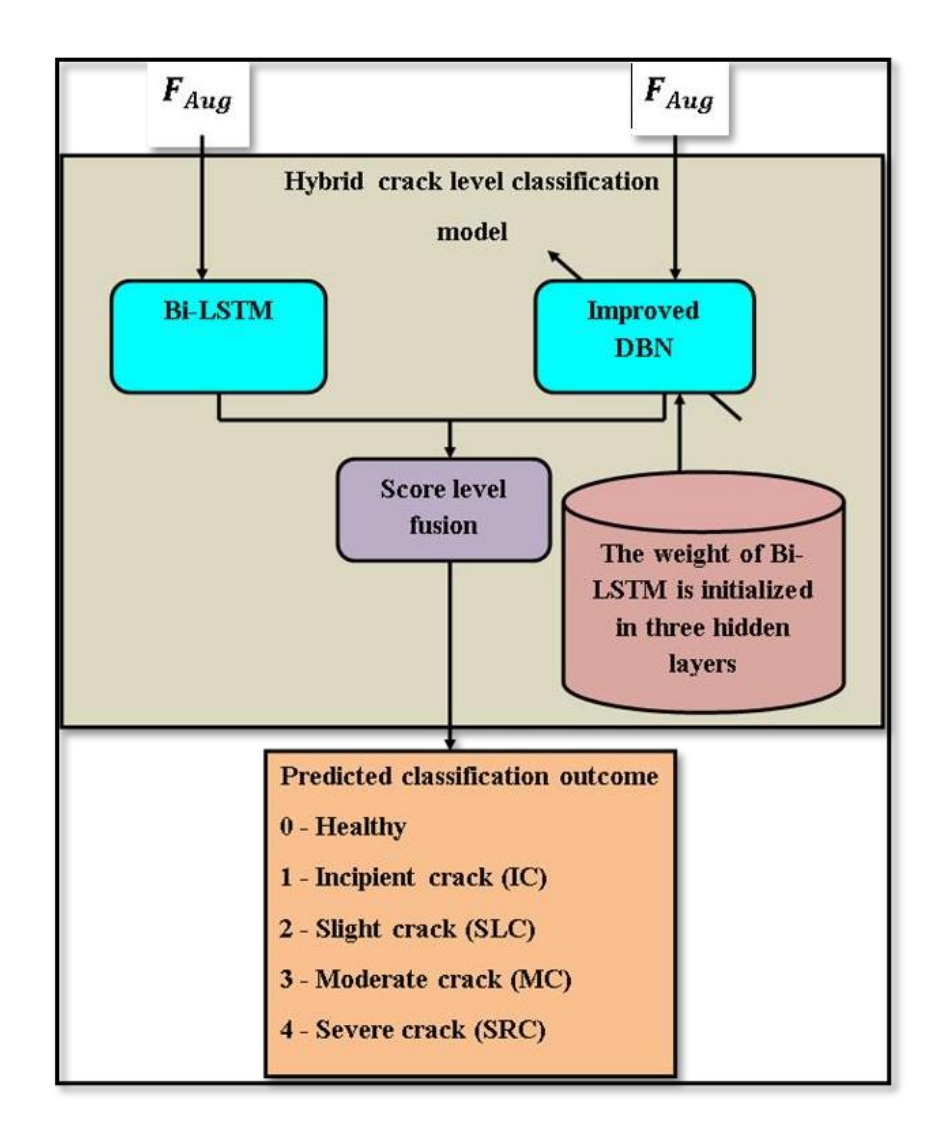


Figure 3. 5: An illustration of the crack-level categorization model.

3.4 BI-LSTM

This research uses the Bi-LSTM [152] to categorize various gear crack levels efficiently. The following Equations (3.24–3.28) are used to implement the LSTM. Here, f_r and c_r represent forget and cell state gate, i_r and o_r denote input and output gate, sig represents the function of the sigmoid.

$$f_r = sig(w_f F_{Aug} + w_f h_{r-1} + \gamma_f)$$
(3.24)

$$i_r = sig(w_i F_{Aug} + w_i h_{r-1} + \gamma_i)$$
(3.25)

$$o_r = sig(w_o F_{Aug} + w_o h_{r-1} + \gamma_o)$$
(3.26)

$$c_r = f_r c_{r-1} + F_{Aug} sig(w_c F_{Aug} + w_c h_{r-1} + \gamma_c)$$
(3.27)

$$h_r = o_r \tanh(c_r) \tag{3.28}$$

where h_r and wrepresent a hidden state and weight factor, γ represents bias term, h_{r-1} shows a hidden layer (HL) in the previous statistic, tanh denoted tangent hyperbolic,

and c_{r-1} represent the prior state cell.

The LSTM model only processes the past input values, ignoring future information. This restriction is addressed by using the Bi-LSTM method, as displayed in Figure 3.5, which consists of two separate hidden layers: the secret layers that are forward and backward. In ascending order, the forward hidden layer processes the data (from the past to the present). In contrast, in descending order, the reverse hidden layer processes the input (from the future to the past), as Equations describes. (3.29) and (3.30). Using a bidirectional strategy, Bi-LSTM can record past and future contextual information, improving the model's predictive accuracy.

$$h_r^{fwd} = tanh(w_{F_{Aug}}^{fwd}F_{Aug_r} + w_{hh}^{fwd}h_{r-1}^{fwd} + \gamma_h^{fwd})$$
(3.29)

$$h_r^{bwd} = tanh(w_{F_{Aug^h}}^{bwd} F_{Aug_r} + w_{hh}^{bwd} h_{r-1}^{bwd} + \gamma_h^{bwd})$$
(3.30)

The result is finally obtained by merging the forward and backward hidden layers, as shown in Equation (3.31).

$$y_r = w_{hy}^{fwd} h_r^{fwd} + w_{hy}^{bwd} h_r^{bwd} + \gamma_y$$
 (3.31)

Consequently, the intermediate scores are produced by the Bi-LSTM model output shown as B^{Out} .

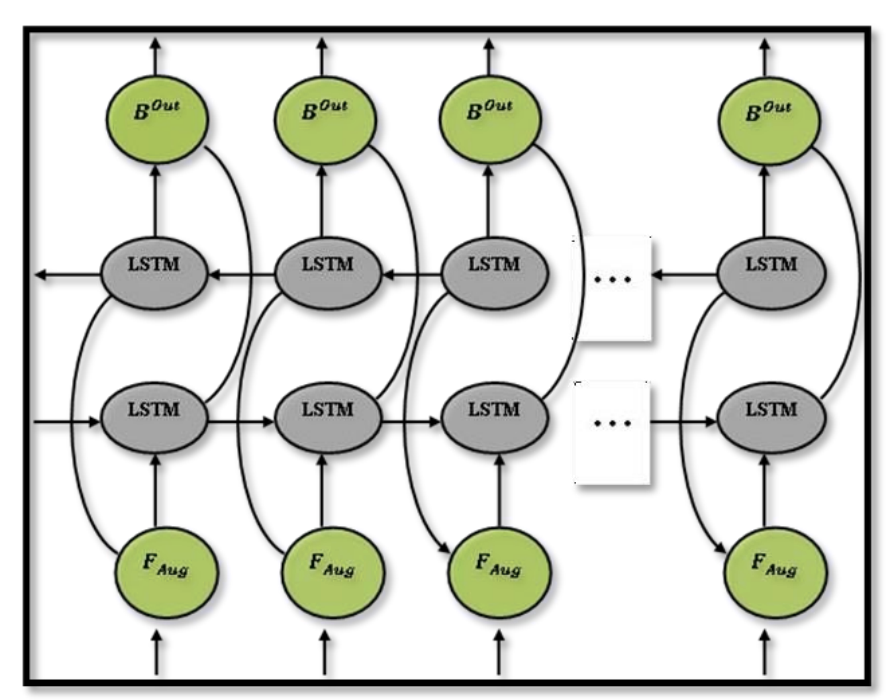


Figure 3. 6: The flow of the proposed model.

3.5 Improved DBN

DBN, consisting of a restricted Boltzmann machine (RBM) with two layers hid-

den and visible, typically requires extensive labeled data for weight initialization, leading to high computational costs and long training times. To address the issue, DBN weights are initialized using the features learned from the Bi-LSTM, which capture essential details about the dispersion of the data, enhancing DBN's capacity to extrapolate to unknown data and accelerate convergence. The three buried layers of the enhanced DBN each contain 100, 50, and 25 neurons and are initialized with Bi-LSTM weights, enabling faster learning and enhanced noise resilience. This approach leads to more efficient and robust signal classification.

$$Egy(u,h) = -\sum_{i=1}^{w} u_i b_i - \sum_{j=1}^{n} h_j d_j - \sum_{i=1}^{w} \sum_{j=1}^{n} h_j u_i m_{i,j}$$
(3.32)

The upgraded DBN seeks to identify a stable state with the fewest energy errors. The probability distribution that separates the hidden and visible layers is explained by Equation (3.33).

$$r(u,h) = \frac{1}{E_{Sum}e^{-Egy(u,h)}}$$
 (3.33)

Where E_{sum} refers to the whole energy of every layer, apparent and hidden; By guaranteeing effective learning and reducing training errors, this energy function is essential to model optimization.

An overview of energy for each visible and concealed layer is assessed as a proportional function to guarantee a normalized distribution. Then, Equations (3.34) and (3.35) determine the probability distribution of the visible and hidden parameters. These equations allow for modeling the relationships between the hidden and visible layers, facilitating efficient learning by optimizing the weights and biases based on the energy function.

$$r(u_i = 1|h) = \frac{1}{1 + exp(-b_i \sum_{j=1}^n h_j m_{i,j})}$$
(3.34)

$$r(h_j = 1|u) = \frac{1}{1 + exp(-d_j - \sum_{i=1}^n u_i m_{i,j})}$$
(3.35)

In order for the network to capture intricate correlations between input and output, in output, using an activation function, non-linearity is introduced into DBN. Despite their widespread use, classic activation functions like sigmoid and ReLU suffer from the vanishing gradient issue. When gradients propagate across the layers during training, they get progressively smaller, which hinders convergence and makes weight updates more difficult. Many call this problem the "non-zero-centered problem," which is addressed by utilizing the hybrid Swi-Mish activation function (S-MAF), blending the Mish and Swish functions. While the Mish function is roughly zero-centered and helps to enhance weight updates by limiting gradients that are too large in one direction, the smooth curve offers

a Swish function that permits flow during backpropagation. Consequently, the S-MAF improves network efficiency, provides smoother transitions, and mitigates the vanishing gradient issue. Equation (3.36) provides a mathematical expression for the S-MAF.

$$Swi - Mish(y) = Max[Swish(y), Mish(y)]$$
(3.36)

Where
$$Swish(y) = y. sigmoid(y) = y. \frac{1}{1+e^{-y}}$$
 and $Mish(y) = y. tanh[ln(1+e^2)].$

The Swi-Mish activation function derivative is then expressed using Equation (3.37).

$$Swi - Mish'(y) = Max[Swish'(y), Mish'(y)]$$
(3.37)

Swish'(y) = Swish(y) + sigmoid(y)[1 - Swish(y)]Mish'(y)

=
$$tanh[Softplus(y) + y * sec h^2[Softplus(y) * Softplus'(y)]]$$

$$Softplus'(y) = sigmoid(y) Softplus(y) = ln[1 + e^x]$$
(3.38)

As a result, the intermediate scores are produced by the IDBN model and can be shown as D^{Out} . The Swi-Mish activation function with IDBN is shown in Figure 3.7.

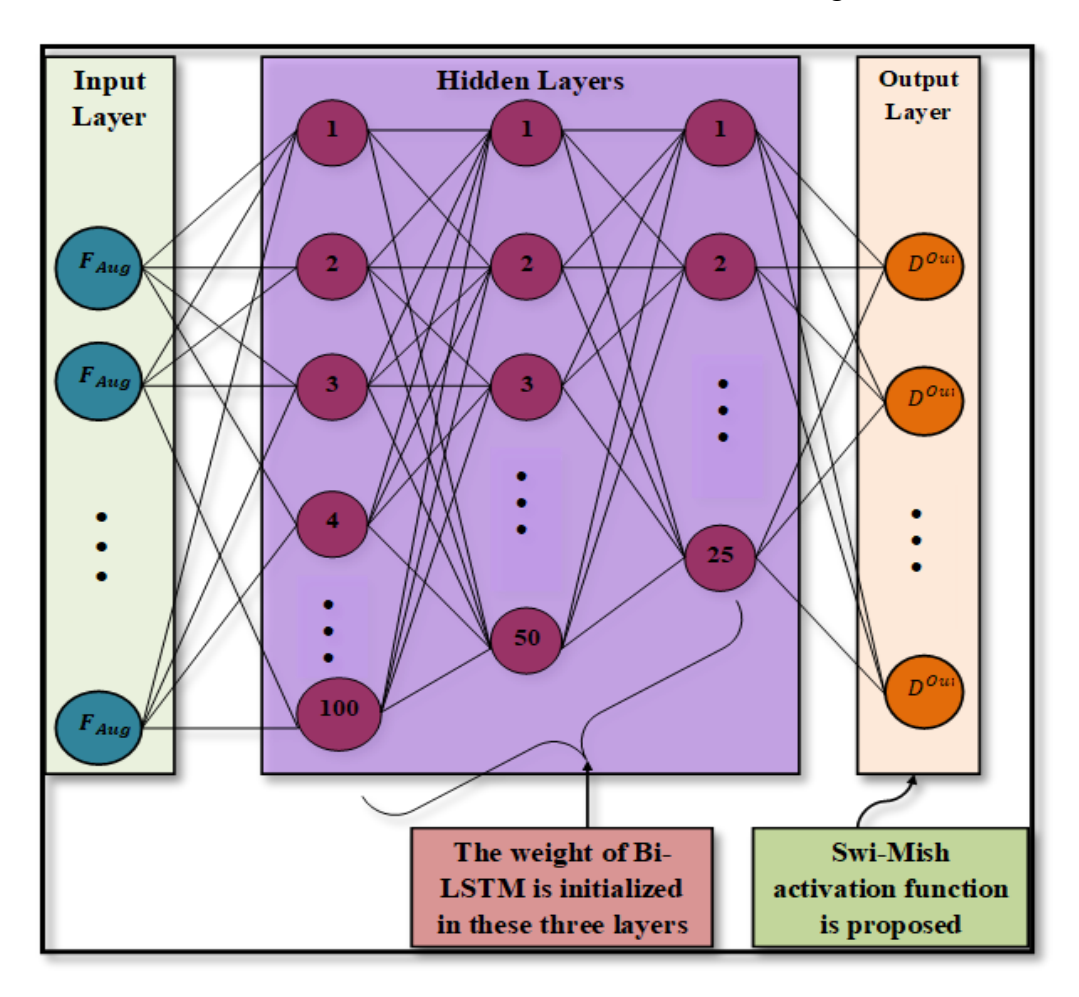


Figure 3. 7: Swi-Mish activation function with IDBN.

3.5.1 Score Level Fusion

In this study, score level fusion [153] is used to combine the outputs from IDBN and Bi-LSTM. After separately training the models with the training dataset to determine individual class scores, they are assessed using the same data, denoted as B^{Out} and D^{Out} for Bi-LSTM and IDBN, respectively. These scores, representing the estimated probabilities for each class, are normalized using Min-Max normalization to mitigate the impact of score magnitude, as shown in Equation (3.36). After that, a sum rule method is utilized to fuse the normalized scores, where the scores from both models are summed for each data point, as represented in Equation (3.39).

$$S^{Norm} = \frac{s_i - min(s_i)}{max(s_i) - min(s_i)} \tag{3.39}$$

Additionally, the sum rule-based fusion strategy is used to normalize scores in accordance with Equation (3.40).

$$S^{Fuse} = \sum_{i=1}^{m} S^{Norm} \tag{3.40}$$

As a result, the score-fused method provides five labels for the different levels of gear crack detection output.

3.6 Data Acquisition and Experimental Analysis

This study conducted multiple experiments using a Spectra Quest MFS to collect vibration signals, as shown in Figure 3.8 and Figure 3.9. The dataset used for experimentation is considered from the previous study [154]. The experiments were performed under var- ying rotational speeds and torque. The key components of the test rig included a magnetic brake, an A-bearing housing plate, a belt and pulley system, and an AC induction motor. Additionally, the magnetic brake provided the necessary test torque, while a variable frequency drive (VFD) regulated the motor speed. The system includes a 1-horsepower, 2850 rpm AC motor, flexible coupling, a gearbox, ball bearings, and a magnetic brake. Motion is transmitted through a 19 mm shaft, with a belt pulley driving the gearbox. A tri-axial accelerometer (PCB-Piezotronics 356A26, S/N: 355339) is mounted on the gear- box to capture vibration data, connected to an OROS-OR34 DAQ system, and analyzed via NV Gate software. Vibration signals were recorded at torques from 0 to 4 Nm and speeds such as 15 Hz, 20 Hz, 25 Hz, and 30 Hz, with both healthy and faulty gears acceleration readings recorded at 12.8 kHz sampling over three axes.

In this research, the bevel gearbox is given in Table 3.3. A total of five pinion gears were examined, comprising four faulty gears: incipient crack, moderate crack, small crack, severe crack, and one healthy gear. Figure 3.10 shows the several gear conditions that were

looked at. A CNC and wire EDM were used to introduce the crack faults. A Dewinter Optical Inc. optical microscope (model DEW507) was used to measure the crack length.

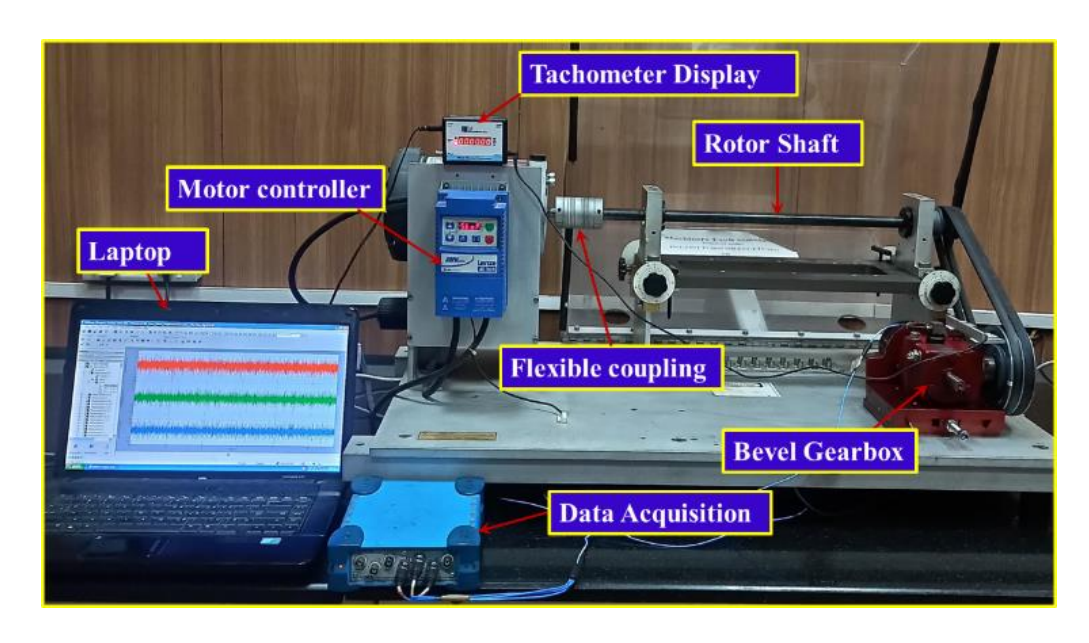


Figure 3. 8: Experimental Setup.

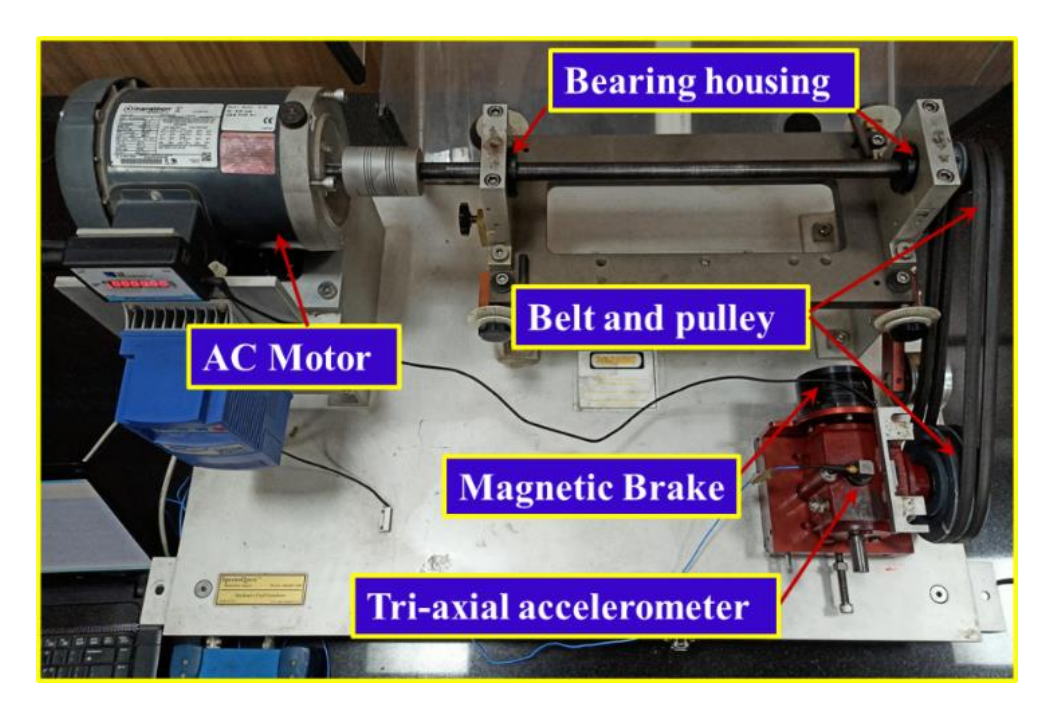


Figure 3. 9: Electromechanical elements analytical test rig.

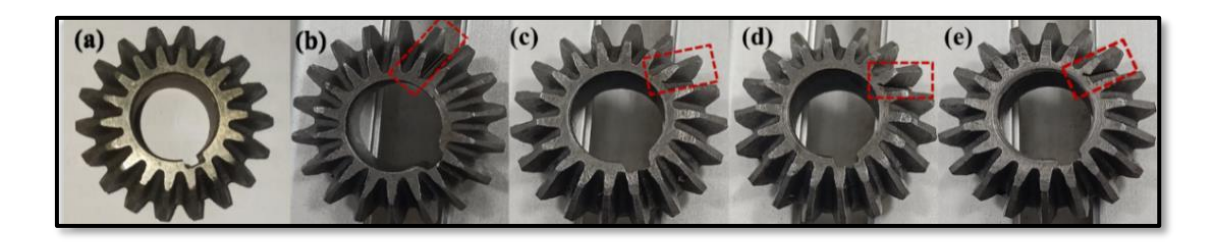


Figure 3. 10: Gear health: (a) Healthy (b) A 0.25 mm crack-length gear; (c) a 0.50 mm crack-length gear; (d) a 0.75 mm crack-length gear; and (e) a 1.00 mm crack-length gear.

Table 3. 3: Gearbox Description

Specification of Gearbox	Pinion	Gear
Pitch diameter	28.576 mm	42.8626 mm
Module	2 mm	2 mm
angle Pressure	20°	20°
Material	Forged steel	Forged steel
Number of teeth	18	27
Pitch angle	33°42'	56°18'

3.7 Results and Discussion

3.7.1 Simulation Procedure

The proposed methodology in this research was simulated using Python 3.7, with an Intel Core i7 CPU@ 2.90 GHz and 16 GB of RAM (15.7 GB usable).

3.7.2 Performance Evaluation

Its accuracy and computation time are investigated to evaluate the proposed method's effectiveness. The trade-off between calculation time and accuracy is balanced to have the best learning rate. Below is a thorough explanation of the computation time and accuracy.

3.7.3 Evaluation of Learning Rate Vs Accuracy

Table 3.4 shows how accuracy and learning rate are correlated. A hyperparameter known as the learning rate regulates the model parameters during training. The suggested model is evaluated with 0.1, 0.05, 0.01, and 0.001 rates. The model's accuracy at a frequency of 30 Hz is roughly 99.8% when learning at a rate of 0.001, 93.6% at a rate of 0.1, 93.8% at a rate of 0.01, and 93.8% at a rate of 0.05. A learning rate of 0.001 yields the maximum accuracy. While lesser learning rates employ smaller steps, greater learning rates produce larger steps. Instability during training could result from the approach to overshooting the loss function's minimum due to unreasonably high learning rates.

Table 3. 4: Learning Rate vs. Accuracy Analysis

Different operating speed (Hz)	Learning Rate					
	0.1	0.01	0.05	0.001		
	Accuracy of performance with varying learning rates					
15	0.9368	0.9410	0.9418	0.9965		
20	0.9372	0.9393	0.9405	0.9982		
25	0.9380	0.9389	0.9393	0.9948		
30	0.9368	0.9380	0.9386	0.9982		

3.7.4 Evaluation of Rate of Learning Vs Computational Time

The correlation between calculation time and learning rate is depicted in Figure 3.11. Conversion speed and accuracy must be matched to find the optimal learning rate. The model successfully converges at the ideal learning rate, preventing issues like overshooting or less-than-perfect solutions. The model is evaluated at learning rates of 0.1, 0.05, 0.01, and 0.001. Longer calculation times correlate with higher learning rates. Using 0.001 as the learning rate, the computational time at a frequency of 15 Hz is roughly 1 second, 3.5 seconds for 0.1, 3.48 seconds for 0.01, and 2.25 seconds for 0.05. The best option for better performance is a learning rate of 0.001, which takes the least amount of computational time.

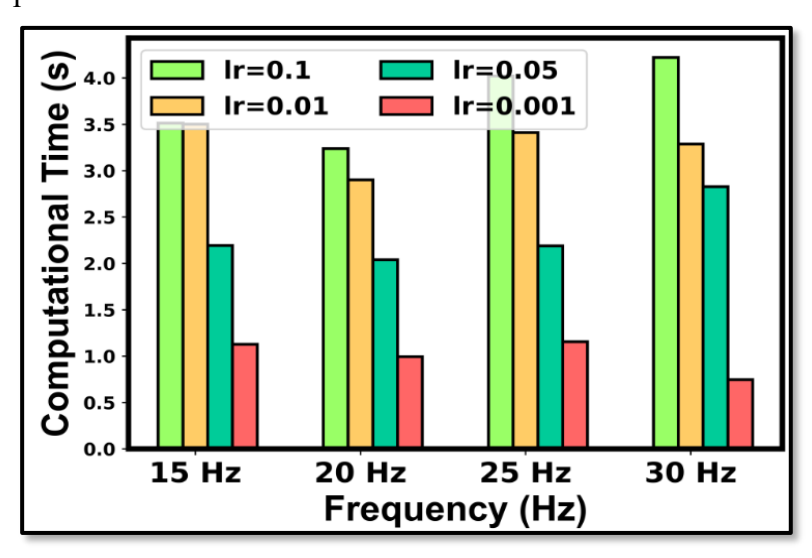


Figure 3. 11: Evaluation of Learning Rate Vs. Computational Time.

3.7.5 Confusion Matrix Evaluation on Proposed Method

The Bi-LSTM-IDBN model's confusion matrices for the various frequency ranges are shown in Figure 3.12. The confusion matrix compares the actual and predicted targets, with values inside each rectangle representing the prediction outcomes. The classification includes five distinct classes: healthy, SLC (crack small), IC (incipient crack), MC (moderate crack), and SRC (severe crack). The four key classification conditions, TP, FP, TN, and FN are displayed. Diagonal values represent correct predictions, while off-diagonal areas reflect incorrect predictions.

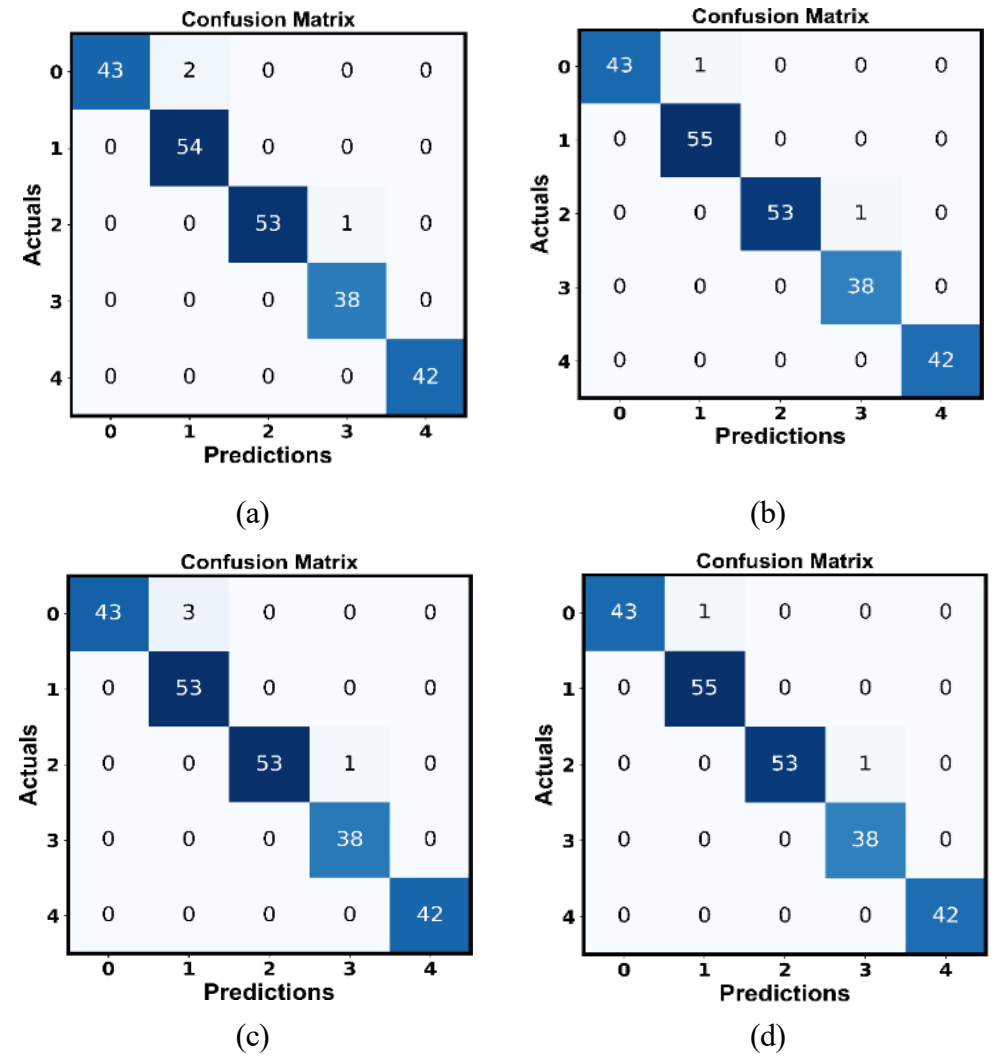


Figure 3. 12: Confusion matrix for proposed approach a)15 Hz, b) 20 Hz, c) 25 Hz, and d) 30 Hz.

3.7.6 Comparative Analysis

To successfully determine the various gear crack levels, the suggested strategy was contrasted with current approaches in terms of accuracy, precision, and F-measure. It was also evaluated against the latest technologies, such as OWPD and feed-forward neural networks (FFNN). Other classifiers, including deep convolutional neural networks (DCNN), SVM, Bi-GRU, RNN, Bi-LSTM-IDBN, and RF, were also contrasted with the Bi-LSTM-IDBN model.

3.7.7 Analysis of Precision, Accuracy, and F-Measure

In order to assess the suggested technique's efficacy, we change the percentage of training data between 60%, 70%, 80%, and 90% while maintaining a constant learning rate of 0.001. The improved CEEMDAN methodology contrasts the performance with traditional methods for identifying gear crack faults using accuracy, precision, and F-measure. Furthermore, a comparison is made between the proposed model and existing

classifiers. The analysis's findings, which are displayed in Figures 3.13(a) through 3.13(d), demonstrate that the recommended approach performs better than the others in precisely detecting gear crack faults at different levels.

The model must have strong F-measure scores to accurately identify the various gear crack levels. By exhibiting better precision values, the proposed method outperformed traditional techniques. In particular, the proposed reached a high f-measure of 100% at 30 Hz and a training percentage of 90%. In contrast, other models such as D-Net at 96.13%, M-Net at 95.70%, RF at 97.42%, SVM at 96.99%, RNN at 98.28%, Bi-GRU at 96.13%, Bi-LSTM at 96.13%, and DCNN at 95.27% recorded lower precision scores. These results show how adaptable and versatile the suggested model is, effectively detecting various gear crack levels through the use of a mixed classification technique.

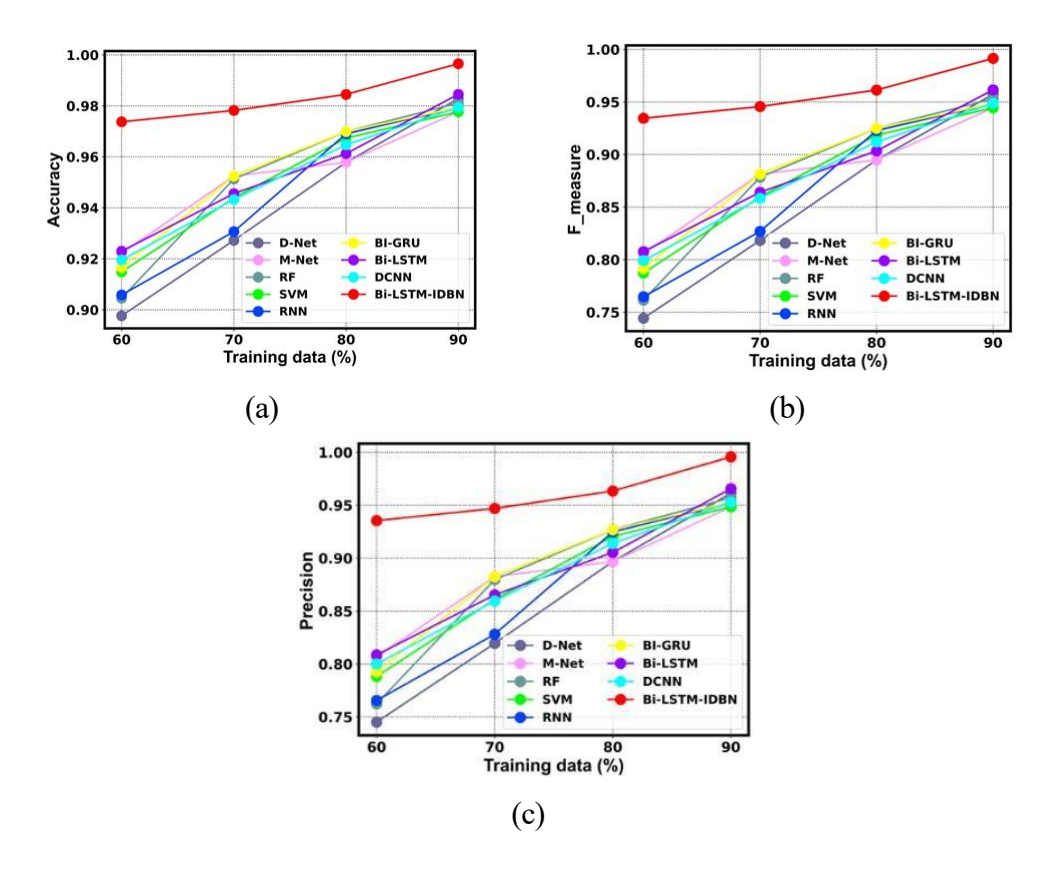


Figure 3. 13(a): Evaluation of proposed methods in comparison to traditional techniques for 15 Hz, a) Accuracy, b) F-measure, and c) Precision.

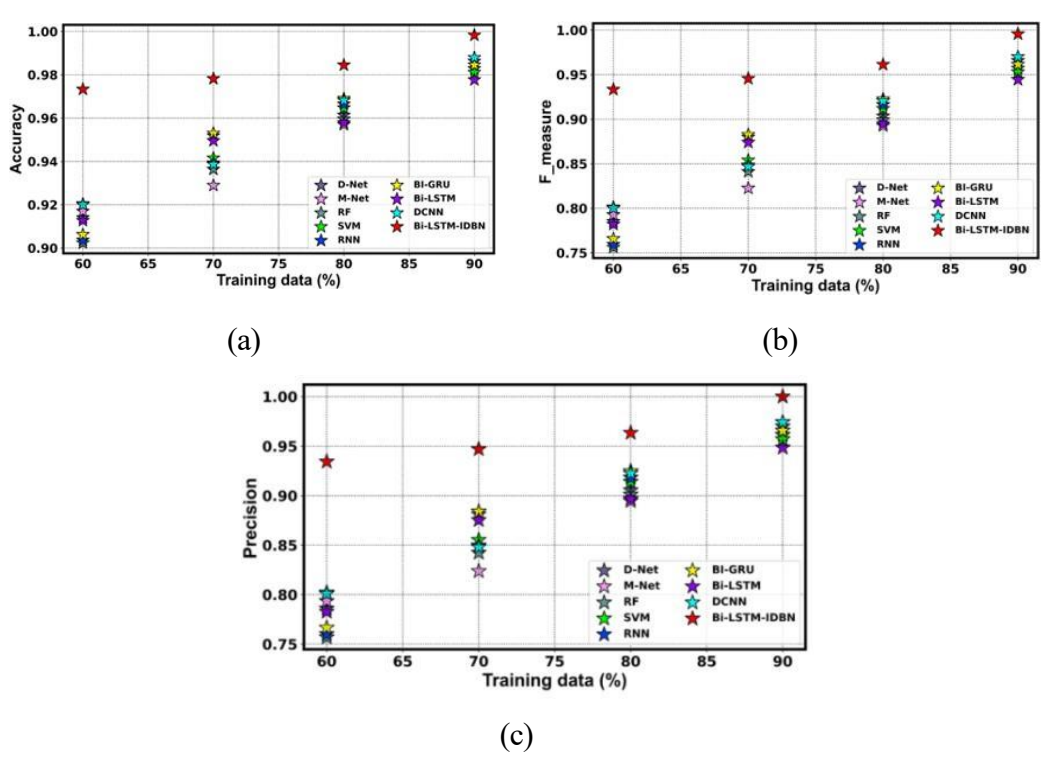


Figure 3. 13(b): Evaluation of proposed method in comparison to traditional techniques for 20 Hz: a) Accuracy, b) F-measure, and c) Precision.

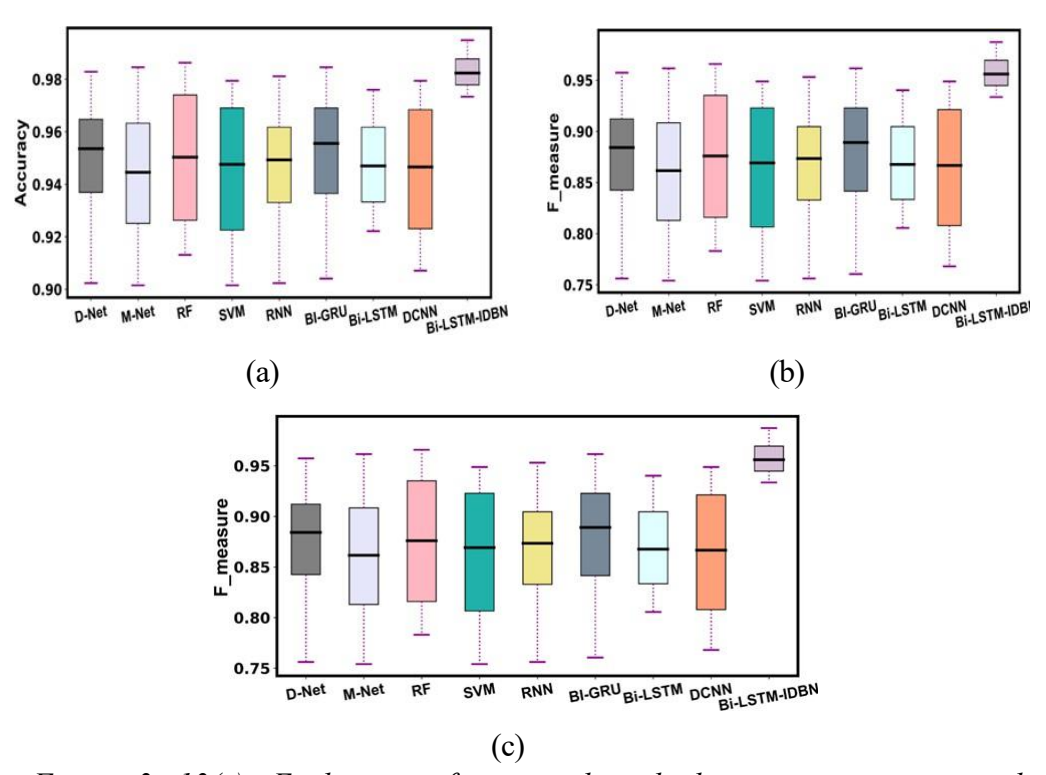


Figure 3. 13(c): Evaluation of proposed method in comparison to traditional techniques for 25 Hz: a) Accuracy, b) F-measure, and c) Precision.

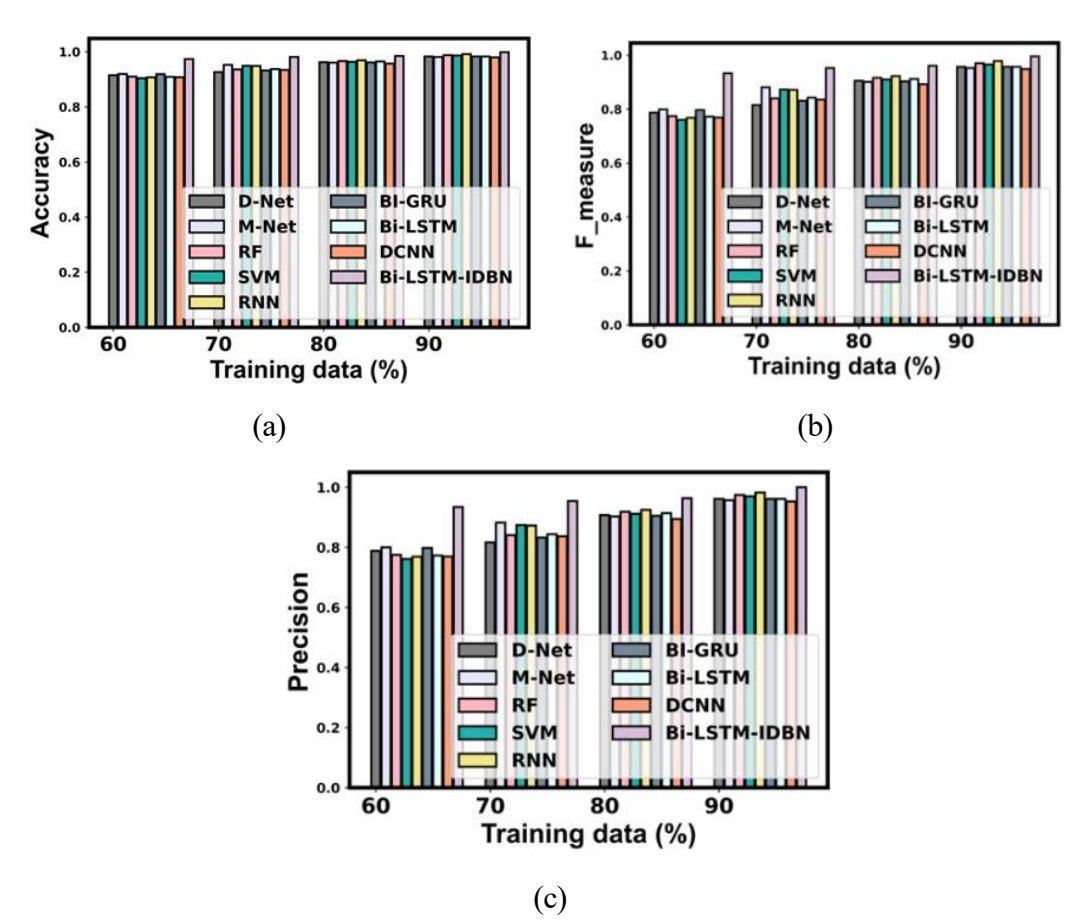


Figure 3.13(d): Evaluation of proposed method in comparison to traditional techniques for 30 Hz: a) Accuracy, b) F-measure, and c) Precision.

3.7.8 Computation Time Analysis

As illustrated in Figure 3.14, the computational time analysis of the suggested technique was contrasted with those of other methods for identifying various levels of gear cracks based on the existing methods. The model should reduce computation time to determine gear crack levels precisely. Compared to conventional approaches, the Bi-LSTM-IDBN approach showed noticeably faster computation times. This model reduced the computation time to 0.993 seconds at 20 Hz, which was quicker than other models, which took 6.52 seconds for D-Net, 5.63 seconds for M-Net, 1.378 seconds for RF, 7.813 seconds for Bi-GRU, 3.623 seconds for Bi-LSTM, 5.688 seconds for SVM, 1.593 seconds for RNN, and 2.121 seconds for DCNN. Furthermore, the proposed outperformed all other techniques, recording a low computational time of 1.155 seconds at 25 Hz. As a result, in every frequency range, the proposed (Bi-LSTM-IDBN) technique continuously outperforms in terms of computing efficiency. According to experimental data, this approach allows for more accurate gear crack detection than other approaches and saves computational time.

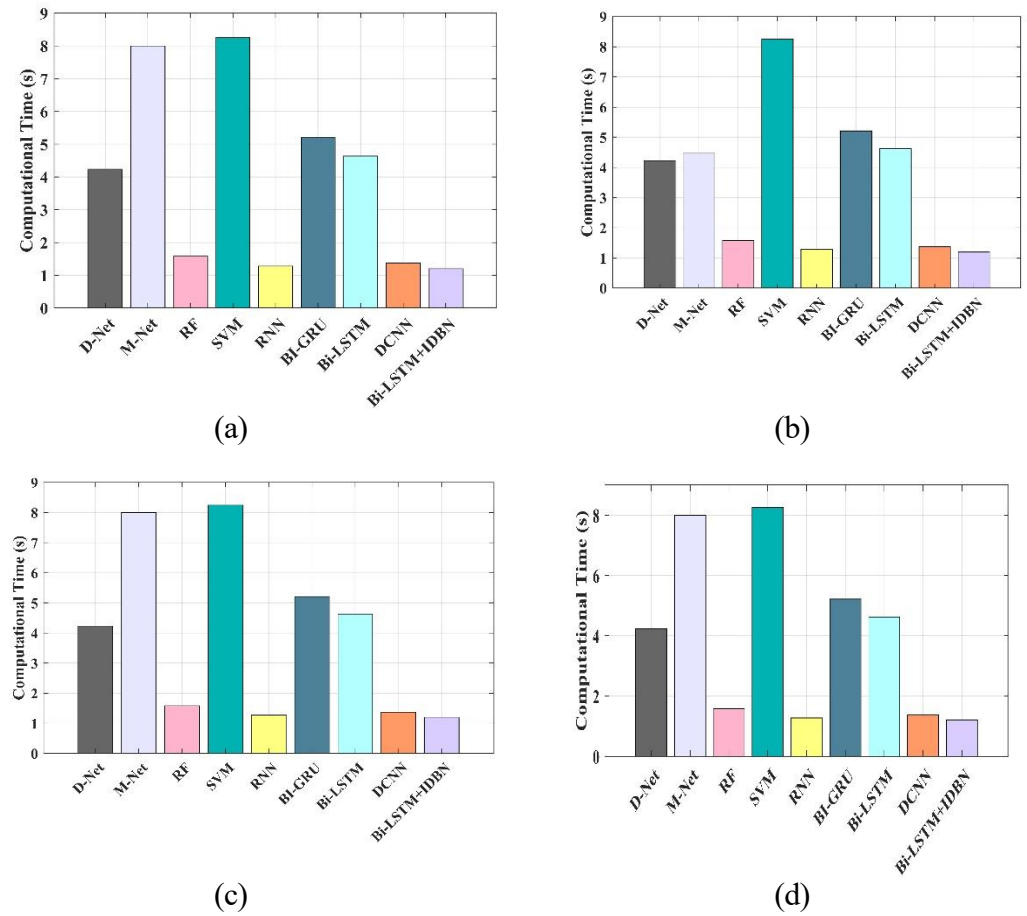


Figure 3. 14: Computational time comparison between traditional and proposed approaches for (a) 15 Hz, (b) 20 Hz, (c) 25 Hz, and (d) 30 Hz.

3.7.9 Ablation Analysis of Proposed Method

Comprehensive ablation research was carried out to evaluate the impact of specific characteristics on the Bi-LSTM-IDBN model's performance for gear crack diagnosis. The comparison of models using traditional CEEMDAN, cross-correntropy, and DBN with Bi-LSTM-IDBN is summarized in Table 3.5. At 15Hz, the suggested method achieves an accuracy of 99.65%, outperforming the conventional CEEMDAN with 98.28%, cross-correntropy with 98.45%, and DBN with 98.62%. Additionally, the precision of Bi-LSTM-IDBN is 99.57%, significantly higher than the precision of the other models: CEEMDAN with 96.13%, cross-correntropy with 96.56%, and DBN with 96.99%. These results show the effectiveness of the Bi-LSTM-IDBN technique powered by the CEEMDAN algorithm for increased feature extraction, combined classification, and signal decomposition.

Table 3. 5: Evaluation of ablation at 15 Hz, 20 Hz, 25 Hz, and 30 Hz using the proposed method with existing techniques

Metrics	Proposed Model	Combining traditional CEEMDAN with the pro- posed method	Traditional cross- correntropy in Bi-LSTM- IDBN	Bi-LSTM- IDBN with existing DBN	
		Frequency = 15 Hz			
Specificity	0.9988	0.9902	0.9912	0.9923	
Sensitivity	0.9871	0.9530	0.9573	0.9616	
Accuracy	0.9964	0.9827	0.9846	0.9861	
F-measure	0.9913	0.9571	0.9614	0.9657	
Precision	0.9956	0.9612	0.9655	0.9698	
FDR	0.0041	0.0385	0.0342	0.0301	
FNR	0.0128	0.0466	0.0423	0.0384	
MCC	0.9892	0.9464	0.9517	0.9571	
FPR	0.0011	0.0097	0.0084	0.0074	
NPV	0.9966	0.9880	0.9888	0.9902	
		Frequency = 20 Hz			
FDR	0	0.0385	0.0427	0.0326	
Specificity	1	0.9902	0.9891	0.9903	
Sensitivity	0.9913	0.9530	0.9488	0.9526	
FNR	0.0084	0.0467	0.0512	0.0446	
F-measure	0.9956	0.9571	0.9528	0.9456	
Precision	1	0.9611	0.9578	0.9613	
Accuracy	0.9981	0.9827	0.9810	0.9722	
FPR	0	0.0095	0.0108	0.0097	
NPV	0.9977	0.9880	0.9872	0.9788	
MCC	0.9945	0.9464	0.9410	0.9588	
		Frequency = 25 Hz			

Precision	0.9913	0.9655	0.9572	0.9614
Sensitivity	0.9828	0.9573	0.9488	0.9530
NPV	0.9956	0.9892	0.9870	0.9880
F-measure	0.9870	0.9616	0.9528	0.9573
Specificity	0.9979	0.9913	0.9891	0.9902
Accuracy	0.9947	0.9846	0.9810	0.9829
FPR	0.0022	0.0087	0.0108	0.0097
MCC	0.9838	0.9518	0.9410	0.9466
FDR	0.0086	0.0344	0.0428	0.0387
FNR	0.0171	0.0426	0.0511	0.0469
	Frequer	ncy = 30 Hz		
Specificity	1	0.9904	0.9588	0.9882
NPV	0.9977	0.9880	0.9653	0.9861
Sensitivity	0.9913	0.9530	0.9357	0.9445
FPR	0	0.0097	0.0097	0.0116
F-measure	0.9956	0.9571	0.9657	0.9488
FDR	0	0.0385	0.036854	0.0471
Accuracy	0.9981	0.9829	0.9557	0.9792
MCC	0.9945	0.9466	0.9255	0.9359
Precision	1	0.9612	0.9689	0.9528

3.7.10 Comparison of Existing Methods

Table 3.6 provides an explanation of the backpropagation FFNN and compares the upgraded CEEMDAN study with OWPD. Furthermore, the model must generate more accurate accuracy ratings in order to identify gear cracks at various levels. The accuracy of the upgraded CEEMDAN approach is 99.82% in this case, while the accuracy of the backpropagation FFNN and OWPD is lower at 80.65% and 98.33%, respectively.

Table 3.6: Evaluation of improved CEEMDAN compared to OWPD and backpropagation FFNN.

	Backpropagation FFNN for gear fault detection	OWPD	Proposed work
Signal	Vibration	Vibration	Vibration
Optimizer or	Gradient Decent	Cat Boost	Gradient Decent
learning strategy		Algorithm	
Test instance and sample rate Defect conditions	200 (50 X 4), 12,500 sample/s Crack defects 1 mm, 2 mm, and 3 mm	lengths (0, 5 mm,	75 X 2000 samples Crack defects 0.25 mm, 0.5 mm, 0.75
		10 mm and 15 mm)	mm, and 1 mm
Operation	600, 700, 800, 900,	600,	15,20, 25, 30 Hz
conditions	100 rpm 0%, 25%,	900,1200,1500	0,1,2,3,4 Nm loads
	50%, 75%, 100% loads	rpm	
Accuracy	80.65%	98.33%	99.82%

3.8 Conclusion

This chapter presented a new approach for detecting gearbox faults. The first step in the procedure was gathering data, which was then preprocessed by breaking down the input signal using an improved CEEMDAN algorithm. Features based on time, frequency, and entropy were recovered from the decomposed signal. Data augmentation was used to create random samples based on the feature's minimum and maximum values to enhance the feature set even more. Bi-LSTM and IDBN classifiers were combined to create a hybrid crack-level classification model fed these improved features. A Bi-LSTM weight was assigned to the first three layers of DBN to enhance classification performance. The classifier scores were then fused at the score level to divide crack levels into five groups. With an accuracy of 99.21% and 100%, the Bi-LSTM-IDBN strategy continuously beat

traditional techniques, according to the data. With a 90% training percentage and outstanding performance, especially at higher frequencies, this method proved to be an excellent solution for accurately and efficiently detecting gear cracks.

Chapter 4

Hybrid Architecture Based on Modified LinkNet and DenseNet for Integrated Fault Detection in Electromechanical Systems

In EM systems, commonly utilized across various industrial applications, an electric motor serves as the prime mover, typically coupled with a mechanical load such as a gearbox, rotor, or pump. Effective condition monitoring (CM) is essential for these systems, and vibration monitoring has proven to be a reliable method for fault identification. However, EM systems can experience combined faults involving simultaneous motor and load issues. Diagnosing these combined faults presents a significant challenge due to the fault's compounding consequences and overlapping symptoms. This issue is resolved by suggesting a modified LinkNet and DenseNet (MLiDNet) categorization of the fault model. This model incorporates combined DL classifiers, entropy-based feature extraction, and sophisticated signal processing techniques. Signal pre-processing is done with the ISSWT, and feature extraction focuses on entropy-based properties such as norm, enhanced spectral, threshold, and wavelet energy entropy. Efficient fault classification is the goal of the combined DL classifier, MLiDNet. With a precision of 99.68%, an Fmeasure of 99.37%, and an incredible accuracy of 99.78%, the suggested approach requires less computing time than current methods. These results show that the Modified LinkNet and DenseNet (MLiDNet) model holds strong potential as an effective solution for accurately detecting combined faults in EM systems.

4.1 Introduction

Belt pulley drives, gearboxes, couplings, rotor-bearing systems, electric motors or generators, and other mechanical and electrical components form an EM system [155,156]. Industrial or manufacturing processes may be stopped by catastrophic breakdowns caused by the failure of any of these components [157–158]. Consequently, early fault detection and continuous monitoring in EM systems are critical to prevent widespread system failures. This proactive approach allows for scheduling preventive and CBM during downtime, significantly reducing the risk of extended operational disruptions [160-163]. Such strategies enhance system performance and availability

while minimizing maintenance costs [164, 165]. Vibration measurements, in particular, play a vital role in diagnosing issues within gear systems, ensuring their reliability and safety. Usually, eddy current measurements, vibration, and acoustic emissions are used to diagnose gear faults. DL-based fault detection methods have recently gained popularity and successfully diagnosed faults in rotating machinery [166, 167].

Faults in EM systems can generally be classified into electrical and mechanical categories. Electrical issues in IM include insulation failures, rotor bar breakage, and stator winding issues [168–170]. Conversely, mechanical faults include rotor imbalances, misalignments, gearbox or belt-pulley faults, and bearing failures. Since the IM is the primary driver related to mechanical parts, including shafts, bearings, rotor systems, and gearboxes, this study specifically focuses on mechanical failures in IMs and their coupled loads. However, these methods frequently need rather big and well-balanced training datasets, which are challenging to acquire in real-world applications, in order to provide significant results [171]. This study focuses on faults such as imbalanced rotors in mechanical loads, bearing faults, and unbalanced loads in motors. These faults are crucial because they can significantly affect the longevity and performance of EM systems. Methods including noise monitoring, current signal analysis, and vibration monitoring are employed to find these issues; vibration monitoring is particularly valued due to its ability to identify mechanical faults.

Advanced signal processing techniques are crucial for identifying possible faults in electromechanical systems, and they play a major role in early fault detection [172, 173]. These methods, which can be non-invasive or invasive, are essential for finding errors before they cause system breakdowns. Common tools include FFT, CWT, DWT, HHT, and WPT [174]. These methods have drawbacks despite their significance, including high computing cost and vulnerability to non-stationary signals. By concentrating on the instantaneous frequencies of signals, the SSWT enhances time-frequency representation; nonetheless, it still faces challenges in noisy environments and with high computing complexity [175]. To address these challenges, the improved SSWT was developed. By improving noise reduction and offering superior time-frequency decomposition for more precise fault identification, ISSWT emerges as a more reliable and effective substitute for conventional SSWT techniques, which are computationally demanding and susceptible to noise.

4.2 Proposed Methodology

This research presents a reliable proposed fault detection model for detecting coupled failures in EM systems, especially those involving IM and rotor systems. Five essential procedures make up the method for effectively classifying and detecting faults in these kinds of systems. The suggested structure is shown in Figure 4.1. The data-collecting portion of the model begins with experiments using an MFS to capture vibration data. Following data collection, the signal is decomposed using the ISSWT method during pre-processing. This sophisticated pre-processing method enhances its quality and makes fault identification easier by dissecting the input signal into its constituent parts.

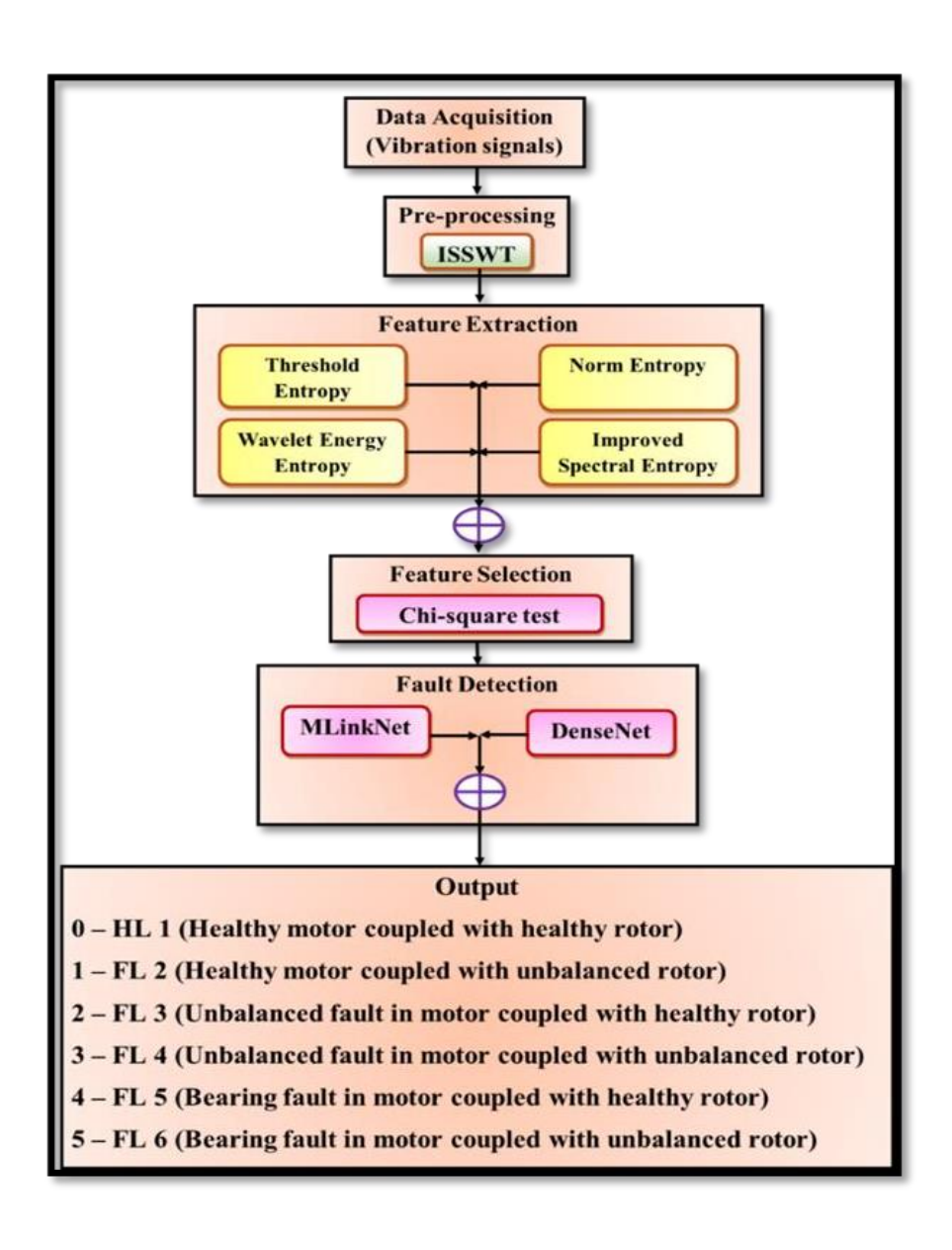


Figure 4. 1: The suggested MLiDNet model for fault detection.

Following pre-processing, the signal's essential properties are captured using feature extraction. Features are extracted, including wavelet energy entropy, threshold entropy, enhanced SE, and norm entropy. The Chi-Square (CS) test is then used for feature selection to identify the most relevant aspects and significantly impact fault identification. Finally, a combined technique incorporating dense net (D-Net) and MLink Net, the MLiDNet approach, is used to carry out fault detection. The benefits of both DL architectures are used in this combined model to categorize EM faults accurately.

4.2.1. Pre-processing: Improved Synchro-Squeezing Wavelet Transform Technique

In signal processing, pre-processing is crucial because the quality and data's applicability are enhanced prior to additional evaluation. The input signal x is appropriately prepared in the proposed fault detection system for EM systems thanks to pre-processing. The input signal is divided into frequency components using signal decomposition, usually using ISSWT. By adding a de-noising phase prior to applying the CWT, ISSWT improves on the traditional SSWT [175]. In contrast to SSWT, which applies CWT directly, ISSWT enhances the level of time-frequency decomposition quality by removing noise via threshold-based de-noising. The current SSWT is sensitive to noise, which affects the precision of fault identification by distorting the time-frequency representation of the signal. ISSWT solves this challenge by enhancing fault detection accuracy and decomposition reliability by offering a more precise representation.

In order to eliminate unwanted noise, the input signal (x) data is subjected to threshold-based de-noising during the pre-processing stage. The signal is subsequently denoised and split into time-frequency components using CWT. This is followed by realigning the wavelet coefficients' energy using the synchro-squeezing transformation. In the SSWT, synchro-squeezing improves the signal's time-frequency localization by moving data from the frequency-scale level to the time plane, as shown in equation (4.1). The map provides a definition of this function. $(B,c) \rightarrow (B,\omega(c,B))$, where B stands for time, c for scale, and ω for frequency. A better understanding of the signal's properties is made possible by the improved time-frequency representation made possible by ISSWT, which helps the MLiDNet model detect faults better.

$$T_{SS}(\omega_{\alpha}, B) = (\Delta \omega)^{-1} \sum_{c_k : |\omega(c_k, B) - \omega_{\alpha}| \le \Delta \omega/2} w_{SS}(c_k, B) c_k^{\frac{-3}{2}} (\Delta c)_k$$

$$\tag{4.1}$$

A denoised signal's CWT can be shown as $w_{SS}(c_k, B)$ in Equation (4.1), which

discretized the variable frequency ω and the variable scale c_k . In particular, the frequency bins were represented by discrete values ω_{α} , at which the synchro-squeezed transform $T_{SS}(\omega,B)$ was evaluated. With $\Delta\omega$ signifying the bin size, these bins were specified by the intervals $\omega_{\alpha-1/2} - \Delta\omega/2to\omega_{\alpha+1/2} + \Delta\omega/2$. Likewise, the scale values Δc were calculated using $c_k - c_{k-1} = (\Delta c)\alpha$. The contributions from these discrete bins were then added up to calculate the synchro-squeezed transform $T_{SS}(\omega,B)$.

Equation (4.2) provides a mathematical illustration of how to apply the denoising threshold in ISSWT to eliminate undesired element noise in the signal input x.

Denoised signal,
$$x_d^* = \begin{cases} u * x_d + \lambda - \frac{\lambda}{2\beta + 1}; x_d < -\lambda \\ sign(x_d) \cdot \frac{\alpha}{(2\beta + 1) \cdot \lambda^{2\beta}} * |x_d|^{2\beta + 1}; |x_d| \le \lambda \\ u * x_d - \lambda + \frac{\lambda}{2\beta + 1}; x_d > \lambda \end{cases}$$
(4.2)

In Equation (4.2), α and β are the variable elements where $\alpha = \begin{cases} 1; \beta > 0 \\ 0; \beta = 0 \end{cases}$ and $\beta \in$

(0,4). u represent the control element, which is formulated by $u = 1 - e^{-\left[\frac{x(t) - \lambda^2}{\lambda}\right]}$ and λ represent the threshold, which is determined using Equation (4.3), where $\sigma = \frac{median(x(t))}{0.6745}$.

$$\lambda = \sigma \sqrt{2 \ln(N)} \tag{4.3}$$

Once the input signal has been de-noised x, the signal denoised x_d^* subsequently travels through the CWT process, as illustrated in Equations (4.4) and (4.5).

$$w_{SS}(c_k, B) = \int x_d^*(t) \cdot c^{-1/2} \overline{\psi\left(\frac{t-B}{c}\right)} dt$$
(4.4)

$$p_{x} = w_{SS}(c_{k}, B) = \frac{A}{4\pi} \cdot c^{-1/2} \overline{\hat{\psi}(c\rho)} \cdot e^{iB\rho}$$
 (4.5)

The outputs of the signal decomposition from the existing SSWT and the proposed ISSWT at 10 Hz, 20 Hz, and 30 Hz are compared for dataset 1 in Figure 4.2. These signals are used as input for processing by both ISSWT and SSWT. The results of applying the traditional SSWT to the signals sample at 10 Hz, 20 Hz, and 30 Hz are shown in Figure 4.2 (a). These images depict the signal's time-frequency obtained via SSWT. The presence of noise and less distinct frequency components is observed, indicating the limitations of SSWT in handling noise effectively. At 10 Hz, 20 Hz, and 30 Hz, the output of the proposed method employed on the same sample signals is displayed in Figure 4.2(b). The

proposed output displays a more precise frequency and signal temporal representation than the current output. By effectively removing noise, the ISSWT produces a signal with greater accuracy and more identifiable frequency components. The ISSWT applies to the CWT after a threshold-based reduction of the noise phase.

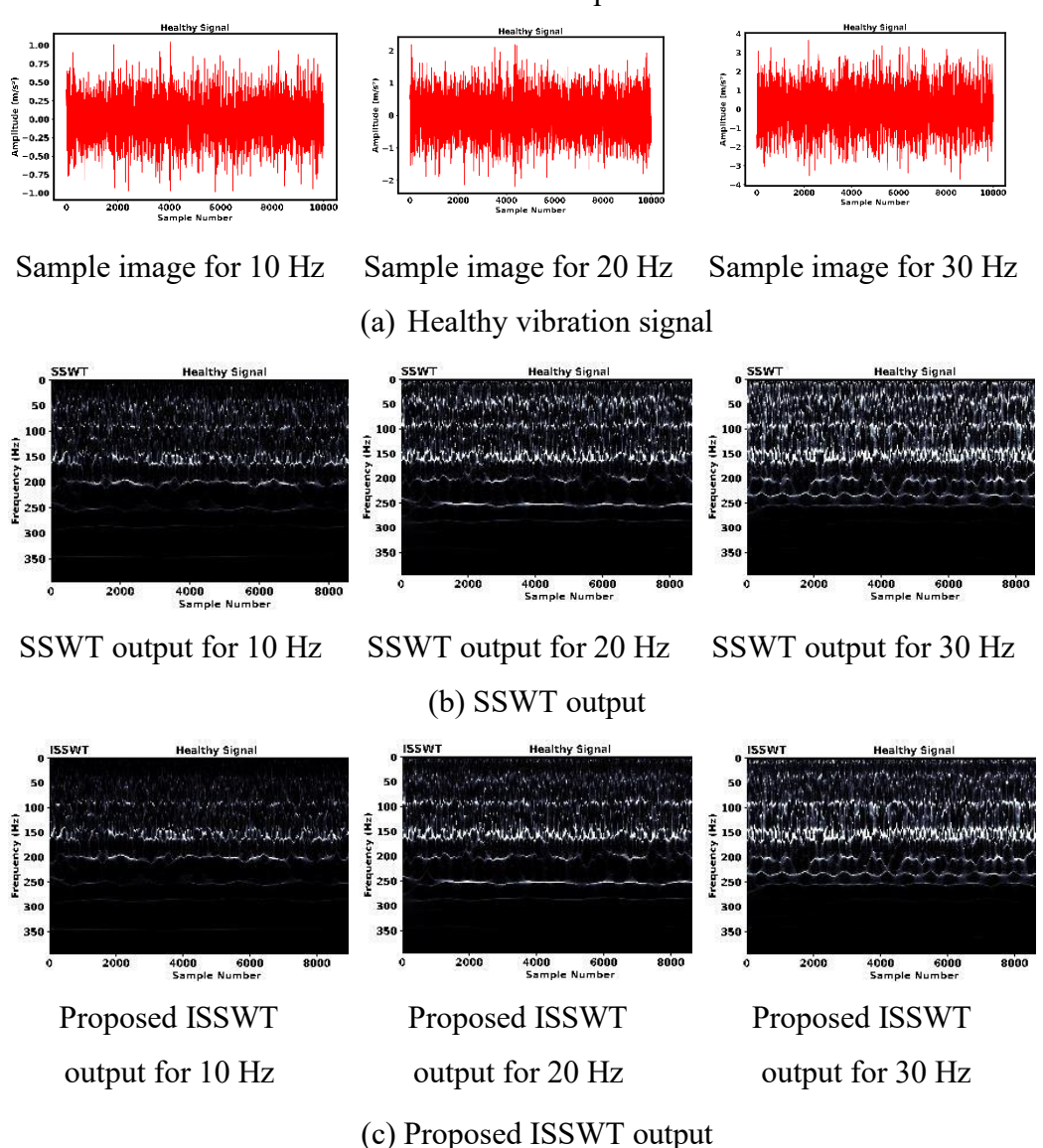


Figure 4. 2: Signal analysis of the following: (a) healthy vibration signal, (b) SSWT output, and (c) recommended ISSWT output for dataset 1.

ISSWT produces an improved output compared to the existing method, which uses CWT straight to signal noise because the de-noising step eliminates unnecessary noise from the input signal. Figure 4.3 shows more distinct element frequencies due to the improved clarity of time-frequency representation. Because of this, ISSWT improves fault identification accuracy and simplifies the understanding of signal properties. Essential features are retained when noise is eliminated from the denoised signal, resulting in more accurate time-frequency decomposition. The quality of the analysis of time and frequencies was raised by effectively eliminating noise; pre-processing with the

suggested method significantly improves fault identification reliability and accuracy in the suggested electromechanical system diagnosis model. The signal pre-processed is generated from the input signal x by the proposed method is shown as p_x .

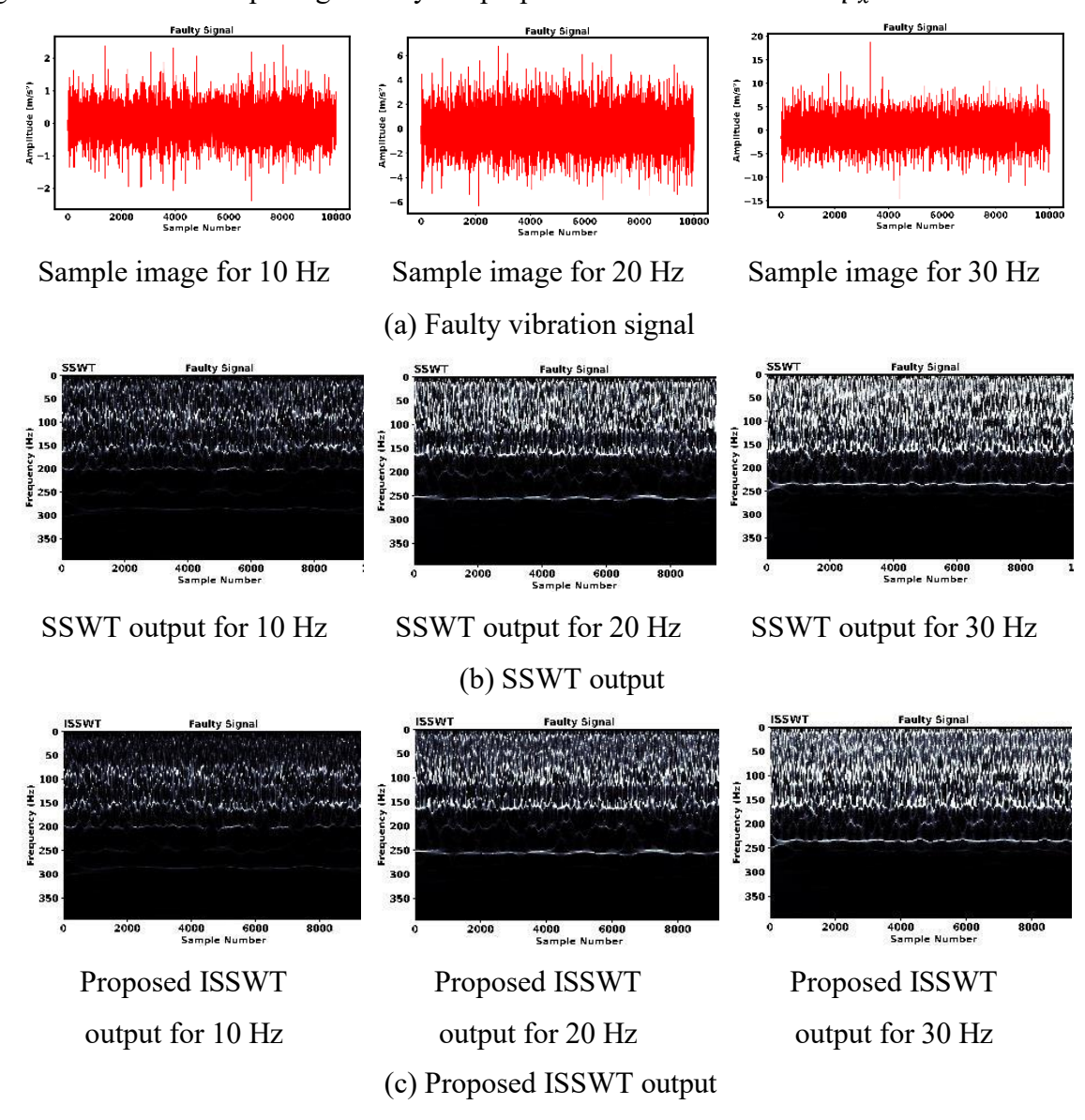


Figure 4. 3: Analysis of the following signals: (a) faulty vibrational signal, (b) SSWT output, and (c) suggested output for dataset 1.

Figure 4.4 compares the outputs of the proposed and the conventional methods for dataset 2 for breakdown signal at 30 Hz, 35 Hz, 40 Hz, 45 Hz, and 50 Hz. Both the proposed and current processes use these signals as input. Figure 4.4 (a) displays the result of the conventional method utilized for the signal sample at 30 Hz, 35 Hz, 40 Hz, 45 Hz, and 50 Hz. SSWT's challenges in effectively handling noise are highlighted by the reported presence of noise and less discernible frequency components. The output of the suggested approach employed on the same signal test at 10 Hz, 20 Hz, and 30 Hz is shown in Figure 4.4 (b). Compared to the current method, the output of the suggested

methodology more clearly displays the time-frequency of the signals. The ISSWT generates more frequency elements and enhances signal quality by efficiently eliminating noise. The proposed approach incorporates a threshold-based noise reduction stage prior to applying the CWT.

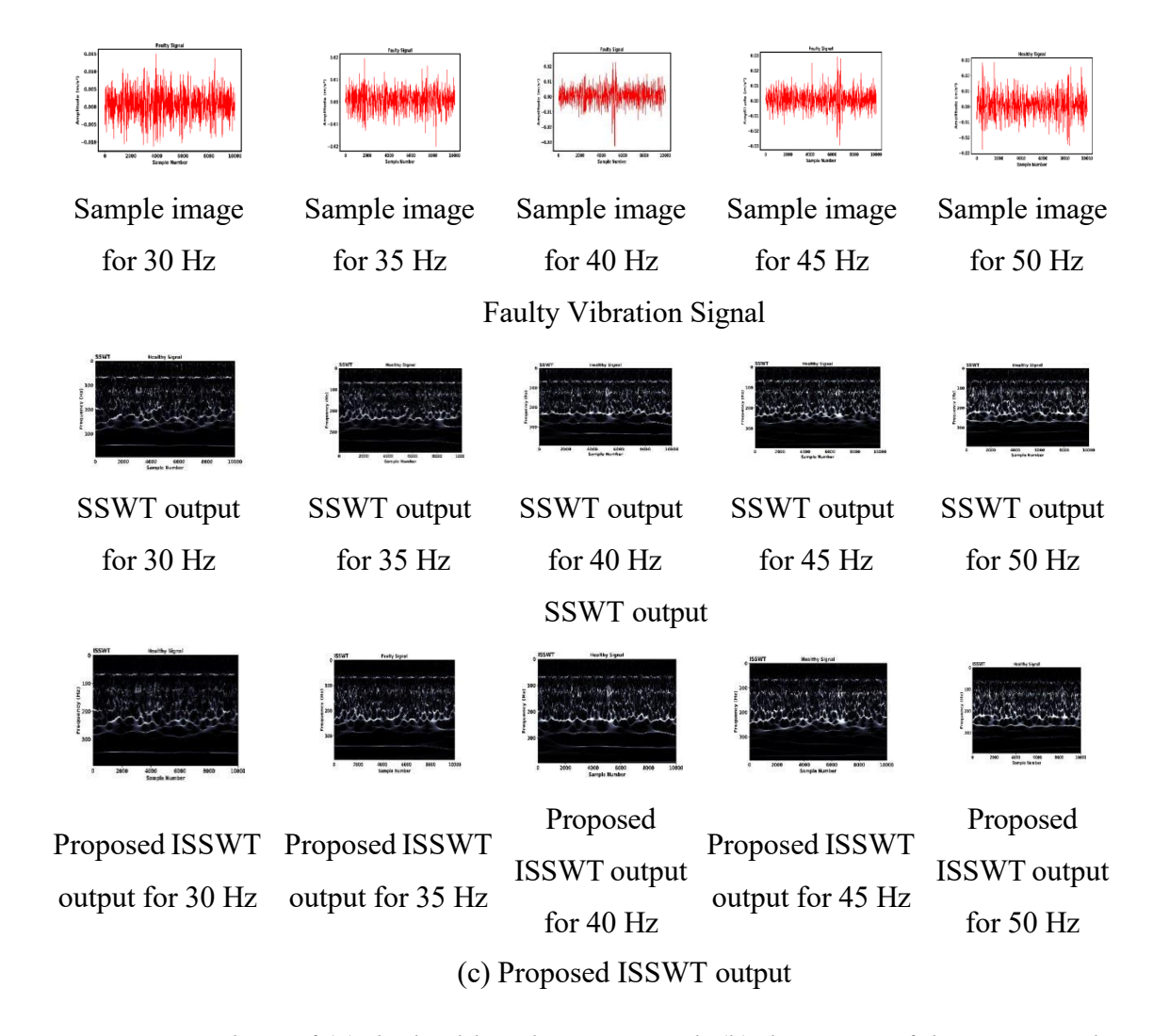
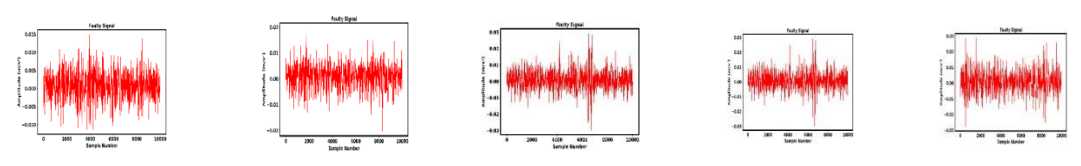


Figure 4. 4: Analysis of (a) the healthy vibrating signal, (b) the output of the SSWT, and (c) the output of the proposed technique for dataset 2.

As a result, ISSWT improves fault diagnosis reliability and facilitates understanding of the signal properties in Figure 4.5. When noise is eliminated from the denoised signal, key properties are retained, improving the time-frequency decomposition's accuracy. The proposed fault detection model's accuracy and dependability are generally significantly increased by pre-processing with ISSWT, which successfully eliminates noise and raises the bar for time-frequency analysis.



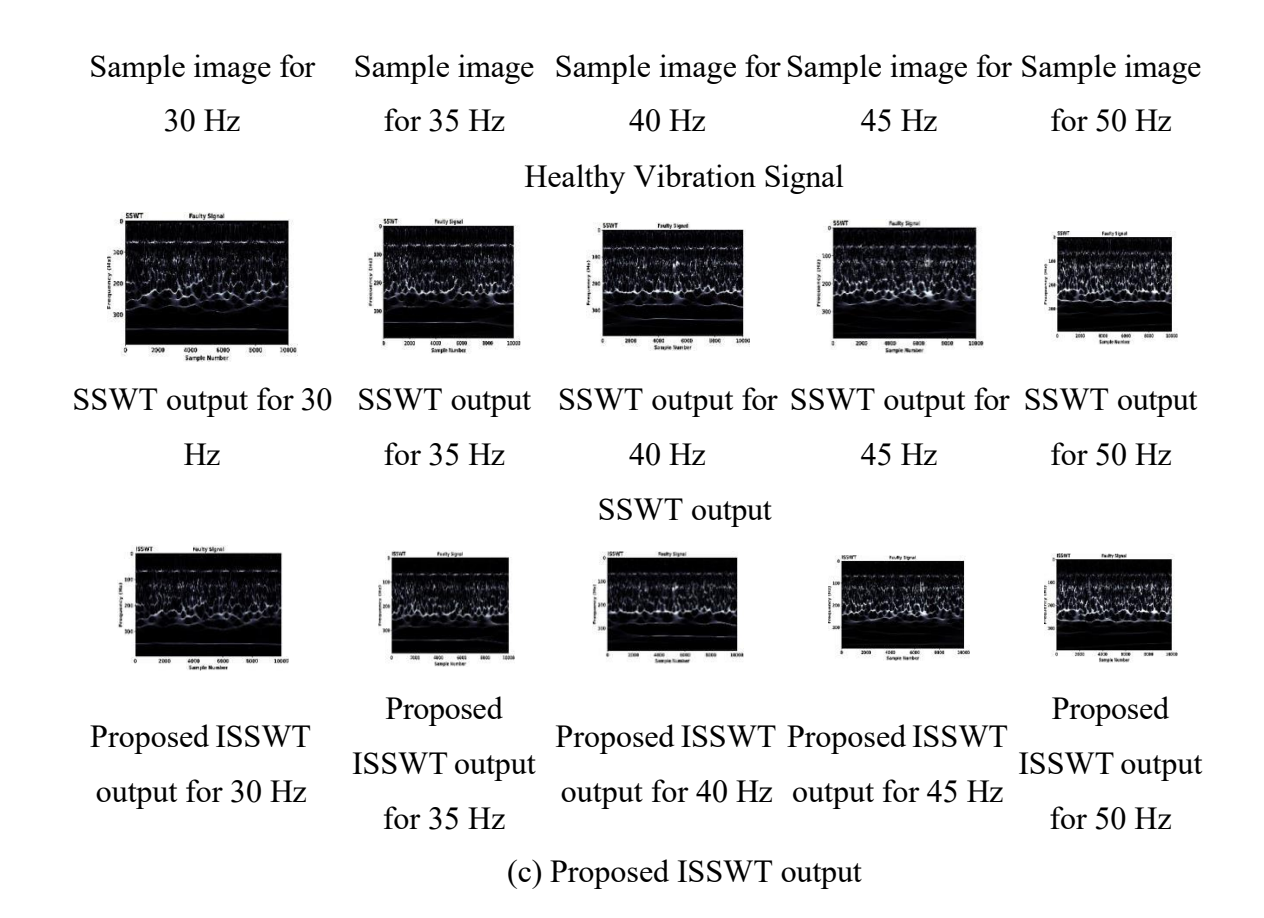


Figure 4. 5: Analysis of the following signals: (a) faulty vibrating signal, (b) SSWT result, and (c) output from the proposed technique for dataset 2.

Table 4. 1 (a): Quantitative Analysis of signals for dataset 1

Frequency	Method	Healthy Signal SNR (dB)	Healthy Signal MSE	Faulty Signal SNR (dB)	Faulty Signal MSE
10 Hz	CWT	18.9	0.018	18.5	0.019
10 Hz	SSWT	20.2	0.015	19.9	0.016
10 Hz	ISSWT	23.1	0.009	22.8	0.01
20 Hz	CWT	19.7	0.016	19.2	0.017
20 Hz	SSWT	21.5	0.013	21.1	0.014
20 Hz	ISSWT	24.2	0.008	23.9	0.009
30 Hz	CWT	20.4	0.014	20	0.015
30 Hz	SSWT	22.5	0.011	22.2	0.012
30 Hz	ISSWT	25.3	0.007	25	0.007

Table 4. 1 (b): Quantitative Analysis of signals for dataset 2

Frequency	Method	Healthy Signal SNR (dB)	Healthy Signal MSE	Faulty Signal SNR (dB)	Faulty Signal MSE
30 Hz	CWT	20.5	0.016	21	0.017
30 Hz	SSWT	22.3	0.012	22.6	0.012
30 Hz	ISSWT	25.1	0.007	25.4	0.007
35 Hz	CWT	21	0.014	21.6	0.014
35 Hz	SSWT	23.1	0.01	23.4	0.01
35 Hz	ISSWT	26	0.006	26.2	0.006
40 Hz	CWT	21.9	0.012	22.5	0.012
40 Hz	SSWT	23.9	0.009	24.3	0.009
40 Hz	ISSWT	26.8	0.005	27.1	0.005
45 Hz	CWT	22.5	0.01	23	0.01
45 Hz	SSWT	24.6	0.008	25	0.008
45 Hz	ISSWT	27.5	0.005	27.8	0.005
50 Hz	CWT	23.1	0.009	23.6	0.009
50 Hz	SSWT	25.2	0.007	25.6	0.007
50 Hz	ISSWT	28	0.004	28.3	0.004

The superiority of the proposed ISSWT method over SSWT has been quantitatively validated using SNR and MSE, as shown in Table 4.1 (a) and Table 4.1 (b). ISSWT consistently achieves higher SNR and lower MSE, confirming its improved de-noising performance. Additionally, a comparative analysis with standard CWT is performed, which showed lower SNR and higher MSE than ISSWT, due to poorer time-frequency resolution.

4.2.2. Feature Extraction

Features such as improved wavelet energy entropy, norm entropy, SE, and threshold entropy are extracted throughout this method. Every feature provides distinct insights into the signal's underlying dynamics, such as frequency distribution, complexity, and randomness.

4.2.3. Norm Entropy

From a signal-processed p_x norm entropy [176] is extracted by calculating the probability range of the signal and measuring the degree of Uncertainty or randomness in the distribution as measured by a statistical metric developed in Equation (4.6).

$$fe^{N_{ent}} = N_{ent} = \left| p_{x_i} \right|^{\gamma} \tag{4.6}$$

where γ denotes the threshold that is calculated using $\mu[y]$, where $\mu-mean$, and

 p_{x_i} is the coefficient of the processed signal p_x . The pre-processed signal p_x can be used to detect faults by extracting norm entropy, which provides essential details about its underlying properties. As a result, fe^{Nent} is the extracted norm entropy.

4.2.4 Improved Spectral Entropy

SE is a statistic that is used to measure how complicated or unpredictable a signal's frequency content is. Demonstrating how consistent energy is distributed throughout multiple frequency bins sheds light on the spatial distribution of frequency elements inside the signal. It is computed mathematically using Equation (4.7), and R_z represents the relative energy in the z^{th} frequency bin.

$$S_{ent} = \sum_{z} R_{z} \log \left(\frac{1}{R_{z}}\right) \tag{4.7}$$

The conventional SE extraction method has limitations that can affect fault detection accuracy and reliability of entropy estimation. These limitations include susceptibility to aliasing artifacts, spectral leakage, reduced spectral resolution due to noisy or irregular entropy estimates without frequency-domain smoothing, and improper windowing and zero-padding techniques. For fault identification, the method of extracting enhanced SE from the processed signal p_x is essential. It uses a methodical approach to improve entropy estimation's precision and dependability. The following steps are part of this process.

Steps in the Process of Extracting Improved Spectral Entropy:

Windowing: This entails giving the pre-processed signal p_x a window function. This stage minimizes artifacts caused by the abrupt termination of the signal by decreasing the signal closer to zero at its edges, hence reducing spectral leakage. Windowing lowers sidelobe values in the resultant spectrum and improves frequency resolution. Equation (4.8) formulates the window function W(t) as an application to the already processed signal $p_x(t)$.

$$p_x^W(t) = p_x(t) * W(t)$$
 (4.8)

Zero-padding: By adding zeros to a window, a technique known as zero-padding raises the spectrum's frequency resolution without introducing new data. Particularly for short-duration signals, it aids in the interpolation of the frequency plane representation, producing a smoother spectrum. The mathematical expression for the windowed signal's zero-padding phase is given by Equation (4.9).

$$p_{x}^{W}(t); 0 \le t \le k$$

$$p_{x}^{ZP}(t) = \begin{cases} 0; k \le t < k_{total} \end{cases}$$
(4.9)

Here, k denoted the signal windowed length and $k_{total} > k$ represents the after zero-padding length.

Computation of DFT: By converting the signal from the time domain into the frequency domain, the Cooley-Tukey Radix-2 FFT method (C-TR2FFT) effectively calculates the DFT, reducing complex computation and facilitating faster dataset processing. Prior to reaching the base case, the C-TR2FFT method repeatedly splits the input sequence of length Q into smaller subsequences. The technique works with complex-valued sequence input, where the k^{th} frequency-domain sample of the input sequence is denoted by $p_x(k)$. The primary equations controlling the computation of $p_x(k)$ and $p_x\left(k+\frac{Q}{2}\right)$ for a Radix-2 FFT, which divides the series input into smaller problems of size 2, are as follows at each level of recursion:

1. Butterfly Operation:

The Radix-2 FFT technique uses butterfly operations, which include intricate multiplications and adds, to calculate FFT values for each stage after splitting the inputs into odd and even-indexed sub-sequences.

2. Twiddle Factor:

Each butterfly operation uses the twiddle factor $e^{-\frac{2\pi j}{Q}.k}$ to give the odd and even indexed subsequences' components a weight. Where k is the current FFT output sample's index, and Q is the input sequence's length. The C-TR2FFT algorithm's $p_x(k)$ and $p_x\left(k+\frac{Q}{2}\right)$ computation equations are written as follows in light of these factors:

$$p_x(k) = Ev_k + e^{-\frac{2\pi j}{Q}k}.Od_k$$
 (4.10)

$$p_{x}\left(k+\frac{Q}{2}\right) = Ev_{k} - e^{-\frac{2\pi j}{Q}.k}.0d_{k}$$

$$\tag{4.11}$$

In Equation (4.10) and Equation (4.11), the terms Ev_k and Od_k show the FFT results for the zero-padded $p_x^{ZP}(t)$ signal's even and odd-indexed subsequences, respectively. $e^{-\frac{2\pi j}{Q}\cdot k}$ indicates that the index k twiddle factor is an integer that spans from $k=0,1,\ldots,\frac{Q}{2}-1$.

$$Ev_k = \sum_{q=0}^{\frac{Q}{2}-1} p_x^{ZP}(2q) e^{-\frac{2\pi j}{Q}k}$$
(4.12)

$$Od_k = \sum_{q=0}^{\frac{Q}{2}-1} p_x^{ZP} (2q+1) e^{-\frac{2\pi j}{Q} \cdot k}$$
(4.13)

These formulas show how the findings from the preceding step and the proper twiddle factors are utilized to determine the FFT ranges for neighboring frequency bins. This procedure is repeated until each frequency bin's FFT values are determined.

Magnitude Spectrum: The DFT's complex Fourier coefficients are used to compute the magnitude spectrum, which gives details on the energy or amplitude of the different elements of the frequency of the signal and permits additional examination of its frequency content.

$$p_{x}^{M}(k) = |p_{x}^{DFT}(k)|$$
 (4.14)

Frequency Smoothing: To increase the SE estimate's accuracy, frequency smoothing reduces the effect of artifacts or high-frequency noise by lowering amplitude spectrum noise and fluctuations.

$$p_{x}^{S}(k) = \frac{1}{L} \sum_{r=k-\frac{L}{2}}^{k+\frac{L}{2}} p_{x_{i}}^{M}(k)$$
(4.15)

The frequency smoothing applied to the resulting magnitude spectrum is shown in the equation above, in which L is the window smoothing.

Normalization: It is intended to guarantee that the spectrum magnitude scale is constant, usually falling between 0 and 1. This stage makes it easier to compare signals and guarantees that the SE computation remains constant despite variations in the signal's total energy level.

$$p_{\chi}^{N}(k) = \frac{p_{\chi}^{S}(k)}{\sum_{k=0}^{Q-1} p_{\chi}^{S}(k)}$$
(4.16)

Computation of Improved SE: Finally, using the normalized magnitude spectrum, improved SE IS_{ent} is calculated. In this step, the spectral information entropy of the signal is measured, which quantifies the frequency content's complexity or randomness. For fault detection, the calculated enhanced SE is a useful characteristic.

$$fe^{IS_{ent}} = IS_{ent} = -\sum_{k=0}^{Q-1} p_x^{N}(k) \log_2 p_x^{N}(k)$$
 (4.17)

Improved SE extraction enhancements significantly improve the feature's quality and

resilience, which enhances the extract SE $fe^{IS_{ent}}$ is defined as the performance of the suggested fault recognition model.

4.2.5 Threshold Entropy

In order to get insight into signal fluctuations and anomalies, entropy [176] assesses the signal value distribution that surpasses a particular threshold level. Equation (4.18) formulates the threshold entropy expression, where γ is the threshold, which is calculated using $\mu[y]$, where $\mu - mean$, and p_{x_i} is the covariance of the previously processed signal p_x .

$$fe^{Th_{ent}} = Th_{ent} = \begin{cases} 1; if |p_{x_i}| > \gamma \\ 0; elsewhere \end{cases}$$
(4.18)

As a result, the extracted threshold entropy is given as $fe^{Th_{ent}}$.

4.2.6 Wavelet Energy Entropy

For fault identification, wavelet energy entropy [177] must be extracted from the preprocessed signal. This process involves decomposing the signal into multiple frequency components using wavelet transform and computing the energy distribution across each frequency band. The resulting energy distribution provides valuable insights into the signal's energy variations across different frequency ranges. This distribution is used to compute wavelet energy entropy, which quantifies the complexity or randomness of the signal. The pre-processed signal's wavelet energy entropy estimation p_x is displayed in the equation below.

$$fe^{WE_{ent}} = WE_{ent} = -\sum_{z}^{\Sigma_{z}} R_{z} log \tag{4.19}$$

where, R_z represent the average wavelet energy, which is calculated using $R_z = \frac{E_z}{E}$. The total of the wavelet component energies E is determined as $E = \sum_z E_z$ wherein the wavelet coefficient's energy is associated with z^{th} decomposition level, $E_z = d_z^2$. The d_z represent the coefficient of wavelet related to z^{th} the level of breakdown. The wavelet energy entropy that was extracted is given as $fe^{WE_{ent}}$. The MLiDNet-based fault identification model can diagnose faults in EM systems more reliably and efficiently thanks to effective feature extraction.

4.3 Feature Selection using Chi-Square Test

The CS test [178] is used in this study to identify features for the MLiDNet fault identification model. By assessing each feature's statistical importance with respect to the

fault situation, the CS statistics are calculated to determine whether the distribution of each feature is unaffected by the desired variable or if there is a meaningful correlation. Through the observed frequency for each feature category denoted as ob_q and the frequency expected for each feature category under a condition of independence with the target variable denoted as ex_q , Equation (4.20) formulates the CS computation of statistical value. High CS and low p-value features are used to identify fault models because they are thought to be more discriminative.

$$\chi^2 = \frac{\sum (ob_q - ex_q)^2}{ex_q} \tag{4.20}$$

Consequently, the characteristics chosen for each signal by the CS test are represented by ' fs_x '.

4.4 Fault Detection via Modified LinkNet and DenseNet Network Model

Figure 4.6 shows the MLiDNet model that was suggested in this investigation. This hybrid model incorporates DL architecture to improve categorization, particularly D-Net and Modified LinkNet (ML-Net). Specifically, the MLiDNet framework relies heavily on the modified L-Net model.

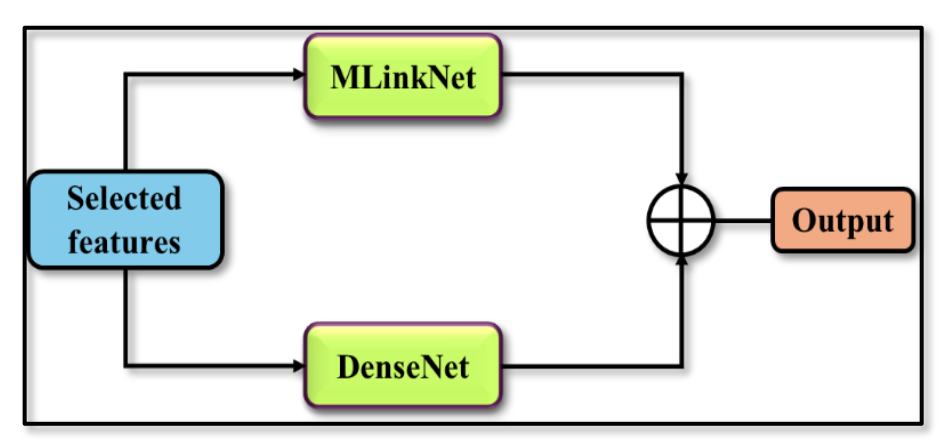


Figure 4. 6: Model fusion between ML-Net and D-Net.

An advancement over the traditional L-Net, ML-Net adds the CBNSKR layer. The hybridization of the proposed system provides a number of benefits. ML-Net enhances feature extraction's generalization and robustness by managing data skewness and kurtosis. D-Net provides Additional data analysis, which simultaneously uses densely connected layers to record complex feature representations. This collaboration makes use of both models' advantages, with D-Net extracting fine-grained features and ML-Net handling issues with data distribution. The hybrid technique improves efficiency and precision in fault detection of EM systems by offering a thorough knowledge of the data. Furthermore, the proposed model's capacity to recognize fault circumstances is further im- proved by using CS test results for feature selection, guaranteeing precise and trustworthy fault detection. In industrial contexts, this combination strategy improves maintenance procedures and operating efficiency.

4.4.1 Structure of Modified Link-Net Model

Each pixel in an image is classified into predetermined classes using the CNN model for semantic segmentation known as L-Net [179,180]. It has a skip-connected encoder-decoder structure that maintains spatial details when up-sampling. As a component of the MLiDNet-based fault identification model, this work presents a modified version, ML-Net. A CBNSKR layer, which is not present in traditional L-Net, is incorporated into ML-Net to manage kurtosis and skewness in the asymmetry and non-uniformity measurements of statistical input data. These distributional characteristics must be addressed for performance, particularly in complicated datasets. In the MLiDNet structure, the outcome of the CS feature selection process is sent into the ML-Net model for EM system failure detection. This input is essential for differentiating between faulty and healthy circum- stances since it contains selected features (fs_x). The CBNSKR layer efficiently manages kurtosis and skewness, while ML-Net enables it to extract intricate patterns and delicate traits from the input. This all-encompassing method improves the model's accuracy and resilience in detecting faults, which increases industry maintenance and operational efficacy.

To effectively manage input data and extract significant features, the proposed model's architecture is organized with a number of layers placed in a particular order (Figure 4.7). An outline of the layers and their features is provided below:

• Initial Block: Using initial processing techniques like inversion and

functions activated to extract fundamental features, this block acts as a starting point for the input or selected characters (fs_x) .

- Encoder Blocks (1 to 4): The ML-Net model uses convolutional layers to extract information from each encoder block. After training has been stabilized by Batch Normalization (BN), the model is given non-linearity using Rectified Linear Unit (ReLU) function activation, which enables it to discover complex correlations in the data. By reducing the size of feature maps, max pooling preserves crucial information while lowering spatial dimensions.
- **CBNSKR Layer:** This unique feature ensures stable and efficient model training by mitigating the impacts of skewness and kurtosis in the distribution of input using tailored BN approaches. Equation (4.21) provides a mathematical expression for the process that is carried out in the CBNSKR layer, while Equations (4.22) and (4.23), respectively, display the expressions of the traditional BN.

$$CBNSKR = \phi * \left[\frac{\varphi_P(fs_\chi) - \mu}{\rho * \sigma * K(fs_\chi)} \right] + \chi \tag{4.21}$$

In Equation (4.21), $\varphi_P(fs_x)$ represent skewness reduction, and it is represented as $\varphi_P(fs_x)$ $\begin{cases} fs_x^P, iffs_x \geq 0 \\ -(-fs_x)^P, iffs_x < 0 \end{cases}$ where P > 1. $K(fs_x)$ represent the kurtosis reduction, and it is denoted as $K(fs_x) = \frac{\sum_{a=1}^U [fs_{x_a} - f\widehat{s}_x]^4}{\sigma^4.U}$. The reduction of skewness factor ρ represented as $\rho = 3$. $\left[\frac{\widehat{fs}_x - median}{\sigma}\right]$. The input data (selected attributes) mean is \widehat{fs}_x , U represents the number of input-selected features, σ represent the standard deviation, ϕ represent the rescaling factor, and χ represent the recentering factor.

$$BN = \phi * \widehat{fs_{\chi}} + \chi \tag{4.22}$$

$$BN = \phi * \left[\frac{f s_x - \mu}{\sigma} \right] + \chi \tag{4.23}$$

Decoder Blocks (4 to 1): Convolutional layers precede BN and ReLU activation processes in each decoder block, which operate identically to the encoder blocks. To create segmentation maps, these elements cooperate

to enhance the feature maps and recreate the features. Additionally, the

feature patterns are further enhanced by the usage of max pooling.

- Layer CBNSKR (following Decoder Blocks): This layer improves the normalization of feature activation, like the CBNSKR layer that comes before the decoder blocks, which leads to improved data generalization and more efficient learning.
 - **Final Block:** The final result of fault detection is produced after further processing and refinement in this block.

The ML-Net model's CBNSKR layers improve BN to manage kurtosis and skewness in the input data, which stands for imbalances and erroneous model training due to deviations from the normal distribution. Through the reduction of these anomalies, the tailored BN approaches enhance the model's stability, resilience, and rate of convergence, resulting in improved fault detection performance and accuracy. By combining feature selection outcomes with ML-Net's sophisticated capabilities, the MLiDNet framework makes it possible to accurately and consistently detect faults in EM systems. In industrial contexts, this greatly improves maintenance procedures and operating efficiency. The ML-Net model's output for identifying EM system faults is defined as $d^{MLinkNet}$. The RELU activation function is employed in ML-Net along with the 'rmsprop' optimizer, 80 epochs, a learning rate of 0.001, and categorical cross-entropy.

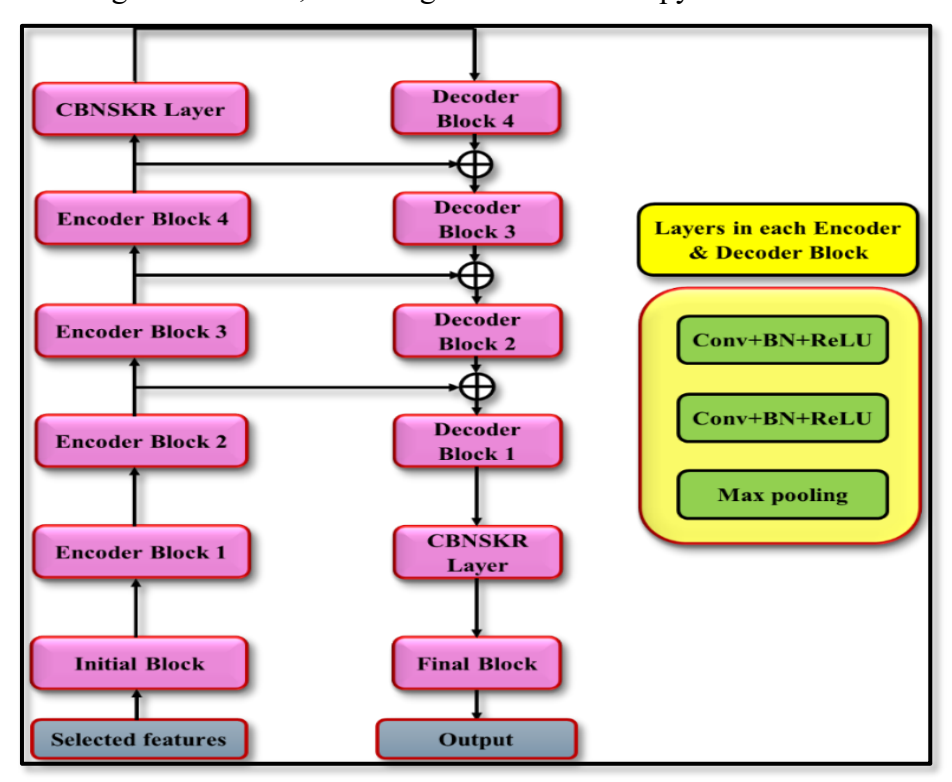


Figure 4. 7: A structural perspective of the ML-Net model.

4.4.2 Structure of Dense-Net Model

One DL architecture that is well-known for its efficient feature propagation and costeffective parameter usage is D-Net. D-Net is incorporated into the Milden architecture in this study to detect faults in EM systems. The D-Net model uses dense connections and feature reuse to improve fault detection. During the feature selection phase, the D-Net model uses the most valuable features to identify problems based on the CS test results (fs_x) . Figure 4.8 depicts the structural structure of the D-Net architecture, which is made up of several basic layers, as described below.

- Convolutional Layers: Convolution operations are used on the input data to extract features. A dense connection within the network is made possible by the output of each layer being transmitted to later layers.
- **Dense Blocks:** In order to promote feed-forward connections between layers and improve feature reuse and gradient flow, D-Net introduces dense connections within convolutional layers.
- Transition Layers: Transition layers, which usually include BN, traditional layers, and pooling algorithms like max pooling or average, are used to down-sample feature maps from dense blocks in an effort to lower the computational complexity and spatial dimension.
- Global Average Pooling Layer: This layer at the network's end calculates an average score for each feature map to aggregate spatial information. As a result, the entire input image is summarized in a fixed-length feature vector.
- Layer Fully Connected: In order to map the characters extracted to the required number of output classes for classification tasks, an entirely interconnected layer may be included in the network. Class probabilities are usually generated using SoftMax activation.

The D-Net component of the MLiDNet-based IM fault identification model uses its dense connection and effective feature propagation to process specific characteristics in order to identify faults inside IMs, resulting in reliable and accurate fault identification. With the output designated as $d^{DenseNet}$, this improves maintenance and operating

efficiency in industrial environments. By combining ML-Net with D-Net, the MLiDNet model makes use of D-Net's in-depth feature extraction and ML-Net's ability to handle distributional problems, leading to a more reliable and efficient fault identification solution for EM systems. The categorical crossover entropy is 0.001, and the activation function is taken into account. RELU with the "Adam" optimizer is used in D-Net.

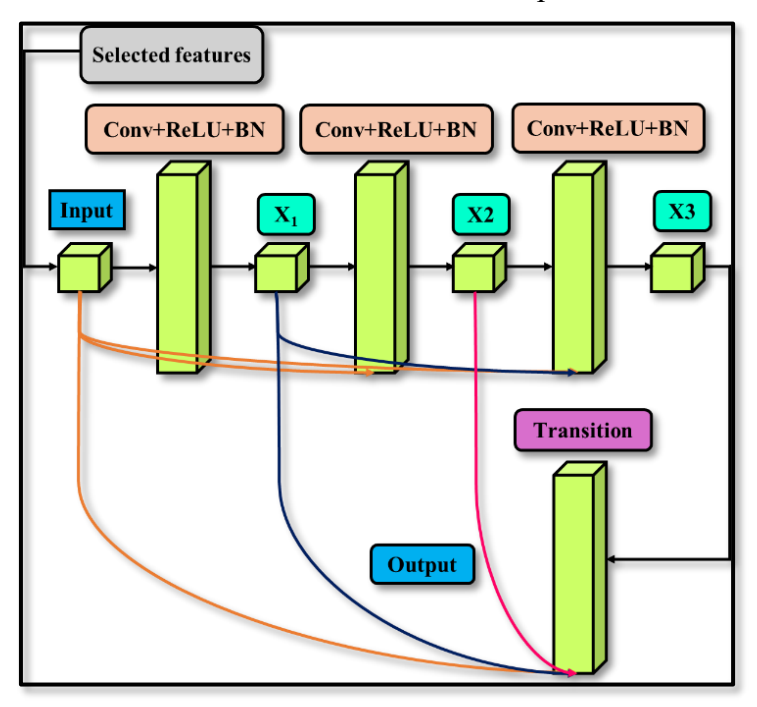


Figure 4. 8: D-Net method structure.

In the MLiDNet approach, the average of the outputs from the D-Net and ML-Net is defined as d_x , and the final product can be categorized into six types of labels:

- 0 Healthy motor coupled with healthy rotor (HL-1)
- 1 Healthy motor coupled with unbalanced rotor (FL-2)
- 2 Unbalanced fault in motor coupled with healthy rotor (FL-3)
- 3 Unbalanced fault in motor coupled with unbalanced rotor (FL-4)
- 4 Bearing fault in motor coupled with healthy rotor (FL-5)
- 5 Bearing fault in motor coupled with unbalanced rotor (FL-6)

The numbers 0, 1, 2, 3, 4, and 5 represent the equivalent outputs for these labels, respectively.

4.5 Data Acquisition and Experimental Specifics for Datasets 1 and 2

Datasets 1 and 2 are the two datasets taken into consideration in this research. Dataset 2 makes use of the benchmark dataset, while Dataset 1 is experimentally captured.

4.6 Description of Dataset 1

An MFS was used to conduct an experiment, depicted in Figure 4.9. An external rotor is connected to a 0.5 horsepower, 50 Hz, three-phase IM via a flexible coupling to form the MFS. A centrally located disc in the rotor is intended to produce imbalance. The mass of the disc positioned in the middle is 0.68 kg. Two external bearings support the ends of this rotor. On the other end, a belt drive links the rotor to a pulley, which is then attached to a gearbox. A magnetic brake clutch is also included with this gearbox. As seen in Figure 4.10, a clutch for magnetic brakes is fastened to the gearbox in order to provide the IM with an external load. A speed controller or VFD is also connected to the IM to change the speed. A tri-axial accelerometer is employed to collect vibration signals in three orthogonal directions. Figure 4.11 displays the accelerometers utilized in this study. The tachometer, which measures the motor speed, was powered by a constant DC supply. In order to assess these compounded faults, vibration signals are recorded in this inquiry. A direct adhesive mounting method attaches a tri-axial accelerometer to the top of the gearbox to record vibration data. The gear vibration signals are recorded by an OROS-OR34 DAQ coupled with this accelerometer. Next, a laptop running the signal analysis software NV Gate is connected to the DAQ. The motor's top and the rotor's left bearing are two separate locations from which vibration data is captured in the triaxial directions. The time-domain unprocessed data was obtained using a sampling rate of 6.4 kHz. Ten seconds of a vibration signal were captured. As well as four loads of 0, 1, 2, and 3 Nm cover a range of motor speeds from 10 Hz to 30 Hz. The combined six categories of faults are taken into account. To create the rotor's unbalance intentionally, a screw is driven into a hole in the disc at a certain angle and radial distance. The rotor disc has 24 slots or holes where an irregular mass can be inserted to cause unbalance. The rotor is shown in a balanced and healthy state in Figures 4.12 and 4.13. An unbalanced rotor fault is illustrated in Figure 4.14, where the motor becomes unbalanced due to the attachment of a weight. An internal view of a motor with an internal bearing fault is depicted in Figure 4.15, where an outer race fault creates an inherent bearing fault in one bearing and an interior race fault in the other.

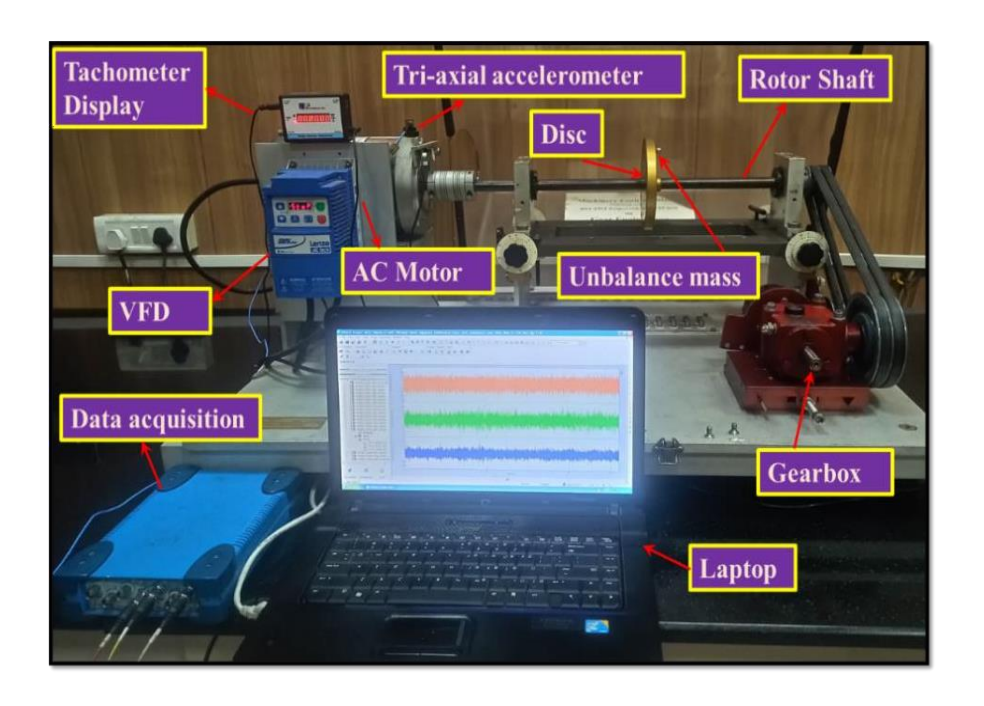


Figure 4. 9: Experimental test rig setup used for rotating machinery fault diagnosis.

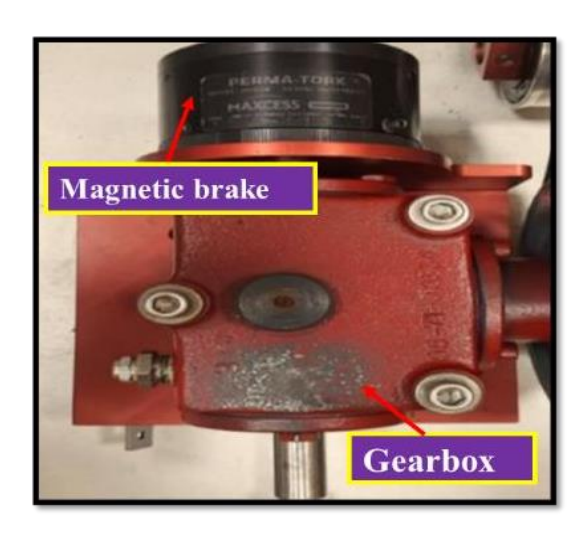


Figure 4. 10: Magnetic Brake with a gearbox and magnetic.

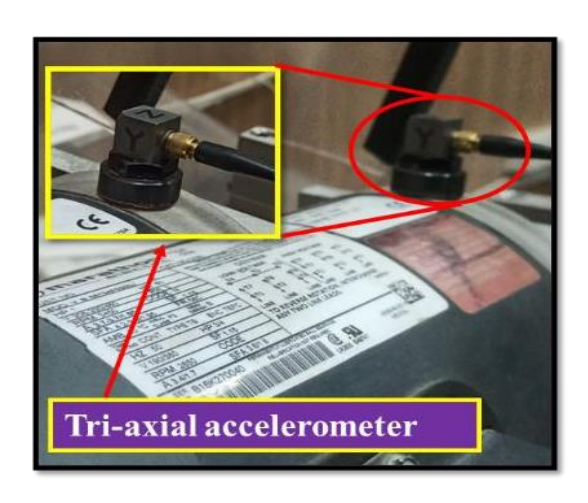


Figure 4. 11: Installed tri-axial accelerometer on IM.

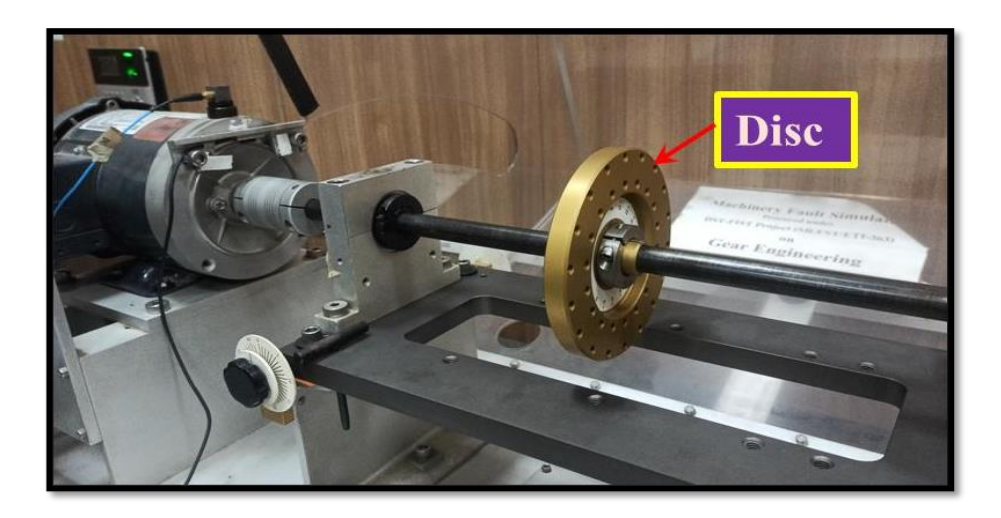


Figure 4. 12: Healthy Rotor.

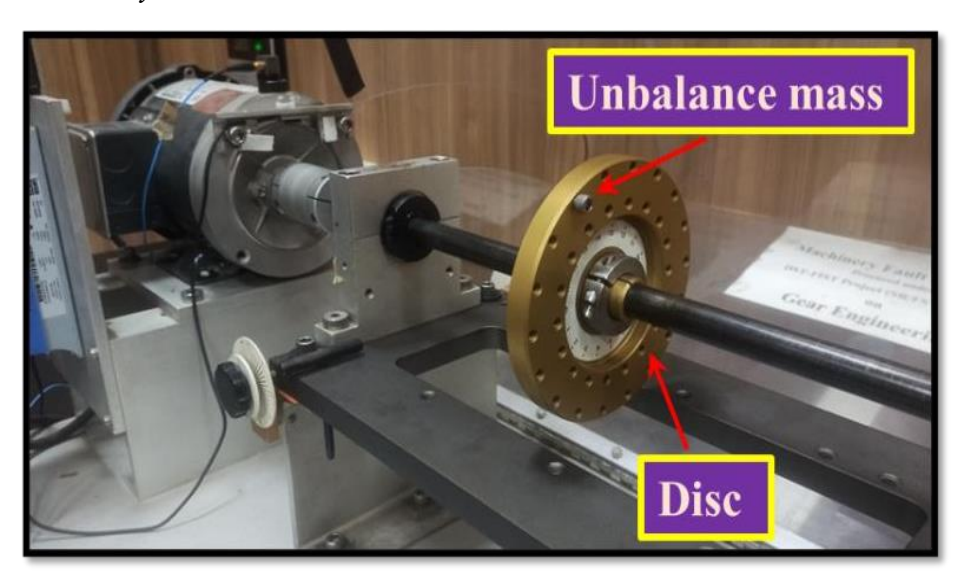


Figure 4. 13: Unbalanced Rotor.

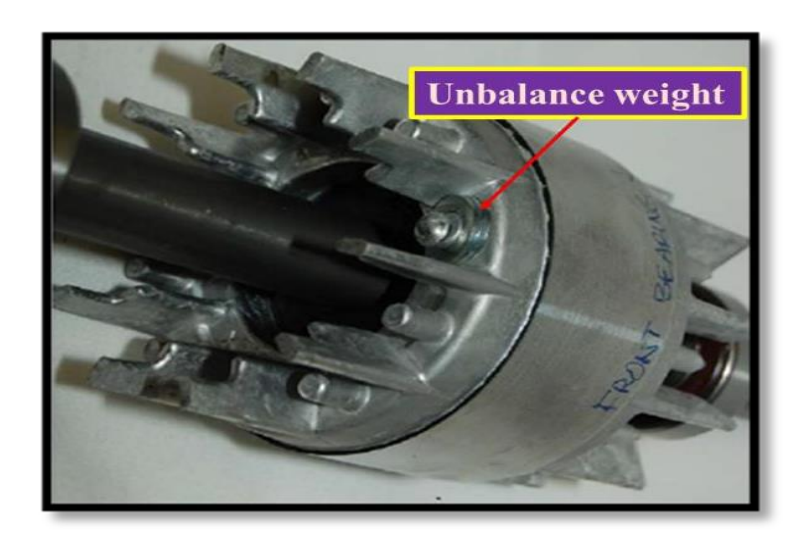


Figure 4. 14: Unbalanced rotor fault in the motor.

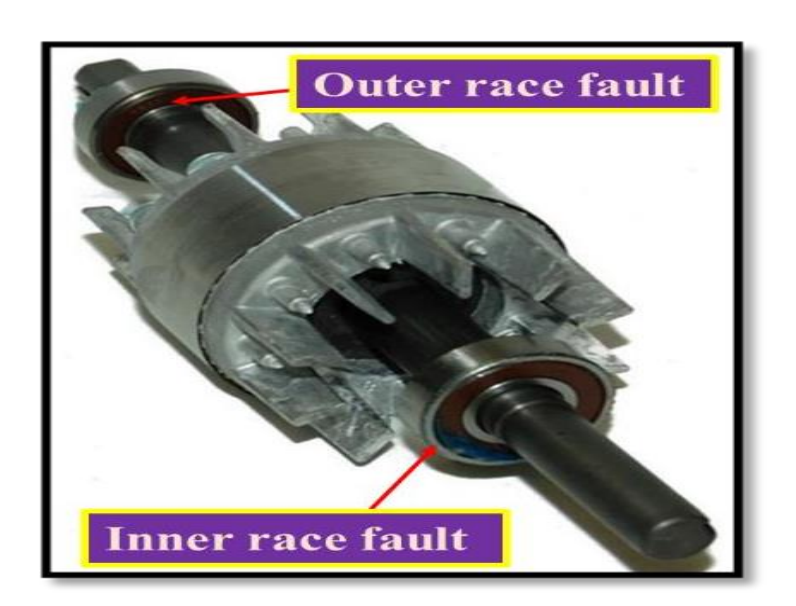


Figure 4. 15: Bearing fault in the motor.

4.7 Description of Dataset 2

This dataset is representative of all commercial gearbox data for dataset 2 [181]. Helical gears undergo testing. Two accelerometer signals acquired by sensors matching and one signal channel make up the dataset. Here, only the second channel is used to test the suggested model. Shaft speeds fall into the following range: 30, 35, 40, 45, and 50 Hz. It is made up of six helical labels (0–5). The good is indicated by the helical label 0, while the chipped gear is shown by the helical label 1. The helical label 2 indicates that the inner fault is bent, the bearing combination is broken, and the gear is broken. The helical label 4 indicates a bearing inner fault, the helical label 5 indicates a bent shaft, and the gear is faulty.

4.8 Results and Discussion

4.8.1 The Simulation Process

Python 3.7 was used to implement the proposed fault identification paradigm for EM systems. The simulation system had an Intel Core (TM) i7-10,700 processor running at 2.90 GHz and with 16.0 GB of installed RAM. Details of the testing and training data for Datasets 1 and 2 are shown in Tables 4.2 and 4.3.

Table 4. 2: Specifics of training and testing are essential for 10 Hz, 20 Hz, and 30 Hz for dataset 1

			10 Hz	
Pre augn	nentation	457	Post augmentation	3157
	60%	70%	80%	90%
Train	1893	2208	2524	2840
Test	1262	947	631	315
			20 Hz	
Pre augmentation		460	Post augmentation	3160
	60%	70%	80%	90%
Train	1895	2211	2527	2843
Test	1263	947	631	315
			30 Hz	
Pre augmentation		460	Post augmentation	3160
	60%	70%	80%	90%
Train	1895	2211	2527	2843
Test	1263	947	631	315

Table 4. 3: Specifics of training and testing are essential for 30 Hz, 35 Hz, 40 Hz, 45 Hz, and 50 Hz for dataset 2

			30	Hz			
Pre augn	nentation	2	4	Po	ost	33	24
				augme	ntation		
	60%	70)%	80)%	90%	
Train	1993	23	25	26	558	29	90
Test	1331	99	97	60	64	332	
			35	Hz			
Pre augn	nentation	2	4	Po	ost	33	24
				augme	ntation		
	60%	70)%	80)%	90	1%
Train	1993	2325	2658	2990	Train	1993	2325
Test	1331	997	664	332	Test	1331	997
			40	Hz			
Pre augn	nentation	24		Post		2224	
		24		augmentation		3324	
	60%	70)%	80)%	90	19%
Train	1993	23	25	26	558	29	90
Train	1331	99	97	60	64	33	32
			45	Hz			
Pre augn	nentation	•	4	Po	ost	33	24
		2	, 4	augme	ntation	33	4
	60%	70)%	80)%	90	1%
Train	1993	2325	2658	2990	Train	1993	2325
Train	1331	997	664	332	Train	1331	997
			50	Hz			
Pre augn	nentation		1	Po	ost	22	24
		24		augmentation		3324	
60%		70)%	80)%	90	1%
Train	1993	2325	2658	2990	Train	1993	2325
Train	1331	997	664	332	Train	1331	997

4.8.2 Evaluation of Performance

A thorough investigation was conducted in order to compare MLiDNet's effectiveness with conventional techniques for fault detection. The evaluation of numerous crucial metrics, such as accuracy, F-measure, and reliability, is part of this thorough inquiry. The assessment also included methods including computational time analysis, matrix of confusion analysis, and ablation investigations. An in-depth analysis of the MLiDNet method's relative performance was also provided by comparing its effectiveness against both conventional classifiers.

4.8.3 Confusion Matrix Evaluation on Proposed Method for Dataset 1

The suggested method's three distinct matrices of confusion are displayed in Figure 4.16 for the 10 Hz, 20 Hz, and 30 Hz operating frequency ranges. The total number of tests for each course is shown in each matrix cell. The classification is divided into six classes. TN, FN, TP, and FP are examined.

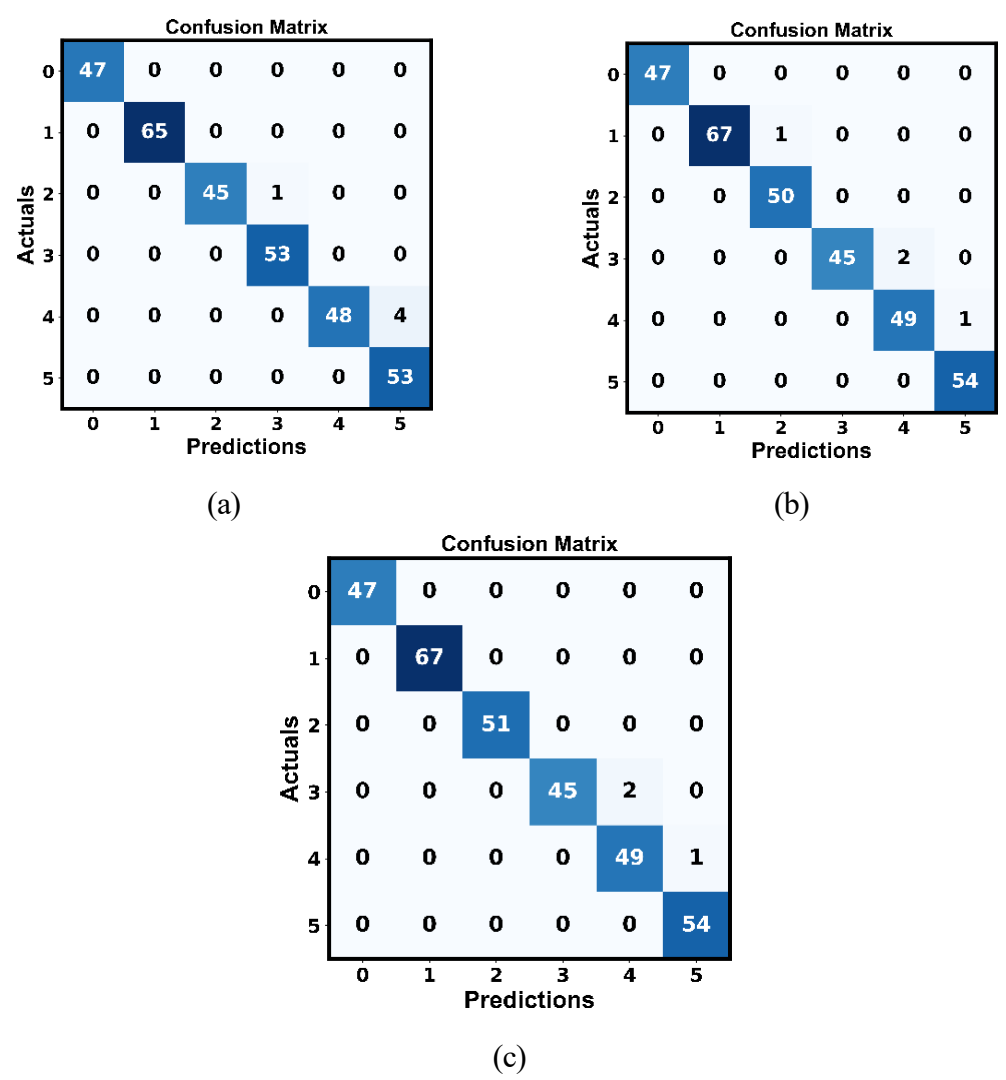


Figure 4. 16: Matrix of Confusion proposed model a) 10, b) 20, and c) 30 Hz for dataset 1.

In particular, Figure 16(a) displays the proposed MLiDNet model confusion matrix that was obtained for fault identification at 10 Hz. In this matrix, each row represents the fault classes, and the fault classes predicted by the proposed model are shown in each column. The values inside the cells indicate the number of entries for the actual and expected classes. At 10 Hz, for example, the first row and first column cell display the number of events correctly recognized as HL-1. The second row and third column cell also show the number of cases that were misclassified as FL-3 at 10 Hz while the actual class was FL-2.

4.8.4 Confusion Matrix Analysis on Proposed Method for Dataset 2

Figure 4.17 shows the MLiDNet method's three confusion matrices for the 30, 35, 40, 45, and 50 Hz operating frequency bands. The matrix's cells each indicate how many tests are required for a given class. The categorization has the following six classes. FN, FP, TP, and TN are the four situations explored.

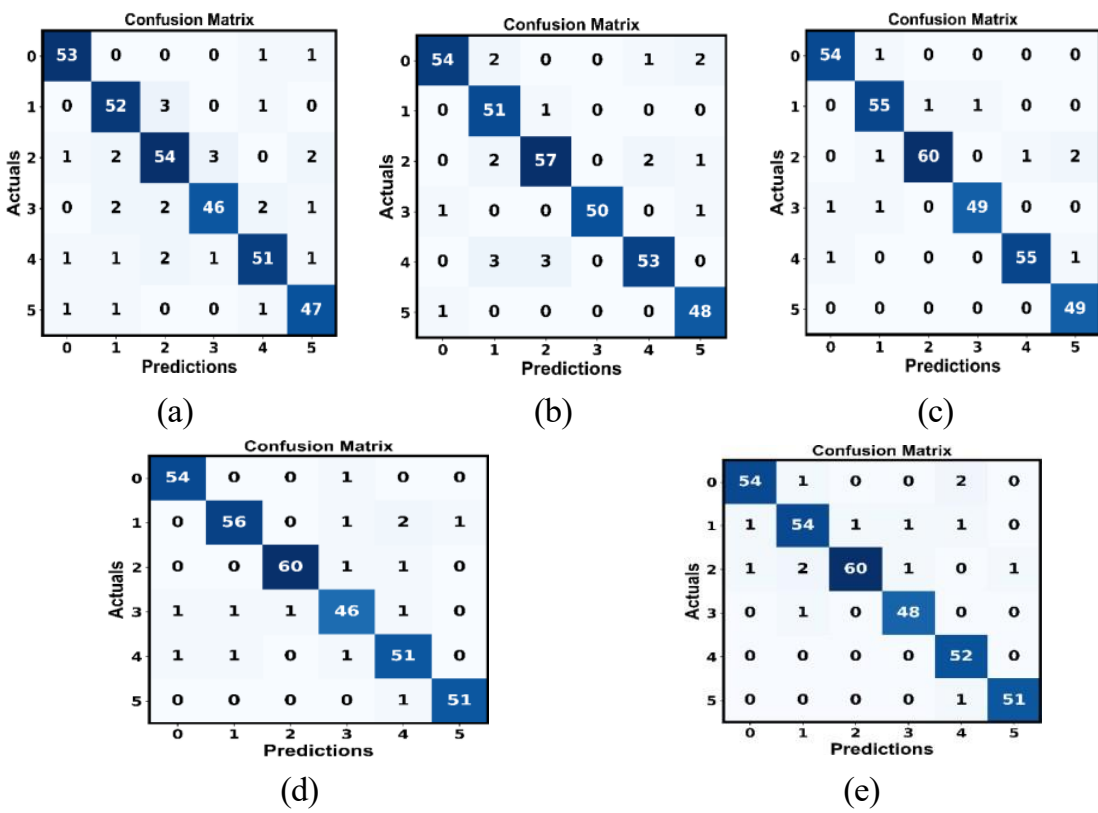


Figure 4. 17: Matrix of Confusion proposed model (a) 30 Hz, (b) 35 Hz, (c) 40 Hz, (d) 45 Hz, and (e) 50 Hz for dataset 2.

In particular, Figure 4.17 (a) displays the confusion matrix that results from using the suggested proposed model for identifying faults at 30 Hz. Each row of this confusion matrix displays the actual fault classes, and each column displays the anticipated classes derived from the suggested model. The number of instances in the cells shows how many instances of each combination of current and anticipated classes are assigned to that com-

bination. For instance, the cell in row 1, column 1 displays the number of cases that were accurately recognized as HL-1 at 10 Hz. Similarly, the cell in row 2, column 3 displays the number of cases incorrectly classified as FL-3 at 30 Hz while the true class was FL-2.

4.8.5 Analysis by Comparison for Dataset 1

In this comparison, the efficacy of the proposed method in fault detection is assessed against six well-known models: CNN [182], DT [183], S-Net, SVM, MSFFCNN, E-Net, Hybrid Wavelet-CNN, and L-Net. Each model's fault identification accuracy is assessed using key performance indicators, such as accuracy, precision, and F-measure, which also minimize FN and FP. The effect of several frequency ranges on model performance was also investigated. The MLiDNet method's comparison with traditional methods offers essential information about each strategy's relative advantages and disadvantages. A detailed comparison of the MLiDNet approach against existing over a range of training data scenarios is provided by the study's results, which are illustrated in Figures 4.18, 4.19, and 4.20.

Furthermore, maximizing accuracy, F-measure, and precision [184] ratings are essential for EM systems to detect faults effectively. At a frequency of 10 Hz, Figure 4.18 illustrates the effectiveness of the suggested and current fault detection techniques. CNN outperforms the conventional models with a precision of 93.45%, an accuracy of 80.44%, and an F-measure of 80.38%. However, with 97.84% precision, 93.59% accuracy, and 93.51% F-measure, MLiDNet surpasses these measures, proving its efficacy in fault diagnosis. The proposed method consistently outperforms existing models, demonstrating their scalability and stability.

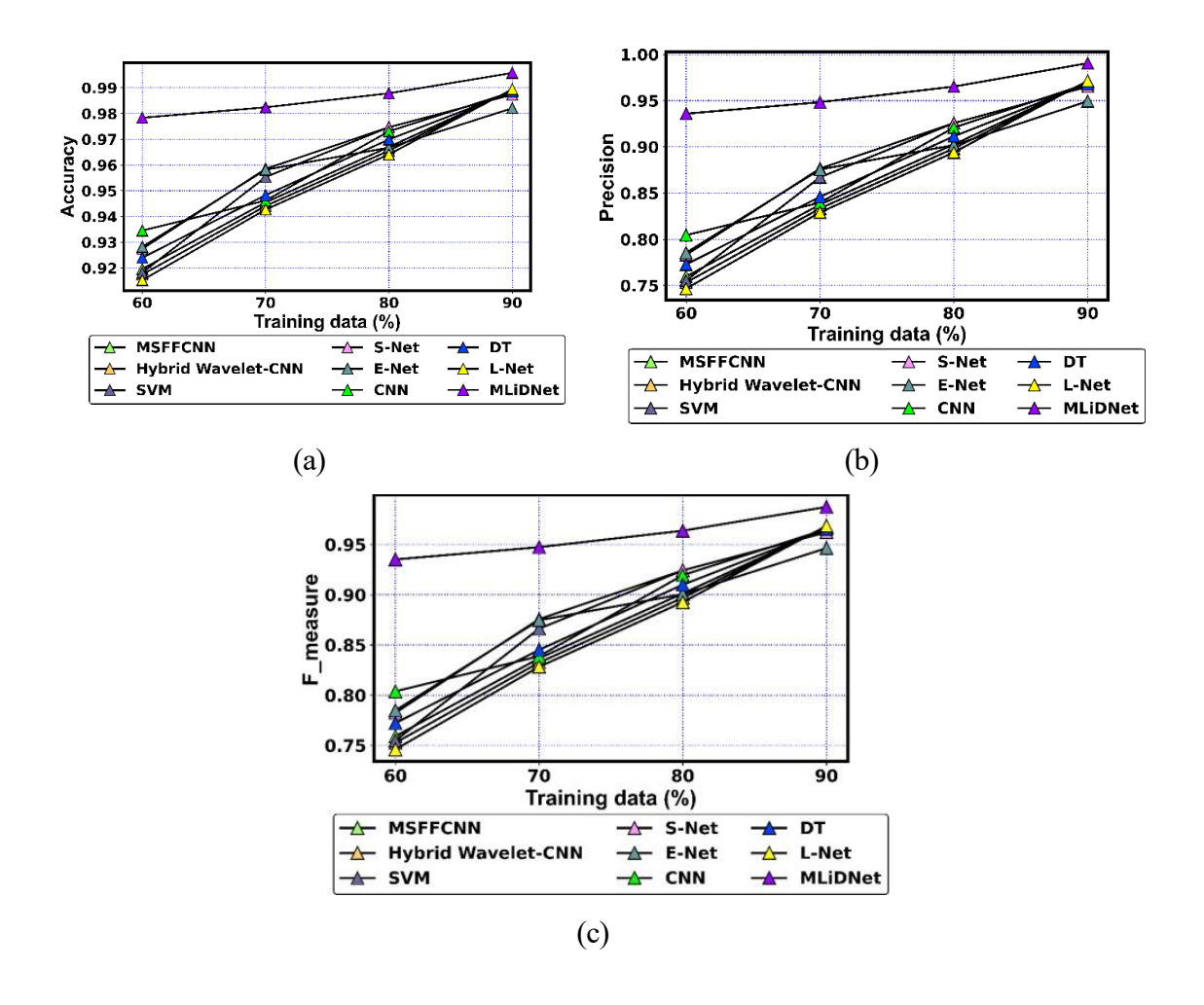


Figure 4. 18: Evaluation of suggested and traditional methods in comparison at 10 Hz for dataset 1.

The comparative evaluation is extended to proposed and existing methods at 20 Hz in Figure 4.19. Compared to traditional models, MLiDNet performs considerably better on training data, with a 60% improvement. At 97.82% precision, 93.72% accuracy, and 93.66% F-measure, MLiDNet significantly outperforms other methods. Even with 70%, MLiDNet performs exceptionally well, achieving 98.32% precision, 95.26% accuracy, and 95.46% F-measure. The suggested approach maintains its clear advantage in terms of accuracy and precision, even while older models produce competitive results. MLiDNet further demonstrates its supremacy at 90%, achieving better results.

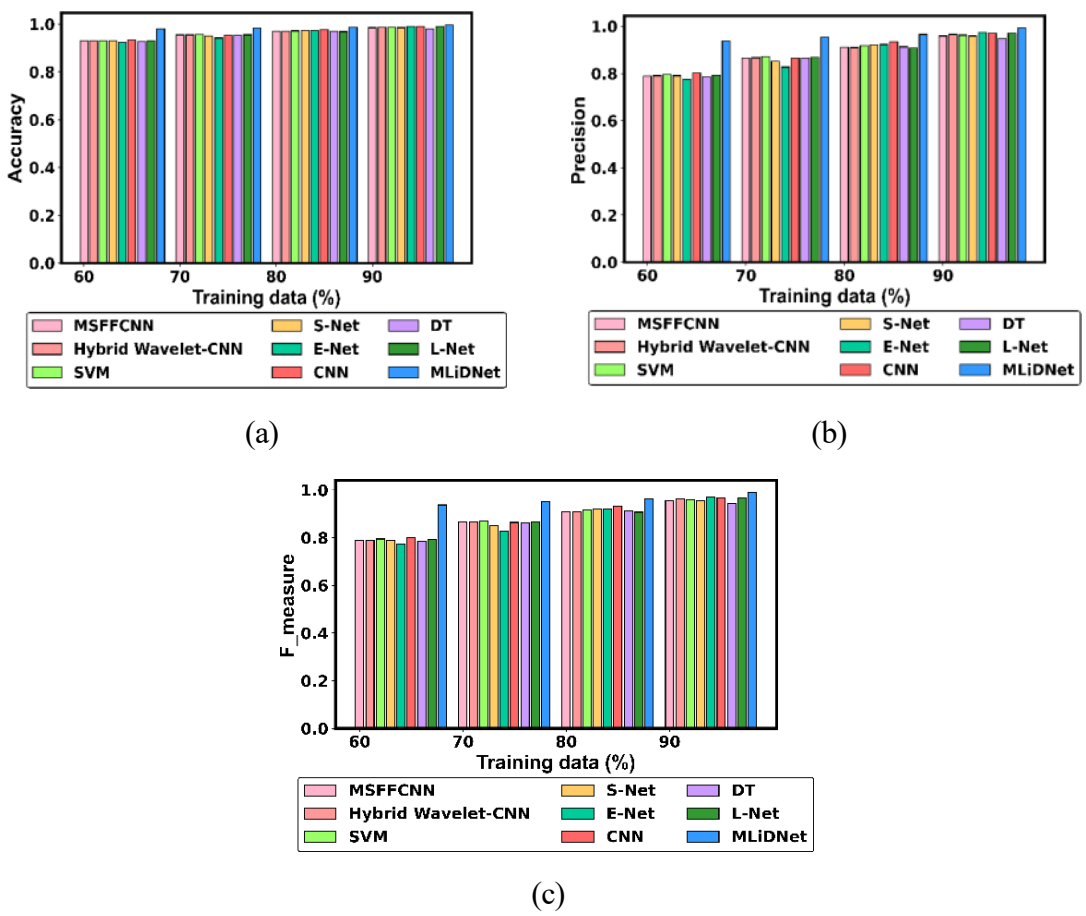


Figure 4. 19Evaluation of suggested and traditional methods in comparison at 20 Hz for dataset 1.

In the performance analysis shown in Figure 4.20, multiple fault detection models were examined at 30 Hz. Using 60.1% training data, the proposed method showed its superiority in accurately identifying combined errors with 97.73% precision, 93.28% accuracy, and 93.20% F-measure. MLiDNet fared better than conventional methods. MLiDNet demonstrated exceptional performance, reaching a peak of 99.79% accuracy and 99.68% precision even with 80% and 90% training data, confirming its effectiveness in fault identification. Based on these findings, the suggested approach outperforms traditional approaches in terms of precision, accuracy, and dependability.

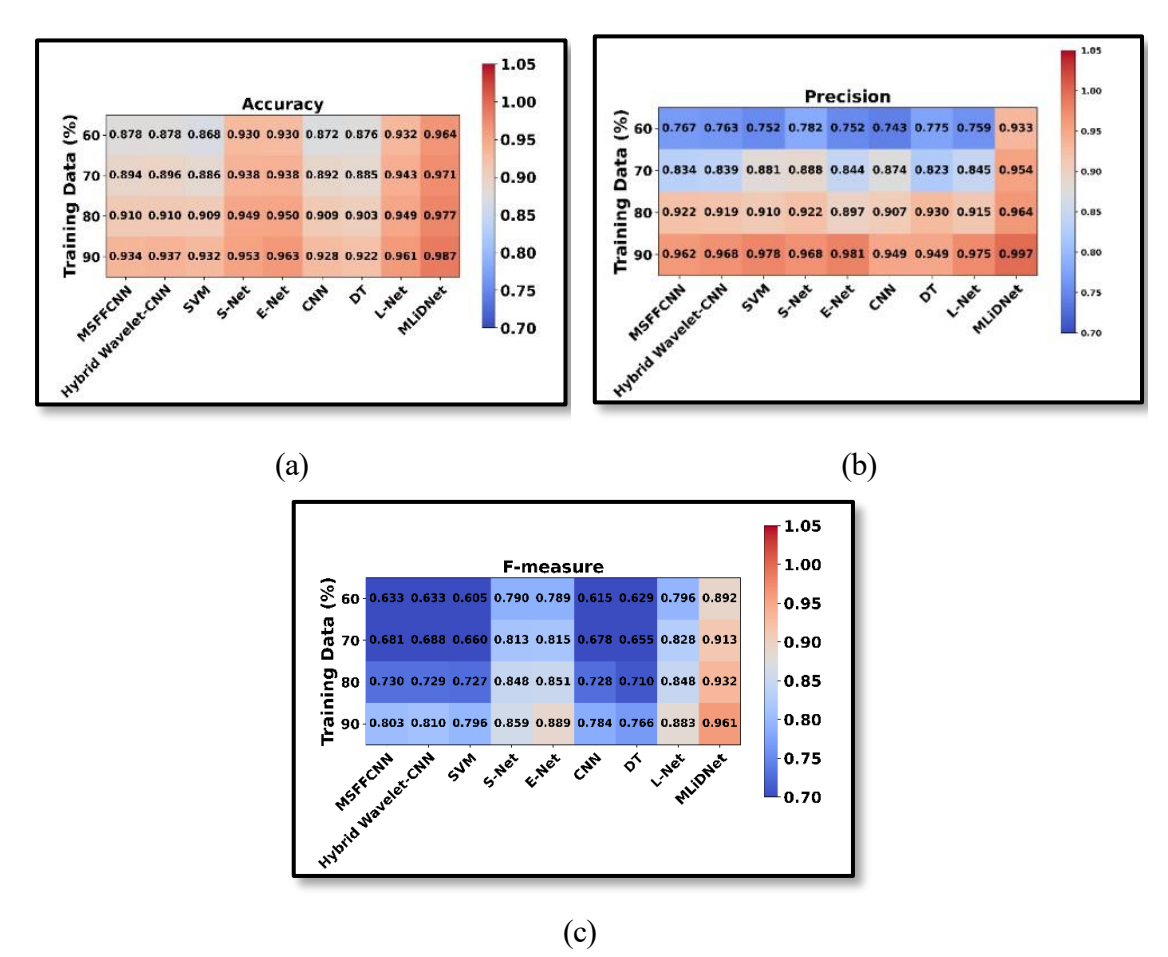


Figure 4. 20: Evaluation of proposed and traditional methods in comparison at 30 Hz for dataset 1.

4.9 Analysis of Comparisons for Dataset 2

The effectiveness of the suggested and traditional fault detection techniques at 30 Hz is compared in the comparison analysis shown in Figure 4.21. With a precision of 82.34%, an accuracy of 94.35%, and an F-measure of 82.28%, CNN distinguishes itself from the traditional models. The proposed method surpasses these metrics with a precision of 97.74%, accuracy of 94.69%, and F-measure of 95.61%, proving the hybrid structure's efficacy in fault identification. CNN and proposed still excel even when 70% of the training data is used.

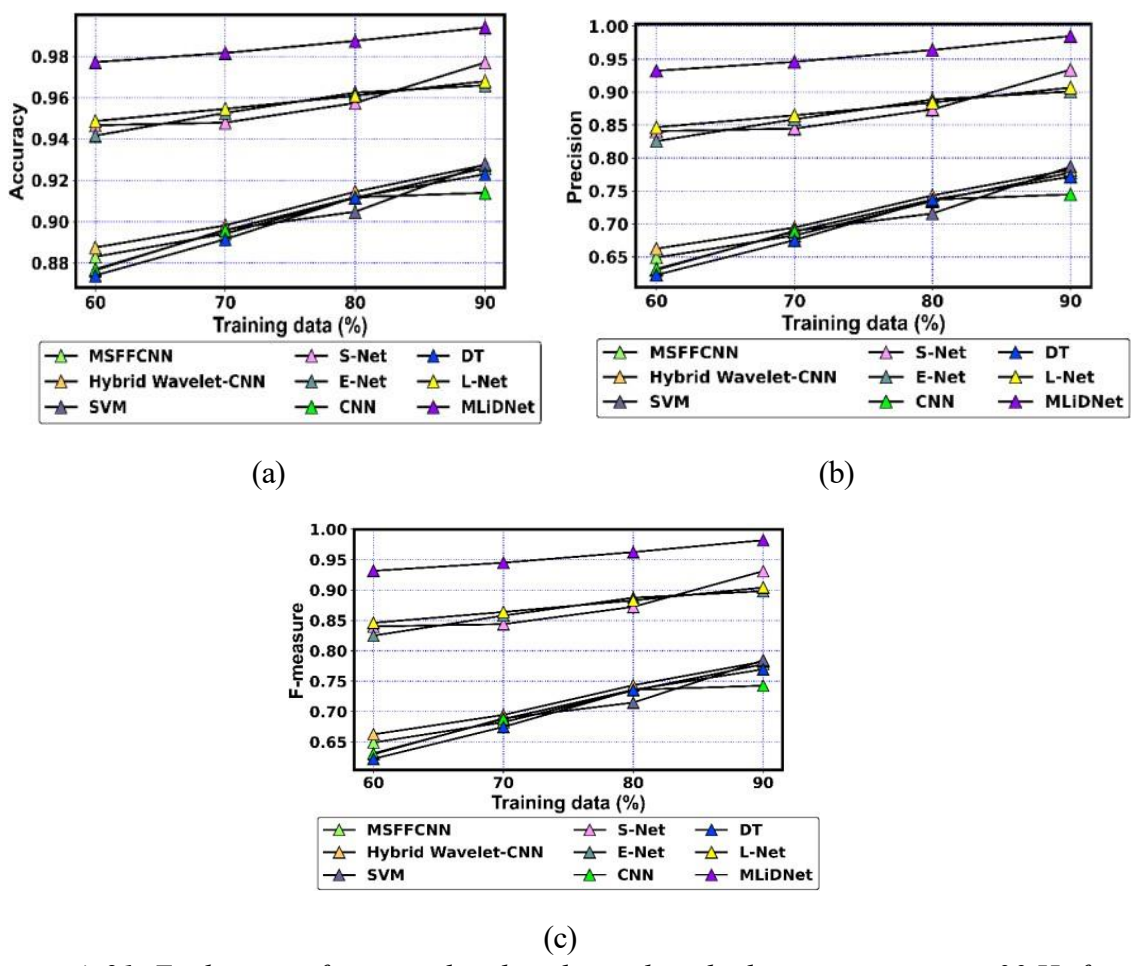


Figure 4. 21: Evaluation of proposed and traditional methods in comparison at 30 Hz for dataset 2.

Figure 4.22, which compares the proposed method to conventional techniques at 35 Hz, demonstrates how well the proposed performs using 60% of the training data. In particular, the proposed outperforms other models with a precision of 95.13%, accuracy of 97.32%, and F-measure of 94.65%. The proposed method consistently outperforms traditional models, even when they yield competitive results.

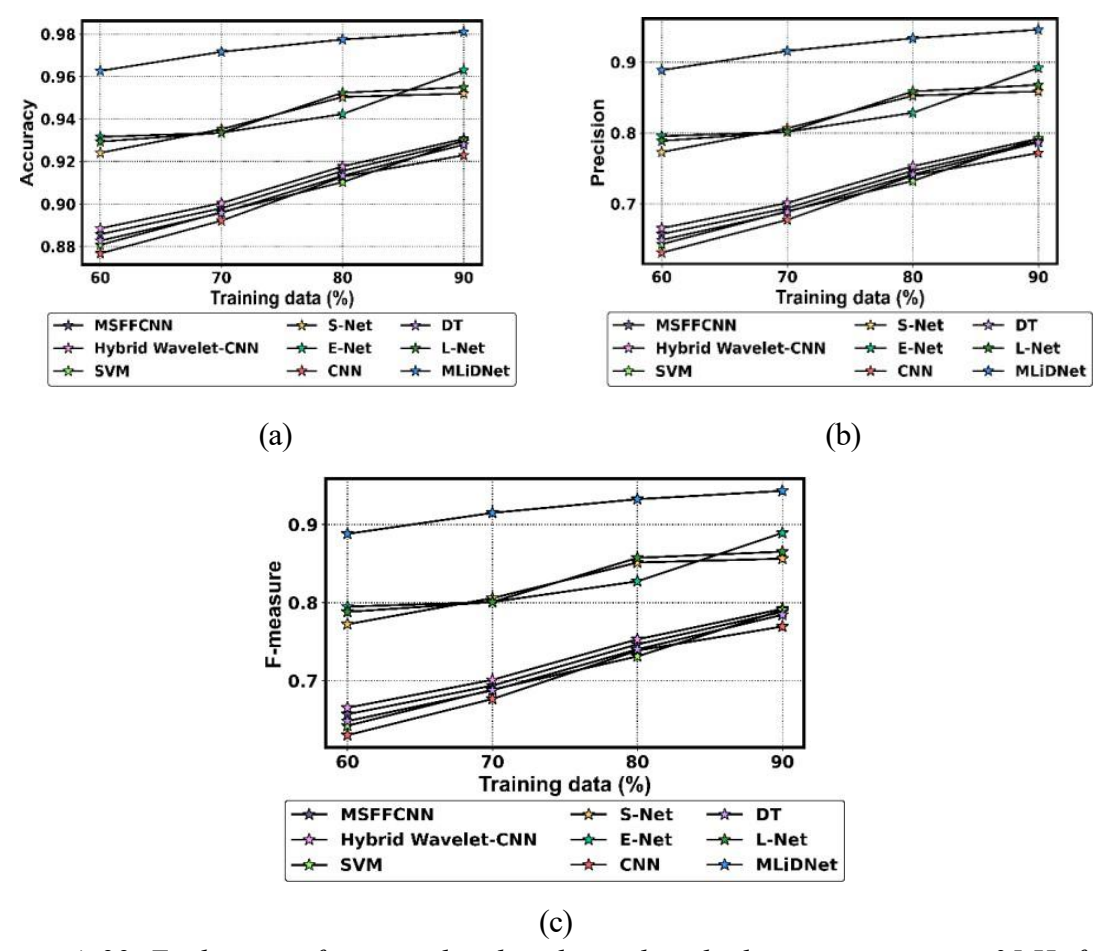


Figure 4. 22: Evaluation of proposed and traditional methods in comparison at 35 Hz for dataset 2.

Figure 4.23 shows the performance evaluation of several fault detection systems at varying learning percentages for 40 Hz. With 97.72% precision, 93.27% accuracy, and 93.30% F-measure, MLiDNet demonstrated its supremacy in accurately detecting combined mistakes with 60%. With 70%, MLiDNet outperformed traditional techniques with 97.72% precision, 95.36% accuracy, and 95.26% F-measure.

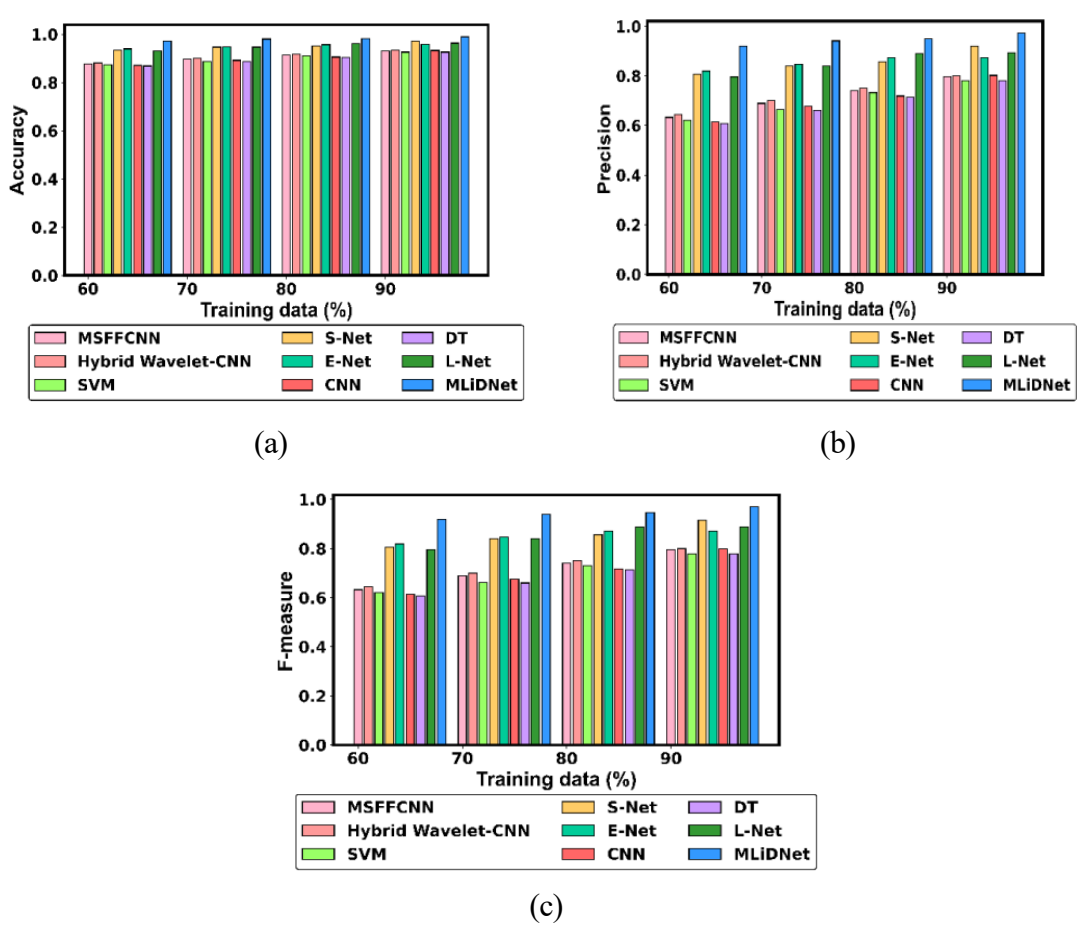


Figure 4. 23: Evaluation of proposed and traditional methods in comparison at 40 Hz for dataset 2.

Even at 80% and 90%, the impressive results of 98.79% precision and 98.78% accuracy showcase the efficacy of the recommended fault identification technique (Figure 4.24). These results show that the proposed approach outperforms conventional methods in terms of accuracy, precision, and reliability.

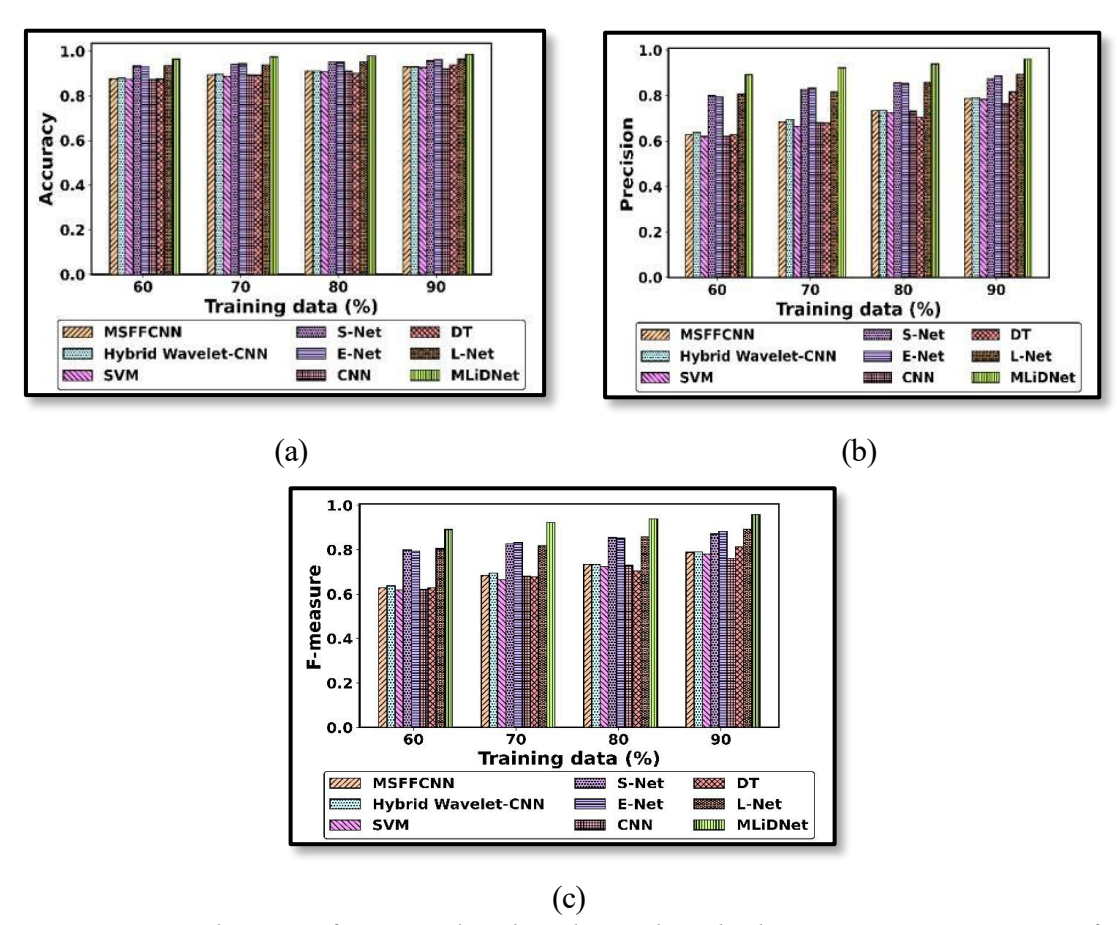


Figure 4. 24: Evaluation of proposed and traditional methods in comparison at 45 Hz for dataset 2.

The suggested approach remains dominant with a precision of 98.24%, an accuracy of 94.83%, and an F-measure of 94.74% (Figure 4.25). MLiDNet continuously beats other models when training data reaches 80% and 90%, proving its stability and scalability. Fault detection effectiveness is demonstrated by MLiDNet's maximum precision of 99.28%, accuracy of 99.45%, and F-measure of 92.74%.

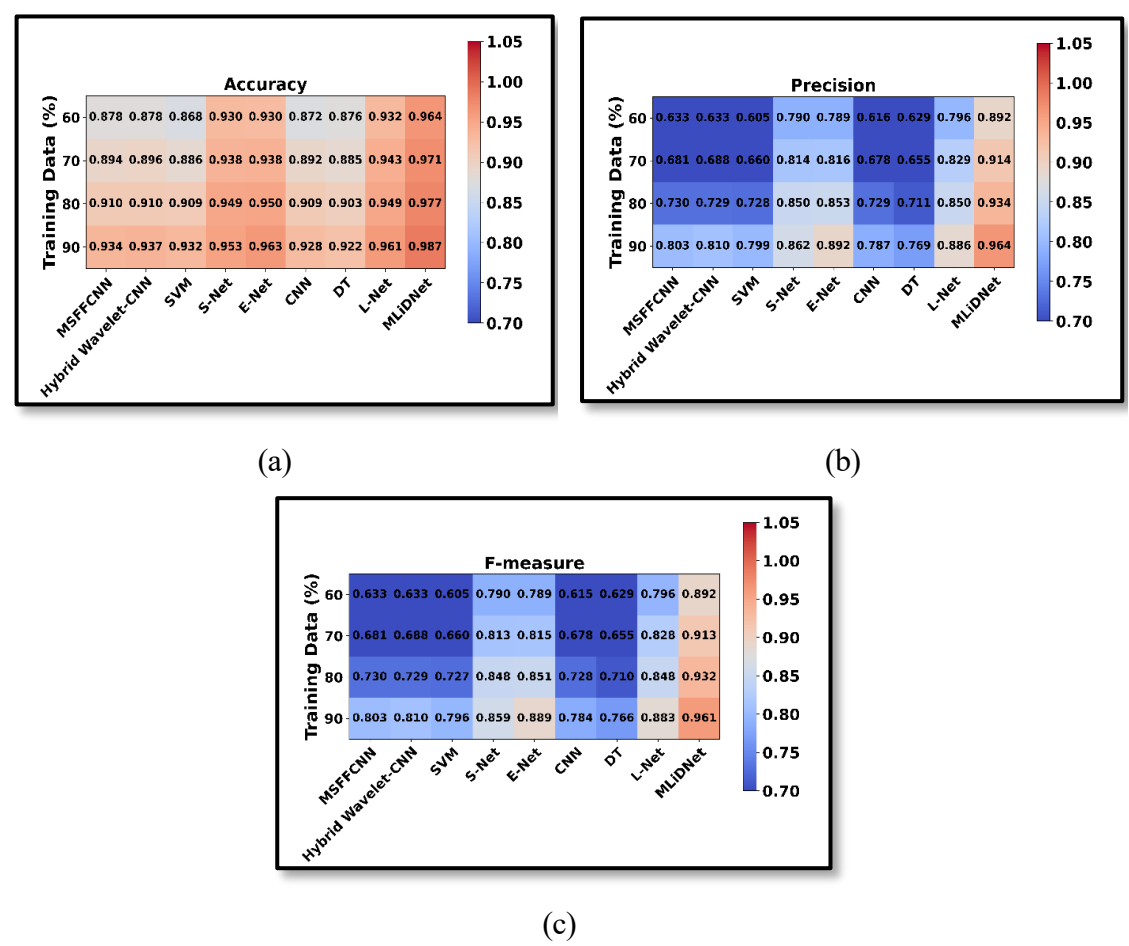


Figure 4. 25: Evaluation of proposed and traditional methods in comparison at 50 Hz for dataset 2.

4.10 Evaluation of Computation Time for Dataset 1

According to Table 4.4, the suggested combined model performs better computationally than existing techniques at a frequency of 10 Hz. With 60% of the training data, it takes 1.48 seconds to compute, and at 90%, it slightly increases to 2.08 seconds, which is the shortest computing time. Conventional models, in contrast, operate much more slowly and significantly as the amount of training data grows. CNN and DT models perform substantially worse at more significant percentages of training data despite showing faster processing speeds at lower percentages. With processing times of 11.24 seconds at 90%, L-Net exhibits the worst performance, mainly when training with larger datasets. MLiDNet is a very successful model for identifying faults.

Table 4. 4: Analysis of MLiDNet's computational time in comparison to traditional models at 10 Hz

Calculation time (seconds) at various percentages of training data (%)										
Models	60%	70%	80%	90%						
E-Net	6.64	7.41	8.98	9.12						
Hybrid Wavelet-CNN	5.17	5.97	9.85	9.97						
SVM	4.12	4.39	5.36	5.61						
L-Net	1.56	6.04	9.06	11.24						
CNN	2.11	2.22	4.32	4.56						
MSFFCNN	4.20	4.48	5.47	5.72						
S-Net	5.05	5.85	9.66	9.75						
DT	2.28	2.56	4.29	6.43						
MLiDNet	1.48	1.50	2.05	2.08						

Table 4.4 compares the computing effort of the existing models at 20 Hz with the suggested combined model. MLiDNet reaches its maximum speed of 1.54 seconds at 60% training data and maintains its efficiency at 90% training data, needing 2.57 seconds. On the other hand, when training data accumulates, a number of models exhibit considerable increases in calculation time. For instance, SVM rises from 3.12 seconds at 60% to 8.66 seconds at 90%, while S-Net and E-Net achieve 6.55 and 9.12 seconds at 90%, respectively. CNN and DT also experienced time increases, going from 1.78 to 5.37 seconds and 2.49 seconds to 7.59 seconds, respectively. L-Net peaks at 12.56 seconds at 90%. The efficiency of MLiDNet makes it ideal for fault detection.

Table 4. 5: Analysis of MLiDNet's computational time in comparison to traditional models at 20 Hz

Calculation time (seconds) at various percentages of training data (%)									
Models	60%	70%	80%	90%					
E-Net	6.54	7.59	8.45	9.12					
Hybrid Wavelet-CNN	4.68	5.62	5.90	6.68					
SVM	3.12	4.14	5.14	8.66					
L-Net	7.46	7.73	11.74	12.56					
CNN	1.78	3.33	4.12	5.36					
MSFFCNN	3.18	4.22	5.24	8.83					
S-Net	4.58	5.53	5.80	6.55					
DT	2.49	3.17	6.01	7.59					
MLiDNet	1.53	2.43	2.48	2.58					

Table 4.6 compares the suggested and traditional models' computational times at 30 Hz for various percentages of training data. Even with more enormous datasets, the proposed method can maintain low computational requirements, as demonstrated by achieving a computational time of 1.40 seconds with 60% of training data, slightly increasing to 1.85 seconds for 90% of training data. Other models' computation times, however, are significantly longer. At larger data volumes, DT indicates decreased efficiency.

Table 4. 6: Analysis of MLiDNet's computational time in comparison to traditional models at 30 Hz

Calculation time (seconds) at various percentages of training data (%)									
Models	60%	70%	80%	90%					
E-Net	5.28	6.01	6.52	6.87					
Hybrid Wavelet-CNN	8.21	10.12	10.44	11.47					
SVM	3.45	3.56	3.75	6.64					
L-Net	3.82	5.33	6.76	7.18					
CNN	2.03	2.51	2.65	3.21					
MSFFCNN	3.523	3.64	3.83	6.77					
S-Net	8.05	9.92	10.23	11.25					
DT	1.46	3.41	3.79	4.68					
MLiDNet	1.39	1.69	1.76	1.85					

Nevertheless, L-Net shows a noticeable increase in computation time at 90% of training data, reaching a peak of 7.18 seconds. With its exceptional accuracy and short calculation time, the suggested approach is the best model for real-time fault identification.

4.11 Evaluation of Computation Time for Dataset 2

At 30 Hz, Table 4.7 shows that the proposed combined model outperforms current methods computationally. It records the fastest computation time of 1.83 seconds with 60% of training data and significantly improves to 2.90 seconds at 90%. When it comes to fault identification, the proposed method is very efficient, providing increased accuracy while drastically cutting down on calculation time.

Table 4. 7: Analysis of MLiDNet's computational time in comparison to traditional models at 30 Hz

Calculation time (seconds) at various percentages of training data (%)									
Models	60%	70%	80%	90%					
E-Net	9.77	11.27	13.05	14.69					
Hybrid Wavelet-CNN	9.67	11.28	12.67	14.25					
SVM	9.80	11.45	12.86	14.77					
L-Net	5.55	6.53	7.36	8.54					
CNN	3.05	3.52	4.06	4.66					
MSFFCNN	10.00	11.68	13.12	15.07					
S-Net	9.48	11.06	12.42	13.97					
DT	3.15	3.62	4.10	4.67					
MLiDNet	1.83	2.15	2.49	2.90					

The proposed method's computational time evaluation at a frequency of 35 Hz is compared with conventional models in Table 4.8. At 6.37 seconds, MLiDNet performs the fastest when 60% of the training data is used. With a computation time of 4.12 seconds, this efficiency is maintained when the training data approaches 90%. But for other models, the increase in calculation time is more noticeable as training data sizes increase. SVM, for example, shows a significant decrease in efficiency when its computation time rises from 6.24 seconds at 60% to 9.66 seconds at 90%.

Table 4. 8: Analysis of MLiDNet's computational time in comparison to traditional models at 35 Hz

Calculation time (seconds) at various percentages of training data (%)									
Models	60%	70%	80%	90%					
E-Net	8.39	6.58	7.70	8.73					
Hybrid Wavelet-CNN	6.66	7.31	8.38	9.67					
SVM	6.24	7.54	8.73	10.12					
L-Net	2.65	3.75	4.28	4.82					
CNN	9.56	9.75	11.09	12.58					
MSFFCNN	6.37	7.69	8.91	10.32					
S-Net	5.74	7.17	8.21	9.47					
DT	3.23	11.04	12.39	13.88					
MLiDNet	6.36	3.09	3.57	4.11					

Table 4.9 displays the suggested combined model's computational time evaluation at a frequency of 40 Hz in contrast to other training data models. The proposed computation time is only 2.08 seconds when 60.01% of the training data is used, and it slightly increases to 3.23 seconds when 90.01% of the training data is used. This outcome shows that MLiDNet can sustain low processing needs despite increasing training data. However, the computation times of other models are substantially longer.

Table 4. 9: Analysis of MLiDNet's computational time in comparison to traditional models at 40 Hz

Calculation time (seconds) at various percentages of training data (%)									
Models	60%	70%	80%	90%					
E-Net	4.44	4.98	5.69	6.41					
Hybrid Wavelet-CNN	7.61	8.98	10.49	11.86					
SVM	2.26	2.65	3.05	3.51					
L-Net	6.04	6.82	7.96	9.38					
CNN	9.05	10.48	12.20	14.07					
MSFFCNN	2.30	2.71	3.11	3.58					
S-Net	7.47	8.80	10.28	11.63					

DT	9.37	10.82	12.12	13.64
MLiDNet	2.08	2.42	2.77	3.23

From 9.81 seconds at 60% of the training data to 15.13 seconds at 90%, the S-Net model, for example, has the longest computation time (Table 4.10). The E-Net model's computation time rises from 5.07 to 7.74 seconds within the same range. Specifically, CNN's time rises from 2.47 seconds at 60.01% to 3.83 seconds at 90.01%, whilst DT's time decreases from 7.08 seconds to 11.12 seconds, indicating a decrease in efficiency.

Table 4. 10: Analysis of MLiDNet's computational time in comparison to traditional models at 45 Hz

Calculation time (seconds) at various percentages of training data (%)									
Models	60%	70%	80%	90%					
E-Net	9.95	11.20	13.17	15.42					
Hybrid Wavelet-CNN	5.86	6.72	7.73	9.03					
SVM	5.76	6.61	7.58	8.88					
L-Net	9.72	10.97	12.90	15.12					
CNN	5.06	5.78	6.62	7.741					
MSFFCNN	2.48	2.91	3.27	3.84					
S-Net	7.07	8.21	9.48	11.13					
DT	5.06	5.81	6.86	7.98					
MLiDNet	1.59	1.85	2.12	2.36					

In Table 4.11, the computational time of L-Net, however, also increases dramatically, peaking at 10.49 seconds at 90% of training data. The suggested approach is ideal for fault identification because of its high accuracy and low processing load.

Table 4. 11: Analysis of MLiDNet's computational time in comparison to traditional models at 45 Hz

Models	60%	70%	80%	90%
E-Net	9.04	10.17	11.57	12.97
Hybrid Wavelet-CNN	4.82	5.65	6.62	7.77
SVM	5.00	5.72	6.55	7.35
L-Net	6.91	7.76	9.10	10.49
CNN	2.69	3.04	3.52	4.11
MSFFCNN	5.10	5.83	6.68	7.49
S-Net	4.74	5.56	6.47	7.60
DT	4.56	5.13	5.96	6.76
MLiDNet	2.16	2.50	2.85	3.22

In Table 4.11, CNN and DT models have comparatively low initial computation times; nevertheless, when the proportion of training data increases, there is a noticeable increase in calculation time. CNN's time increases from 2.69 seconds at 60% to 4.10 seconds at 90%, whereas DT's time decreases from 4.57 seconds to 6.76 seconds, indicating lower efficiency with higher data volumes.

4.12 Ablation Evaluation for Dataset 1

Ablation analysis is the deliberate process of disabling or removing specific system components to see how their absence affects functionality or performance. Comparing the performance of the proposed method to the conventional approaches at 10 Hz, 20 Hz, and 30 Hz was the aim of the ablation investigation. The results show that the suggested method consistently shows higher accuracy and was studied, offering crucial information about its effectiveness.

Table 4. 12: Ablation analysis of proposed method compared to existing models at 10 Hz for dataset 1

Measures	Prop- Conv SE	L-Net	Prop- without feature selection	ML- Net	Prop- Conv SSWT	D-Net	Prop- Conv L-Net	Pro- posed
Specificity	0.9901	0.9797	0.9771	0.9918	0.9916	0.9576	0.9903	0.9981
NPV	0.9897	0.9797	0.9771	0.9918	0.9904	0.9576	0.9891	0.9967
Precision	0.9555	0.8987	0.8862	0.8993	0.9587	0.8683	0.9524	0.9904
MCC	0.9432	0.8784	0.8631	0.8762	0.9468	0.8460	0.9393	0.9847
FPR	0.0087	0.0202	0.0056	0.0058	0.0081	0.0056	0.0096	0.0018
Accuracy	0.9840	0.9662	0.9620	0.9764	0.9851	0.9427	0.9830	0.9956
F-measure	0.9527	0.8985	0.8860	0.8993	0.9557	0.8683	0.9494	0.9872
FNR	0.0502	0.1012	0.0439	0.0445	0.0472	0.0430	0.0533	0.0156
Sensitivity	0.9497	0.8987	0.8860	0.8993	0.9527	0.8683	0.9466	0.9841

At 10 Hz, Table 4.12 demonstrates that the suggested method performs noticeably better than traditional models in every metric. Using a 99.57% accuracy rate, MLiDNet outperforms the existing models. These outcomes show how much better MLiDNet is at fault detection. Additionally, in terms of specificity (99.80%) and sensitivity (98.42%), MLiDNet performs better than the other modeling. It has an excellent precision of 99.35% and an F-measure of 98.83%. The high effectiveness of the proposed method in differentiating between fault and non-fault circumstances is demonstrated by its MCC, which stands at 98.48%. The model's excellent dependability in forecasting non-fault cases is shown by its NPV of 99.68%, while the lowest FPR and FNR among the models under comparison are 0.0019 and 0.0157, respectively.

Table 4. 13: Ablation evaluation of dataset 1 using the suggested approach in comparison to current models at 20 Hz

Prop-			Prop-		Prop-		Prop-	
Measures	Conv	L-Net	without	ML-	Conv	D-Net	Conv	Pro-
112000000	SE SE		feature selection	Net	SSWT	2 1 (0)	L-Net	posed
Specificity	0.9911	L-Net	0.9765	0.9912	0.9898	0.9571	0.9898	0.9986
NPV	0.9897	0.9810	0.9766	0.9912	0.9885	0.9570	0.9887	0.9973
Precision	0.9556	0.9811	0.8829	0.8961	0.9493	0.8652	0.9493	0.9935
MCC	0.9432	0.9050	0.8593	0.8723	0.9357	0.8423	0.9357	0.9887
FPR	0.0088	0.8860	0.0234	0.0236	0.0101	0.0228	0.0101	0.0013
Accuracy	0.9840	0.0188	0.9608	0.9753	0.9821	0.9417	0.9821	0.9967
FDR	0.0443	0.9683	0.0425	0.0431	0.0506	0.0417	0.0507	0.0063
F-measure	0.9526	0.0949	0.8829	0.8962	0.9463	0.8653	0.9463	0.9904
FNR	0.0503	0.9051	0.0466	0.0473	0.0565	0.0456	0.0567	0.0126
Sensitivity	0.9497	0.0948	0.8828	0.8961	0.9433	0.8652	0.9433	0.9872

With an accuracy of 99.68%, MLiDNet continues to perform well at 20 Hz, as shown in Table 4.13. It outperforms the existing methods. Among the models tested, the proposed model also has the best sensitivity (98.74%) and specificity (99.87%). Additionally, the F-measure shows its accuracy at 99.36% and efficacy at 99.05%. Its durability in fault detection is demonstrated by its NPV of 99.84% and MCC of 98.86%. The suggested model has the fewest mistakes in identifying healthy faults, with the lowest FPR at 0.0013 and FNR at 0.0126.

Table 4. 14: Ablation analysis of dataset 1 using the suggested approach in comparison to conventional techniques at 30 Hz

		Prop-	Prop-	Prop-	Prop-			
Metrics Proposed	•	Conv	Conv	without	L-Net	D-Net	ML-	
111001105	Toposcu	SSWT	SE	L-Net	feature	21,00	2 1 (00	Net
		55 ** 1	SL.	E Titt	selection			
Accuracy	0.9978	0.9820	0.9894	0.9883	0.9673	0.9683	0.9479	0.9818
Sensitivity	0.9905	0.9433	0.9654	0.9622	0.9018	0.9050	0.8838	0.9154
Specificity	0.9993	0.9898	0.9942	0.9936	0.9803	0.9810	0.9607	0.9950
Precision	0.9968	0.9493	0.9715	0.9683	0.9018	0.9050	0.8838	0.9154
F-measure	0.9936	0.9463	0.9684	0.9653	0.9018	0.9050	0.8838	0.9154
MCC	0.9924	0.9356	0.9621	0.9583	0.8822	0.8860	0.8646	0.8955
NPV	0.9981	0.9886	0.9930	0.9924	0.98038	0.9810	0.9607	0.9950
FPR	0.0006	0.0101	0.0057	0.0063	0.01962	0.0189	0.0192	0.0199
FNR	0.0094	0.0566	0.0345	0.0377	0.0681	0.0949	0.0667	0.0691
FDR	0.0031	0.0506	0.0284	0.0316	0.0481	0.0949	0.0471	0.0488

With an accuracy of 99.78% at 30 Hz, the proposed methods perform better than the model without feature selection, as indicated in Table 4.14. The model's performance is outstanding, with a 99.05% sensitivity and a 99.93% specificity. A 99.67% accuracy rate and a 99.36% F-measure further illustrate its remarkable fault detection capabilities. The suggested method's effectiveness is further demonstrated by a 99.81% NPV and a 99.24% MCC. The model's low FPR of 0.0006 and FNR of 0.0094 demonstrate its ability to differentiate faults from non-faults reliably.

Table 4. 15: Cross-speed generalization performance trained on 10 Hz and 20 Hz, tested on 30 Hz for Dataset 1

	Prop-		Prop-	ML-	Prop-		Prop-	
Measure	Conv-	L-Net	w/o	NIL-	Conv-	D-Net	Conv-	Proposed
	SE		FS	Net	SSWT		L-Net	
Specificity	0.9020	0.8955	0.8891	0.9062	0.9115	0.8820	0.9188	0.9408
NPV	0.9010	0.8923	0.8880	0.9040	0.9091	0.8805	0.9167	0.9391
Precision	0.8550	0.8487	0.8402	0.8623	0.8705	0.8308	0.8742	0.9103
MCC	0.8205	0.8102	0.8007	0.8345	0.8450	0.7931	0.8508	0.8924
FPR	0.0980	0.1045	0.1109	0.0938	0.0885	0.1180	0.0812	0.0592
Accuracy	0.9190	0.9123	0.9068	0.9251	0.9300	0.8980	0.9337	0.9432
F-measure	0.8510	0.8455	0.8370	0.8600	0.8691	0.8280	0.8720	0.9077
FNR	0.0855	0.0908	0.0920	0.0830	0.0785	0.0951	0.0745	0.0523
Sensitivity	0.9145	0.9092	0.9080	0.9170	0.9215	0.9049	0.9255	0.9477

Table 4.15 evaluated the model by training on 10 Hz and 20 Hz data and testing on 30 Hz, for Dataset 1. It is found that the performance of the proposed model under this condition is moderately lower compared to same-speed training-testing scenarios, particularly in terms of accuracy.

4.13 Ablation Study of Proposed Fault Diagnosis for Dataset 2

Ablation analysis systematically shuts down or ignores specific system components to observe effects in absence based on operation or performance. The proposed ablation result was to compare its performance to that of conventional methods at 30 Hz, 35 Hz, 40, 45 Hz, and 50 Hz. The results provide essential information about the usefulness of the suggested strategy, demonstrating that it consistently exhibits enhanced accuracy across all frequencies investigated.

Table 4. 16: Ablation evaluation of proposed method compared to existing models at 30 Hz for dataset 2

Measures	Prop- Conv SE	L-Net	Prop- without feature selection	ML-Net	Prop- Conv SSWT	D-Net	Prop- Conv L-Net	Pro- posed
Specificity	0.9942	0.9810	0.9950	0.9950	0.9898	0.9607	0.9936	0.9993
NPV	0.9930	0.9810	0.9950	0.9698	0.9886	0.9607	0.9924	0.9981
Precision	0.9715	0.9050	0.9154	0.7955	0.9493	0.8838	0.9683	0.9968
MCC	0.9621	0.8860	0.8955	0.7486	0.9356	0.8646	0.9583	0.9924
FPR	0.0057	0.0189	0.0199	0.0439	0.0101	0.0192	0.0063	0.0006
Accuracy	0.9894	0.9683	0.9818	0.9408	0.9820	0.9479	0.9883	0.9978
FDR	0.0284	0.0949	0.0488	0.7931	0.0506	0.0471	0.0316	0.0031
F-measure	0.9684	0.9050	0.9154	0.2194	0.9463	0.8838	0.9653	0.9936
FNR	0.0346	0.0948	0.0691	0.2243	0.0567	0.0666	0.0378	0.0093
Sensitivity	0.9654	0.9050	0.9154	0.7907	0.9433	0.8838	0.9622	0.9905

At 30 Hz, MLiDNet performs better than conventional models on all statistical measures, as shown in Table 4.16. MLiDNet's better fault detection capabilities are demonstrated by its 99.39% accuracy, which outperforms models utilizing conventional methods. With a sensitivity of 97.91% and a specificity of 99.69%, MLiDNet also performs exceptionally well. It also records an accuracy rate of 98.49% and an excellent F-measure of 98.20%. The high MCC of 97.84% further demonstrates the proposed method's ability to discriminate between faulty and non-faulty circumstances. The model's NPV of 99.56% indicates that it is highly reliable in forecasting non-fault cases. It is noteworthy for having the lowest FNR of 0.0208 and the lowest FPR of 0.0030.

Table 4. 17: Ablation examination of dataset 2 using the suggested approach in comparison to current approaches at 35 Hz

Measures	Prop- Conv SE	L-Net	Prop- without feature selection	ML-Net	Prop- Conv SSWT	D-Net	Prop- Conv L-Net	Pro- posed
Specificity	0.9536	0.9735	0.9602	0.9746	0.9573	0.9411	0.9615	0.9891
NPV	0.9526	0.9721	0.9591	0.9735	0.9561	0.9399	0.9602	0.9878
Precision	0.7687	0.8678	0.8017	0.8139	0.7866	0.7856	0.8078	0.9458
MCC	0.7196	0.8382	0.7591	0.7705	0.7411	0.7438	0.7662	0.9317
FPR	0.0366	0.0187	0.0431	0.0439	0.0426	0.0424	0.0432	0.0030
Accuracy	0.9218	0.9549	0.9329	0.9468	0.9278	0.9141	0.9349	0.9808
FDR	0.2312	0.1321	0.1981	0.2011	0.2132	0.1942	0.1921	0.0540
F-measure	0.7664	0.8652	0.7993	0.8113	0.7844	0.7834	0.8054	0.9431
FNR	0.2357	0.1374	0.2029	0.2061	0.2178	0.1987	0.1971	0.0596
Sensitivity	0.7641	0.8626	0.7970	0.808	0.7820	0.7810	0.8028	0.9402

Table 4.17 shows an accuracy of 98.09%, demonstrating MLiDNet's continued outstanding performance at 35 Hz. The accuracy and efficacy of the F-measure are 94.59% and 94.31%, respectively. MCC of 93.17% demonstrates its resilience in fault identification. The proposed method achieves better results with a low FPR of 0.011 and an FNR of 0.053.

Table 4. 18: Ablation evaluation of the proposed method compared to existing approaches at 40 Hz

			Prop-					
	Prop-		without		Prop-		Prop-	Pro-
Measures	Conv SE	L-Net	feature	ML-Net	Conv	D-Net	Conv	posed
			selection		SSWT		L-Net	•
Specificity	0.9531	0.9783	0.9567	0.9710	0.9579	0.9375	0.9518	0.9945
NPV	0.9519	0.9771	0.9556	0.9698	0.9566	0.9364	0.9508	0.9933
Precision	0.7656	0.8918	0.7837	0.7955	0.7897	0.7681	0.7597	0.9728
MCC	0.7160	0.8668	0.7376	0.7486	0.7446	0.7228	0.7089	0.9640
FPR	0.0468	0.0216	0.0432	0.0439	0.0420	0.0424	0.0481	0.0054
Accuracy	0.9209	0.9629	0.9268	0.9408	0.9288	0.9083	0.9188	0.9898
FDR	0.7633	0.8891	0.7814	0.7931	0.7874	0.7658	0.7574	0.9700
F-measure	0.2388	0.1134	0.2209	0.2242	0.2148	0.2164	0.2446	0.0327
FNR	0.2342	0.1081	0.2162	0.2194	0.2102	0.2118	0.2402	0.0271
Sensitivity	0.7611	0.8865	0.7791	0.7907	0.7850	0.7635	0.7552	0.9671

The proposed approach performs better at 98.99% at 40 Hz than the conventional SSWT, as shown in Table 4.18. The model exhibits remarkable performance with the highest significant sensitivity of 96.72% and specificity of 99.46%. Its accuracy of 99.69% and F-measure of 97.39% illustrate its exceptional fault detection performance. The proposed method's effectiveness is further supported by 96.45% MCC and 99.33% NPV. Its capacity to distinguish between real and false faults is demonstrated by its lowest FPR of 0.0054 and FNR of 0.032. The analysis results show that, across all frequencies studied, the suggested approach performs better than conventional approaches.

Table 4. 19: Ablation analysis of the suggested approach compared to existing models at 45 Hz

Measures	Prop- Conv SE	L-Net	Prop- without feature selection	ML- Net	Prop- Conv SSWT	D-Net	Prop- Conv L-Net	Pro- posed
Specificity	0.9579	0.9789	0.9627	0.9771	0.9536	0.9434	0.9542	0.9921
NPV	0.9567	0.9777	0.9615	0.9759	0.9525	0.9423	0.9531	0.9909
Precision	0.7897	0.8948	0.8138	0.8260	0.7687	0.7975	0.7717	0.9609
MCC	0.7447	0.8705	0.7735	0.7851	0.7195	0.7580	0.7231	0.9496
FPR	0.0420	0.0210	0.0372	0.0378	0.0463	0.0365	0.0457	0.0078
Accuracy	0.9289	0.9639	0.9369	0.9509	0.9219	0.9181	0.9229	0.9859
FDR	0.7874	0.8922	0.8113	0.8235	0.7664	0.7951	0.7694	0.9580
F-measure	0.2149	0.1104	0.1910	0.1939	0.2358	0.1872	0.2328	0.0448
FNR	0.2102	0.1051	0.1861	0.1889	0.2312	0.1824	0.2282	0.0391
Sensitivity	0.7611	0.8865	0.7791	0.7907	0.7850	0.7635	0.7552	0.9670

Furthermore, out of all the models analyzed in Table 4.19, the proposed method has the best sensitivity (98.58%) and specificity (99.22%). Its 96.08% accuracy and 95.81% F-measure further support its effectiveness. Its predictive accuracy of 99.09% and MCC of 94.96% show how resilient it is at identifying faults. The suggested method has a low FPR (0.007) and FNR (0.044) and makes the fewest errors when detecting faults and healthy states.

Table 4. 20: Comparison of proposed ablation analysis at 50 Hz with traditional SSWT, SE, and L-Net models

Measures	Prop- Conv SE	L-Net	Prop- without feature selection	ML- Net	Prop- Conv SSWT	D-Net	Prop- Conv L-Net	Pro- posed
Specificity	0.9537	0.9771	0.9518	0.9661	0.9523	0.9328	0.9493	0.9926
NPV	0.9526	0.9759	0.9507	0.9650	0.9512	0.9317	0.9482	0.9916
Precision	0.7688	0.8858	0.7597	0.7711	0.7628	0.7445	0.7476	0.9638
MCC	0.7196	0.8598	0.7088	0.7194	0.7123	0.6946	0.6943	0.9531
FPR	0.0464	0.0228	0.0481	0.0488	0.0476	0.0471	0.0506	0.0073

Accuracy	0.9218	0.9609	0.9189	0.9327	0.9198	0.9005	0.9148	0.9868
FDR	0.7663	0.8832	0.7574	0.7688	0.7603	0.7423	0.7456	0.9611
F-measure	0.2357	0.1194	0.2447	0.2484	0.2416	0.2398	0.2568	0.0418
FNR	0.2310	0.114	0.2403	0.2437	0.2371	0.2353	0.2520	0.0360
Sensitivity	0.7640	0.8805	0.7552	0.7665	0.7583	0.7401	0.7431	0.9583

Comparing the proposed model to the conventional approach in Table 4.20, the proposed accuracy at 50 Hz is 98.69%. The results of the ablation analysis demonstrate that, for every tested frequency, The recommended method routinely performs better than feature extraction and convolutional signal analysis methods.

Table 4. 21: Cross-speed generalization performance trained on 10 Hz and 20 Hz, tested on 30 Hz for Dataset 2

	Prop-		Prop-	ML-	Prop-		Prop-	
Measure	Conv-	L-Net	w/o		Conv-	D-Net	Conv-	Proposed
	SE		FS	Net	SSWT		L-Net	
Specificity	0.9020	0.8955	0.8891	0.9062	0.9115	0.8820	0.9188	0.9408
NPV	0.9010	0.8923	0.8880	0.9040	0.9091	0.8805	0.9167	0.9391
Precision	0.8550	0.8487	0.8402	0.8623	0.8705	0.8308	0.8742	0.9103
MCC	0.8205	0.8102	0.8007	0.8345	0.8450	0.7931	0.8508	0.8924
FPR	0.0980	0.1045	0.1109	0.0938	0.0885	0.1180	0.0812	0.0592
Accuracy	0.9190	0.9123	0.9068	0.9251	0.9300	0.8980	0.9337	0.9432
F-measure	0.8510	0.8455	0.8370	0.8600	0.8691	0.8280	0.8720	0.9077
FNR	0.0855	0.0908	0.0920	0.0830	0.0785	0.0951	0.0745	0.0523
Sensitivity	0.9145	0.9092	0.9080	0.9170	0.9215	0.9049	0.9255	0.9477

Table 4.21 evaluated the model by training on 10 Hz and 20 Hz data and testing on 30 Hz, for Dataset 2. The performance of the proposed model under this condition is found to be moderately lower, especially in terms of accuracy, when compared to training and testing at the same speed. This is primarily due to the variability in signal patterns at different speeds, which affects the learned representations. However, the results still show that the proposed model performs comparatively better than most baseline methods in the same cross-speed setup, indicating some level of generalization.

4. 14 Analysis of the Dataset 1 Receiver Operating Characteristic Curve

The Receiver Operating Characteristic Curve (ROC) displays the relationship between

the TPR and the FPR for different categorization criteria. ROC curves are essential for comparing and assessing how well categorization models perform. The ROC curve study in Figure 4.26 compares the performance of the suggested method and convolutional approaches for detecting EM system failures at 10 Hz, 20 Hz, and 30 Hz frequencies with 60% of the training data. As the ROC curves show, the suggested approach outperforms conventional models at all frequencies.

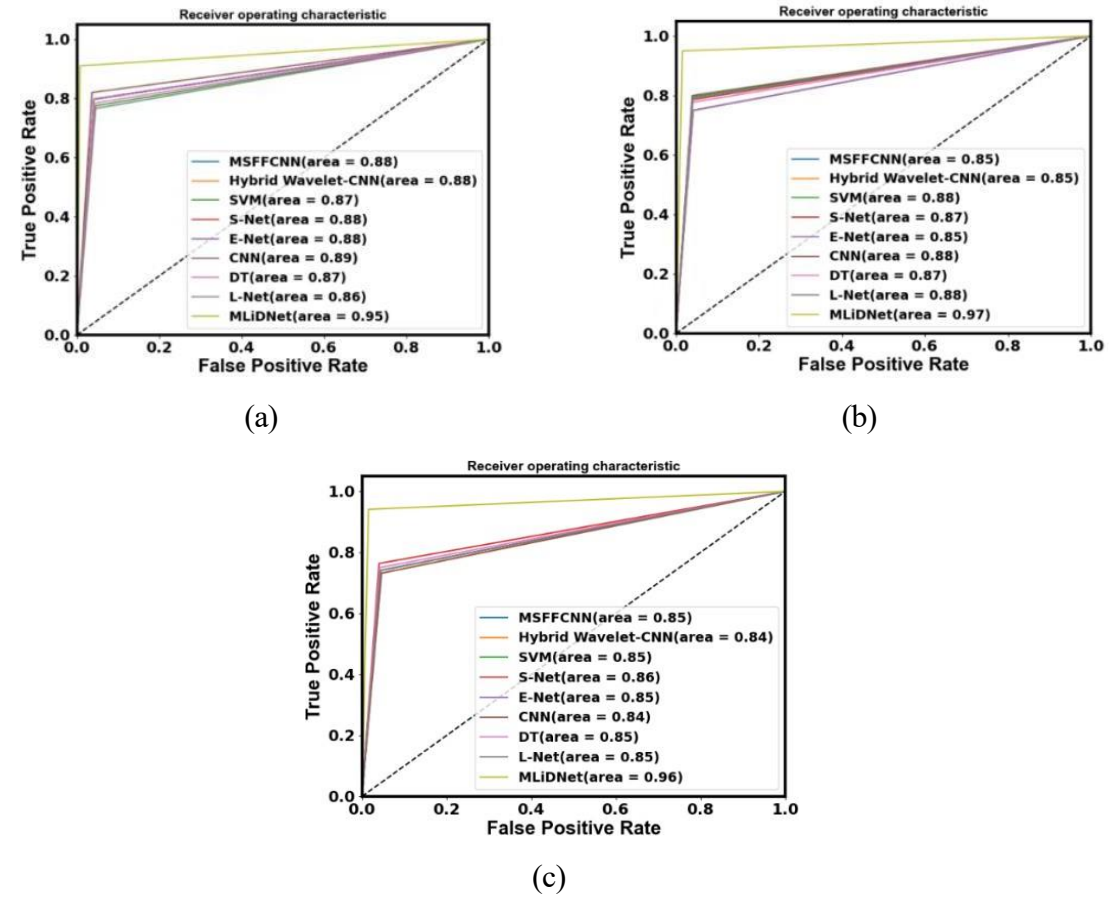


Figure 4. 26: ROC Curve analysis using 60% for dataset 1 at a) 10 Hz, b) 20 Hz, and c) 30 Hz comparing suggested and conventional models.

The efficiency of the proposed model is seen in Figure 4.26 (b), where 60% of the training data is used to obtain an area under curve (AUC) of 0.97 at a frequency of 20 Hz. The results show that the suggested model maintains a low FPR while producing a high TPR across a variety of criteria. When it comes to distinguishing between fault and healthy states at this frequency, the proposed strategy outperforms the existing methods investigated in the study, with an AUC of 0.97. The proposed demonstrates its capacity to precisely identify faults while maintaining low FPR and high TPR without appreciably misclassifying typical situations.

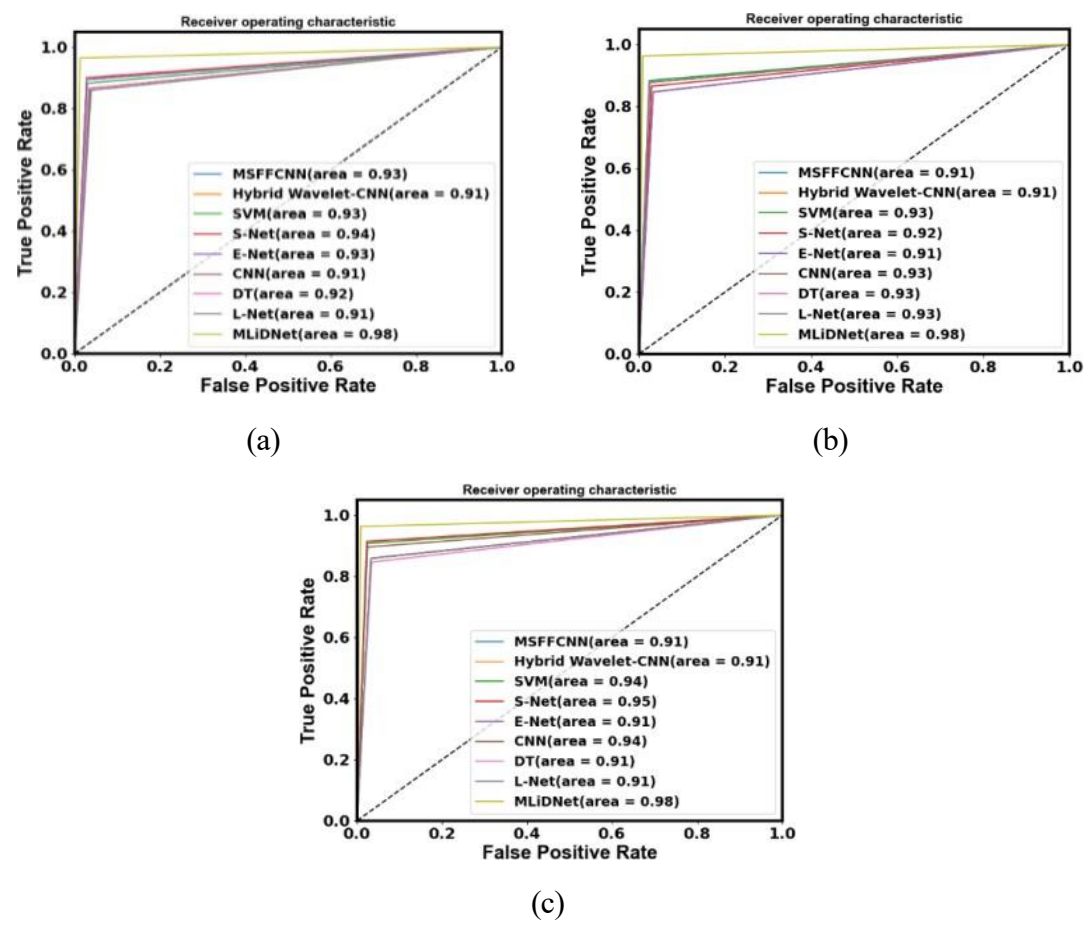


Figure 4. 27: ROC Curve analysis using 70% for dataset 1 at a) 10 Hz, b) 20 Hz, and c) 30 Hz comparing suggested and conventional models.

The examination in Figure 4.27, which makes use of 70% of the training data, highlights the suggested consistency and dependability even with a smaller dataset. The ROC curve study displays the effectiveness of the recommended and traditional fault detection techniques at different frequencies. In comparison to more conventional approaches, the proposed obtains an AUC of 0.98 at 10 Hz. With AUC values of 0.98 at 20 Hz and 30 Hz, MLiDNet maintains its excellent performance, demonstrating its dominance in fault detection.

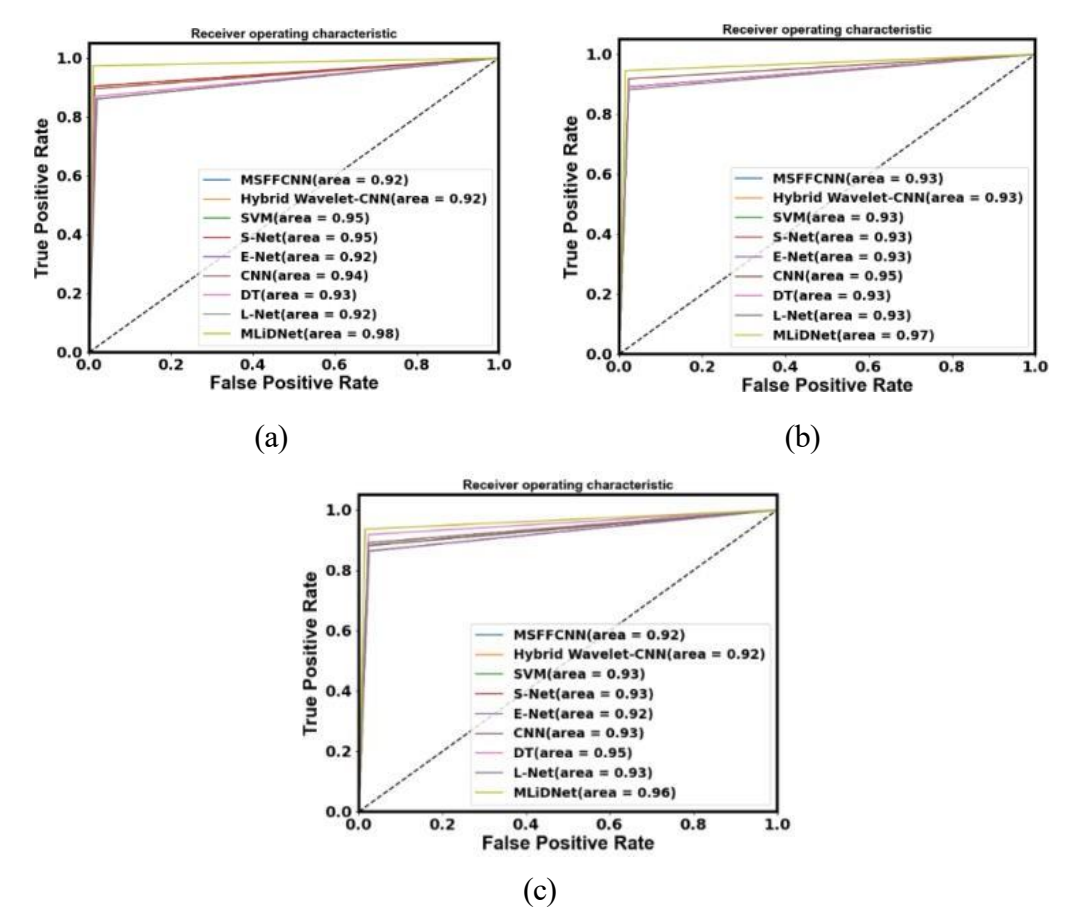


Figure 4. 28: ROC Curve analysis using 80% for dataset 1 at a) 10 Hz, b) 20 Hz, and c) 30 Hz comparing suggested and conventional models.

The ROC analysis in Figure 4.28 provides crucial details regarding the effectiveness of the suggested model across a range of frequencies for training data, 80% when compared to conventional fault recognition techniques. With an AUC of 0.98 at a frequency of 10 Hz (Figure 4.28(a)), MLiDNet performs quite well, outperforming the AUC values of conventional techniques. The outcomes show how effectively MLiDNet can distinguish between faults and healthy circumstances at this frequency.

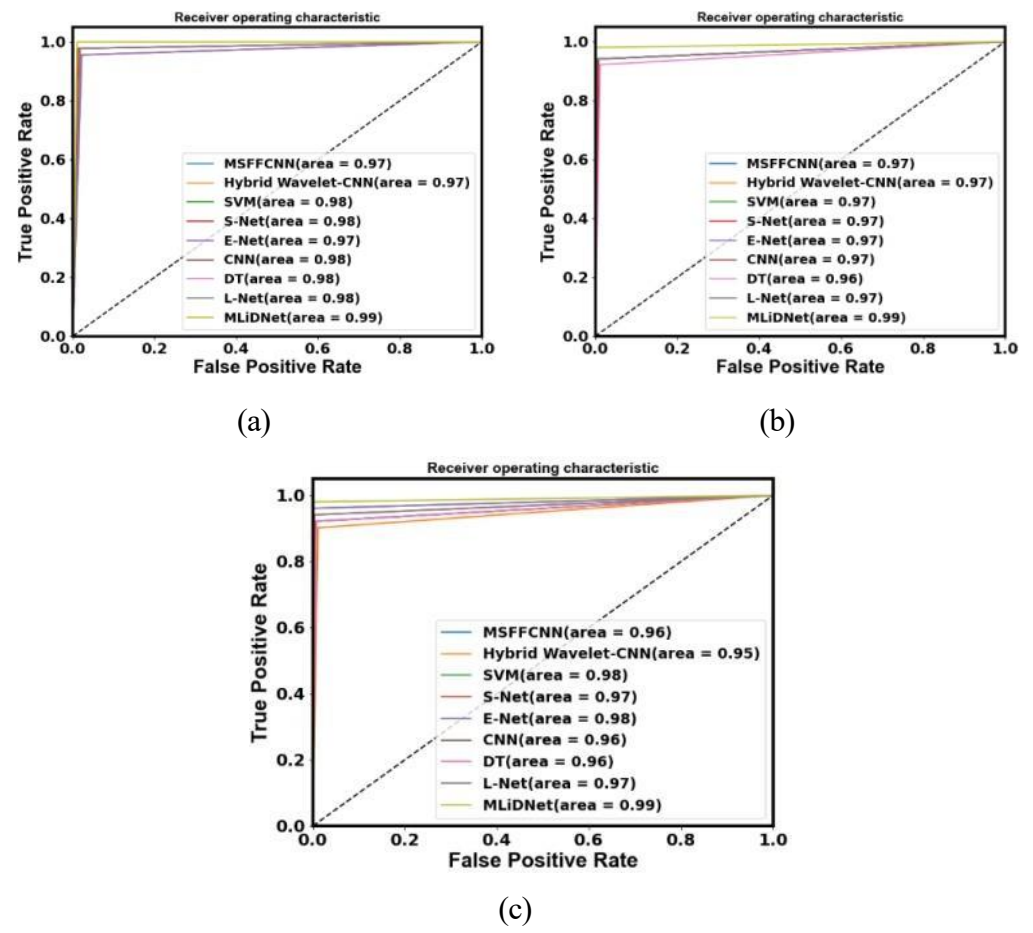


Figure 4. 29: Comparison of the suggested and existing models' ROC curves at a) 10 Hz, b) 20 Hz, and c) 30 Hz using 90% for dataset 1.

With a remarkable AUC of 0.99 at 10 Hz, the proposed exhibits exceptional sensitivity and specificity in differentiating between fault and non-fault circumstances in Figure 4.29 (a), (b), and (c). With AUC values between 0.97 and 0.98, conventional techniques demonstrate superior performance. Even though these techniques work well, MLiDNet performs somewhat better than them, which is indicative of its improved fault detection ability. MLiDNet's steep rise in the ROC curve indicates high TPR and minimal false positives. While conventional techniques display AUC values between 0.96 and 0.98, MLiDNet consistently maintains an AUC of 0.99 at 20 Hz and 30 Hz, proving its dependability and efficacy across frequencies.

4.15 Receiver Operating Characteristic Curve Analysis for Dataset 2

The TPR versus the FPR for different classification criteria is shown using a ROC curve. In a random classifier that matches the perfect classifier, the curves graphically represent the trade-off between specificity and sensitivity, while the diagonal line surrounds the upper left corner. ROC curves are essential for evaluating and comparing categorization

models' effectiveness. The ROC curve study in Figures 4.30, 4.31, 4.32, and 4.33 for EM system failure identification across frequency for training data of 60% shows how well the proposed approach performs compared to existing methods. The suggested method outperforms the conventional methods, according to the ROC curves.

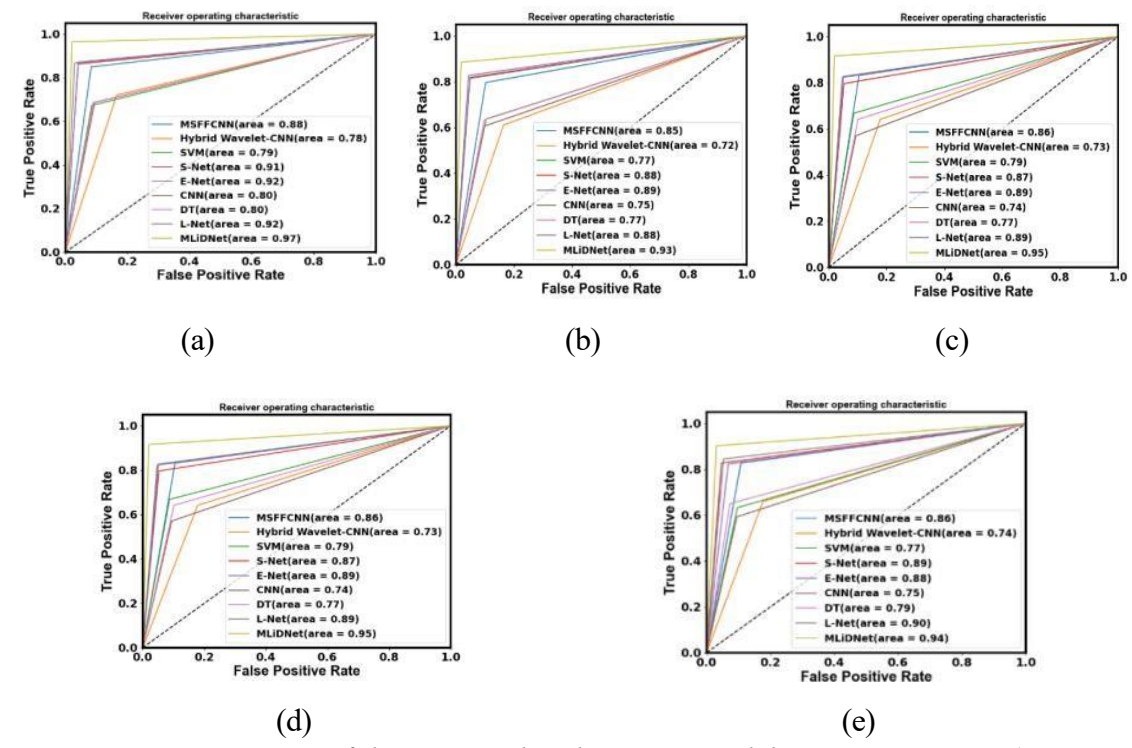


Figure 4. 30: Comparison of the proposed and existing models' ROC curves at a) 30 Hz, b) 35 Hz, c) 40 Hz, d) 45 Hz, and e) 50 Hz using 60% for dataset 2.

Figure 4.30 (a) shows the performance of the MLiDNet model at a frequency of 30 Hz with 60% training data, where its AUC of 0.97 indicates that it maintains a low FPR and a high TPR across a range of criteria. As demonstrated by the AUC value of 0.95, the method performs better than any other conventional model evaluated in the study for differentiating between fault and healthy situations at this frequency. The curve's sharp upward slope and low FPR show that the proposed model can accurately identify errors while lowering the proportion of incorrectly classified normal conditions. The findings demonstrate the MLiDNet model's dependability and efficacy in fault identification.

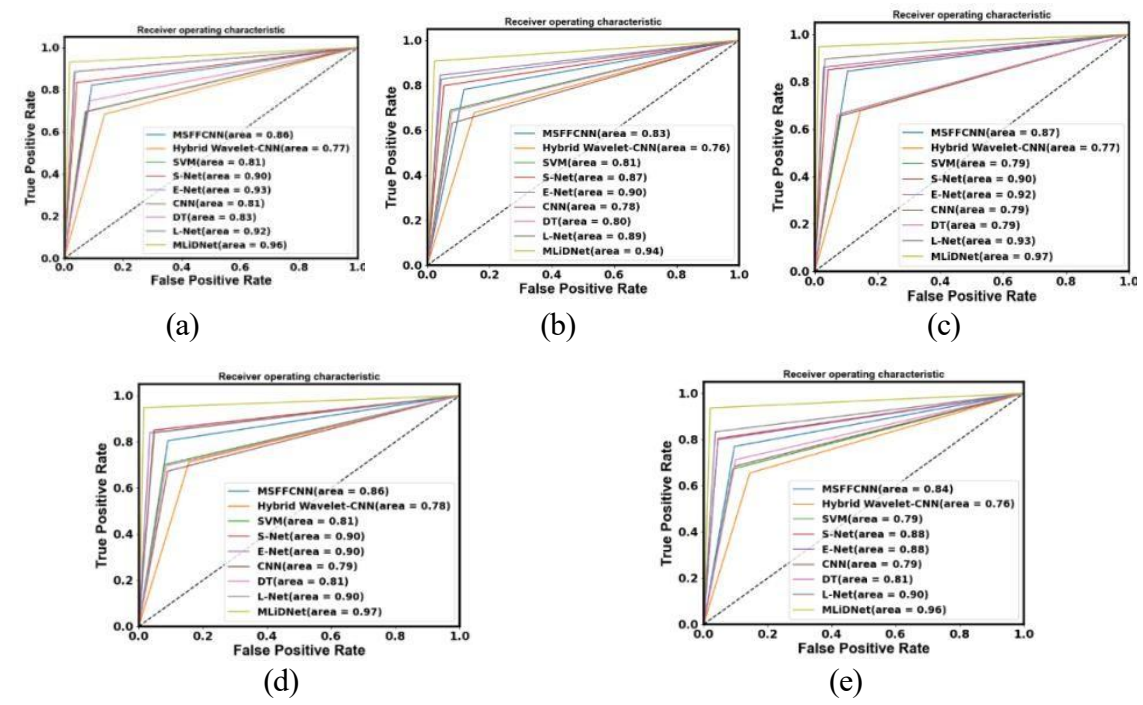


Figure 4. 31: Comparison of the suggested and existing models' ROC curves at a) 30 Hz, b) 35 Hz, c) 40 Hz, d) 45Hzand e) 50 Hz using 70% for dataset 2.

MLiDNet is reliable and consistent even when just a small portion of the dataset is used for training, as shown by the analysis in Figure 4.31, which used 70% of the training data. Thorough ROC curve comparisons could provide essential insights into how well the proposed model and traditional fault detection methods perform at various frequencies. The proposed model performs admirably at 30 Hz, with an amazing AUC of 0.96 Figure 4.31(c), (d), illustrating how MLiDNet is better than previous techniques.

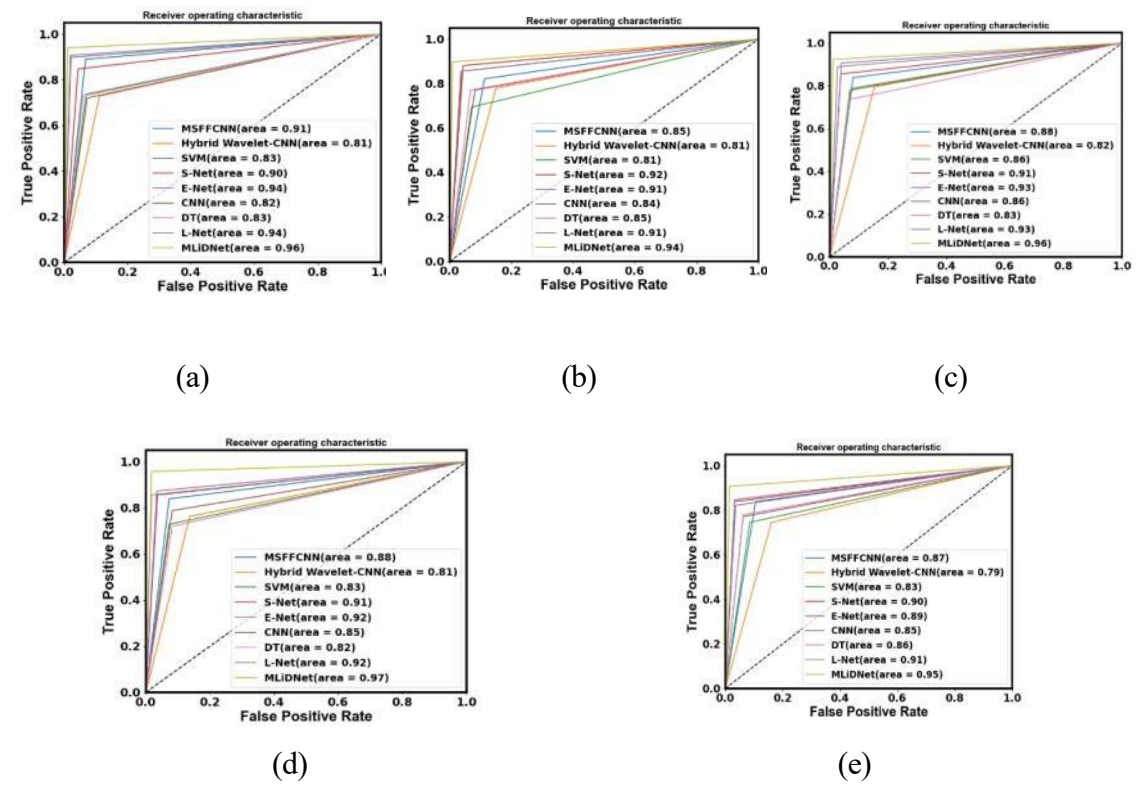


Figure 4. 32: With 80% for dataset 2, the ROC Curve performance compares the suggested and conventional models at a) 30 Hz, b) 35 Hz, c) 40 Hz, d) 45 Hz, and e) 50 Hz.

The ROC curve analysis offers valuable insights when comparing the proposed model to conventional fault detection techniques at different frequencies. It is shown in Figures 4.32 and 4.33 with training data of 80% and 90%, respectively. At a frequency of 45 Hz, MLiDNet performs better than more conventional techniques, obtaining an AUC of 0.97 (Figure 4.32(a)), demonstrating the suggested model's improved capacity to discriminate between problems and favorable conditions at this frequency.

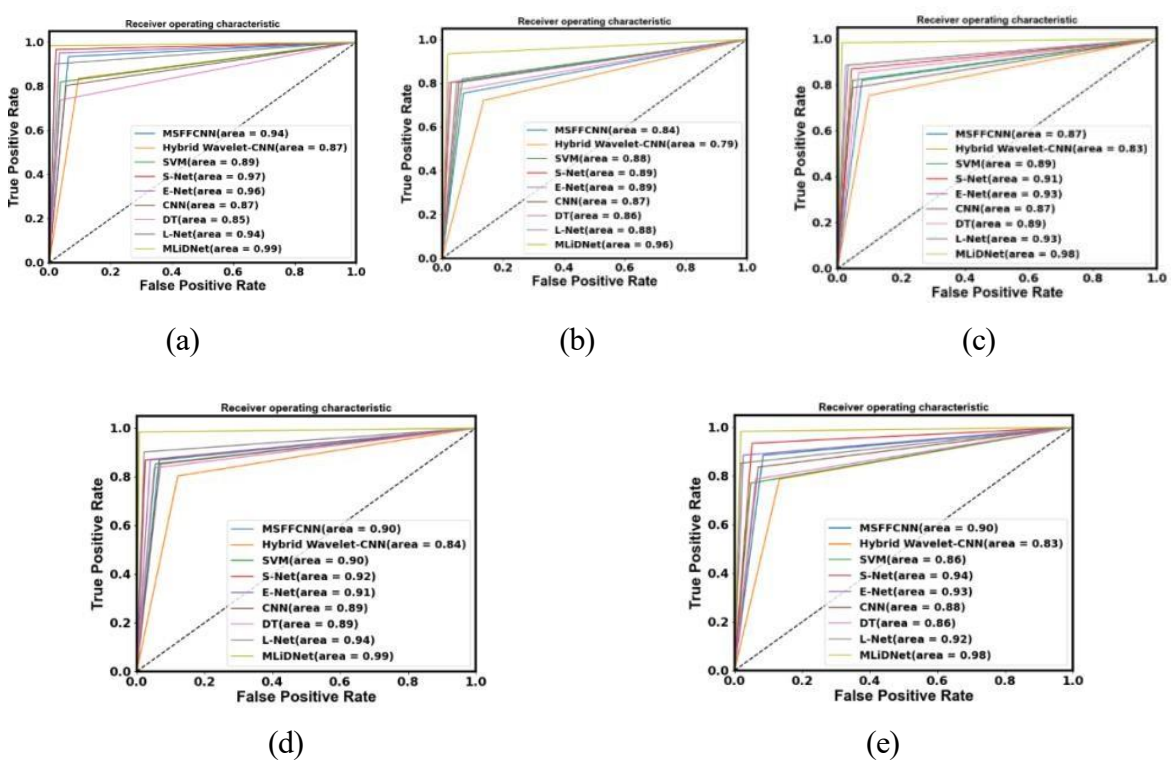


Figure 4. 33: With 90% for dataset 2, ROC curve performance comparing suggested and existing models at a) 30 Hz, b) 35 Hz, c) 40 Hz, d) 45 Hz, and e) 50 Hz.

Once more, the suggested method exhibits outstanding performance with an AUC of 0.99 at 50 Hz, proving its dependability and efficiency in fault detection jobs across a spectrum of operating frequencies. Traditional methods do reasonably well, with AUC values between 0.96 and 0.98. Even at higher frequencies, the proposed consistently high AUC value shows how reliable and resilient it is at accurately identifying faults in EM systems.

4.16 Conclusion

This chapter proposes a novel MLiDNet-based method for electromechanical fault detection that attempts to solve issues caused by electrical and mechanical imbalances. The suggested combined model outperforms conventional methods by combining modified L- Net and D-Net designs. When dataset 1 is thoroughly compared at several operating frequencies (10, 20, and 30 Hz), it is evident that MLiDNet continuously performs better than traditional techniques, obtaining more significant performance measures. After training on 90% of the data, the model produces remarkable results with an F-measure of 99.37%, accuracy of 99.68%, and precision of 99.79% at a frequency of 30 Hz. With 90% of the data, MLiDNet requires just 2.57 seconds, and with 60% of the data, it takes 1.54 seconds. On the other hand, the computational time of other models rises noticeably with

the volume of training data. For dataset 2, MLiDNet continuously outperforms conventional techniques in a thorough evaluation across a range of operating frequencies. MLiD- Net outperforms other models with a 97.42% accuracy rate, 95.23% precision rate, and 94.75% F-measure. With remarkable AUC values, ROC curve analysis validates the MLiDNet suggested model's robustness and dependability.

Chapter 5

Conclusion and Future Scope

This chapter presents the results of this study, presenting the essential advancements made in using combined DL and sophisticated signal processing techniques for gearbox and EM system fault diagnosis and detection. Furthermore, it discusses the potential expansion of this research to incorporate more advanced methods and techniques for further enhancing fault detection accuracy and system efficiency in future applications.

5.1 Conclusion

In conclusion, this research substantially adds to the EM systems and gearboxes field. It is essential for preserving the effectiveness and dependability of automotive and industrial machines. By deploying novel combined DL methodologies, it is possible to diagnose faults in the gearbox and EM system and effectively handle the vibration signals generated by different gears. The first combines Bi-LSTM with RNN models while enhancing them with the OAHCSA technique in weight optimization and achieves exceptional ac- curacies at various frequencies. It signifies the effectiveness and adaptability of the new method in accurately identifying and categorizing the detected faults in the gearbox. The research is conducted focusing on assessing potential damage to a gear with varying levels of crack severity. The initial multi-step process involved two distinct methods: CEEMDAN for pre-processing and the Bi-LSTM and IDBN classifiers. The research ex- tends the study in the diagnosis of multiple failures in EM systems using the introduction of the so-called MLiDNet, which combines different signal processing technologies like enhanced ISSWT and entropy-based feature extraction. This approach demonstrates the ability of the model-dual use of advanced signal processing and wellknown deep-learning classifiers to accurately diagnose the most complex fault scenarios, including combined faults in the EM system. The methods demonstrate outstanding potential for practical application in industry since they allow for robust and accurate fault detection and classification within gearboxes and EM systems.

Major Findings

The significant findings of the works are as follows.

- The proposed OAHCSA-HC model approach attains exceptional performance metrics, with a maximum classification accuracy, specificity, sensitivity, precision, and F1-score of 99.62%, 99.88%, 99.54%, 99.79%, and 99.66%, respectively.
- The model without statistical features reaches an accuracy of 86.9%, highlighting the benefit of feature selection and optimization. The proposed OAHCSA- HC model achieves the highest accuracy of 99.2%, indicating excellent performance. Also, in terms of computational complexity, the proposed OAHCSA- HC consistently shows the lowest computational time across all tested frequencies (15 Hz, 20 Hz, 25 Hz, and 30 Hz), with times of 3.305 seconds at 15 Hz,
 - 3.529 seconds at 20 Hz, 3.663 seconds at 25 Hz, and 4.153 seconds at 30 Hz. The outcomes highlight how well the OAHCSA-HC model balances high fault detection accuracy with minimal computational overhead.
- When the training percentage is 90%, the suggested Bi-LSTM-IDBN strategy attains the highest accuracy, achieving 99.65%. The accuracy rates of traditional approaches, on the other hand, are lower: D-Net scored 98.28%, M-Net scored 97.76%, RF scored 98.11%, SVM scored 97.76%, RNN scored 97.93%, Bi-GRU scored 97.93%, and Bi-LSTM scored 98.45%, and DCNN scored 97.93%.
- In the ablation study, the Bi-LSTM-IDBN model achieved an accuracy of 99.65% at 15 Hz, outperforming models utilizing traditional CEEMDAN, conventional cross-correntropy, and standard DBN, which attained accuracies of 98.28%, 98.45%, and 98.62%, respectively. Notably, at 20 Hz, the Bi-LSTM-IDBN model demonstrated a significantly reduced computation time of 0.9937 seconds. In contrast, traditional approaches exhibited substantially higher computational costs, with D-Net requiring 6.53 seconds, M-Net 5.64 seconds, RF
 - 1.388 seconds, SVM 5.668 seconds, RNN 1.583 seconds, Bi-GRU 7.823 seconds, Bi-LSTM 3.633 seconds, and DCNN 2.101 seconds.
- The suggested MLiDNet continuously beats traditional methods, achieving 97.42% accuracy, 95.23% precision, and 94.75% F-measure. In the Ablation

- investigation, the accuracy of the proposed model is 98.69% at 50 Hz, compared to 91.99% for the traditional SSWT.
- The accuracy without feature selection is 91.89%, 96.09% for the L-Net, 90.05% for the D-Net, and 93.27% for the ML-Net. MLiDNet's computation time is only 2.08 seconds when 60% of the training data is used, and it slightly increases to 3.23 seconds when 90% of the training data is used. This outcome shows that MLiDNet can sustain low processing requirements even as the volume of training data grows. However, the computation times of other models are substantially longer.

5.2 Future Scope

This thesis focuses on essential challenge-based CM approaches for fault detection in bevel gears and EM systems. However, several areas still require further investigation. To further this research, the following study directions are suggested for future work.

- The proposed approach can also be used to diagnose combined local faults at the micron level that may occur in a gearbox.
- Additionally, the methodology can be extended to analyze various gear types for fault diagnosis, including spur gears, helical gears, planetary gears, and others.
- Incorporating advanced signal processing into the model can enhance its ability to manage noisy or low-quality data, improving real-time data processing and enabling on-the-fly adjustments in dynamic environments.
- This approach can potentially be used in the aerospace and automotive diagnostics industries. Still, more effort is needed to integrate advanced optimization techniques to improve efficiency and reduce time consumption for industrial applications.

REFERENCES

- [1] Wu B., Yuegang L. Research on gear fault diagnosis and feature extraction method. In 2020 International Conference on Artificial Intelligence and Electromechanical Automation (AIEA)2020; 512-515. IEEE.
- [2] Gu Z., Mian Z., Yue M., Kesheng W., Hongbiao X., Jiwei C., Taoyong W., Ruitong X., Jie L. Intelligent fault diagnosis of a planetary gearbox based on dynamic frequency energy ratio scheme. Measurement Science and Technology 2021; 32 (10): 104013.
- [3] Hamid MNA, Ismail M., Yusuf ZNM. Frequency Domain Technique for Characterizing Spur Gears Defect Pattern. In IOP Conference Series: Materials Science and Engineering2020; 815(1): 012006. IOP Publishing.
- [4] Tama BA., Malinda V., Seungchul L., Sunghoon L. Recent advances in the application of deep learning for fault diagnosis of rotating machinery using vibration signals. Artificial Intelligence Review2023; 56(5): 4667-4709.
- [5] Jayaswal P., Wadhwani AK., Mulchandani KB. Machine fault signature analysis. Int J Rotating Mach2008. https://doi.org/10.1155/2008/583982.
- [6] Davies A. Handbook of Condition Monitoring: Techniques and Methodology.1998.
- [7] Keith MR. An introduction to predictive maintenance 2002; 42.
- [8] Rao SS. Mechanical vibrations2012; 9781461404. https://doi.org/10.1007/978-1-4614-0460-6.
- [9] Ebersbach S., Peng Z., Kessissoglou NJ. The investigation of the condition and faults of a spur gearbox using vibration and wear debris analysis techniques. Wear2006; 260: 16–24. https://doi.org/10.1016/j.wear.2004.12.028.
- [10] Lebold M., Mcclintic K., Campbell R., Byington C., Maynard K. Review of vibration analysis methods for gearbox diagnostics and prognostics. 54th Meet Soc Mach Fail Prev Technol2000; 623–34.
- [11] Eftekharnejad B., Mba D. Seeded fault detection on helical gears with acoustic emission. Appl Acoust2009; 70: 547–55. https://doi.org/10.1016/j.apacoust.2008.07.006.
- [12] Henriquez P., Alonso JB., Ferrer MA., Travieso CM. Review of automatic fault diagnosis systems using audio and vibration signals. IEEE Trans Syst Man, Cybern Syst2014; 44: 642–52. https://doi.org/10.1109/TSMCC.2013.2257752.

- [13] Bellini A., Immovilli F., Rubini R., Tassoni C. Diagnosis of bearing faults in induction machines by vibration or current signals: A critical comparison. Conf Rec- IAS AnnuMeet (IEEE Ind Appl Soc2008; 46: 1350-9. https://doi.org/10.1109/08IAS.2008.26.
- [14] McFadden PD. Detecting fatigue cracks in gears by amplitude and phase demodulation of the meshing vibration. J Vib Acoust Trans ASME1986; 108: 165–70. https://doi.org/10.1115/1.3269317.
- [15] Wang W. Early detection of gear tooth cracking using the resonance demodulation technique. Mech Syst Signal Process2001; 15: 887–903. https://doi.org/10.1006/mssp.2001.1416.
- [16] Baydar N., Ball A. Detection of gear deterioration under varying load conditions by using the instantaneous power spectrum. Mech Syst Signal Process2000; 14: 907–21. https://doi.org/10.1006/mssp.1999.1281.
- [17] Sawalhi N., Randall RB. Gear parameter identification in a wind turbine gearbox using vibration signals. Mech Syst Signal Process2014; 42: 368–76. https://doi.org/10.1016/j.ymssp.2013.08.017.
- [18] Pandya Y., Parey A. Failure path based modified gear mesh stiffness for spur gear pair with tooth root crack. Eng Fail Anal2013; 27: 286–96. https://doi.org/10.1016/j.engfailanal.2012.08.015.
- [19] Shen CH., Wen J., Arunyanart P., Choy FK. Vibration Signature Analysis and Parameter Extractions on Damages in Gears and Rolling Element Bearings. ISRN Mech Eng2011; 1–10. https://doi.org/10.5402/2011/402928.
- [20] Mark WD., Reagor CP. Static-transmission-error vibratory-excitation contributions from plastically deformed gear teeth caused by tooth bending-fatigue damage. Mech Syst Signal Process2007; 21: 885–905. https://doi.org/10.1016/j.ymssp.2006.05.002.
- [21] Shipley EE. Gear failures. Mach Des1967;1–8. https://doi.org/10.1016/b978-075065154-7/50107-8.
- [22] Bajrić R., Sprečić D., Zuber N. Review of vibration signal processing techniques towards gear pairs damage identification. Int J Eng Technol IJET-IJENS2011; 11: 124–8.
- [23] Nie M., Wang L. Review of condition monitoring and fault diagnosis technologies for wind turbine gearbox. Procedia CIRP2013; 11: 287–90. https://doi.org/10.1016/j.procir.2013.07.018.

- [24] Giurgiutiu V., Cuc A., Goodman P. Review of Vibration-Based Helicopters Health and Usage. Prevention2001; 1–10.
- [25] Samuel PD, Pines DJ. A review of vibration-based techniques for helicopter transmission diagnostics2005; 282. https://doi.org/10.1016/j.jsv.2004.02.058.
- [26] Lei Y., Lin J., Zuo MJ., He Z. Condition monitoring and fault diagnosis of planetary gearboxes: A review. Meas J Int Meas Confed2014; 48: 292–305. https://doi.org/10.1016/j.measurement.2013.11.012.
- [27] Randall RB. A new method of modeling gear faults. J Mech Des Trans ASME1041982; 259–67. https://doi.org/10.1115/1.3256334.
- [28] Mcfadden PD., Smith JD. A signal processing technique for detecting local defects in a gear from the signal average of the vibration. Proc Inst Mech Eng Part
 C J Mech Eng Sci1985; 199: 287–92. https://doi.org/10.1243/PIME PROC 1985 199 125 02.
- [29] Bonnardot F., El Badaoui M., Randall RB., Danière J., Guillet F. Use of the acceleration signal of a gearbox in order to perform angular resampling (with limited speed fluctuation). Mech Syst Signal Process2005; 19: 766–85. https://doi.org/10.1016/j.ymssp.2004.05.001.
- [30] Mahgoun H., Chaari F., Felkaoui A. Detection of gear faults in variable rotating speed using variational mode decomposition (VMD), Mechanics and Industry 2016; 17(2).doi: 10.1051/meca/2015058.
- [31] Sharma V., Parey A. Gear crack detection using modified TSA and proposed fault indicators for fluctuating speed conditions, Measurement (Lond)2016; 90: 560–575, doi: 10.1016/j.measurement..04.076.
- [32] Igba J., Alemzadeh K., Durugbo C., Eiriksson ET. Analysing RMS and peak values of vibration signals for condition monitoring of wind turbine gearboxes, Re- new Energy2016; 91: 90–106.doi: 10.1016/j.renene.2016.01.006.
- [33] Youssef W., Guillet F., Elbadaoui M. Gear spall width estimation using maximum kurtosis property, in IFAC Proceedings Volumes 2009;1715–1719. doi: 10.3182/20090706-3-FR-2004.0319.
- [34] Delgado-Arredondo PA., Garcia-Perez A., Morinigo-Sotelo D., Osornio-Rios RA., Avina-Cervantes JG., Rostro-Gonzalez H., et al. Comparative Study of Time-Frequency Decomposition Techniques for Fault Detection in Induction Motors Using Vibration Analysis during Startup Transient. Shock Vib, 2015. https://doi.org/10.1155/2015/708034.

- [35] Kim J., Sang-Kwon L. Identification of tooth fault in a gearbox based on cyclostationarity and empirical mode decomposition. Structural Health Monitoring2018; 17 (3): 494-513.
- [36] Adam AM. Time-frequency domain analysis of exchange rate market integration in Southern Africa Development Community: A Hilbert-Huang Transform approach. PhD diss.2022.
- [37] Maitra GM. Handbook of gear design. Tata McGraw-Hill Publ. Co Ltd1994; 16: 536.
- [38] Li Z., Jiang Y., Wang X., Peng Z. Multi-mode separation and nonlinear feature extraction of hybrid gear failures in coal cutters using adaptive non-stationary vibration analysis, Nonlinear Dyn2016; 84(1): 295–310.doi: 10.1007/s11071-015-2505-3.
- [39] Salameh JP., Cauet S., Etien E., Sakout A., Rambault L. Gearbox condition monitoring in wind turbines: A review, Mechanical Systems and Signal Processing2018;0 111: 251–264.doi: 10.1016/j.ymssp.2018.03.052.
- [40] Černe B., Petkovšek M., Duhovnik J., Tavčar J. Thermo-mechanical modeling of polymer spur gears with experimental validation using high-speed infrared thermography, Mech Mach Theory2020; 146.doi: 10.1016/j.mechmachtheory.2019.103734.
- [41] Yatsugi K., Pandarakone S.E., Mizuno Y., Nakamura H. Common Diagnosis Approach to Three-Class Induction Motor Faults Using Stator Current Feature and Support Vector Machine. IEEE Access 2023; 11: 24945-24952. https://doi:10.1109/ACCESS.2023.3254914.
- [42] Pietrzak P., Wolkiewicz M. Fault diagnosis of PMSM stator winding based on continuous wavelet transform analysis of stator phase current signal and selected artificial intelligence techniques. Electronics2023; 12(7):1543. https://doi.org/10.3390/electronics12071543.
- [43] Hajiaghas S, Rafiee Z., Salemnia A., Aghamohammadi M., Soleymaniaghdam T. A new strategy for induction motor fault detection based on wavelet transform and probabilistic neural network. In 2019 5th Conference on Knowledge Based Engineering and Innovation (KBEI) 2019; 118-123. https://doi:10.1109/ACCESS.2023.3254914

- [44] Abid FB, MarwenS, Ahmed B.Robust interpretable deep learning for intelligent fault diagnosis of induction motors. IEEE Transactions on Instrumentation and Measurement 2019; 69(6): 3506-3515.
- [45] Kim, Min-Chan, Jong-Hyun Lee, Dong-Hun Wang, and In-Soo Lee. "Induction motor fault diagnosis using support vector machine, neural networks, and boosting methods." Sensors 23, no. 5 (2023): 2585.
- [46] Singh M., Gafoor SA. Incipient fault detection in stator windings of an induction motor using Stockwell transform and SVM. IEEE Trans Instrum Meas2020; 69(12): 9496-9504. https://doi: 10.1109/TIM.2020.3002444
- [47] Jiang BS., Kin W.P., Chun LY. A fault diagnostic method for induction motors based on feature incremental broad learning and singular value decomposition.

 IEEE Access2019; 7: 157796-157806. https://doi: 10.1109/ACCESS.2019.2950240
- [48] Parvathi SB., Hemamalini S. Rational-dilation wavelet transform based torque estimation from acoustic signals for fault diagnosis in a three-phase induction motor. IEEE Trans Industry Inform, 2018; 15(6): 3492-3501. https://doi: 10.1109/TII.2018.2874463
- [49] Li Z., Yan X., Yuan C., Peng Z., Li L. Virtual prototype and experimental research on gear multi-fault diagnosis using wavelet-autoregressive model and principal component analysis method, Mech Syst Signal Process 2011; 25(7): 2589–2607. doi: 10.1016/j.ymssp.2011.02.017.
- [50] Saravanan N., Ramachandran KI. Incipient gear box fault diagnosis using discrete wavelet transform (DWT) for feature extraction and classification using artificial neural network (ANN), Expert Syst Appl2010; 37(6): 4168–4181.doi: 10.1016/j.eswa.2009.11.006.
- [51] Sharma V., Parey A. Frequency domain averaging based experimental evaluation of gear fault without tachometer for fluctuating speed conditions," Mech Syst Signal Process2017; 85: 278–295.doi: 10.1016/j.ymssp.2016.08.015.
- [52] Iorgulescu M., Beloiu R. Vibration and current monitoring for fault's diagnosis of induction motors. Annals of the University of Craiova, electrical engineering series 2008; (32): 102-107.
- [53] Chang SC., Yacamini, R. Experimental study of the vibrational behaviour of machine stators. IEE Proceedings-Electric Power Applications 1996; 143(3): 242-250.

- [54] Maruthi GS., Vittal KP. Electrical fault detection in three phase squirrel cage induction motor by vibration analysis using MEMS accelerometer. In 2005 International Conference on Power Electronics and Drives 2005.
- [55] Yen GG., Lin, KC. Wavelet packet feature extraction for vibration monitoring. IEEE transactions on industrial electronics 2000; 47(3): 650-66ystems IEEE.
- [56] Da Silva AM., PovinelliRJ., Demerdash NA. Induction machine broken bar and stator short-circuit fault diagnostics based on three-phase stator current envelopes. IEEE Transactions on Industrial Electronics2008; 55(3): 1310-1318.
- [57] Benbouzid MEH., Vieira M., Theys, C. Induction motors' faults detection and localization using stator current advanced signal processing techniques. IEEE Transactions on power electronics1999; 14(1): 14-22.
- [58] Blodt M., Granjon P., Raison B., Rostaing G. Models for bearing damage detection in induction motors using stator current monitoring. IEEE transactions on industrial electronics2008; 55(4): 1813-1822.
- [59] Akcay H., Germen E. Identification of acoustic spectra for fault detection in induction motors. In AFRICON 2013;1-5. IEEE.
- [60] Alsaedi MA. Fault Diagnosis of Three-Phase Induction Motor: A Review. Optics. Special Issue: Applied Optics and Signal Processing2015; 4(1-1): 1-8.
- [61] Kral C., Habetler TG., Harley RG., Pirker F., Pascoli G., Oberguggenberger H., Fenz CJM. A comparison of rotor faulty detection technique with respect to the assessment of fault severity. In 4th IEEE international conference on diagnostics fr Electric machines, power electronics and deives, 2003. SDEMPED 2003; 265-270, IEEE, 2003
- [62] Hu C., Smith W.A., Randall R.B., Peng Z. (2016), Development of a gear vibration indicator and its application in gear wear monitoring. Mech Syst Signal Process, 76–77, 319–36. https://doi.org/10.1016/j.ymssp.2016.01.018.
- [63] Sharma S, Shalabh KT. Residual signal–based condition monitoring of planetary gearbox using electrical signature analysis. Journal of Vibration and Control 2024; 30(11-12): 2430-2439.
- [64] Allmark MatthewJ. Condition monitoring and fault diagnosis of tidal stream turbines subjected to rotor imbalance faults. PhD diss., Cardiff University 2016.
- [65] Elforjani M., Mba D. Detecting natural crack initiation and growth in slow speed shafts with the Acoustic Emission technology. Eng Fail Anal2009;16:2121–9. https://doi.org/10.1016/j.engfailanal. 02.005.

- [66] Kim J., Sang-Kwon L. Identification of tooth fault in a gearbox based on cyclostationarity and empirical mode decomposition. Structural Health Monitoring2018; 17 (3): 494-513.
- [67] Palmgren A. Ball and Roller Bearing Engineering. Philadelphia: S.H. Burbank and Co, 1947.
- [68] Qiu J., Seth BB., Liang SY., Zhang C. damage mechanics approach for bearing lifetime prognostics, Mechanical Systems and Signal Processing2002; 16(5): 817–829, Sep., https://doi.org/10.1006/mssp.2002.1483
- [69] Gupta P., Pradhan MK. Fault detection analysis in rolling element bearing: A review, Materials Today: Proceedings2017; 4(2): 2085–2094. https://doi.org/10.1016/j.matpr.2017.02.054
- [70] Howard I. A Review of Rolling Element Bearing Vibration "Detection, Diagnosis and Prognosis, Department of Defence, Melbourne1994.
- [71] Saruhan H. Sandemir S., Çiçek A., Uygur I. Vibration analysis of rolling element bearings defects, Journal of Applied Research and Technology2014; 12(3): 384–395, Jun., https://doi.org/10.1016/s1665-6423(14)71620-7
- [72] Althubaiti A., Faris E., Joao AT. Fault diagnosis and health management of bearings in rotating equipment based on vibration analysis—a review. Journal of Vibroengineering2022; 24(1): 46-74.
- [73] Avdaković S., Maja MD., Edina Sadiković ED., Šiljak A. Fault Diagnostics in Wind Turbines Utilizing Advanced Signal Processing Techniques-A Literature Review. In International Symposium on Innovative and Interdisciplinary Applications of Advanced Technologies2024; 731-748. Cham: Springer Nature Switzerland.
- [74] Chandra NH., Sekhar AS. Fault detection in rotor bearing systems using time frequency techniques. Mechanical Systems and Signal Processing2016; 72: 105-133.
- [75] Rai A, Sanjay H. Upadhyay. A review on signal processing techniques utilized in the fault diagnosis of rolling element bearings. Tribology International 2016; 96: 289-306.
- [76] Aghababaeyan, Zohreh, Manel Abdellatif, Lionel Briand, S. Ramesh, and Mojtaba Bagherzadeh. "Black-box testing of deep neural networks through test case diversity." IEEE Transactions on Software Engineering 49, no. 5 (2023): 3182-3204.

- [77] Wan Peng, Bolan L, Ben L, Fanshuo L, Junwei Z, Wenhao F, Jingxian T. Engine modelling architecture study for hybrid electric vehicle diagnosis application. Energy 2023; 282: 128408.
- [78] Li Heng, Qing Z, Xianrong Q, Yuantao S. K-SVD-based WVD enhancement algorithm for planetary gearbox fault diagnosis under a CNN framework. Measurement Science and Technology 2019; 31(2): 025003.
- [79] Zhang Y, Yunfei D, Yangtian Z, Fudi G. A Review of Machine Learning-Based Icing Prediction Methods for Wind Turbine Blades. In International conference on the Efficiency and Performance Engineering Network 2024; 100-109. Cham: Springer Nature Switzerland.
- [80] Han Y., Chen S., Gong C., Zhao X., Zhang F., Li Y. Accurate SM disturbance observer-based demagnetization fault diagnosis with parameter mismatch impacts eliminated for IPM motors, IEEE Trans. Power Electron2023; 38(5): 5706-5710, May.
- [81] Manarikkal, Imthiyas, Faris Elasha, and David Mba. "Diagnostics and prognostics of planetary gearbox using CWT, auto regression (AR) and K-means algorithm." Applied Acoustics 184 (2021): 108314.
- [82] Liu H., Wang W., Xiang C., Han L., Nie H. A de-noising method using the improved wavelet threshold function based on noise variance estimation. Mech Syst Signal Process 2018; 99: 30–46. https://doi.org/10.1016/j.ymssp.2017.05.034
- [83] Shao S., Yan R., Lu Y., Wang P., Gao RX. DCNN-based multi-signal induction motor fault diagnosis. Trans Instrum Meas2019; 69(6):2658–2669. https://doi.org/10.1109/TIM.2019.2925247
- [84] Choudhary A., Mishra RK., Fatima S., Ketan P.B. Multi-input CNN based vibroacoustic fusion for accurate fault diagnosis of induction motor. Eng Appl Artif. Intell. 2023; 120: 105872. https://doi.org/10.1016/j.engappai.2023.105872
- [85] Sun W., Zhao R., Yan R., Shao S., Chen X. Convolutional discriminative feature learning for induction motor fault diagnosis. IEEE Trans Industr Inform2017; 13(3): 1350–1359. https://doi.org/10.1109/TII.2017.2672988
- [86] El-Dalahmeh M., Al-Greer M., Bashir I., Mo'ath El-Dalahmeh., Demirel A., Keysan O. Autonomous fault detection and diagnosis for permanent magnet synchronous motors using combined variational mode decomposition, the Hilbert-Huang transform, and a convolutional neural network. ComputElectr Eng2023;

- 110: 108894. https://doi.org/10.1016/j.compeleceng.2023.108894
- [87] Song Y., Du J., Li S., Long Y., Liang D., Liu Y., Wang Y. Multi-scale feature fusion convolutional neural networks for fault diagnosis of electromechanical actuator. Appl Sci2023; 13(15): 8689. https://doi.org/10.3390/app13158689
- [88] He Z., Pengpeng C., Chenxi L., Kanjian Z., Haikun W., Yihua H. Compound fault diagnosis for photovoltaic arrays based on multi-label learning considering multiple faults coupling. Energy Conversion and Management 2023; 279: 116742.
- [89] Xu X., Cao D., Zhou Y., Gao J. Application of neural network algorithm in fault diagnosis of mechanical intelligence. Mech Syst Signal Process2020a; 141: 106625
- [90] Yang D., Yilun L., Songbai L., Xuejun L., Liyong M. Gear fault diagnosis based on support vector machine optimized by artificial bee colony algorithm. Mechanism and Machine Theory2015; 90: 219-229.
- [91] Wan L., Kun G., Gen Z., Xinpan Y., Changyun L., Xiaojun D. An efficient rolling bearing fault diagnosis method based on spark and improved random forest algorithm. IEEE Access2021; 9: 37866-37882.
- [92] Li Y. Exploring real-time fault detection of high-speed train traction motor based on machine learning and wavelet analysis. Neural Computing and Applications 2022; 34(12): 9301-9314.
- [93] Gao S., Lintao X., Yimin Z., Zhiming P. Rolling bearing fault diagnosis based on SSA optimized self-adaptive DBN. ISA transactions2022; 128, 485-502.
- [94] Niu G., Xuan W., Michael G., Stephen M., Bin Z. An optimized adaptive PReLU-DBN for rolling element bearing fault diagnosis. Neurocomputing2021;445: 26-34.
- [95] Zhao X., Jiaxin W., Yonghong Z., Yunqing S., Lihua W. Fault Diagnosis of Motor in Frequency Domain Signal by Stacked De-noising Auto-encoder. Computers, Materials & Continua2018; 57(2).
- [96] Chen R., Siyang C., Miao H., David H., Baoping T. Rolling bearing fault severity identification using deep sparse auto-encoder network with noise added sample expansion. Proceedings of the Institution of Mechanical Engineers, Part O: Journal of Risk and Reliability2017; 231 (6): 666-679.
- [97] Liu H., Jianzhong Z., Yang Z., Wei J., Yuncheng Z. Fault diagnosis of rolling bearings with recurrent neural network-based autoencoders. ISA transactions 2018; 77: 167-178.

- [98] Jiang H., Xingqiu L., Haidong S., Ke Z. Intelligent fault diagnosis of rolling bearings using an improved deep recurrent neural network. Measurement Science and Technology2018; 29(6): 065107.
- [99] Wang Z., Yingxue T., Yanping D., Shuihai D., Huijuan B. (2023). Optimization of gearbox fault detection method based on deep residual neural network algorithm. Sensors, 23(17), 7573.
- [100] Lin, Shih-Lin. "Intelligent fault diagnosis and forecast of time-varying bearing based on deep learning VMD-DenseNet." Sensors 21, no. 22 (2021): 7467.
- [101] Wang, Jing, Xiwei Fan, Yunlong Zhang, Xuefei Zhang, Zhijie Zhang, Wenyu Nie, Yuanmeng Qi, and Nan Zhang. "Railway Tracks Extraction from High Resolution Unmanned Aerial Vehicle Images Using Improved NL-LinkNet Network."

 Drones 8, no. 11 (2024): 611.
- [102] Babu, T. Narendiranath, P. SahirNowshad Ali, D. Rama Prabha, V. Noor Mohammed, Razia Sultana Wahab, and S. Vijayalakshmi. "Fault Diagnosis in Bevel Gearbox Using Coiflet Wavelet and Fault Classification Based on ANN Including DNN." Arabian Journal for Science and Engineering 47, no. 12 (2022): 15823-15849.
- [103] Contreras Urgilés, Rafael Wilmer, José Maldonado Ortega, Esteban Rocano, and Jorge Chiluisa. "Classification of Mechanical Failures in Provoked Ignition Engine by Means of ANN and SVM." In International Conference on Science, Technology and Innovation for Society, pp. 161-172. Cham: Springer Nature Switzer-land, 2022.
- [104] Kim HS, Min JK and Song JB. Multiple-Degree-of-Freedom Counterbalance Robot Arm Based on Slider-Crank Mechanism and Bevel Gear Units. IEEE Trans- actions on Robotics 2016; 32:230–235.
- [105] Zhao D, Li J, Cheng W and He Z. Generalized Demodulation Transform for Bearing Fault Diagnosis Under Nonstationary Conditions and Gear Noise Interferences. Chinese Journal of Mechanical Engineering (English Edition).2019a; 32.
- [106] Zhou Z, Li T, Zhao Z, Sun C, Yan R and Chen X. Differentiable Architecture Search for Aeroengine Bevel Gear Fault Diagnosis. International Conference on Sensing, Measurement and Data Analytics in the Era of Artificial Intelligence, ICSMD 2020 Proceedings, Institute of Electrical and Electronics Engineers Inc.

- 2020; 270–274.
- [107] Mu, Yanming, and Xueming He. "Design and dynamic performance analysis of high-contact-ratio spiral bevel gear based on the higher-order tooth surface modification." Mechanism and Machine Theory 161 (2021): 104312.
- [108] Kim J, Han HT, Kang S and Kim C. Development of Novel Bevel-Geared 5 mm Articulating Wrist for Micro-Laparoscopy Instrument. IEEE Robot Autom Lett 2019; 4:3711–3718.
- [109] Mu Y, He X, Fang Z. An innovative ease-off flank modification method based on the dynamic performance for high-speed spiral bevel gear with high-contact-ratio. Mechanism and Machine Theory. 2021; 162:104345.
- [110] Zhao W, Wang L and Mirjalili S. Artificial hummingbird algorithm: A new bioinspired optimizer with its engineering applications. Comput Methods Appl Mech Eng 2022; 388.
- [111] Sun, Liang, Yuzhu Zhou, Hengmin Huang, Chuanyu Wu, and Guofeng Zhang.

 "Analysis and design of a spatial planetary noncircular gear train for rice seedling transplanting based on three given positions." Transactions of the ASABE 63, no. 1 (2020): 165-176.
- [112] Li Y, Zhou Z, Sun C, Yan R and Chen X. Domain Adaptive Sparse Transformer for Aeroengine Bevel Gear Fault Diagnosis. ICSMD 2021 2nd International Conference on Sensing, Measurement and Data Analytics in the Era of Artificial Intelligence, Institute of Electrical and Electronics Engineers Inc. 2021.
- [113] Shang Z, Zhao Z, Zhou Z, Sun C, Sun Y and Yan R. Denoising Fused Wavelets Net for Aeroengine Bevel Gear Fault Diagnosis. ICSMD 2021 2nd International Conference on Sensing, Measurement and Data Analytics in the Era of Artificial Intelligence, Institute of Electrical and Electronics Engineers Inc. 2021.
- [114] Wang K. Phase information at tooth mesh frequency for gear crack diagnosis. In 2007 2nd IEEE Conference on Industrial Electronics and Applications 2007; (pp. 2712-2717). IEEE.
- [115] Neupane, Dhiraj, Mohamed Reda Bouadjenek, Richard Dazeley, and Sunil Aryal. "Data-driven Machinery Fault Detection: A Comprehensive Review." arXiv preprint arXiv:2405.18843 (2024).
- [116] Kumar, T. Praveen, M. Saimurugan, RB Hari Haran, S. Siddharth, and K. I. Ramachandran. "A multi-sensor information fusion for fault diagnosis of a gearbox utilizing discrete wavelet features." Measurement Science and Technology 30, no.

- 8 (2019): 085101.
- [117] Tin, Hlaing HtakeKhaung. "Removal of noise by median filtering in image processing." 6th Parallel Soft Comput. (PSC 2011) (2011): 1-3.
- [118] Karnewar, Jaykumar S., and Milind V. Sarode. "The combined effect of median and FIR filter in pre-processing of ECG signal using MATLAB." International journal of computer applications 975 (2013): 8887.
- [119] Gupta V, Priya T, Yadav AK, Pachori RB and Rajendra Acharya U. Automated detection of focal EEG signals using features extracted from flexible analytic wavelet transform. Pattern Recognit Lett 2017; 94:180–8.
- [120] Güner S, Cebeci Hİ, Antunes JJM and Wanke PF. Sustainable efficiency drivers in Eurasian airports: Fuzzy NDEA approach based on Shannon's entropy. J Air TranspManag2021; 92.
- [121] AydIn S, Saraoğlu HM and Kara S. Log energy entropy-Based EEG classification with multilayer neural networks in seizure. Ann Biomed Eng 2009; 37:2626–30.
- [122] Sharma, Vikas, and Anand Parey. "A review of gear fault diagnosis using various condition indicators." Procedia Engineering 144 (2016): 253-263.
- [123] Parey A, El Badaoui M, Guillet F and Tandon N. Dynamic modelling of spur gear pair and application of empirical mode decomposition-based statistical analysis for early detection of localized tooth defect. J Sound Vib; 2006; 294:547–61.
- [124] Kao LJ and Chiu CC. Application of integrated recurrent neural network with multivariate adaptive regression splines on SPC-EPC process. J Manuf Syst 2020; 57:109–18.
- [125] Esmael B, Arnaout A, Fruhwirth R, Thonhauser G. A statistical feature-based approach for operations recognition in drilling time series. International Journal of Computer Information Systems and Industrial Management Applications. 2012;4(6):100-8.
- [126] Zhou X, Lin J, Zhang Z, Shao Z, Chen S and Liu H. Improved itracker combined with bidirectional long short-term memory for 3D gaze estimation using appearance cues. Neurocomputing2020b; 390:217–25.
- [127] Askarzadeh A. A novel metaheuristic method for solving constrained engineering optimization problems: Crow search algorithm. Comput Struct2016; 169:1–12.
- [128] Beno MM, R VI, M SS and Rajakumar BR. Threshold prediction for segmenting tumour from brain MRI scans. Int J Imaging SystTechnol2014; 24:129–37.
- [129] Thomas R and Rangachar M. Hybrid Optimization based DBN for Face

- Recognition using Low-Resolution Images. Multimedia Research 2018.
- [130] Shareef SM and Rao RS. A hybrid learning algorithm for optimal reactive power dispatch under unbalanced conditions. Journal of Computational Mechanics, Power System and Control (JCMPS), 1(1), 2018; 26-33.
- [131] Devagnanam J and Elango NM. Optimal resource allocation of cluster using hybrid grey wolf and cuckoo search algorithm in cloud computing. Journal of Networking and Communication Systems, 3(1), 2020; 31-40.
- [132] Ramteke, D.S., Pachori, R.B. &Parey, A. Automated Gearbox Fault Diagnosis Using Entropy-Based Features in Flexible Analytic Wavelet Transform (FAWT) Domain. J. Vib. Eng. Technol. 9, 1703–1713 (2021).
- [133] Chen ZQ, Li C and Sanchez RV. Gearbox Fault Identification and Classification with Convolutional Neural Networks. Shock and Vibration 2015.
- [134] Chen X, Yang X, Zuo MJ, Tian Z (2021). Planetary gearbox dynamic modeling considering bearing clearance and sun gear tooth crack. Sensors. 21(8):2638. https://doi.org/10.3390/s21082638
- [135] Zhang F, Sun W, Wang H, Xu T (2021). Fault diagnosis of a wind turbine gearbox based on improved variational mode algorithm and information entropy. Entropy. 23(7):794. https://doi.org/10.3390/e23070794
- [136] Han H, Ma H, Wang H, Zhu J, Li Z, Liu Z (2022). Dynamic Simulation of Cracked Spiral Bevel Gear Pair Considering Assembly Errors. Machines. 10(10):929. https://doi.org/10.3390/machines10100929
- [137] Mohammed SA, Ghazaly NM, Abdo J (2022). Fault diagnosis of crack on gearbox using vibration-based approaches. Symm. 14(2):417. https://doi.org/10.3390/sym14020417
- [138] Liu Y, Dou S, Du Y, Wang Z (2023). Gearbox Fault Diagnosis Based on Gramian Angular Field and CSKD-ResNeXt. Electron. 12(11):2475. https://doi.org/10.3390/electronics12112475
- [139] Cheng Z, Gao M, Liang X, Liu L (2020). Incipient fault detection for the planetary gearbox in rotorcraft based on a statistical metric of the analog tachometer signal.

 Meas J Int Meas Confed. 151:107069. https://doi.org/10.1016/j.measurement.2019.107069
- [140] Ding J, Xiao D, Li X (2020). Gear fault diagnosis based on genetic mutation particle swarm optimization VMD and probabilistic neural network algorithm. IEEE Access. 8:18456-74. https://doi.org/10.1109/ACCESS.2020.2968382

- [141] Li T, Zhao Z, Sun C, Yan R, Chen X (2021). Domain adversarial graph convolutional network for fault diagnosis under variable working conditions. IEEE Trans Instrum Meas.70:1-0. https://doi.org/10.1109/TIM.2021.3075016
- [142] Jorani RM, Haddar M, Chaari F, Haddar M (2023). Gear Crack Detection Based on Vibration Analysis Techniques and Statistical Process Control Charts (SPCC). Machines. 11(2):312. https://doi.org/10.3390/machines11020312
- [143] Brito LC, Susto GA, Brito JN, Duarte MA (2022). An explainable artificial intelligence approach for unsupervised fault detection and diagnosis in rotating machinery. Mech Syst Signal Process. 163:108105. https://doi.org/10.1016/j.ymssp.2021.108105
- [144] Yu J, Liu X (2022). One-dimensional residual convolutional auto-encoder for fault detection in complex industrial processes. Int J Prod Res. 60(18):5655-74.
- [145] Chen Y, Liang X, Zuo MJ (2019). Sparse time series modeling of the baseline vibration from a gearbox under time-varying speed condition. Mech Syst Signal Process. 134:106342. https://doi.org/10.1016/j.ymssp.2019.106342
- [146] Ma Y, Jia X, Bai H, Wang G, Liu G, Guo C (2020). A new fault diagnosis method using deep belief network and compressive sensing. J Vibroengineering. 22(1):83-97. https://doi.org/10.21595/jve.2019.20850
- [147] Chen, Zihan. "Rolling bearing fault diagnosis with compressed signals based on hybrid compressive sensing." Journal of Vibroengineering 24, no. 1 (2022): 18-29.
- [148] Wu Y, Noonan JP, Agaian S (2011). Shannon entropy-based randomness measurement and test for image encryption. https://doi.org/10.1016/j.ins.2012.07.049
- [149] Chen W, Wang Z, Xie H, Yu W (2017). Characterization of surface EMG signal based on fuzzy entropy. IEEE Trans Neural Syst Rehabil Eng. https://doi.org/10.1109/TNSRE.2007.897025
- [150] Liu, Chuliang, Jianping Tan, and Zhonghe Huang. "Maximum correntropy criterion-based blind deconvolution and its application for bearing fault detection." Measurement 191 (2022): 110740.
- [151] Niño-Adan I, Manjarres D, Landa-Torres I, Portillo E (2021). Feature weighting methods: A review. Expert Systems with Applications. 184:115424.
- [152] Rahman MM, Watanobe Y, Nakamura K (2021). A bidirectional LSTM language model for code evaluation and repair. Symmetry. 13(2):247.

- [153] Horng SJ, Chen YH, Run RS, Chen RJ, Lai JL, Sentosal KO (2019). In: Parallel and Distributed Computing, Applications and Technologies, PDCAT Proceedings.
- [154] Ramteke, D. S., Parey, A., & Pachori, R. B. (2023). A New Automated Classification Framework for Gear Fault Diagnosis Using Fourier–Bessel Domain-Based Empirical Wavelet Transform. Machines, 11(12).
- [155] Nakamura, Hisahide, and Yukio Mizuno. "Diagnosis for slight bearing fault in induction motor based on combination of selective features and machine learning." Energies 15, no. 2 (2022): 453.
- [156] Pietrzak, Przemyslaw, Wolkiewicz M (2023) Fault diagnosis of PMSM stator winding based on continuous wavelet transform analysis of stator phase current signal and selected artificial intelligence techniques. Electronics 12(7):1543. https://doi.org/10.3390/electronics12071543
- [157] Aroui, T., Y. Koubaa, and A. Toumi. "Application of feed-forward neural network for induction machine rotor faults diagnostics using stator current." Journal of Electrical Systems (JES) 3, no. 4 (2007): 213-226.
- [158] Shao, Siyu, Yan R, Lu Y, Wang P, Gao RX (2019) DCNN-based multi-signal induction motor fault diagnosis. Trans Instrum Meas 69(6):2658-2669. https://doi:10.1109/TIM.2019.2925247
- [159] Choudhary, Anurag, Mishra RK, Fatima S, Ketan Panigrahi B (2023) Multi-input CNN based vibro-acoustic fusion for accurate fault diagnosis of induction motor. Eng Appl ArtifIntell 120:105872. https://doi: 10.1016/j.engappai.2023.105872
- [160] Sun, Wenjun, Siyu Shao, Rui Zhao, Ruqiang Yan, Xingwu Zhang, and Xuefeng Chen. "A sparse auto-encoder-based deep neural network approach for induction motor faults classification." Measurement 89 (2016): 171-178.
- [161] Ruiz, Jordi-Roger Riba, Antonio Garcia Espinosa, Luís Romeral, and Jordi Cusidó. "Demagnetization diagnosis in permanent magnet synchronous motors under non-stationary speed conditions." Electric power systems research 80, no. 10 (2010): 1277-1285.
- [162] Samiullah, Muhammad, Ali H, Zahoor S, Ali A (2024) Fault Diagnosis on Induction Motor using Machine Learning and Signal Processing. arXiv preprint arXiv:2401.15417.

- [163] Talhaoui, Hicham, Ameid T, Aissa O, Kessal A (2022) Wavelet packet and fuzzy logic theory for automatic fault detection in induction motor. Soft Comput 26(21):11935-11949. https://doi.org/10.1007/s00500-022-07028-5
- [164] Hakim E, Uri S, Bahiuddin I, Arifianto R, Alim Ritonga S (2024) Entropy-Based Feature Extraction and K-Nearest Neighbors for Bearing Fault Detection. Kinetik: Game Technology, Information System, Computer Network, Computing, Electronics, and Control 21-28. https://doi.org/10.22219/kinetik.v9i1.1814
- [165] Elbouchikhi, Elhoussin, Amirat Y, Feld G, Benbouzid M (2018) Generalized likelihood ratio test based approach for stator-fault detection in a PWM inverter-fed induction motor drive. IEEE Trans Industr Electron 66(8):6343-6353. https://doi: 10.1109/TIE.2018.2875665.
- [166] Zhou, K., Diehl, E., & Tang, J. (2023). Deep convolutional generative adversarial network with semi-supervised learning enabled physics elucidation for extended gear fault diagnosis under data limitations. Mechanical Systems and Signal Processing, 185, 109772. https://doi.org/10.1016/j.ymssp.2022.109772
- [167] Xiao, Y., Shao, H., Wang, J., Yan, S., & Liu, B. (2024). Bayesian variational transformer: A generalizable model for rotating machinery fault diagnosis. Mechanical Systems and Signal Processing, 207, 110936. https://doi.org/10.1016/j.ymssp.2023.110936
- [168] Haroun, Smail, Amirouche Nait Seghir, and Said Touati. "Multiple features extraction and selection for detection and classification of stator winding faults." IET Electric Power Applications 12, no. 3 (2018): 339-346.
- [169] Jiang, Sai Biao, Pak Kin Wong, Renchu Guan, Yanchun Liang, and Jia Li. "An efficient fault diagnostic method for three-phase induction motors based on incremental broad learning and non-negative matrix factorization." IEEE Access 7 (2019): 17780-17790.
- [170] Parvathi Sangeetha B, Hemamalini S (2018) Rational-dilation wavelet transform based torque estimation from acoustic signals for fault diagnosis in a three-phase induction motor. IEEE Trans Industr Inform 15(6), 3492-3501. https://doi: 10.1109/TII.2018.2874463
- [171] Fu, Y., Zhong, M., Huang, J., Jiang, Y., Sun, W., Lou, Y., & Yuqing, Z. (2024).
 Denoising Diffusion Probabilistic Model Enhanced Tool Condition Monitoring
 Method Under Imbalanced Conditions. Measurement Science and Technology.

DOI 10.1088/1361-6501/ad86d5

- [172] Gyftakis, Konstantinos N, Spyropoulos DV, Mitronikas ED (2020) Advanced detection of rotor electrical faults in induction motors at start-up. IEEE Transactions on Energy Conversion 36(2):1101-1109. https://doi: 10.1109/TEC.2020.3025786
- [173] Gundewar SK, Kane PV (2021) Condition Monitoring and Fault Diagnosis of Induction Motor. J. Vib. Eng. Technol 9:643–674. https://doi.org/10.1007/s42417-020-00253-y
- [174] Amanuel T, Ghirmay A, Ghebremeskel H, Ghebrehiwet R, Bahlibi W (2021) Comparative Analysis of Signal Processing Techniques for Fault Detection in Three Phase Induction Motor. Journal of Electronics and Informatics 3:61-76. https://doi.org/10.36548/jei.2021.1.006
- [175] Zhou Y, Shang, Q, Guan C (2023) Three-Phase Asynchronous Motor Fault Diagnosis Using Attention Mechanism and Hybrid CNN-MLP By Multi-Sensor Information. IEEE Access 11: 98402-98414. https://doi: 10.1109/AC-CESS.2023.3307770.
- [176] Wu, Na, Wei Y-Q (2013) Research on wavelet energy entropy and its application to harmonic detection in power system. International Journal of Applied Physics and Mathematics 3(1):31. https://doi: 10.7763/IJAPM.2013.V3.168
- [177] Lahkar, Biraj, and Singh J (2022) Twitter Text Sentiment Analysis: A Comparative Study on Unigram and Bigram Feature Extractions. International Research Journal of Engineering and Technology 2022:431–43.
- [178] Ruba T, Tamilselvi R, Parisa Beham M, Gayathri M. (2023) Segmentation of a Brain Tumour using Modified LinkNet Architecture from MRI Images. Journal of Innovative Image Processing 5(2):161-180. https://doi: 10.36548/jiip.2023.2.007
- [179] Ding, Kevin PL, Martin S, Li B (2020) Improving batch normalization with skewness reduction for deep neural networks. 2020 25th International Conference on Pattern Recognition (ICPR)7165-7172. https://doi.org/10.1109/ICPR48806.2021.9412949
- [180] Yin, Lifeng, Hong P, Zheng G, Chen H, Deng W. (2022) A novel image recognition method based on DenseNet and DPRN. Applied Sciences 12(9):4232. https://doi.org/10.3390/app12094232.
- [181] Hu, Yang; Li, Xudong (2019), "bearing and gearbox data for fault diagnostics

- application", Politecnico di Milano, V1, doi: 10.17632/fkp3nn4tp7.1.
- [182] Chen, Xiaohan, Beike Zhang, and Dong Gao. "Bearing fault diagnosis base on multi-scale CNN and LSTM model." Journal of Intelligent Manufacturing 32, no. 4 (2021): 971-987.
- [183] Abid, Firas Ben, MarwenSallem, and Ahmed Braham. "Optimized SWPT and decision tree for incipient bearing fault diagnosis." In 2019 19th International Conference on Sciences and Techniques of Automatic Control and Computer Engineering (STA), pp. 231-236. IEEE, 2019.
- [184] Horng SJ, Chen YH, Run RS, Chen RJ, Lai JL, Sentosal KO (2019). In: Parallel and Distributed Computing, Applications and Technologies, PDCAT Proceedings.

LIST OF PUBLICATIONS

- 1. **Andhale, Y.,** Parey, A. Gearbox fault detection using entropy-based feature extraction and hybrid classifier. *Proceedings of the Institution of Mechanical Engineers, Part D: Journal of Automobile Engineering.* 2024; https://doi.org/10.1177/09544070241305703. IF: 1.5
- Andhale, Y., Parey, A. Enhanced CEEMDAN-Based Deep Hybrid Model for Automated Gear Crack Detection. J. Vib. Eng. Technol. (2024). https://doi.org/10.1007/s42417-024-01532-8. IF:2.1
- 3. **Andhale, Y.,** Parey, A. Modified LinkNet and DenseNet-Based Hybrid Architecture for Combined Fault Detection in an Electromechanical System. *J. Vib. Eng. Technol.* https://doi.org/10.1007/s42417-024-01589-5. IF:2.1